



PhD-FSTM-2026-010  
The Faculty of Science, Technology and Medicine

## DISSERTATION

Defence held on 03/02/2026 in Luxembourg

to obtain the degree of

DOCTEUR DE L'UNIVERSITÉ DU LUXEMBOURG  
EN SCIENCES DE L'INGÉNIEUR

by

**Maxence PAOLETTI**  
Born on 6 August 1996 in Arlon, Belgium

LOAD TRANSFER MECHANISMS OF  
STEEL-CONCRETE COMPOSITE COLUMNS WITH  
CIRCULAR REINFORCED COMPOSITE DOWELS

### Dissertation defence committee

Prof. Dr. Markus Schäfer, dissertation supervisor  
*Professor, Université du Luxembourg*

Prof. Dr. Numa Joy Bertola, Chairman  
*Professor, Université du Luxembourg*

Prof. Dr. Marko Pavlovic, Vice-chairman  
*Professor, Technische Universiteit Delft*

Prof. Dr. Wolfgang Kurz  
*Professor, Rheinland-Pfälzische Technische Universität Kaiserslautern-Landau*

Prof. Dr. Steffen Anders  
*Professor, Bergische Universität Wuppertal*



# Statement of originality

*I declare that this thesis:*

- is the result of my own work. Any contribution from any other party, and any use of generative artificial intelligence technologies, have been duly cited and acknowledged;
- is not substantially the same as any other that I have submitted, and
- is not being concurrently submitted for a degree, diploma, or other qualification at the University of Luxembourg or any other University or similar institution except as specified in the text.

*With my approval, I furthermore confirm the following:*

- I have adhered to the rules set out in the University of Luxembourg's Code of Conduct and the Doctoral Education Agreement, in particular with regard to Research Integrity.
- I have documented all methods, data, and processes truthfully and fully.
- I have mentioned all the significant contributors to the work.
- I am aware that the work may be screened electronically for originality.

I acknowledge that if any issues are raised regarding good research practices based on the review of the thesis, the examination may be postponed pending the outcome of any investigation of such issues. If a degree was conferred, any such subsequently discovered issues may result in the cancellation of the degree.



# Acknowledgments

This thesis is the result of nearly four years of research conducted at the University of Luxembourg within the *LinCoCo* project, funded by the Luxembourg National Research Fund through an AFR Individual grant. Along the way, I was fortunate to receive help, encouragement, and expertise from many people who made this work possible.

I am especially grateful to *Prof. Markus Schäfer*, my supervisor, for his invaluable guidance and steady support throughout my academic journey. I also sincerely appreciate the opportunity to pursue this research, the resources and encouragement he provided, and, in particular, the independence and academic freedom he trusted me with throughout the development of this thesis.

I would also like to express my sincere appreciation to the CET and Jury members, *Prof. Markus Schäfer*, *Prof. Wolfgang Kurz*, *Prof. Steffen Anders*, *Prof. Numa Bertola*, and *Prof. Marko Pavlovic*, for their feedback and continued support throughout this project, and for the time they devoted to reading and reviewing this thesis.

To the laboratory team—*Gilbert Klein*, *Mehdi Saeidi*, *Marc Seil*, *Cyrille Inglebert*, *Ken Adam*, *Vicente Reis*, *Claude Colle*, and *Ilcho Jandreeski*—thank you for your technical expertise, practical support, and constructive input, which were essential for the experimental work. I also warmly thank *John Gurski* and his team at the University of Wuppertal for their availability and assistance during the testing of the final specimens.

I am grateful to *Dr. Renata Obiala*, *Riccardo Zanon*, *Omer Anwaar*, and *Rui Matos* from Arcelor-Mittal Luxembourg for their support with the procurement and delivery of materials for the experimental programme, as well as for their helpful advice and continued assistance throughout the project.

I would like to thank my colleagues and former colleagues—*Tom Berna*, *Riccardo Zanon*, *Dr. Firat Yolaçan*, *Dr. Pellumb Zogu*, *Dr. Qiuni Fu*, *Sonia Daneshgari*, *Dr. Özgün Ergün*, *Monica Louie*, and *Dr. Jovan Fodor*—for your support and the engaging discussions that made this journey both enriching and enjoyable.

Most of all, I am deeply grateful to my family, my friends, and *Eva* for making these years feel lighter and more joyful. To my parents: thank you for your constant support, your encouragement, and your calm confidence in me throughout my years of study and the writing of this thesis. To my friends: thank you for the laughter, the encouragement, and the countless good moments that kept me grounded. And to *Eva*: thank you for your patience, for always being there for me, and for putting up with my bad jokes—more often than anyone should have to.



# Abstract

Concrete-encased steel (CES) composite columns with H-shaped steel cores are increasingly used in high-rise and heavily loaded structures because they combine high strength, stiffness, and fire resistance. In these members, load introduction zones are critical, as shear transfer between steel and concrete governs composite action. Current design provisions treat the steel-concrete bond very conservatively and rely on headed studs, which become inefficient in high-strength concrete and require dense arrangements to carry high interface shear.

This thesis investigates circular reinforced composite dowel (CRCD) connectors acting together with natural bond in CES columns, particularly when connectors are placed on both the web and the flanges of H-shaped profiles. CRCD connectors are formed by pre-perforating the steel element and placing a traversing rebar through the opening before concreting. The aim is to quantify the combined contribution of bond and CRCD connectors to shear transfer, identify the governing failure mechanisms and slip capacity, and develop predictive models, including reliability assessment, for load-introduction zones in CES columns.

To this end, 45 specific push-out tests were carried out on 15 configurations with HEB 200 and HEA 360 sections. The test matrix covered pure-bond specimens; single and multiple CRCD connectors on the web; connectors on the flanges; and combined web+flange layouts, using normal- and high-strength concrete and systematically varying the number of connectors, their spacing, the opening diameter, and the rebar diameter. A three-dimensional nonlinear finite element model in ABAQUS was calibrated against these tests and used for a parametric study on connector geometry and layout. On this basis, a semi-empirical equation was derived for the connection shear resistance, calibrated by reliability analysis in line with EN 1990. Additional expressions were proposed to estimate the stiffness, associated with the adhesion, and the slip capacity, to support geometric optimisation of connectors on both the web and the flanges.

The results show that CRCD connectors markedly enhance shear transfer compared to pure bond, and that placing connectors on the flanges is mechanically feasible even with limited cover, enabling higher connector density over a given embedded length. In HEB 200 specimens, the web and flanges layout achieved up to 101% higher plateau resistance than a comparable web-only configuration. The finite element model accurately reproduced the ultimate and plateau resistance and captured the observed failure modes. The semi-empirical resistance model predicts test results with an average error of about 7% and supports a design partial safety factor of 1.62 within the investigated parameter range.

**Keywords:** load introduction zone, circular reinforced composite dowel, steel-concrete bond



# List of Publications

The work presented in this thesis has led to the following publications:

## Journal Articles

1. Paoletti, M., & Schäfer, M. (2024). *Transfer of shear force in circular reinforced composite dowel: A review*. *Structures*. Elsevier Ltd. doi.org/10.1016/j.istruc.2024.106992
2. Zanon, R., Schäfer, M., Paoletti, M., Ruiz, G., de la Rosa, A., & Wolf, S. (2025). *Push-out tests on steel sections encased in steel fibre reinforced concrete*. *Steel Construction*. Ernst&Sohn. doi.org/10.1002/stco.202400038
3. Paoletti, M., & Schäfer, M. (2026). *Shear behaviour of composite shear connectors for load introduction zone in concrete-encased steel composite columns*. *Journal of Building Engineering*. Elsevier Ltd. (Under Review)
4. Paoletti, M., & Schäfer, M. (2025). *Experimental and numerical investigation of composite shear connectors on flanges and web in concrete-encased steel columns*. *Structures*. Elsevier Ltd. (Submitted)

## Conference Papers

1. Paoletti, M. (2023). *Load introduction zone connection in composite columns*. *Proceedings of the Young Engineers Colloquium*. IABSE. Dresden, Germany.
2. Paoletti, M., & Schäfer, M. (2023). *Load transfer of circular reinforced composite dowel connector: a comparison of existing analytical equations*. *Proceedings of Eurosteel 2023*. Ernst&Sohn. Amsterdam, Netherlands. doi.org/10.1002/cepa.2613
3. Paoletti, M., & Schäfer, M. (2025). *Improving shear transfer in composite columns with reinforced composite dowel connectors*. *Proceedings of the 10<sup>th</sup> International Conference on Composite Construction*. Blaine, USA.

As a result, some figures, tables, and parts of text can overlap. The listed papers and articles have been published before the publication date of the final version of this thesis.



# Contents

<b>Acknowledgments</b>	<b>v</b>
<b>Abstract</b>	<b>vii</b>
<b>List of Publications</b>	<b>ix</b>
<b>Symbols</b>	<b>xxv</b>
<b>Abbreviations</b>	<b>xxxix</b>
<b>1 Introduction</b>	<b>1</b>
1.1 Motivation . . . . .	1
1.2 Objectives . . . . .	4
1.3 Scope and domain of validity . . . . .	5
1.4 Structure . . . . .	6
<b>2 State of the Art</b>	<b>9</b>
2.1 Load introduction zone . . . . .	9
2.1.1 Conclusion . . . . .	13
2.2 High-strength concrete . . . . .	14
2.2.1 General . . . . .	14
2.2.2 Mechanical properties . . . . .	15
2.2.3 Conclusion . . . . .	16
2.3 Bond interaction . . . . .	17
2.3.1 General . . . . .	17
2.3.2 Normative aspect . . . . .	18
2.3.3 Parametric analysis . . . . .	19
2.3.4 Conclusion . . . . .	21
2.4 Circular reinforced composite dowel . . . . .	21
2.4.1 Rib-type . . . . .	23
First investigations . . . . .	23
Mechanical model . . . . .	23
Concrete dowel action . . . . .	24
Composite dowel action . . . . .	26
2.4.2 Plug-in-type . . . . .	28
2.4.3 Conclusion . . . . .	28

2.5	Group of shear connectors . . . . .	29
	Steel strips positioned in parallel . . . . .	29
	Overlapping of stresses . . . . .	30
	Load distribution over the connectors . . . . .	31
2.5.1	Conclusion . . . . .	33
2.6	Synthesis and research gap . . . . .	34
2.6.1	Summary of the state of the art . . . . .	34
2.6.2	Identified research gaps . . . . .	34
<b>3</b>	<b>Experimental Investigations</b>	<b>37</b>
3.1	Overview of test specimens . . . . .	37
3.2	Production of specimens . . . . .	42
3.3	Materials . . . . .	43
3.3.1	Concrete . . . . .	43
3.3.2	Structural steel . . . . .	45
3.3.3	Steel reinforcement . . . . .	45
3.4	Test setup . . . . .	46
3.5	Instrumentation . . . . .	48
3.5.1	Extensometer . . . . .	48
3.5.2	Strain gauges . . . . .	49
3.6	Loading procedure . . . . .	51
3.7	Results and discussion . . . . .	53
3.7.1	Steel-concrete interfacial bond . . . . .	53
	Load-slip behavior . . . . .	54
	Cyclic loading behavior . . . . .	57
	Crack patterns . . . . .	58
	Discussion . . . . .	59
3.7.2	Multiple connectors on web and connectors spacing . . . . .	61
	Load-slip behavior . . . . .	62
	Cyclic loading behavior . . . . .	69
	Impact of the strain gauges . . . . .	69
	Post-peak stiffness . . . . .	70
	Crack patterns . . . . .	72
	Shear connector failure . . . . .	73
	Strains distribution . . . . .	74
	Discussion . . . . .	78
3.7.3	Shear connectors layout on web and scale-up . . . . .	81
	Load-slip behavior . . . . .	81
	Cyclic loading behavior . . . . .	83
	Post-peak stiffness . . . . .	83
	Crack patterns . . . . .	84
	Shear connector failure . . . . .	85

	Discussion . . . . .	85
3.7.4	Shear connectors on flanges and scale-up . . . . .	86
	Load-slip behavior . . . . .	87
	Cyclic loading behavior . . . . .	88
	Post-peak stiffness . . . . .	88
	Crack patterns . . . . .	89
	Shear connector failure . . . . .	89
	Discussion . . . . .	90
3.7.5	Shear connectors on the web + flanges and scale-up . . . . .	90
	Load-slip behavior . . . . .	91
	Cyclic loading behavior . . . . .	92
	Post-peak stiffness . . . . .	93
	Crack patterns . . . . .	94
	Shear connector failure . . . . .	94
	Discussion . . . . .	96
3.8	Summary and conclusions . . . . .	98
<b>4</b>	<b>Numerical Investigations</b>	<b>101</b>
4.1	Finite element model . . . . .	101
4.1.1	General . . . . .	101
4.1.2	Materials modeling . . . . .	105
	Concrete . . . . .	105
	Traversing rebar . . . . .	106
	Structural steel . . . . .	107
	Reinforcement . . . . .	107
	Cohesive layer . . . . .	107
4.2	Model validation . . . . .	108
4.3	Model sensitivity . . . . .	112
4.3.1	General . . . . .	113
	Symmetric model . . . . .	113
	Mesh size . . . . .	113
	Quasi-static loading and mass scaling . . . . .	114
4.3.2	Interaction . . . . .	115
	Steel–concrete interface . . . . .	115
	Traversing rebar–concrete interface . . . . .	115
	Lateral pressure . . . . .	115
4.3.3	Concrete block . . . . .	116
	CDP model parameters . . . . .	116
	Concrete compressive and tensile strength . . . . .	116
4.3.4	Traversing rebar . . . . .	117
4.3.5	Cohesive layer . . . . .	117
4.4	Numerical analysis . . . . .	118

4.4.1	Decomposition of the shear resistance components . . . . .	118
4.4.2	Analysis of the adhesion interface . . . . .	121
4.4.3	Analysis of the traversing rebar failure . . . . .	122
4.4.4	Analysis of the stress distribution along the traversing rebar . . . . .	123
4.4.5	Study of the position of the reinforcement in the opening . . . . .	123
4.5	Parametric study . . . . .	124
4.5.1	Impact of the traversing rebar diameter . . . . .	125
4.5.2	Impact of the opening diameter . . . . .	126
4.5.3	Impact of the traversing rebar steel grade . . . . .	127
4.5.4	Impact of the web and flange thickness . . . . .	127
4.5.5	Impact of the concrete compressive strength . . . . .	129
4.5.6	Impact of the concrete cover . . . . .	130
4.5.7	Impact of connectors layout . . . . .	131
	Connectors on web . . . . .	131
	Connectors on flanges . . . . .	133
	Connectors on web & flanges . . . . .	134
4.5.8	Conclusions from the parametric study . . . . .	136
<b>5</b>	<b>Semi-Empirical Model</b> . . . . .	<b>139</b>
5.1	Existing analytical models . . . . .	139
5.2	Proposed semi-empirical model . . . . .	141
5.2.1	Evaluation of the stiffness . . . . .	143
5.2.2	Determination of the interfacial friction resistance . . . . .	145
5.2.3	Calculation of the resistance of CRCD connectors . . . . .	146
	Considering the group of shear connectors . . . . .	146
	Determining the strength components . . . . .	148
	Considering the resistance of the steel profile . . . . .	150
	Adding the impact of the steel element thickness . . . . .	151
	Considering shear connectors on the web and the flanges . . . . .	153
5.2.4	Prediction of the resistance for CRCD connectors combined with friction . . . . .	154
5.2.5	Prediction of the slip capacity of the shear connectors . . . . .	156
5.3	Statistical evaluation of the proposed semi-empirical model . . . . .	158
5.3.1	Design assisted by testing for calibrating the shear resistance of the connectors combined with friction . . . . .	159
5.3.2	Design assisted by testing for calibrating the stiffness . . . . .	164
5.4	Discussion on the limits of the proposed model . . . . .	165
5.4.1	Limits related to the steel surface treatment . . . . .	165
5.4.2	Limits to the introduced parameters in the developed model . . . . .	165
5.4.3	Assumption regarding the adhesion contribution to initial stiffness . . . . .	166
5.5	Design considerations . . . . .	168
5.5.1	Shear connection . . . . .	168
5.5.2	Detailing and constructability . . . . .	170

<b>6 Conclusion</b>	<b>173</b>
6.1 Conclusion . . . . .	173
6.1.1 Main contributions . . . . .	173
6.1.2 Exploratory contributions . . . . .	175
6.1.3 Limitations . . . . .	176
6.2 Future research . . . . .	177
Material variations . . . . .	177
Geometrical variations and detailing . . . . .	177
Structural configurations and full-scale behaviour . . . . .	177
Long-term and cyclic performance . . . . .	178
Analytical and numerical methods . . . . .	178
Design and practical implementation . . . . .	178
<b>A Energy balance of FEA</b>	<b>179</b>
<b>B Results from the design model</b>	<b>181</b>
B.1 CRCD resistance: prediction <i>vs.</i> FE results . . . . .	182
B.2 CRCD + friction resistance: prediction <i>vs.</i> test results . . . . .	183
B.3 Statistical assessment according to EN1990 . . . . .	184
<b>C Design example</b>	<b>185</b>
C.1 Considering headed stud shear connectors . . . . .	186
C.1.1 Design of composite connectors . . . . .	186
C.1.2 Verification of steel strength . . . . .	187
C.1.3 Verification of shear resistance of concrete surfaces . . . . .	187
C.2 Considering circular reinforced composite dowel shear connectors . . . . .	189
C.2.1 Design of composite connectors . . . . .	189
Only on the web . . . . .	189
On the web and the flanges . . . . .	190
C.2.2 Verification of steel strength . . . . .	192
C.2.3 Verification of shear resistance of concrete surfaces . . . . .	192
Only on the web . . . . .	192
On the web and the flanges . . . . .	194
C.3 Conclusion . . . . .	195
<b>Bibliography</b>	<b>197</b>



# List of Figures

1.1	Steel-concrete composite construction details. . . . .	2
2.1	Different load introduction ways into CES columns: (a) steel connection; (b) concrete connection; and (c) composite connection (Sauerborn and Kretz, 2018). . . . .	10
2.2	Stress-deformation relationship for normal- and high-strength concrete. . . . .	15
2.3	Drying and autogenous shrinkage for normal-strength concrete and high-performance concrete (fib, 2008). . . . .	16
2.4	Shear transfer mechanisms by pure bonding: a) different components of the bond resistance (Goralski and Hegger, 2006; Johansson, 2003); b) typical bond stress-slip curve (Wang et al., 2019). . . . .	17
2.5	Configuration of a specific push-out test and the load distribution along the steel profile for different load levels (Roeder, Chmielowski, and Brown, 1999). . . . .	18
2.6	Representation of the highly confined concrete zones depending on the steel profile section (Chen and Lin, 2006). . . . .	20
2.7	Types of composite dowels according to 1-102 (2022). . . . .	21
2.8	Different types of CRCD shear connectors. . . . .	22
2.9	First test on continuous connector developed by Leonhardt et al. (1987). . . . .	23
2.10	Mechanical model for: (a) concrete dowel connector; and (b) reinforced composite connector. . . . .	24
2.11	Mechanical model of a concrete dowel: a) global representation; b) diagram of stress action on the concrete dowel; c) concrete dowel in shear. . . . .	25
2.12	Influence of the rib thickness on the concrete dowel failure mode. . . . .	25
2.13	Influence of the relative opening size compared to the rebar diameter in the failure mode: (a) large opening compared to the rebar diameter; (b) almost equal diameter of opening and the rebar. . . . .	27
2.14	Comparison of the failure mode of CRCD connectors in function of the concrete compressive strength. . . . .	28
2.15	Different types of group connectors for composite dowel connectors: a) multiple connectors on a steel strip; b) multiple connectors on parallel steel strips; c) multiple connectors positioned on web and flanges of an H-shape steel profile. . . . .	30
2.16	Stresses in grouped concrete dowel connectors and their intensification as connector spacing decreases. . . . .	31
2.17	Distribution of loads between each connector considering an increasing load from 400kN to a relative slip between steel and concrete of 2mm. Experimental results from Zhang et al. (2017a) specimen G60-20. . . . .	32

3.1	Description of the experimental specimens with HEB200. . . . .	39
3.2	Description of the experimental specimens with HEA360. . . . .	40
3.3	Production of the specimens. . . . .	42
3.4	Test set-up in Luxembourg. . . . .	47
3.5	Test set-up in Wuppertal. . . . .	47
3.6	Positions of the displacement transducers. . . . .	48
3.7	Coordinates of the LVDTs positions. . . . .	49
3.8	Positions of the strain gauges on series B1, C1, C2, and C4. . . . .	50
3.9	Details of the installation of the strain gauges. . . . .	50
3.10	General loading procedure. . . . .	52
3.11	Loading procedure with recording of the stiffness of the shear connector(s). . . . .	53
3.12	Load-slip curve for series A1, A2 and A3. . . . .	55
3.13	Stick-slip behavior. . . . .	56
3.14	Cyclic loading for series A1, A2 and A3. . . . .	58
3.15	Crack patterns for series A1, A2 and A3. . . . .	58
3.16	Impact of the concrete compressive strength on series relying on bond only with a HEB200. . . . .	59
3.17	Influence of the cross-section size on bond resistance. . . . .	60
3.18	Load-slip curve for series B1, B2, C1, C2, C3, C4, and C5, featuring a HEB 200 section. . . . .	63
3.19	Static load-slip curve for series B1, B2, C1, C2, C3, C4, and C5, featuring a HEB 200 section. . . . .	64
3.20	Construction of the "static" load-slip curve to consider the effect of concrete relaxation. . . . .	65
3.21	Typical load-slip curve. . . . .	65
3.22	Cyclic loading for series B1, B2, C1, C2, C3, C4, and C5. . . . .	69
3.23	Representation of epoxy and sanded zones. . . . .	70
3.24	Post-peak stiffness of specimen B2.3. . . . .	71
3.25	Post-peak stiffness of specimen C3.3. . . . .	71
3.26	Post-peak stiffness of specimen C5.3. . . . .	72
3.27	Crack patterns for series B1, B2, C1, C2, C3, C4 and C5. . . . .	73
3.28	Failure mode of a CRCD connector. . . . .	74
3.29	Plastic deformation of the steel web. . . . .	74
3.30	Comparison of strain distribution for different loading along the length. . . . .	75
3.31	Comparison of strain distribution for different loading along the perimeter of spec- imen C2.3. . . . .	76
3.32	Comparison of strains distribution with the applied load for different strain gauge positions. . . . .	77
3.33	Impact of the number and distance of multiple CRCD connectors on the shear force. . . . .	78
3.34	Comparison of the shear force-slip curves with the concrete grade. . . . .	80
3.35	Load-slip and static load-slip curves for Series D1 and D2. . . . .	82
3.36	Cyclic loading for series D1, and D2. . . . .	83
3.37	Post-peak stiffness of specimen D1.3. . . . .	84
3.38	Post-peak stiffness of specimen D2.3. . . . .	84

3.39	Crack patterns for Series D1 and D2. . . . .	85
3.40	Shear connector failure for Series D1. . . . .	85
3.41	Analysis of Series D1 and D2. . . . .	86
3.42	Load-slip and static load-slip curves for Series E1. . . . .	87
3.43	Cyclic loading for series E1. . . . .	88
3.44	Post-peak stiffness for Series E1. . . . .	89
3.45	Crack patterns for Series E1. . . . .	89
3.46	Shear connector failure for Series E1. . . . .	90
3.47	Load-slip and static load-slip curves for Series F1 and F2. . . . .	91
3.48	Cyclic loading for series F1, and F2. . . . .	93
3.49	Post-peak stiffness for series F1. . . . .	93
3.50	Post-peak stiffness for Series F2. . . . .	94
3.51	Crack patterns for Series F1 and F2. . . . .	94
3.52	Shear connector failure for series F2. . . . .	95
3.53	Shear connector failure for series F1. . . . .	95
3.54	Analysis of Series F2 and C5. . . . .	96
3.55	Analysis of Series F1, D1 and E1. . . . .	97
4.1	Description of the finite element model. . . . .	101
4.2	Mesh, boundary conditions, and contacts of the numerical model. . . . .	102
4.3	Shear forces components when considering CRCD connectors with friction. . . . .	103
4.4	Shear strength of the different components in function of the number of connectors for concrete compressive strength C50/60 and C80/95. . . . .	104
4.5	Simplification of the FE model for an easier mesh. . . . .	105
4.6	Stress-strain curves for the concrete under (a) compression, and (b) tension. . . . .	106
4.7	Stress-strain curves for steel: (a) traversing rebar, (b) structural steel, and (c) rein- forcement. . . . .	107
4.8	Stress-strain curves for adhesion bond. . . . .	108
4.9	Comparison of the experimental and the FEA shear-slip curves for all Series. . . . .	110
4.10	Comparison between the average of Series A2, without shear connector, and B2, with a shear connector. . . . .	111
4.11	Comparison of the experimental and the FEA failure modes. . . . .	112
4.12	Impact of the half model assumption and the mesh size in the most critical elements: concrete dowel and traversing rebar. . . . .	114
4.13	Comparison for series C2 between: (a) the internal (ALLIE), kinetic (ALLKE), and artificial (ALLAE) energies; (b) the mass scaling factors. . . . .	114
4.14	Influence of different parameters impacting the steel-concrete interaction. . . . .	116
4.15	Impact of the parameters from the CDP model. . . . .	116
4.16	Influence of the concrete compressive and tensile strength. . . . .	117
4.17	Impact of the parameters for the shear and ductile damage for metals. . . . .	117
4.18	Impact of the parameters of the cohesive behavior. . . . .	118

4.19	Decomposition of the load shear-slip curve in the different shear components for Series C2. . . . .	119
4.20	Decomposition of the load shear-slip curve in the different shear components for all Series. . . . .	120
4.21	Distribution of the bond stress for different loading in series C3. . . . .	121
4.22	Distribution of the stiffness degradation for different loading in series C3. . . . .	121
4.23	Failure mechanism of the traversing rebar in series C3. . . . .	122
4.24	Von Mises and shear stress of the traversing rebar for Series C2. . . . .	123
4.25	Impact of the position of the traversing on the rebar in the opening. . . . .	124
4.26	Impact of the traversing rebar diameter. . . . .	126
4.27	Impact of the opening diameter. . . . .	127
4.28	Impact of the steel grade of the traversing rebar. . . . .	127
4.29	Impact of the thickness of the web. . . . .	128
4.30	Impact of the thickness of the flanges. . . . .	129
4.31	Impact of the concrete cover on the shear resistance of CRCD connectors positioned on the flanges. . . . .	131
4.32	Comparison of different configurations with one row of CRCD connectors on the web. . . . .	132
4.33	Comparison of different configurations with one row of CRCD connectors on the web. . . . .	132
4.34	Influence of the layout for connectors on the web. . . . .	133
4.35	Comparison of different configurations with CRCD connectors on the flanges. . . . .	133
4.36	Comparison of different configurations with 4 CRCD connectors. . . . .	134
4.37	Comparison of CRCD on web, on flanges, and combined for a constant embedded length. . . . .	134
4.38	Comparison of different configurations with one row of CRCD connectors on the web. . . . .	135
5.1	Semi-empirical model for predicting the shear resistance of CRCD connectors combined with bond, compared to a typical shear-slip curve from tests (see Chapter 3). . . . .	141
5.2	Procedure to determine the stiffness and the plateau resistance according to the proposed semi-empirical model. . . . .	142
5.3	Variation of stiffness with the number of connectors. . . . .	143
5.4	Variation of the stiffness with the product of the concrete compressive strength and the embedded surface. . . . .	144
5.5	Coefficient $\varphi$ in function of the number of connectors . . . . .	148
5.6	Representation of the resisting components in a CRCD connector: (a) undeformed situation stated in an additive model; (b) real situation stated in a composite model. . . . .	149
5.7	Coefficient $\alpha$ as a function of the concrete compressive strength. . . . .	150
5.8	Impact of the thickness of the steel element and the traversing rebar on the failure mode. . . . .	151

5.9	Ratio $\beta/\sqrt{d_s/t}$ in function of the ratio $\sqrt{d_s/t}$ . . . . .	152
5.10	Comparison of the shear resistance prediction for CRCD connectors with the results from FEA. . . . .	154
5.11	Comparison of the shear resistance prediction, for CRCD connectors combined with the bond, with the results from experiments. . . . .	155
5.12	Comparison of the developed semi-empirical model with the experimental results. . . . .	156
5.13	Evaluation of the slip capacity $s$ with the geometrical parameters of the CRCD connectors. . . . .	157
5.14	Comparison between theoretical and experimental resistance and statistical results of the reliability analysis . . . . .	163
5.15	Comparison between theoretical and experimental stiffness and statistical results of the reliability analysis . . . . .	164
A.1	Comparison between the internal (ALLIE), kinetic (ALLKE), and artificial (ALLAE) energies for all series. . . . .	180
C.1	Detail of the load introduction zone. . . . .	185
C.2	Detail of the concrete-encased steel section. . . . .	186
C.3	Sections where to verify the shear resistance of the concrete surfaces. . . . .	188
C.4	Detail of the load introduction zone for CRCD connectors positioned on the web. . . . .	190
C.5	Detail of the load introduction zone for CRCD connectors positioned on the web and the flanges. . . . .	191
C.6	Detail of the different areas in the concrete-encased steel section. . . . .	193



# List of Tables

3.1	Overview of the tested configurations with a HEB 200. . . . .	38
3.2	Overview of the tested configurations with a HEA 360. . . . .	39
3.3	Detailed description of the specimens. . . . .	41
3.4	Description of the concrete composition. . . . .	43
3.5	Summary of the concrete mechanical properties. . . . .	44
3.6	Relationship between concrete compressive strength on cylinders and cubes. . . . .	45
3.7	Mechanical properties of the steel profiles. . . . .	45
3.8	Mechanical properties of the reinforcement bars for the first phase. . . . .	46
3.9	Mechanical properties of the reinforcement bars for the second phase. . . . .	46
3.10	Description of the series relying only on bond resistance. . . . .	54
3.11	Results for series relying only on the bond resistance. . . . .	57
3.12	Summary of the series A2 and A3 comparing the section size impact on the bond resistance. . . . .	61
3.13	Description of the series with multiple connectors on the web of HEB200. . . . .	62
3.14	Experimental results for series with multiple CRCD connectors on the web of HEB200. . . . .	68
3.15	Experimental results for series with multiple CRCD connectors on the web of HEA360. . . . .	83
3.16	Experimental results for series with multiple CRCD connectors on the flanges of HEA360. . . . .	88
3.17	Experimental results for series with multiple CRCD connectors on the web and the flanges. . . . .	92
3.18	Summary of the main failure modes for each series. . . . .	99
4.1	Mechanical properties of adhesion at the steel–concrete interface. . . . .	108
4.2	Results from the finite element analysis and the error compared to the experimental tests. . . . .	109
5.1	Analytical equations to predict the resistance of rib-type and plug-in-type CRCD connectors. . . . .	140
5.2	Specimen considered to evaluation the parameter $\varphi$ . . . . .	147
5.3	Limits of the basic variables $X_i$ in the representative test database. . . . .	159
5.4	Mean values and coefficient of variation of the basic variables $X_i$ . . . . .	160
5.5	Analysis of the SLS characteristic load to the adhesion resistance and cycling load. . . . .	167
B.1	Comparison between the predictions of the CRCD connectors resistance by the proposed equations and FE results. . . . .	182

B.2	Comparison between the predictions of the CRCD connectors combined with friction resistances by the proposed equations and test results. . . . .	183
B.3	Statistical analysis of current equations. . . . .	184

# Symbols

## Global quantities

$EA$	Axial stiffness of the composite member
$EI$	Flexural stiffness of the composite member
$L$	Total length of the column or specimen (global)
$\lambda$	Slenderness ratio of the column
$N_{Ed}$	Design axial load in the composite column
$N_{Rd}$	Design axial resistance of the composite column
$N_c$	Axial load carried by concrete in the composite section
$N_s$	Axial load carried by steel in the composite section
$M$	Bending moment in the composite member (global)
$V_{Ed}$	Design shear force of the shear connection
$V_{Rd}$	Design shear resistance of the shear connection
$s$	Relative slip between steel and concrete
$s_{ser}$	Slip at serviceability load level
$s_u$	Ultimate slip capacity of the connection
$s_f$	Failure slip capacity of the shear connectors
$s_r$	Slip at the beginning of residual load
$k_s$	Initial (secant) shear stiffness of the connection
$P$	Shear load transferred across the interface (generic)
$P_u$	Ultimate shear resistance of a specimen
$P_p$	Plateau shear resistance of a specimen
$P_r$	Residual shear resistance of a specimen
$P(s)$	Shear resistance at a prescribed slip $s$ (e.g. $P(2 \text{ mm})$ )
$\Delta$	Axial shortening of the column
$G_k$	Characteristic permanent action
$Q_k$	Characteristic variable action
$P_{SLS}$	Shear load at characteristic serviceability limit state
$f_{ck}$	Characteristic cylinder compressive strength of concrete
$f_{cm}$	Mean cylinder compressive strength of concrete
$f_c$	Measured/used concrete compressive strength (context-dependent in the- sis)
$E_c$	Modulus of elasticity of concrete
$E_s$	Modulus of elasticity of steel (profile or rebar)

$f_{ct,sp}$	Measured concrete tensile splitting strength on cylinder
$f_{ct,fl}$	Measured concrete tensile flexural strength on prism
$f_{ctm}$	Mean concrete tensile strength
$f_y$	Yield strength of steel (generic)
$f_u$	Ultimate tensile strength of steel (generic)
$R_{p0,2}$	Yield strength of the steel at 0.2% proof strain
$R_m$	Ultimate tensile strength of the steel
$A$	Elongation capacity of steel
$\tau_u$	Ultimate shear strength (adhesion and friction)
$\tau_r$	Residual shear strength (friction)

## Geometry and connector parameters

$d_s$	Diameter of traversing rebar (CRCD connector, generic)
$d_{s,w}$	Diameter of traversing rebar for connectors on the web
$d_{s,f}$	Diameter of traversing rebar for connectors on the flange
$d_c$	Diameter of circular opening in the steel element (generic)
$d_{c,w}$	Diameter of opening in the web
$d_{c,f}$	Diameter of opening in the flange
$t_w$	Thickness of the steel web
$t_f$	Thickness of the steel flange
$t$	Generic steel thickness of steel profile (web or flange)
$n$	Total number of CRCD connectors in a specimen
$n_w$	Number of CRCD connectors placed on the web
$n_f$	Number of CRCD connectors placed on the flanges
$A_s$	Cross-sectional area of traversing rebar (generic)
$A_{s,w}$	Area of traversing rebar for a web connector
$A_{s,f}$	Area of traversing rebar for a flange connector
$A_c$	Effective concrete dowel area engaged by a connector (generic)
$A_{c,w}$	Effective concrete dowel area engaged by a web connector
$A_{c,f}$	Effective concrete dowel area engaged by a flange connector
$A_b$	Contact area between H-section and reinforced concrete
$d_s/d_c$	Ratio of traversing rebar diameter to opening diameter
$d_s/t$	Ratio of traversing rebar diameter to steel thickness

## Finite element model

$\mu$	Friction coefficient at the steel-concrete interface
$p$	Effective lateral pressure on concrete
$\tau_r$	Bond/friction shear stress at the steel-concrete interface (often $\tau_r = \mu p$ )
$P_{friction}$	Shear resistance contribution from steel-concrete friction
$\sigma_c$	Concrete compressive stress

$\sigma_t$	Concrete tensile stress
$\varepsilon_1$	Strain at ultimate concrete compressive strength in adopted law
$\zeta$	Normalized strain $\zeta = \varepsilon / \varepsilon_1$
$n$	Concrete-law parameter, $n = \varepsilon_1 E_c / f_{cm}$
$G_F$	Concrete fracture energy (tension softening)
$w_1$	Crack opening at end of first softening branch, $w_1 = G_F / f_{ctm}$
$w_c$	Crack opening at zero stress, $w_c = 5G_F / f_{ctm}$
$d_c$	Concrete damage parameter in compression
$d_t$	Concrete damage parameter in tension
$\epsilon$	CDP flow potential curvature
$f_{b0} / f_{c0}$	CDP biaxial/uniaxial compressive strength ratio
$\psi$	CDP dilation angle
$K_c$	CDP ratio of the second stress invariant on the tensile meridian to that on the compressive meridian
$\varepsilon_{sh}$	Strain at start of strain hardening (trilinear law)
$\varepsilon_u$	Ultimate strain of steel
$\bar{\varepsilon}_{pl}^0$	Equivalent plastic strain at onset of damage
$\varepsilon_{pl}^n$	Uniaxial plastic strain at onset of damage
$\theta$	Stress triaxiality
$\theta_s$	Shear stress ratio used in shear damage calibration
$\bar{u}_{pl}^f$	Displacement at failure in damage evolution law
$L_{ch}$	FE characteristic length used in $\bar{u}_{pl}^f = 10 \bar{\varepsilon}_{pl}^0 L_{ch}$
$K_{nn}$	Cohesive normal elastic stiffness
$K_{ss}, K_{tt}$	Cohesive shear elastic stiffness in the two local shear directions
$t_{nn}$	Nominal stress in normal direction
$t_{ss}, t_{tt}$	Nominal stresses in the two shear directions

## Semi-empirical model

$P_{exp}$	Experimental shear resistance from push-out tests
$P_{FEA}$	Shear resistance obtained from finite element analysis
$P_{pred}$	Shear resistance predicted by the semi-empirical model
$P_{p,exp}$	Experimental plateau resistance (including friction and connectors)
$P_{p,pred}$	Predicted plateau resistance from the semi-empirical model
$P_{CRCD,1}$	Ultimate shear resistance of a single CRCD connector
$P_{CRCD,n}$	Approximate shear resistance of a group of $n$ CRCD connectors
$P_{CRCD,exp}$	Experimental resistance of the CRCD connector group
$P_{CRCD,n,2}$	Refined predicted resistance of the CRCD group (including thickness factor)
$P_{c,1}$	Concrete dowel contribution to resistance of a single connector
$P_{s,1}$	Rebar contribution to resistance of a single connector
$P_{c,1,w}$	Concrete contribution for a single connector on the web
$P_{s,1,w}$	Rebar contribution for a single connector on the web

$P_{c,1,f}$	Concrete contribution for a single connector on the flange
$P_{s,1,f}$	Rebar contribution for a single connector on the flange
$P_{Rk}$	Characteristic shear resistance of connector group combined with friction
$P_{Rd}$	Design shear resistance derived from $P_{Rk}$
$P_{Rk,conservative}$	Conservative characteristic resistance
$k_{s,k}$	Characteristic stiffness
$k_{s,d}$	Design stiffness
$s_{FEA}$	Slip capacity obtained from FE analysis
$k_{exp}$	Experimental initial stiffness of the connection
$k_{pred}$	Predicted initial stiffness from the semi-empirical model
$s_{pred}$	Predicted slip capacity from the semi-empirical model
$\eta$	Proportionality parameter in $k_{s,pred} = \eta f_c A_b$
$k$	Stiffness parameter
$\alpha$	Reduction coefficient for effective concrete strength in dowel action
$\varphi$	Group-effect reduction factor for connector resistance
$\beta$	Coefficient accounting for influence of thickness $t$
$f_{sm,w}$	Mean yield strength of traversing rebar in the web
$f_{sm,f}$	Mean yield strength of traversing rebar in the flange
$f_{sk,w}$	Characteristic yield strength of traversing rebar in the web
$f_{sk,f}$	Characteristic yield strength of traversing rebar in the flange
$f_{uk}$	Characteristic ultimate tensile strength of structural steel
$f_{um}$	Mean ultimate tensile strength of steel profile

## Statistical and reliability notation

$r$	Generic resistance random variable
$r_t$	Theoretical resistance predicted by the model
$g_{r_i}(X)$	Resistance function of the basic-variable vector $X$
$r_e$	Experimental resistance
$r_m$	Mean resistance
$r_k$	Characteristic resistance
$r_d$	Design resistance
$r_n$	Nominal resistance computed with nominal basic-variable values
$b$	Mean correction factor so that $r = b r_t \delta$
$b_{LS}$	Least-squares estimate of the correction factor
$\delta$	Model error random variable
$\Delta$	Natural logarithm of model error, $\Delta = \ln \delta$
$s_{\Delta}^2$	Sample variance of $\Delta$
$V_r$	Coefficient of variation of total resistance $r$
$V_{r_t}$	Coefficient of variation of theoretical resistance $r_t$ (basic variables)
$V_{\delta}$	Coefficient of variation of model error $\delta$
$V_{X_i}$	Coefficient of variation of basic variable $X_i$

$X$	Vector of basic variables entering the resistance function
$X_m$	Mean value vector of basic variables
$\rho$	Correlation coefficient between experimental and predicted values
$\sigma_{r_e}$	Standard deviation of experimental resistance sample
$\sigma_{r_t}$	Standard deviation of theoretical resistance sample
$Q_\delta$	Lognormal dispersion parameter associated with $V_\delta$
$Q_{rt}$	Lognormal dispersion parameter associated with $V_{rt}$
$Q$	Lognormal dispersion parameter associated with $V_r$
$\alpha_\delta$	Allocation factor of total variability associated with model error
$\alpha_{rt}$	Allocation factor of total variability associated with basic variables
$k(p)$	Fractile factor of the $t$ -distribution for probability $p$
$t_p(\nu)$	$p$ -fractile of the $t$ -distribution with $\nu$ dof
$\nu$	Degrees of freedom for $t$ distribution
$k_n$	Characteristic fractile factor for finite sample size
$k_{d,n}$	Design fractile factor for finite sample size
$k_\infty$	Asymptotic fractile factor for infinite sample size
$k_{d,\infty}$	Design fractile factor for infinite sample size
$\gamma_M$	Partial safety factor
$\gamma_M^*$	Corrected partial safety factor when nominal values are used
$\gamma_V$	Partial safety factor for shear connectors
$\gamma_{Ri}$	Partial safety factor class
$k_c$	Correction factor, ratio of the nominal and characteristic resistance
VAR	Variance operator
CoV	Coefficient of variation (generic)



# Abbreviations

CRCD	Circular Reinforced Concrete Dowel
CES	Concrete-Encased Steel
CFST	Concrete-Filled Steel Tube
HSC	High-Strength Concrete
LVDT	Linear Variable Differential Transformer
NSC	Normal-Strength Concrete
SCM	Supplementary cementitious Materials
UHPC	Ultra-High Performance Concrete
FE	Finite Element
FEM	Finite Element Method
FEA	Finite Element Analysis
CDP	Concrete Damage Plasticity (constitutive model in ABAQUS)
ULS	Ultimate Limit State
SLS	Serviceability Limit State
ACI	American Concrete Institute
AIJ	Architectural Institute of Japan
AISC	American Institute of Steel Construction
EC2	Eurocode 2: Design of Concrete Structures
EC3	Eurocode 3: Design of Steel Structures
EC4	Eurocode 4: Design of Composite Steel and Concrete Structures
HEA	European wide-flange H-beam, type A
HEB	European wide-flange H-beam, type B



## Chapter 1

# Introduction

### 1.1 Motivation

The construction industry is facing increasing challenges related to climate change, including higher embodied carbon requirements and the need to reduce greenhouse gas emissions across the entire building lifecycle (Cabeza et al., 2014; Chamasemani et al., 2023). At the same time, concerns about resource depletion and the environmental impact of material extraction are becoming more pressing, driving the industry toward more responsible material use and circular economy strategies (Almusaed et al., 2024). These combined pressures are accelerating the demand for lighter, more efficient, and higher-performing structural elements that can meet sustainability targets while maintaining safety and reliability. As a result, innovative material systems and hybrid structural solutions—such as steel-concrete composites—are increasingly being explored as viable pathways to reduce structural weight and enhance material efficiency (Hegger and Rauscher, 2008).

Steel-concrete composite construction offers an effective solution for achieving slender structural designs with high load-bearing efficiency (Saw and Liew, 2000; Hegger et al., 2009). Among the various composite members, steel-concrete composite columns consist of steel sections that are either encased in or filled with concrete (Fig. 1.1). This thesis focuses on concrete-encased steel (CES) composite columns, which have attracted significant interest in recent years (Moradian and Hassan, 2024; Du et al., 2021) due to their technical and architectural benefits.

A CES column comprises a structural steel core—typically an I-, H-, or built-up section—fully surrounded by reinforced concrete. Combining reinforced concrete (RC) with structural steel offers several advantages over traditional RC or steel members alone (Lacki, Derlatka, and Kasza, 2018). The concrete improves fire resistance and provides lateral restraint to the steel section, thereby mitigating local and global buckling (Lai, Liew, and Hoang, 2019; Johnson, 2004). However, CES columns require longitudinal and transverse reinforcement to prevent spalling of the concrete when subjected to axial load, elevated temperatures, or seismic actions (Mishra and Kumar, 2022; Lai and Liew, 2021). Adequate confinement of the concrete core is essential for the development of sufficient plastic hinge rotation capacity (El-Tawil and Deierlein, 1999). Conversely, the dense reinforcement cage in CES columns can complicate concrete placement, particularly in beam-column connection zones (Mu, Yasojima, and Kanakubo, 2019).

The efficiency of steel-concrete composite columns can be further improved through the use of high-strength materials. Incorporating high-performance concrete or high-strength steel enables

optimisation of column dimensions, increases ultimate load capacity, and enhances economic and resource efficiency (Hegger and Rauscher, 2008). However, high-strength concrete exhibits a more brittle response than normal-strength concrete, which can limit the development of plastic strains in the encased steel section (Hanswille, Schäfer, and Bergmann, 2020; Bogdan et al., 2023). Moreover, concrete spalling becomes a critical concern (Li et al., 2020) and may govern the ultimate resistance of the member. Consequently, numerous research efforts (Lai, Liew, and Hoang, 2019; Ellobody and Young, 2011; Kim et al., 2012) have focused on investigating the global behaviour of CES columns incorporating high-strength materials.

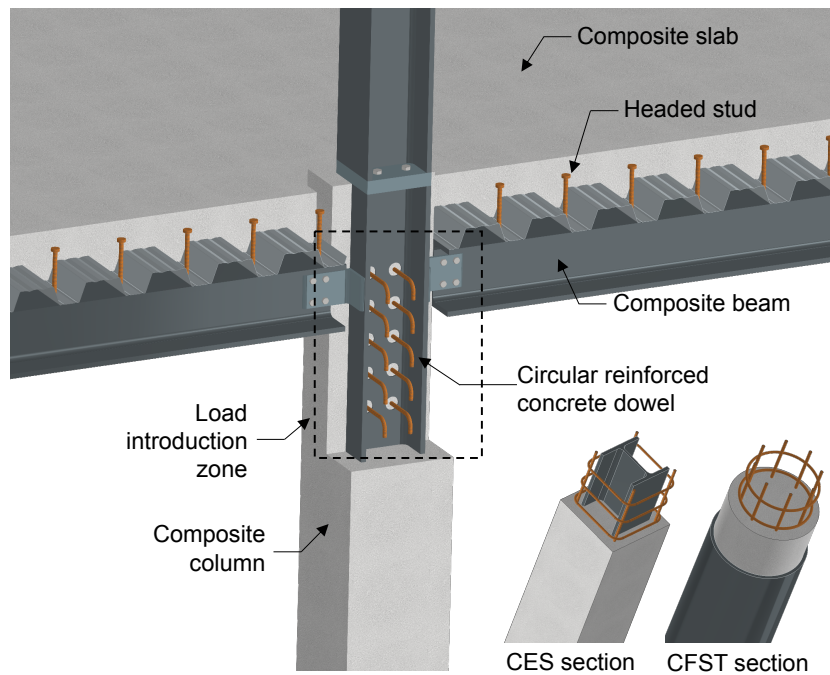


FIGURE 1.1: Steel-concrete composite construction details.

Steel-concrete composite structures rely on efficient shear transfer at the steel–concrete interface to ensure composite action and overall structural integrity (Grzeszykowski, Lewandowski-Szewczyk, and Niedośpiiał, 2023; Jacobs and Hajjar, 2010). Effective transmission of shear forces from the steel core to the surrounding concrete is essential for the development of composite behaviour. When the shear demand exceeds the bond strength of the interface, significant relative slip occurs between the steel and concrete (Papastergiou and Lebet, 2014). The natural bond typically fails in a brittle manner and cannot be re-established once lost.

To mitigate slip and ensure reliable shear transfer, mechanical shear connectors are commonly employed (Roeder, Chmielowski, and Brown, 1999; Alenezi et al., 2015). This requirement is especially critical in the load introduction zones of composite columns or piles, where floor beams connect to the steel profile embedded within the reinforced concrete (Fig. 1.1). In these regions, very large forces must be transferred over short distances, making shear connectors indispensable. The increasing use of high-strength materials further amplifies these demands, resulting in even greater shear forces that must be efficiently transmitted between steel and concrete.

Headed studs (Fig. 1.1), the most commonly used mechanical shear connectors, exhibit unfavorable fatigue performance (Ovuoba and Prinz, 2018), relatively high flexibility, and comparatively low shear resistance (Bonilla et al., 2018). Consequently, they need to be densely arranged to support the greater shear forces, which can create constructability challenges. Their applicability is further limited in high-strength concrete (Hegger et al., 2001; Hegger et al., 2006). To overcome these issues, researchers (Leonhardt et al., 1987) have proposed circular reinforced composite dowel (CRCD) connectors as an alternative (Fig. 1.1). These connectors offer high initial stiffness (Wang et al., 2022) and superior load-bearing capacity while maintaining adequate ductility (Kim et al., 2011; Leng et al., 2024; Rauscher et al., 2006). Experimental studies (He et al., 2016; Tan, Fang, and Xiong, 2022) have demonstrated their effectiveness in group arrangements for bridge girder connections using both normal- and high-strength concrete, and Wang et al. (2022) confirmed the feasibility of integrating these connectors into the web of H-shaped steel profiles in composite compressive members with normal-strength concrete.

From a manufacturing perspective, the openings can be realized on the steel in the factory, eliminating the need for specialised welding equipment and on-site generators. In addition, the reinforcement cage can be installed around the steel profile without spatial interference from the shear connection. These advantages facilitate faster and more cost-effective construction, reducing overall fieldwork requirements (Lee, Shim, and Chang, 2005).

Recent research on CRCD connectors has primarily focused on their mechanical behaviour, often neglecting the contribution of natural bond at the steel–concrete interface. Many experimental studies intentionally eliminate bond effects by greasing the steel surface (Di et al., 2018; Wang et al., 2014) or inserting a thin XPS layer (Su et al., 2014). In real structures, however, untreated steel surfaces contribute significantly to bond resistance. This resistance provides high initial stiffness through adhesion, followed by micro-interlocking and Coulomb friction (Wang et al., 2019). Although adhesion strength exhibits considerable variability (Chrzanowski, 2019; Goralski and Hegger, 2006), it remains a key component of initial rigidity.

Design codes (AIJ, 1991; EN1994-1-1, 2004) primarily account for friction when evaluating shear resistance, often overlooking the beneficial contribution of adhesion to stiffness. Yet increased initial stiffness is crucial for efficient shear transfer and for improving axial load distribution within composite members (Grzeszykowski, Lewandowski-Szewczyk, and Niedoślą, 2023).

By leveraging the high initial stiffness provided by natural adhesion, the serviceability performance of composite compressive members can be markedly improved. However, the reliability of this contribution is highly dependent on the surface condition and treatment of the steel profile (Chrzanowski, 2019; Goralski and Hegger, 2006). In parallel, the strategic placement of CRCD connectors on the web and/or flanges of the steel section can ensure robust shear transfer at the steel–concrete interface, thereby preventing brittle and irreversible failures in the ultimate limit state.

The *LinCoCo* research project (*Load Introduction for Steel-Concrete Composite Columns Using High-Performance Materials*) was initiated to address the key challenges associated with load introduction zones in composite columns. The project investigated a novel approach involving the use of circular reinforced composite dowel shear connectors placed on both the web and flanges of an

H-shaped steel section, while simultaneously utilising the natural interfacial bond between steel and concrete to enhance shear transfer.

A total of 45 push-out specimens were designed and tested. The experimental results served as the basis for calibrating a detailed finite element (FE) model, which was subsequently used to obtain deeper insights into the behaviour and interaction of the underlying shear-transfer mechanisms. The validated FE model also enabled an extensive parametric study, thereby broadening the scope of the experimental work.

Building on the combined numerical and experimental findings, the project developed a semi-empirical model able to predict both the stiffness and resistance of the combined connector-bond system. The model's reliability was statistically evaluated in accordance with EN1990 (2002).

This thesis presents the outcomes of the research project and contributes to advancing the application of high-strength materials in composite construction—ultimately paving the way for lighter structures and a more efficient use of construction materials.

## 1.2 Objectives

The overarching aim of this research project is to investigate the bond at the steel-concrete interface, both on its own and in combination with circular reinforced composite dowel (CRCD) shear connectors placed on the web and flanges of an H-shaped steel section. This work seeks to provide an effective solution for transferring the increasing shear forces that arise in the load introduction zone as structural spans and slenderness ratios grow with the adoption of high-strength materials.

The specific objectives of the project are as follows:

1. **Comprehensive literature review:** Examine existing research on the steel-concrete interfacial bond and the mechanical behavior of composite shear connectors, synthesizing current knowledge and identifying critical research gaps.
2. **Experimental design and specimen production:** Develop the push-out specimen configurations and collaborate with industrial partners to manufacture specimens using high-strength concrete.
3. **Experimental testing campaigns:** Conduct material characterization tests on both steel and concrete, and perform the testing of 45 push-out specimens across three experimental phases.
4. **Numerical investigations:** Develop 3D finite element models to deepen the understanding of the load-transfer mechanisms observed experimentally, and carry out a parametric study to explore configurations beyond the experimental scope.
5. **Analytical investigations:** Propose a semi-empirical model to predict the stiffness and resistance of CRCD connectors in combination with the bond, and statistically evaluate the model using experimental data in accordance with EN1990 (2002).

## 1.3 Scope and domain of validity

The investigations presented in this thesis are restricted to a well-defined set of materials, geometries, and loading conditions. The main elements of this domain of validity are summarized below.

### Materials and surface condition

- Concrete strength classes between C50/60 and C80/95.
- Structural steel sections with sand-blasted and cleaned surfaces; no intentionally rusted, painted, or as-rolled rough steel.
- Concrete cover thicknesses corresponding to the minimum values required by EN1994-1-1 (2004) for the two selected cross-sections.

Because both surface roughness and concrete strength significantly influence the steel–concrete bond and the shear-transfer mechanism, extrapolation of the results to other surface conditions or concrete grades must be made with caution. In addition, perfect uniformity of the steel surface condition across all specimens cannot be guaranteed.

### Geometrical configurations

- Steel profiles limited to HEB 200 and HEA 360 sections.
- Circular reinforced composite dowel (CRCD) connectors investigated in three sizes only.
- Approximate constant ratio between opening diameter and rebar diameter of  $d_c/d_s \approx 3$ .
- Traversing rebars are always placed in a central position within the openings.

As a consequence, the influence of alternative connector geometries, different  $d_c/d_s$  ratios, or eccentric rebar positions is not covered experimentally and is only partially addressed by the numerical parametric study.

### Testing and loading conditions

- Monotonic push-out tests under quasi-static loading.
- No deliberate removal of natural bond at the steel–concrete interface to obtain purely mechanical shear transfer.
- No investigation of geometric imperfections (*e.g.* misalignments, dimensional deviations) or load eccentricities.
- Load introduced only via the steel profile in the push-out tests.

The behavior of CRCD connectors with bonded connections under cyclic or fatigue loading, long-term effects, and the isolated contribution of connectors without bonded connections remains outside the scope of this work.

## Models and analytical formulations

- Finite element models calibrated and validated solely against the experimental dataset generated in this thesis.
- Semi-empirical equations for resistance, stiffness, and slip capacity derived and assessed using the same dataset.

The performance of these models for different geometries, material properties, or loading conditions has not yet been demonstrated and will require further assessment. The design expressions proposed in this thesis should therefore be applied only within the parameter ranges listed above.

These restrictions define the domain of validity of the present work and highlight where additional experimental and numerical research is needed to broaden the applicability and robustness of the findings.

## 1.4 Structure

The thesis begins with the motivation and background for the research before moving to the design, production, and testing of the experimental program. The experimental results are then analyzed and used to calibrate a finite element model. This model is subsequently validated against the experimental findings and employed to conduct an in-depth investigation of the underlying load-transfer mechanisms, as well as to perform a parametric study. The outcomes of both the parametric study and the experiments form the basis for developing a semi-empirical model, which is statistically evaluated in accordance with EN1990 (2002). The thesis concludes with a summary of the key findings and an outlook on future research.

- **Chapter 2: State of the art**

This chapter establishes the foundation for understanding the requirements and constraints governing the load introduction zone. Then, it presents the behavior of high-strength concrete, highlighting its fundamental differences compared with normal-strength concrete. The interfacial bond between steel and concrete, along with the key parameters influencing this bond, is then discussed. Finally, the structural response of a single circular reinforced composite dowel, as well as the collective behavior of groups of shear connectors, is examined.

- **Chapter 3: Experimental Investigations**

Chapter 3 begins by presenting the geometries and production process of the test specimens. The mechanical properties of the constituent materials—concrete, reinforcement steel, and the steel profile—are then characterized. The chapter proceeds with a detailed description of the experimental setup, instrumentation, and loading procedures. Finally, the test results are presented and discussed across five thematic categories: (1) steel-concrete interfacial bond; (2) multiple connectors on the web and connector spacing; (3) shear-connector layout on the web and scale effects; (4) shear connectors on the flanges and scale effects; and (5) shear connectors on both the web and flanges, including scale effects.

- **Chapter 4: Numerical Investigations**

Chapter 4 describes the finite element model developed in ABAQUS, detailing the material constitutive laws, geometric representation, boundary conditions, mesh strategy, and applied loads. The model is validated against the experimental results. A sensitivity study is then performed to assess the influence of key modelling assumptions. The numerical analysis provides deeper insight into the failure mechanisms of both the shear connectors and the interfacial bond—insights that could not be fully captured experimentally. Finally, the chapter presents the parametric study, which investigates a range of geometric variations and connector configurations to extend the findings beyond the tested specimens.

- **Chapter 5: Semi-Empirical Model**

This chapter begins by reviewing the existing equations used to estimate the resistance of circular reinforced composite dowel (CRCDD) shear connectors and highlights the need for a new formulation that accounts for the connector position on both the web and flanges, as well as the contribution of the steel–concrete bond. The proposed semi-empirical model is then introduced and explained in detail. Subsequently, the derivation of the equations for predicting the stiffness and resistance of groups of CRCDD connectors, combined with friction, is presented. The performance of these equations is evaluated by comparing their predictions with the experimental and finite element results. Finally, a statistical assessment of the proposed formulations is carried out in accordance with EN1990 (2002).

- **Chapter 6: Conclusion**

This final chapter provides a comprehensive synthesis of the key findings presented throughout the thesis, highlighting how each chapter contributes to the overall objectives of the work. It also outlines potential directions for future research and opportunities to further advance the understanding and development of the topic.



## Chapter 2

# State of the Art

This chapter presents a review of the current literature relevant to this thesis. Section 2.1 focuses on the structural performance and design challenges associated with the load introduction zone of composite columns—a critical region where external forces are transferred into the steel-concrete composite system. The efficiency of this transfer mechanism is essential for achieving full composite action.

The main objective of this research is to investigate and develop novel shear connectors for use in concrete-encased steel (CES) composite columns as alternatives to the widely used headed stud connectors. Although headed studs are well established in conventional applications, their performance becomes less reliable when used with high-strength concrete (HSC) (Hegger, Gallwoszus, and Rauscher, 2009). Section 2.2 describes the mechanical characteristics of HSC, which differ significantly from those of normal-strength concrete and introduce additional complexities such as reduced ductility and potential fatigue issues affecting the performance of conventional connectors.

The thesis also aims to clarify the role of the natural bond at the steel-concrete interface in the transfer of shear load. Section 2.3 reviews the chemical and mechanical mechanisms governing this interaction and summarizes the key parameters influencing bond performance.

Section 2.4 examines the development of circular reinforced composite dowel (CRCDD) connectors, which originated from the concept of a simple concrete dowel. The subsequent incorporation of a reinforcing bar within the opening fundamentally altered the connector's behavior and improved its mechanical performance. CRCDD connectors were initially developed for beams and later applied to hybrid concrete-steel structures and composite columns.

Finally, because mechanical shear connectors are often arranged in groups to enhance their load-bearing capacity, Section 2.5 reviews current knowledge on group effects. This includes both the potential performance benefits of grouped connectors and the limitations or design challenges associated with their use.

### 2.1 Load introduction zone

The load introduction zone is the region in a steel-concrete composite column where externally applied loads are transferred into the member and redistributed between its constituent materials. Poorly designed load introduction zones can compromise composite action, resulting in slip, insufficient shear transfer, and, in extreme cases, loss of stability. Force transfer in this context refers

to balancing internal forces such that dissimilar materials, such as steel and concrete, act together in a state of composite equilibrium (Jacobs and Hajjar, 2010).

Shear transfer between concrete and steel occurs when the column bends under lateral loads or unequal end moments. It also occurs when axial load is applied to the column through only one of the constituent materials. In the latter case, the shear connection plays a crucial role in redistributing the axial force across all components of the composite element (Grzeszykowski, Lewandowski-Szewczyk, and Niedośpiał, 2023).

Load transfer into concrete-encased steel composite columns can occur in three principal ways, see Fig. 2.1:

- a) **Via a steel connection:** In this configuration, axial load is introduced directly into the structural steel core, commonly through bolted or welded steel plates. The steel section initially resists the applied load, and the subsequent redistribution to the surrounding reinforced concrete occurs via interface shear transfer. This redistribution generates high shear demands at the steel–concrete interface, particularly near the load introduction point. At initial loading ( $t = 0$ ), the concrete is barely cracked and contributes significantly to axial stiffness. As creep and shrinkage develop, however, part of the load shifts towards the steel core. This time-dependent redistribution can exacerbate interface stresses and even lead to premature debonding if shear transfer is inadequate (Sauerborn and Kretz, 2018).

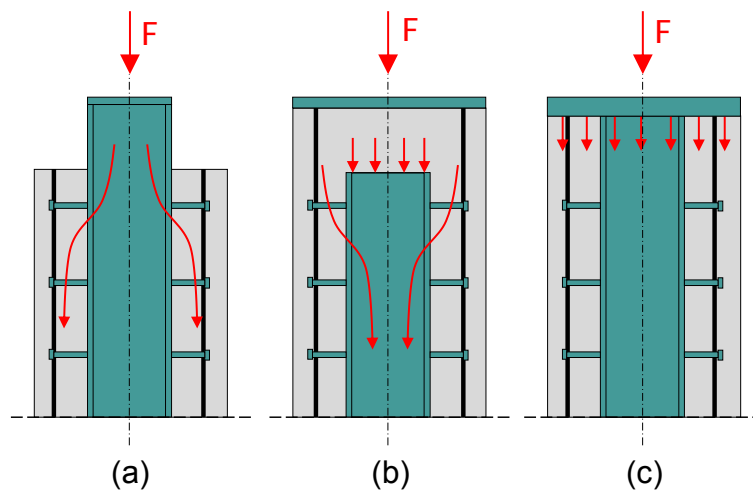


FIGURE 2.1: Different load introduction ways into CES columns: (a) steel connection; (b) concrete connection; and (c) composite connection (Sauerborn and Kretz, 2018).

- b) **Via a concrete connection:** In this approach, the applied load is introduced into the concrete encasement, typically through a reinforced cap or load-spreading block. The force must then be transferred to the embedded steel profile. This scenario is sensitive to the time-dependent behavior of concrete. As concrete undergoes creep and shrinkage, its tensile stiffness decreases, leading to a load shift toward the steel core. As a result, the maximum interface shear force typically occurs at long-term stages ( $t \rightarrow \infty$ ), not at initial loading. The concrete connection method requires careful detailing of the bonding interface and shear connectors to ensure reliable composite action over the column's service life (Sauerborn and Kretz, 2018).

- c) **Via a composite steel–concrete connection:** In this case both materials are engaged simultaneously. A rigid head plate or cast-in-place load-spreading assembly distributes the load to the steel and concrete in proportion to their axial stiffness. Compared with purely steel or concrete load introduction, this method reduces peak interface shear demands and promotes a more uniform stress distribution within the member. Each load path results in a different shear distribution and must be considered in design, particularly with respect to shrinkage, creep, and the development or degradation of bond over time (Sauerborn and Kretz, 2018).

The transfer of shear forces at the steel–concrete interface primarily relies on the natural bond developed by hydration of the concrete on the steel surface, resulting in adhesive and friction resistance. When the design value of longitudinal shear surpasses the design shear strength of this interfacial bond, mechanical shear connectors such as headed studs must be provided (Grzeszykowski and Szmigiera, 2017). Eurocode 4 (EN1994-1-1, 2004) imposes the use of shear connectors in the load introduction zone. Outside this zone, shear connectors may be omitted when the longitudinal shear forces between steel and concrete, as determined by elastic analysis, do not exceed the design bond stresses (Hanswille, Schäfer, and Bergmann, 2020).

AISC (ANSI/AISC360, 2016) recommends evaluating the shear force in proportion to the plastic capacity of the cross-sectional component that receives the transferred axial load. The EN1994-1-1 (2004) addresses this issue, recommending that the maximum shear force be determined from either elastic or plastic theory. Hanswille, Schäfer, and Bergmann (2020) proposes that plastic theory may be used for building columns, provided that the conditions for preventing buckling and for applying the simplified design approach are satisfied.

Shear transfer must occur as quickly as possible to enable full composite action (Jacobs and Hajar, 2010). Dunberry, Leblanc, and Redwood (1987) proposed that, in the ultimate limit state, the load transfer area should not exceed twice the minimum transverse dimension of the composite cross-section above and below the point of load introduction—a recommendation also adopted by the AISC Specification (ANSI/AISC360, 2016). Eurocode 4 (EN1994-1-1, 2004) takes a more conservative approach, limiting the transfer length to the smaller of twice the minimum transverse dimension or one-third of the column’s length.

Design codes focus primarily on the ultimate strength of shear connectors, often neglecting stiffness, which plays a key role at service load levels (Grzeszykowski, Lewandowski-Szewczyk, and Niedośpiał, 2023). In composite columns, the relative slip occurring between steel and concrete may be insufficient for the mechanical shear connectors to fully develop their design strength, raising doubts on their effectiveness (MacRae et al., 2004). Beyond merely resisting shear forces, the connection must also ensure effective distribution of the introduced load among the components of the composite cross-section to achieve proper composite action (Grzeszykowski, Lewandowski-Szewczyk, and Niedośpiał, 2023).

At the serviceability limit state, the requirements for the load introduction zone go beyond the mere avoidance of failure. The shear connection should:

- provide sufficient stiffness to maintain the assumed degree of composite action, so that the axial stiffness  $EA$  and flexural stiffness  $EI$  of the composite column used in global analysis are actually achieved;

- limit relative slip between steel and concrete such that the connection remains predominantly in the elastic range of the load–slip curve (*i.e.* service slip is small compared to the ultimate slip capacity), thereby avoiding excessive residual deformations and damage accumulation;
- ensure an adequately uniform distribution of shear forces between individual connectors along the load introduction length, in particular in long connections where the leading connectors tend to attract higher forces, which is critical for fatigue and long-term performance (Hanswille, Illmann, and Dobelmann, 2024);
- control cracking and local crushing of the concrete around connectors and in the vicinity of the interface, in order to preserve bond and stiffness under repeated loading.

From a modelling point of view, these requirements imply that the interface should be represented by a finite stiffness, derived from an appropriate load–slip relationship at the relevant service load level, rather than as a perfectly rigid bond. This allows the designer to check that a specified fraction of the stiffness-based longitudinal shear demand is actually transferred within the intended load introduction zone (Grzeszykowski, Lewandowski-Szewczyk, and Niedośpiał, 2023).

Recent analytical and numerical studies have shown that the stiffness of the shear connection is not only relevant at serviceability, but also at the ultimate limit state. For realistic axial load levels in slender composite columns, the internal force distribution between steel and concrete is governed by their relative stiffness rather than their plastic capacities. As a result, the longitudinal shear demand in the load introduction zone is more accurately derived from a stiffness-based force allocation than from plastic theory (Grzeszykowski, Lewandowski-Szewczyk, and Niedośpiał, 2023). If the interface is too flexible, only a fraction of this stiffness-based shear can be transferred within the prescribed transfer length, even when the sum of the shear resistances of the connectors exceeds the design shear force. In such cases, part of the load is carried by unintended mechanisms (*e.g.* natural bond outside the designed zone), and the composite cross-section cannot fully mobilise the resistance assumed in design.

From a design perspective, the strength and stiffness of the shear connection fulfill different roles. The strength of individual connectors ensures that local failure is avoided at the ultimate limit state (ULS). The global stiffness of the interface governs (1) how quickly the introduced load is shared between steel and concrete, and (2) how much of the target shear is actually transferred within the load introduction zone. A connection that is strong but too flexible may satisfy strength checks while still providing insufficient composite action over the relevant length of the column. Conversely, a sufficiently stiff connection enables a more effective use of the available shear resistance along the interface (Grzeszykowski, Lewandowski-Szewczyk, and Niedośpiał, 2023).

Both ANSI/AISC360 (2016) and EN1994-1-1 (2004) currently prohibit combining natural bond and mechanical connectors in the design model, due to a lack of understanding of their interaction effects (Wang et al., 2020).

The design of shear connectors follows a rigid-plastic model, where the total connection strength equals the product of the connector resistance  $P_{Rd}$  and the number of connectors  $n$ . This model is valid only when the connectors are sufficiently ductile to redistribute shear forces. For ULS,

ductility is typically verified by a slip capacity of at least 6 mm, or compliance with detailing rules for headed studs (Grzeszykowski, Lewandowski-Szewczyk, and Niedośpiał, 2023).

A paradox arises when the addition of shear studs impairs rather than improves load transfer. Two reasons are proposed: (1) the interference between natural bond and shear studs, which is not accounted for in current design models, may lead to inefficient interaction; and (2) the rigid assumption of the bond interface ignores its actual finite stiffness, which affects early shear behavior (Grzeszykowski, Lewandowski-Szewczyk, and Niedośpiał, 2023).

The conventional rigid–plastic model implicitly assumes an infinitely stiff interface: once the shear demand reaches the design resistance of the connection, the full connector capacity is instantly mobilised, with no associated slip. This simplification is convenient for ULS design, but does not represent the actual behaviour of stud connectors and bond–slip interfaces, which exhibit a pronounced nonlinear load–slip response. In a rigid model, the transfer length collapses to a purely geometric parameter, and the longitudinal shear distribution becomes independent of the actual stiffness of the shear connection. Consequently, such a model cannot capture key phenomena observed in experiments and refined analyses, such as (1) the gradual development of shear along the interface, (2) incomplete shear transfer within the code-prescribed load introduction length, and (3) the strong non-uniformity of stud forces in long connections (Grzeszykowski, Lewandowski-Szewczyk, and Niedośpiał, 2023; Hanswille, Illmann, and Dobelmann, 2024).

Grzeszykowski, Lewandowski-Szewczyk, and Niedośpiał (2023) demonstrated that substantially increasing the stiffness—by an order of magnitude, for example—enables more effective use of the shear connection’s capacity. In general, higher stiffness facilitates more efficient axial load distribution across composite sections. Under larger axial loads, load transfer becomes more effective as the required capacity leads to increased shear-connection stiffness.

Nonetheless, even with increased stiffness, achieving complete shear transfer within the prescribed introduction zone remains challenging. In reality, both natural bond and sparse mechanical connectors contribute to the shear mechanism. The goal is to minimize untransferred shear to preserve composite behavior and structural integrity.

### 2.1.1 Conclusion

The load introduction zone in steel–concrete composite columns is critical because inadequate detailing can lead to poor shear transfer, slip, and loss of composite action. Loads may be introduced into concrete-encased steel columns through the steel core, the concrete encasement, or a combined connection, each generating different interface shear demands and time-dependent effects. Natural bond provides significant shear resistance, but mechanical connectors are required when shear demands exceed bond capacity, as mandated by Eurocode 4 and AISC. Traditional design approaches focus on the ultimate strength of these connectors and adopt a prescribed transfer length, while largely idealising the interface as rigid. Recent research shows, however, that for realistic load levels the distribution of axial forces between steel and concrete—and thus the longitudinal shear demand—is primarily stiffness-controlled, both at serviceability limit state (SLS) and ULS. Ensuring adequate interface stiffness, and understanding its interaction with natural bond, is therefore essential for reliable design of load introduction zones.

## 2.2 High-strength concrete

### 2.2.1 General

Steel-concrete composite structure is a hybrid material composed of steel elements, usually as steel profiles, and reinforced concrete, which is itself a composite material composed of steel reinforcements and concrete. Concrete can be more clearly understood when considered as a composite material composed of aggregate and binder (Caldarone, 2009). High-strength concretes (HSC) contain increased amounts of cementitious materials, often combined with various chemical admixtures and a lower water–cement ratio (ACI, 2010). The primary challenge lies in achieving high mechanical performance while still meeting constructability and durability demands. According to EN1992-1-1 (2023), HSC is defined to have a characteristic compressive strength  $f_{ck} > 50\text{MPa}$ , and a normal-strength concrete  $f_{ck} \leq 50\text{MPa}$ .

Concrete performance depends heavily on the chemical characteristics of its cementitious materials (Caldarone, 2009). Portland cement, the most commonly used type, is produced by heating a mixture of lime, iron, silica, and alumina to about 1400–1550 °C in a rotating kiln, where chemical reactions transform the raw materials. EN197-1 (2000) and EN197-5 (2021) divide the cements into 6 categories depending on the ratio of Portland cement and additional constituents such as blast furnace slag, fly ash, silica fume, or pozzolans.

The addition of supplementary cementitious materials (SCM) to Portland cement plays a significant role in the evolution of HSC. In a classical hydraulic reaction of the Portland cement, the majority of the cement reacts directly to form binding compounds, but around a quarter of the cement will form calcium hydroxide. Pozzolans and latent hydraulic materials react chemically with this byproduct element to create compounds having binding properties. As a result, for the same amount of cement, the binder quantity produced increases, thus increasing the binding capacity of the system. The use of SCM can also benefit from higher early strength, higher late age strength, reduced permeability, lower heat of hydration, and reduced costs (Kosmatka, Kerkhoff, and Panarese, 2002; Sutter, Van Dam, and Munn, 2016).

The mostly used SCMs, *i.e.* fly ash, blast furnace slag, and silica fume, are residues from other industrial processes, improving the sustainability of HSC and decreasing the emissions of carbon dioxide by reducing the quantity of Portland cement (Caldarone, 2009; Sutter, Van Dam, and Munn, 2016). Through the pozzolanic reaction with the byproduct of the hydration reaction of cement, these pozzolans increased the bond between the concrete paste and the aggregate. This results in enhanced compressive strength and improved chemical resistance. Because these particles are much finer than those of Portland cement, they can fill the voids left by free water in the matrix, producing a significantly denser pore structure (ACI, 2010; Sutter, Van Dam, and Munn, 2016). However, some SCMs (and very low  $w/c$ ) can increase water demand for a given workability; high-range water-reducing admixtures (superplasticizers) are therefore commonly used (ACI, 2010).

Aggregates are the second composite material in concrete and have a great influence on the concrete's performance. In high-strength concrete, the interfacial transition zone plays a critical role; therefore, the mechanical properties of the aggregate are decisive (Maso, 1996; Akçaoğlu,

Tokyay, and Çelik, 2004). Taerwe (1992) observed that in HSC, failure planes are more likely to cut through the aggregate particles due to the higher strength of the cement matrix. To enhance the ultimate strength, concrete should act more like a homogeneous material (Neville, 1996). Therefore, aggregates with a similar elastic modulus to cement paste should be chosen. Smaller, angular aggregates with rough surfaces offer a stronger mechanical bond and are therefore better suited for HSC (Neville, 1997).

### 2.2.2 Mechanical properties

Differences between the microstructures of high-strength concrete (HSC) and normal-strength concrete—particularly the stronger bond between hardened cement paste and aggregate—result in HSC exhibiting more brittle and elastic behavior (fib, 2008; ACI, 2010). In HSC, microcracks remain short and do not propagate significantly until the load approaches the ultimate level. Stress is then distributed relatively uniformly among the cracks, leading to sudden, brittle failure. Because cracks in HSC often pass directly through the aggregate grains, brittleness is further increased (Reinhardt, 2000; Rao and Prasad, 2002).

During softening, microcracking develops within a localized fracture zone. The ability of adjacent, uncracked regions to redistribute stress governs the deformation capacity within this zone. As concrete strength increases, this redistribution capacity diminishes, making the material more brittle. This trend is reflected in the steeper post-peak response and reduced ultimate strains characteristic of HSC (fib, 2008; ACI, 2010). As it can be seen in Fig. 2.2, normal-strength concrete has a more ductile behavior than HSC, which shows a brittle failure.

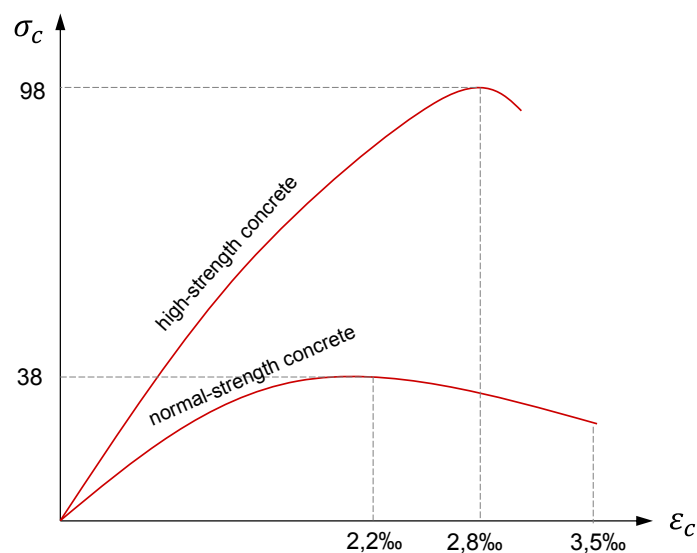


FIGURE 2.2: Stress-deformation relationship for normal- and high-strength concrete.

For higher-strength concretes, increases in compressive strength result in only modest gains in tensile strength (EN1992-1-1, 2023; ACI, 2010). This behavior is partly attributed to the growing brittleness of the cement paste at higher strengths. Because high-strength concrete has a finer, denser pore structure than normal concrete, crack propagation in the paste is less hindered by voids, which promotes the development of internal residual stresses (Rommel, 1994; Mehta and

Monteiro, 2001). In the same way as for normal-strength concrete, multiaxial compression provides higher ultimate strength compared to uniaxial compression. However, this increase in strength due to multiaxial compression decreases when higher concrete grades are considered. This phenomenon will diminish the confinement effect of the concrete dowel in the opening when using HSC.

The pore volume of HSC is significantly lower than that of normal-strength concrete. Since shrinkage is generally linked to the formation and propagation of microcracks, these microcracks may exist as pre-load damage (Guse and Hilsdorf, 1998; Altoubat, 2002) or may form and grow under loading. Owing to its dense microstructure, HSC contains far fewer initial defects and cracks, which results in a more restrained creep response. This reduced creep is primarily due to the higher strength and stiffness and the lower porosity of the hardened cement paste in high-performance concrete. Consequently, all mechanisms contributing to creep are diminished.

Because the hardened cement paste in high-performance concrete is both dense and stiff, the magnitudes of shrinkage and creep deformations are smaller than in normal-strength concrete. While autogenous shrinkage is minor in ordinary concrete, it becomes significantly larger in high-performance concrete, as illustrated in Fig. 2.3. In contrast, drying shrinkage—caused by moisture loss in a dry environment—is greatly reduced in HPC. Overall, total shrinkage, defined as the sum of autogenous and drying shrinkage, remains lower for HPC than for NSC.

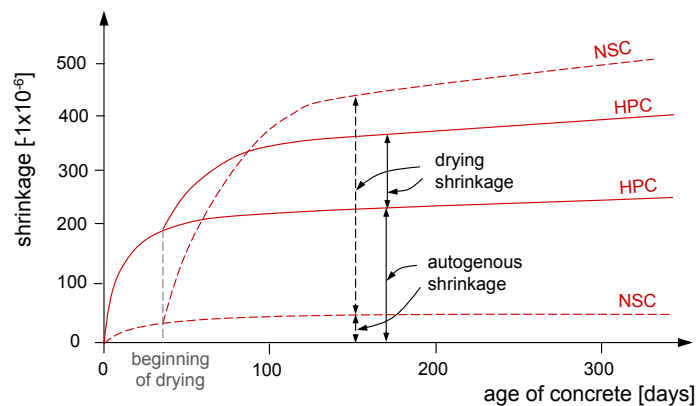


FIGURE 2.3: Drying and autogenous shrinkage for normal-strength concrete and high-performance concrete (fib, 2008).

### 2.2.3 Conclusion

High-strength concrete is achieved by increasing the cement content, reducing the water–cement ratio, incorporating supplementary cementitious materials, and selecting aggregates with stiffness and strength compatible with the cement paste to refine the pore structure and improve the interfacial transition zone. These measures result in a dense and durable matrix with significantly higher compressive strength than normal-strength concrete. However, the same microstructural improvements that provide high stiffness and strength also reduce ductility, increase brittleness, and limit tensile resistance, making the mechanical behavior of HSC fundamentally different from that of conventional mixes.

## 2.3 Bond interaction

### 2.3.1 General

The elementary mechanism for shear transfer in steel-concrete composite elements is the natural bond interaction that occurs at the interface between the steel element and the surrounding concrete. This bond can be classified into three mechanisms (Fig. 2.4a): (1) chemical adhesion, which results from the adhesion of the cementitious binder to the steel surface and is sensitive to slippage; (2) micro-interlocking, which occurs due to the irregular surface of the steel profile (Goralski and Hegger, 2006); and (3) Coulomb friction, which is proportional to the normal pressure and roughness of the surface.

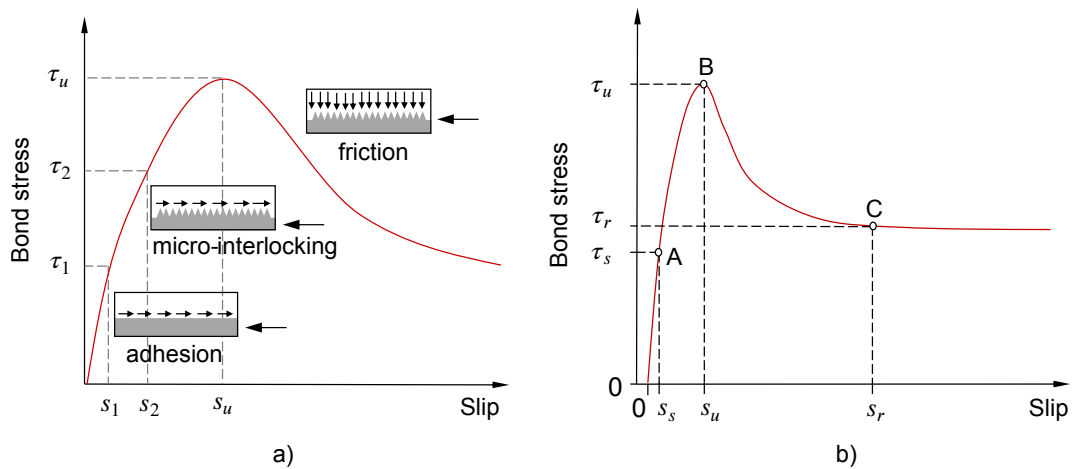


FIGURE 2.4: Shear transfer mechanisms by pure bonding: a) different components of the bond resistance (Goralski and Hegger, 2006; Johansson, 2003); b) typical bond stress-slip curve (Wang et al., 2019).

Numerous studies (Roik, Breit, and Schwalbenhofer, 1984; Roeder, 1985; Wang et al., 2019; Huang et al., 2021; Wang et al., 2023) have been conducted to determine the strength of the bond at the interface between steel and concrete. Indeed, insufficient bond strength can significantly reduce load-bearing capacity and may result in premature buckling failure of the steel profile, causing damage to the surrounding concrete. Previous research has revealed a wide scatter in the experimentally determined adhesion and frictional bond stresses. According to Wium and Lebet (1992) and Wang et al. (2019), the load-slip behavior of the pure bond interaction between a steel element and the surrounding concrete can be described as follows: initially, the bond resistance between steel and concrete is mainly due to chemical adhesion and static friction. Until point A of Fig. 2.4b, a linear behavior is observed, then with the increase in slip, both sliding friction and chemical adhesion collaborate to transmit interfacial shear force until the maximum load resistance is attained at point B. Beyond this threshold, the chemical adhesion begins to slowly degrade along with the load-bearing capability. When a certain load level is reached, the chemical adhesion becomes completely lost, and the load stabilizes at point C based on the contribution of sliding friction.

The experimental results conducted by Roeder (1985), Wium and Lebet (1992), Wang et al. (2019), Huang et al. (2021), and Wang et al. (2023) on an H-shaped steel profile encased in a concrete block showed an exponential distribution of the bond stress along the steel-concrete interface at service load, with the maximum stress located in the loading zone (Fig. 2.5). As the load approached the ultimate capacity of the section, a nearly linear distribution of stress was observed. Assessment of bond stress capacity usually relies on a maximum average stress, assuming a uniform spread along the steel profile. However, because of the exponential stress distribution, the maximum average bond stress should be significantly lower than the maximum local bond stress in the column loading zone. In addition, the length of the contact area between steel and concrete plays a critical role in determining the maximum average bond stress, as the stresses mainly concentrate in the load introduction zone. Thus, a short interface will have a relatively higher maximum average bond stress compared to that of a longer interface. Furthermore, Wang et al. (2019) discovered that the stress of the bond also fluctuates around the perimeter of the steel profile. When cyclic loading is applied, Roeder, Chmielowski, and Brown (1999) observed no deterioration of interface resistance if the loads are less than the slip initiation load, which is about 40% of the maximum load capacity. In contrast, when loads exceeded the slip initiation load, interface degradation became significant as a result of the vulnerability of the adhesion to slippage.

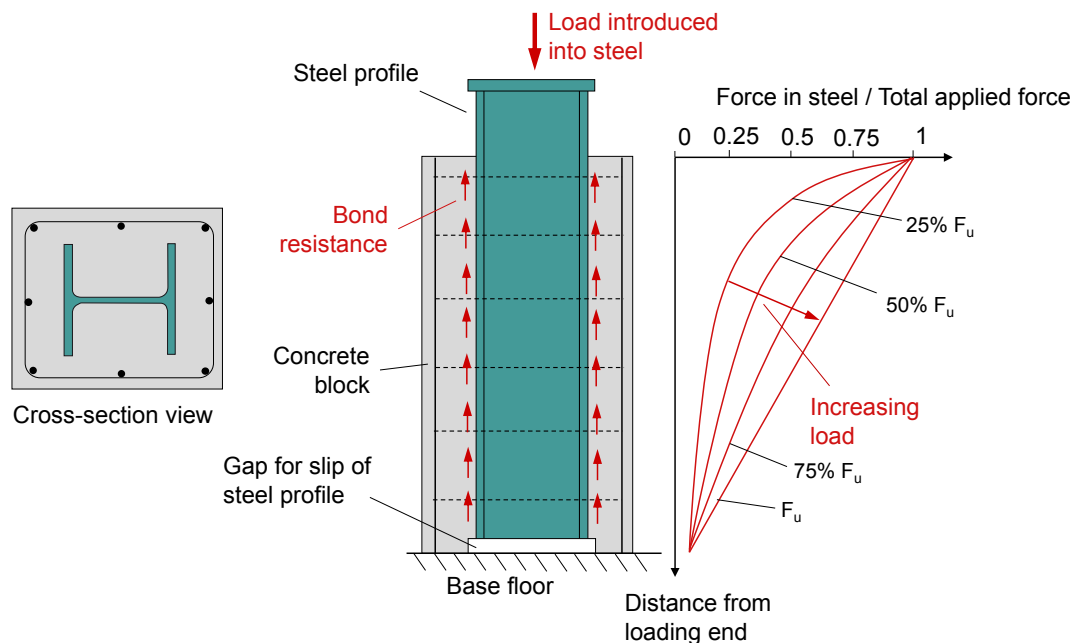


FIGURE 2.5: Configuration of a specific push-out test and the load distribution along the steel profile for different load levels (Roeder, Chmielowski, and Brown, 1999).

### 2.3.2 Normative aspect

Some building design codes have chosen to ignore the natural bond stress at the steel-concrete interface due to the large scatter in the experimental results. For example, ANSI/AISC360 (2016) and JGJ138 (2016) do not consider the resistance to bond. However, other design codes such as EN1994-1-1 (2004) and AS/NZS2327 (2017) consider a value of 0.3 MPa for the bond strength of

fully concrete-encased steel sections, and AIJ (1991) allows a bond stress of a maximum 0.45 MPa. These design codes only take into account the resistance provided by friction for a safe approach.

### 2.3.3 Parametric analysis

In composite beams, shear forces, to ensure the composite action at the interface between steel and concrete, are mainly transmitted using mechanical shear connectors. To evaluate the performance of this connector, it is important to distinguish the component due to the natural bond between steel and concrete surface and the component due to the mechanical connector. Therefore, according to EN1994-1-1 (2004), when push-out tests are carried out, the steel surface is treated to minimize the bond resistance between the two materials. In experimental practice, the forces transferred by steel-concrete bond are often neglected, with the application of grease in the experimental testing to only obtain the resistance of the mechanical shear connector. However, Chrzanowski (2019) proved that these forces are still significant. In concrete-encased steel composite columns, the surface contact between steel and concrete is much larger compared to composite beams since the steel profile is fully embedded in the concrete (not only the top flange). Thus, the bond interaction becomes a major component of the shear capacity of the connection and cannot be neglected.

The bond strength between the steel element and the concrete is influenced by various parameters, as highlighted by Chrzanowski (2019), Huang et al. (2021), Wang et al. (2023), and Zhang et al. (2023). The parameters that impact bond strength comprise steel surface treatment, concrete strength, thickness of concrete cover, level of concrete confinement, specimen geometry, boundary conditions, and time. In addition, uncontrollable parameters of production and casting, such as load application, steel profile imperfections, surface conditions, or environmental conditions, can also influence the bond strength, as shown by Goralski and Hegger (2006). These factors partly explain the large scatter in the bond strength data between the H-shaped steel profile and the surrounding concrete. Hence, as Chrzanowski (2019) concluded, bond strength values determined for one specimen cannot be directly applied to another specimen with a different geometry and conditions.

The main factor influencing the bond resistance between steel and concrete is the surface treatment of the steel (Roik, Breit, and Schwalbenhofer, 1984; Chrzanowski et al., 2019; Wium and Lebet, 1992). As expected in Chrzanowski et al. (2019), samples with rough surfaces, such as rusted steel surfaces or failure scales from the rolling process surface, exhibited greater bond strength than specimens with cleaned surfaces, such as sandblasted or paint thinner. The poorest bond resistance was obtained for the sample with a greased steel surface, although the bond strength between the steel and the concrete was still significant. Experiments conducted by Roik, Breit, and Schwalbenhofer (1984) on H-shaped steel profiles encased in concrete blocks demonstrated that the oiling of the steel surface resulted in a 75% reduction in the strength of the bond compared to the untreated profiles. Chrzanowski (2019) also concluded that the untreated steel surface brings the biggest variation of the bond strength value.

Several studies (Chrzanowski, 2019; Wang et al., 2019; Wium and Lebet, 1992; Huang et al., 2021; Wang et al., 2023; Zhang et al., 2023) have shown that concrete cover has a significant impact

on bond resistance. Increasing the concrete cover can increase the shear capacity and residual bond resistance due to an improvement in the confinement of the concrete surrounding the steel section. However, beyond a certain threshold value of the concrete cover, the confinement effect does not increase the bond behavior anymore. According to the Poisson effect, the application of a vertical load causes the steel section to undergo lateral expansion due to compression, leading to lateral pressure on the surrounding concrete. Greater confinement enhances the normal force on the steel profile, leading to higher friction resistance. Since friction is a component of bond resistance, increasing the concrete cover can improve the initial, ultimate, and residual bond stress between the steel surface and the surrounding concrete.

Wium and Lebet (1992) and Roik, Breit, and Schwalbenhofer (1984) found that as the cross-section size of the steel profile increased, the bond stress transferred to the section at the steel-concrete interface decreased. Specifically, HEB400 profiles achieved up to 50% lower bond stress than HEB200 profiles. Zones between flanges of H-shaped profiles or concrete-filled steel tubes are highly confined (Chen and Lin, 2006), as shown in Fig. 2.6. Therefore, the impact of the scale effect on bond stresses is noticeable, and it decreases as the steel profile section increases.

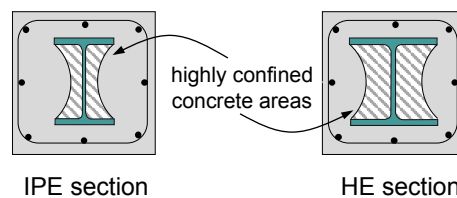


FIGURE 2.6: Representation of the highly confined concrete zones depending on the steel profile section (Chen and Lin, 2006).

According to Wium and Lebet (1992), Wang et al. (2023) and Zhang et al. (2023), increasing the amount of transverse reinforcement improves the confinement of the concrete, enhancing the bonding stress capacity. However, as shown in Roeder, Chmielowski, and Brown (1999), Hawkins (1973) and Huang et al. (2021), concrete confinement has a reduced impact on maximum bond resistance, but it affects post-slip deterioration, which is primarily governed by friction forces. These observations, along with those of Hamdan and Hunaiti (1991), suggest that to ensure satisfactory post-slip behavior, a certain degree of confinement is necessary, but a large amount of confining steel is not required to achieve good bond performance.

The findings of Huang et al. (2021), Wang et al. (2023), and Zhang et al. (2023) have shown that higher concrete compressive strength leads to higher ultimate and residual bond strength. This improvement in shear resistance can be explained by the increase in the chemical bond resistance between steel and the concrete surface with the increase in the concrete class due to an improved cementitious binder. Similar conclusions were obtained by Yoo and Shin (2018) and Shen et al. (2016) for rebars embedded in concrete.

According to Wium and Lebet (1992) and Hunaiti (1991), the age of the specimen can affect the steel-concrete bond. A reduction in bond strength has been observed to be up to 30% for a 360-day specimen compared to a 21-day specimen. This phenomenon was identified as a consequence of the creep and shrinkage effects. As proved by Hawkins (1973), the horizontally cast specimens

exhibited a lower bond capacity compared to those vertically cast. The lower bond capacity was attributed to the segregation of the aggregate and the accumulation of water under the lower flange of the horizontal steel section, which primarily affected the adhesion bond strength.

### 2.3.4 Conclusion

The bond between steel and concrete arises from the combined action of chemical adhesion, micro-interlocking, and Coulomb friction, each contributing differently depending on the load level and slip. Experimental investigations have shown that the performance of this bond is highly variable, with significant scatter in measured stresses. Key parameters such as steel surface treatment, concrete strength, concrete cover, profile size, confinement, casting conditions, and specimen age have been shown to strongly influence bond strength and post-slip behavior. Because of this variability, international design codes have adopted different approaches: some neglect bond resistance entirely for safety, while others prescribe conservative fixed values, typically considering only the frictional contribution. As a result, while the bond provides an essential contribution to shear transfer in steel–concrete composite members, its direct use in design remains simplified and cautious in normative practice.

## 2.4 Circular reinforced composite dowel

Composite dowel shear connectors encompass a broad family of connector types, including the perfobond strip, kombi dowel strip, saw-tooth dowel, puzzle-shaped dowel, and clothoidal dowel, as illustrated in Fig. 2.7. Comprehensive literature reviews of these systems are provided by Heinemeyer (2011), Chrzanowski (2019), and Braun (2018).

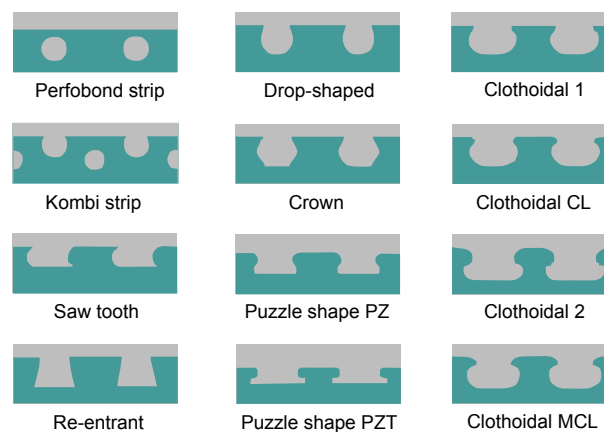


FIGURE 2.7: Types of composite dowels according to 1-102 (2022).

This section focuses on the perfobond shear connector originally developed by Andrä (1990), as it offers the greatest potential for application in H-shaped steel profiles of CES columns with minimal labour intensity. In this thesis, the general term circular reinforced composite dowels (CRCD) is used to refer to this class of connectors.

CRCD shear connectors can be categorized into rib-type and plug-in-type configurations, depending on the relationship between the perforated steel plate and the surrounding concrete (Fig.

2.8). Rib-type CRCDs were developed primarily for transmitting shear forces in composite beams, particularly in bridge construction. They consist of a perforated steel rib welded to the upper flange of a steel girder. Plug-in-type CRCDs are created by perforating the steel structural element that is fully embedded within a concrete block. This results in a fundamentally different mechanical response compared with rib-type systems due to the deeply embedded concrete dowel (Braun, Obiala, and Odenbreit, 2015). Plug-in-type connectors have been investigated in the context of steel–concrete joints for hybrid girders by He et al. (2016) and Zhao et al. (2018). They have also been implemented in notable projects such as the Nujiang Bridge deck (He et al., 2016) and the piles of the Mirna Viaduct (Šavor, 2010). Despite their promising performance, only limited research exists on the use of plug-in-type CRCDs in composite columns. One of the few studies on this topic is the investigation by Wang et al. (2022), which examined their behavior as shear connectors in composite columns.

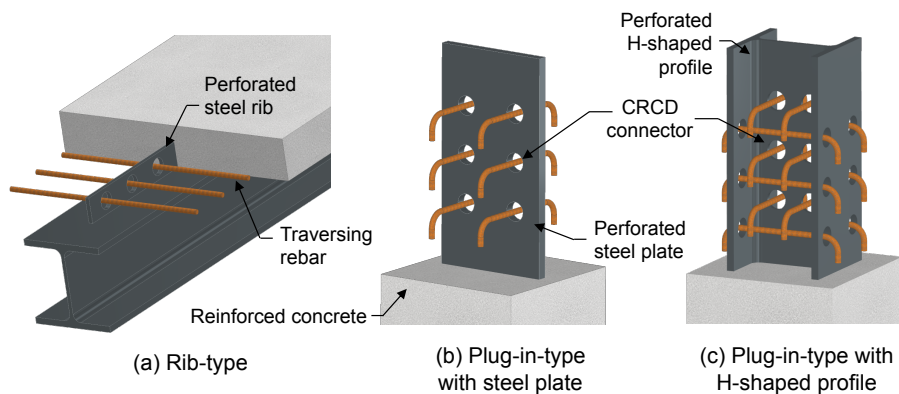


FIGURE 2.8: Different types of CRCD shear connectors.

Rib-type connectors were developed for beam applications requiring high deformation capacity (Fig. 2.8). In push-out tests used to assess their performance, only the behavior of the concrete and/or reinforcing bars is typically considered, while the bond resistance between steel and concrete is intentionally neglected by greasing the steel surfaces because the adhesion phase is brittle. In contrast, plug-in-type connectors are strongly confined by the surrounding steel element and concrete block, producing a pronounced shear-friction effect at the interface. Since the steel element is fully embedded in the concrete, the contact surface between steel and concrete is substantially larger than that of a rib-type connector. Thus, the resistance developed by the bonding interface became a main part of the full strength of the connector. As shown by Chrzanowski et al. (2019), the assumption of neglecting this bonding resistance with grease on the steel surface is not appropriate, especially when considering plug-in-type. Therefore, the performance of plug-in-type connectors is evaluated by a specific push-out characterized by a fully embedded steel element in the concrete block and by considering the full bonding resistance provided by adhesion and friction at the steel-concrete interface.

### 2.4.1 Rib-type

#### First investigations

The development of perfobond connector began in 1985 with Andr a's researches on a new type of continuous connector, used by Leonhardt on a project in 1951, to improve the fatigue behavior of headed studs, as described in Fig. 2.9. Andr a (1990) realized pull-out tests on metal strips punched with rectangular and circular openings embedded in a concrete block. The conclusions showed that the perfobond shear connector, welded to the flange of the steel profile, could act as a shear connector for composite beams. Test results with additional transverse rebars showed a high stiffness and high ductile behavior at larger displacements.

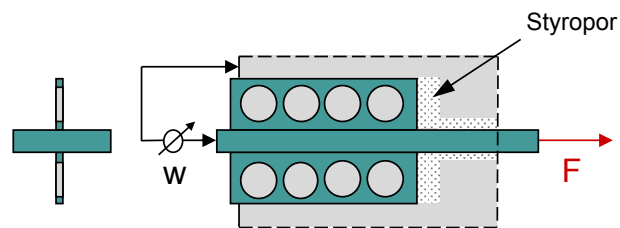


FIGURE 2.9: First test on continuous connector developed by Leonhardt et al. (1987).

The economic potential and technical performance of the shear connector pushed Leonhardt and Andr a to perform further tests (Leonhardt et al., 1987). Dynamic tests highlighted that the perfobond shear connector performed much better than headed studs, *i.e.*, by increasing the load cycles, no increase in slip could be measured. At low load levels, the perfobond acts as a rigid connector, while at increasing load levels, a decrease in stiffness is observed.

#### Mechanical model

Kraus and Wurzer (1997) proposed a mechanical model to describe the load transfer mechanism of concrete dowel connectors. Forces are transmitted from the steel strip to the surrounding concrete by extreme local compression at the contact surface of the opening, see Fig. 2.10a. This area can be distinguished into two zones, A and B. Zone A is characterized by a triaxial compression confining the concrete. This confinement increases the concrete compressive strength and ductility. The pore of the cement zone is the main parameter directing the bearing and deformation behavior of the concrete. With the increase of the load, crushing of the pore sides occurs, and then it will be filled with the damaged concrete. In zone B, the widening of the compression stresses creates tensile forces leading to cracks parallel to the longitudinal shear when transverse stresses exceed the concrete tensile strength. These tensile forces are then transmitted to the transversal reinforcement. Failure occurs when zone A is filled with damaged concrete material and no further volume reduction is possible. The pulverized material causes quasi-hydrostatic pressure on the confining concrete, which leads to splitting of the surrounding concrete.

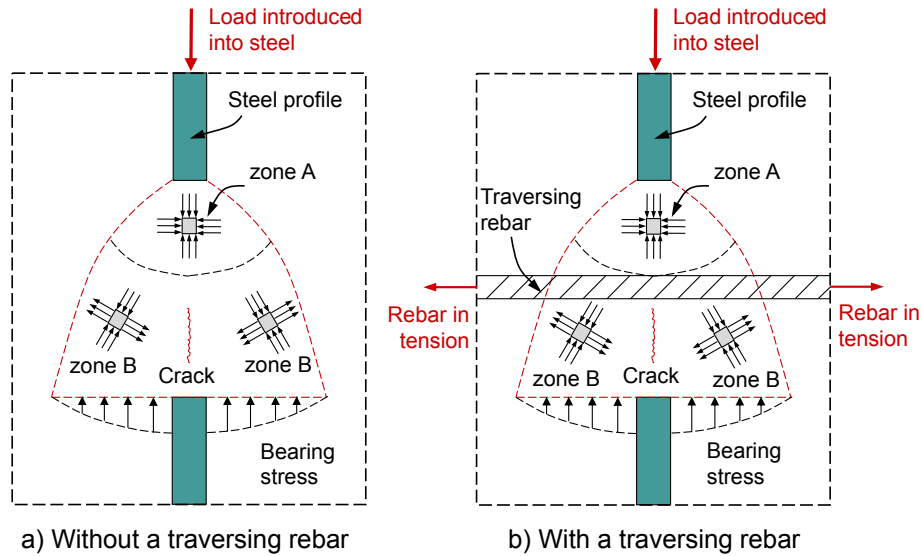


FIGURE 2.10: Mechanical model for: (a) concrete dowel connector; and (b) reinforced composite connector.

Zapfe (2001) identified three failure modes of the concrete dowel, *i.e.*, local pressure failure, punching failure, and shearing off failure. Punching failure has been observed for concrete dowels close to the edge of the slab, where a punch cone is created. Shearing off failure is defined by a double cut shearing off within the concrete material at the edges of the steel web perforation. This failure criterion is limited to concrete dowels located deeply in the concrete slab.

Zheng et al. (2016b) expanded the model from Kraus and Wurzer for the application with a traversing rebar in the opening of the steel rib. The forces are transmitted to the concrete by contact at the opening edge and spread into zones A and B. Zone A is subjected to triaxial compression, leading to crushing of the pore structure (see Fig. 2.10b). In Zone B, the spreading of compressive forces induces transverse tension relative to the steel rib. Cracking develops in Zone B once these transverse stresses exceed the concrete's tensile strength. Shear failure of the connector occurs along inclined planes as a result of both concrete crushing and cracking.

The perforating rebar running through the hole carries the tensile forces generated in Zone B, which in turn increases the transverse compressive forces in Zone A and enhances confinement. This added mechanism improves both the shear capacity and ductility of the circular composite connector. As noted by Wang et al. (2022), the main contribution of the perforating rebar to shear resistance lies in providing adequate confinement, enabling the concrete dowels to develop a highly multiaxial stress state.

### Concrete dowel action

The concrete dowel resistance is directly related to the increase of infill concrete volume in the connector, *i.e.*, to the rib thickness and opening section (Hosseinpour, 2018). The loads in presence for a concrete dowel resistance are described in Fig. 2.11, where  $\sigma_S$  is the compressive stress in the steel strip,  $\sigma_C$  is the confining stress provided by the confinement concrete, and  $\sigma_B$  is the stress from the bearing concrete. The resistance of the concrete is mainly directed by the shear strength of the concrete under multi-axial stresses, represented by parameter  $\tau_{CV}$  in Fig. 2.11c.

Indeed, research (Kraus and Wurzer, 1997; Kang et al., 2014; Su et al., 2014; Zheng et al., 2016a; Zhao et al., 2018; Wang et al., 2022; Roberts and Heywood, 1995) has proved that increasing the opening diameter significantly enhances the load-bearing capacity. However, as Su et al. (2014) have proved, the increase of the bearing capacity is slower than the increase of the opening area. This is due to the decrease of the three-directional constraints on the concrete with the increase of the opening diameter. If the confinement of concrete is reduced, so is the concrete compressive strength. Increasing the hole diameter has a more pronounced effect on enhancing the concrete dowel resistance when the concrete compressive strength is relatively low (Kang et al., 2014).

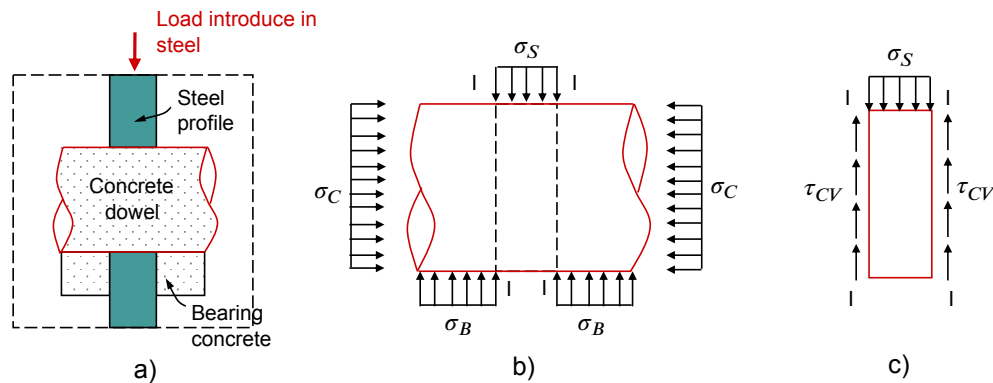


FIGURE 2.11: Mechanical model of a concrete dowel: a) global representation; b) diagram of stress acting on the concrete dowel; c) concrete dowel in shear.

The increase in the rib thickness has only a slight increase on the shear resistance (Zheng et al., 2016a; Wang et al., 2022; Hosseinpour, 2018). However, when the opening section increases, the influence on shear resistance becomes significant with the increasing rib thickness. Ushijima et al. (2001) showed that when a small thickness is considered, the area of 3 axial compressive stress is reduced, leading to a concentration of forces that generate splitting tension, see Fig. 2.12. While considering a larger rib thickness enhanced the compression area and increased the force distribution on the concrete. These compression struts ultimately reach the concrete shear strength on both sides of the rib, causing the connector to shear.

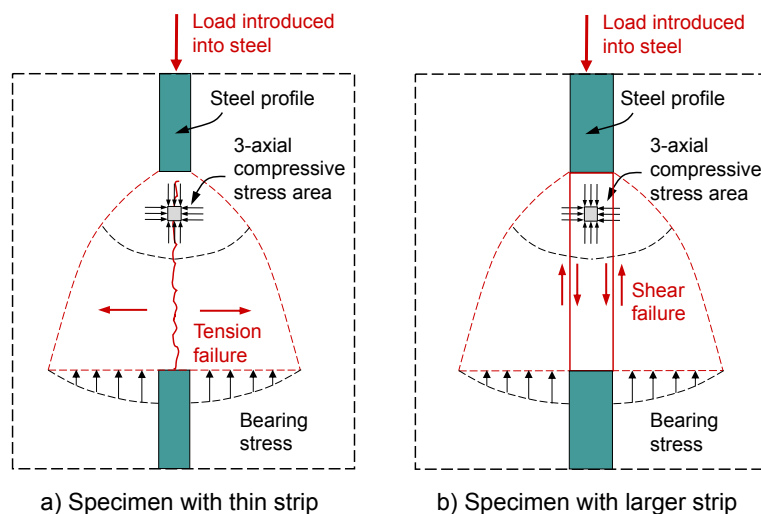


FIGURE 2.12: Influence of the rib thickness on the concrete dowel failure mode.

In case of normal-strength concrete, researchers (Wang et al., 2022; Kraus and Wurzer, 1997; Kang et al., 2014; Hosseinpour, 2018; Oguejiofor and Hosain, 1994; Ahn et al., 2010; Zheng et al., 2016a; Zhao et al., 2018) show that the shear resistance of concrete dowel increased almost linearly with concrete compressive strength. Kang et al. (2014) proved that a clear increase in the shear strength occurred owing to the dowel action when considering HSC (80 MPa).

Zheng et al. (2016b) and Kraus and Wurzer (1997) showed that the variation of the opening shape has a negligible impact on the shear capacity. Indeed, when failure modes are concrete shearing, the shear strength is determined by the shear area of the concrete dowel. On the other hand, Hosseinpour (2018) showed that rectangular and square opening sections provide better shear resistance than circular sections due to the larger top compressive section of the infill concrete and a failure directed by tensile splitting of infill concrete. However, it is not accurate to compare Hosseinpour's results with the other studies. Indeed, in Hosseinpour's experiments, a profile is perforated with openings, and the flanges are filled with concrete. No concrete or reinforcement surrounds this profile and does not prevent the separation of the concrete, which is only kept bonded at the concrete dowel. The concrete is therefore not confined, and the connector cannot develop its full potential due to a failure by tension in the concrete dowel.

### **Composite dowel action**

Research (Wang et al., 2022; Oguejiofor and Hosain, 1994; Cândido-Martins, Costa-Neves, and Vellasco, 2010; Ahn et al., 2010; Su et al., 2014; Zheng et al., 2016a; Zhao et al., 2018) showed at first that the presence of a reinforcing bar in the hole of the steel rib enhanced the shear capacity and ductility of the connector.

When considering a composite dowel, the relative size of the opening compared to the rebar diameter has a great influence on the load-bearing capacity of the connector. Results (Zheng et al., 2016a; Su et al., 2014) showed that on one hand, in a specimen where the rebar has almost the same size as the opening, no concrete surrounds the traversing bar, which is subjected to a pure shear failure, see Fig. 2.13. Wang et al. (2022) observed this effect experimentally: when the web opening diameter is small, increasing the rebar diameter produces only a minor increase in the ultimate shear resistance of the CRCD. However, once the opening becomes sufficiently large, enlarging the perforating rebar diameter leads to a substantial improvement in shear resistance. Braun, Obiala, and Odenbreit (2015), Zheng et al. (2016a), Su et al. (2014), and Wang et al. (2022) concluded that when the rebar is surrounded by enough concrete (larger opening diameter), it experiences a combination of shear and tension, reducing the plastic deformation and enhancing the connector shear resistance.

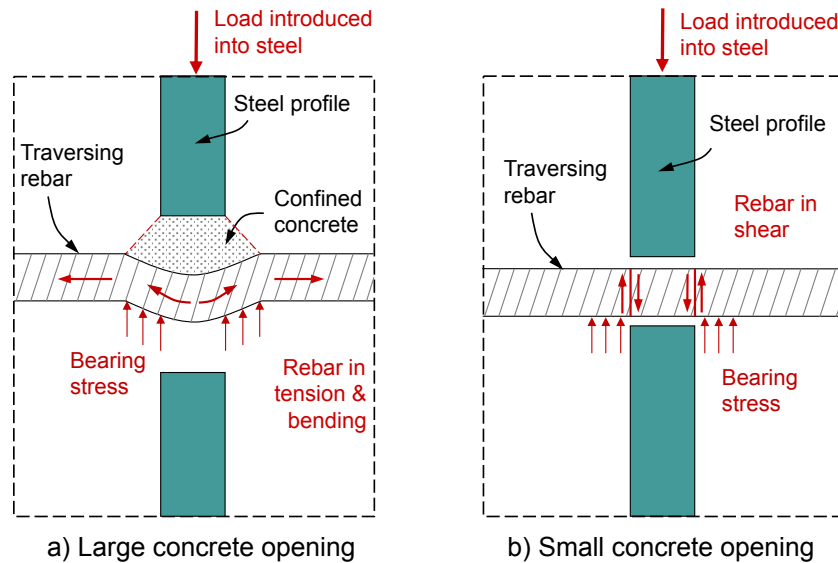


FIGURE 2.13: Influence of the relative opening size compared to the rebar diameter in the failure mode: (a) large opening compared to the rebar diameter; (b) almost equal diameter of opening and the rebar.

This behavior can be attributed to the role of the traversing rebars in shear resistance: their primary contribution is to provide adequate confinement, enabling the concrete dowels to develop a high multiaxial stress state, rather than to increase the shear area directly (Wang et al., 2022). The presence of a reinforcing rebar in the opening allows the composite dowel to resist the splitting forces induced by the loading. With the increase in the load on the connector, the reinforcing bar penetrates the triaxial compressive stress concrete area. This caused the rebar to progressively yield and enhanced the stress in the confined concrete zone until the reinforcing bar pulverized the concrete or failed (Ushijima et al., 2001). Zheng et al. (2016a) proved that by upgrading the steel strength of the rebar, it is possible to gain a non-negligible amount of shear capacity and peak slip.

An interesting outcome from the experiments of Braun, Obiala, and Odenbreit (2015) is that an increase in the concrete compressive strength does not always lead to an increase in the shear capacity of the connection when considering a composite dowel. This phenomenon can be explained as follows: when the concrete strength is high relative to the shear resistance of the traversing rebar, the bar has limited ability to induce local damage in the concrete. As a result, the bar cannot deform significantly, its axis remains nearly straight, and it behaves predominantly in shear—similar to cases with small opening-to-rebar diameter ratios. Conversely, when the bar can locally displace the concrete (by generating localized compression), it is able to deform more freely. This deformation causes the bar to experience a combination of shear and tension, reducing the stiffness of the shear connection. Since the tensile resistance of the rebar exceeds its shear resistance, this allows the connector to sustain higher loads. This behavior is analogous to that observed in shear studs embedded in normal- and high-strength concrete. Figure 2.14 describes this difference in failure mode depending on the concrete compressive strength. The stronger the concrete, the denser the matrix, and the lower the reduction in volume is possible. Thus, the traversing rebar is unable to deform sufficiently and experience less bending deformation, resulting in a more

shear-dominated failure with reduced ductility for the shear connector.

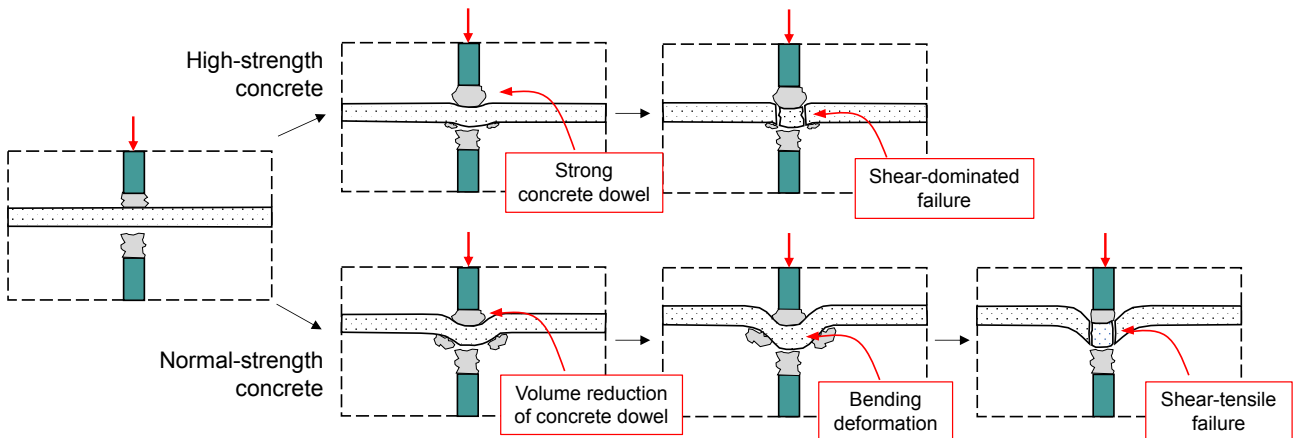


FIGURE 2.14: Comparison of the failure mode of CRCD connectors in function of the concrete compressive strength.

### 2.4.2 Plug-in-type

The bearing capacity of a plug-in-type connector comes from the combination of adhesion and frictional forces at the steel-concrete interface, concrete dowel action, and reinforcing bar passing through the hole resistance. The main difference with the rib-type is the influence of the pure bonding between steel and concrete, which is neglected in the rib-type connector. The failure mode of rib-type connectors is governed primarily by the failure of the concrete slab. In contrast, plug-in-type connectors tend to fail through composite-dowel failure because their deeper embedment in the surrounding concrete provides stronger interfacial restraint (Zhang et al., 2017a). The general results from rib-type connectors are also valid for plug-in-type connectors.

Zhao et al. (2018) and He et al. (2016) have investigated bonded and unbonded interfaces for composite dowel connectors, and results showed that the bonding effect provides a higher shear capacity and stiffness compared to the connector with a grease surface. Wang et al. (2022) and Zhao et al. (2018) describe the load-slip behavior of the composite plug-in connector as follows: during the first loading phase and before the peak load, shear resistance is directed by chemical adhesion and the concrete dowel. Subsequently, the slip increased, and the traversing rebar is activated with a progressive loss of the bonding connection, assisting the concrete dowel to transfer the redistributed force from the steel profile to the surrounding concrete. Afterwards, the residual resistance is composed of the sliding friction, the concrete dowel, and the perforating rebar.

### 2.4.3 Conclusion

Plug-in-type connectors derive their strength from the combined action of adhesion and friction at the steel-concrete interface, and by the interaction between the infill concrete and the traversing reinforcement, which together develop a confined multi-axial stress state within the concrete dowel. The traversing rebar restrains crack propagation and enhances confinement, allowing the concrete dowel to sustain higher shear stresses and deform in a combined shear-tension mode

rather than a purely brittle shear failure. As the load increases, the rebar gradually yields, transferring tensile forces into the surrounding confined concrete and promoting additional load redistribution before ultimate failure. This synergistic mechanism explains the higher shear strength and improved ductility observed in plug-in-type connectors compared to rib-type ones. While the bond at the steel–concrete interface contributes to the initial stiffness, after failure of adhesion, the shear resistance is dictated by the effectiveness of this rebar–concrete interaction combined with the friction at the steel–concrete interface.

## 2.5 Group of shear connectors

Due to the important internal force to be transferred between the steel and concrete components, composite dowel connectors are arranged in groups in order to increase the load-bearing capacity and stiffness of the connection, see Fig. 2.15 (Cândido-Martins, Costa-Neves, and Vellasco, 2010). For rib-type, the majority of research dealt with normal-strength concrete, and Kang et al. (2014) proved that these conclusions were relevant for high-strength concrete. A group of connectors can be formed by perforating more holes in the steel strip or by placing the strips side by side. Chen et al. (2017) proved, by varying the angle between twin strip connectors, that the vertical position of the strip is the optimum in terms of shear capacity. For plug-in-type, a group of connectors can be arranged by placing a connector on the web and flanges in multiple rows or multiple connectors on rows in a steel plate.

### Steel strips positioned in parallel

The study of Ahn et al. (2010) on twin perfobond pointed out that the distance between the two steel strips, welded on the flange, has a small influence on the resistance of the connectors and is negligible for a distance superior to the height of the strip. Due to the overlapping of the stresses from end-bearing plates, concrete dowel, and transverse rebar in the strip opening, the shear capacity of the twin perfobond was not twice the resistance of a single perfobond strip specimen, but around 1.67. Cândido-Martins, Costa-Neves, and Vellasco (2010) presented the same conclusion and added that the side-by-side connectors, see Fig. 2.15b, develop greater stiffness but low ductility and brittle failure compared to the single connector configuration. Zheng et al. (2016a) concluded from their results that the distance between two perfobond strips has little effect on the structural behavior of perfobond connectors.

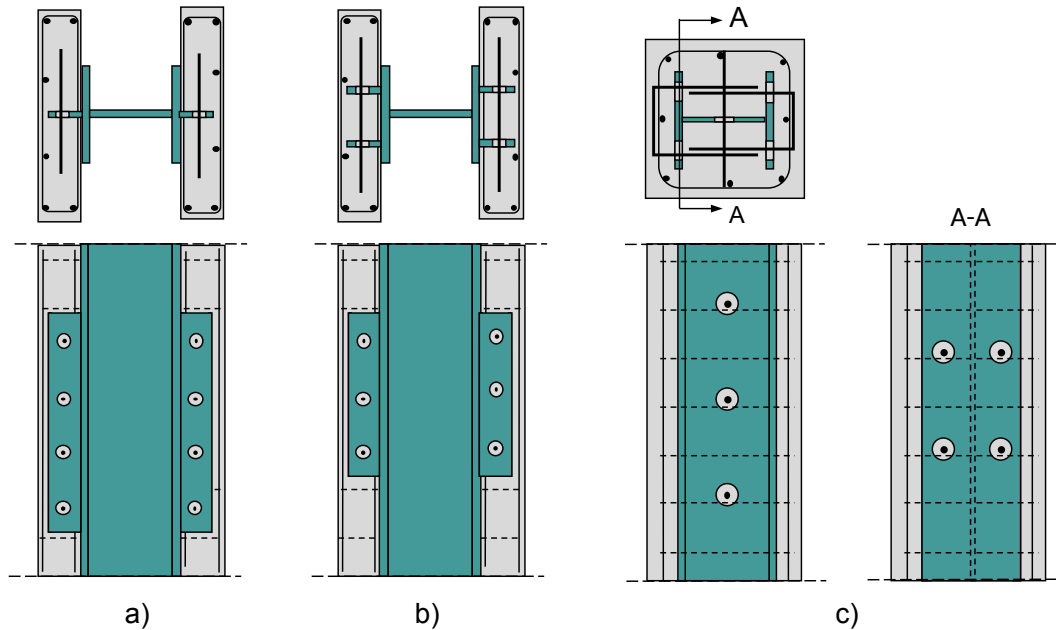


FIGURE 2.15: Different types of group connectors for composite dowel connectors: a) multiple connectors on a steel strip; b) multiple connectors on parallel steel strips; c) multiple connectors positioned on web and flanges of an H-shape steel profile.

### Overlapping of stresses

Concerning a single steel strip, research (Kang et al., 2014; Oguejiofor and Hosain, 1994; Hosseinpour, 2018; Vianna et al., 2008; Vianna et al., 2009; Vianna et al., 2013; Cândido-Martins, Costa-Neves, and Vellasco, 2010; Ahn et al., 2010; Su et al., 2014) showed that the more openings in the strip, the greater the shear capacity. However, when the distance between the openings is reduced, a decrease in the ultimate resistance of the connector is observed. This phenomenon is due to the overlapping of stress fields from the shear connectors, resulting in highly stressed regions. Many studies try to provide a design rule for the space between the openings to reduce the stress concentration of multiple connectors. Oguejiofor and Hosain (1994) proposed a minimal distance between openings of  $2.25 \times$  their diameter to optimize the shear resistance of the group of connectors. Hosseinpour (2018) concluded that, for circular openings, the minimal ratio spacing/diameter is 1.79. Su et al. (2014) results showed that for a space equal to two times the hole diameter, the capacity of the two-holes perfobond strip connector was 10% lower than twice one-hole perfobond connector. Vianna et al. (2008), Vianna et al. (2009), and Vianna et al. (2013) investigated in group of connectors on multiple rows, and results showed that the increase in the number of holes from 2 to 4 did not lead to significant changes in the connection behavior. This may be explained by the stress concentrations generated by the interaction between the stress areas from concrete cylinders formed in different rows. Indeed, the authors respected Oguejiofor and Hosain's rule for the distance between the two openings, but not between the rows. Inconveniently spaced holes, as concluded by Oguejiofor and Hosain (1994), limit the interlocking effect of neighboring holes due to cracks around a hole.

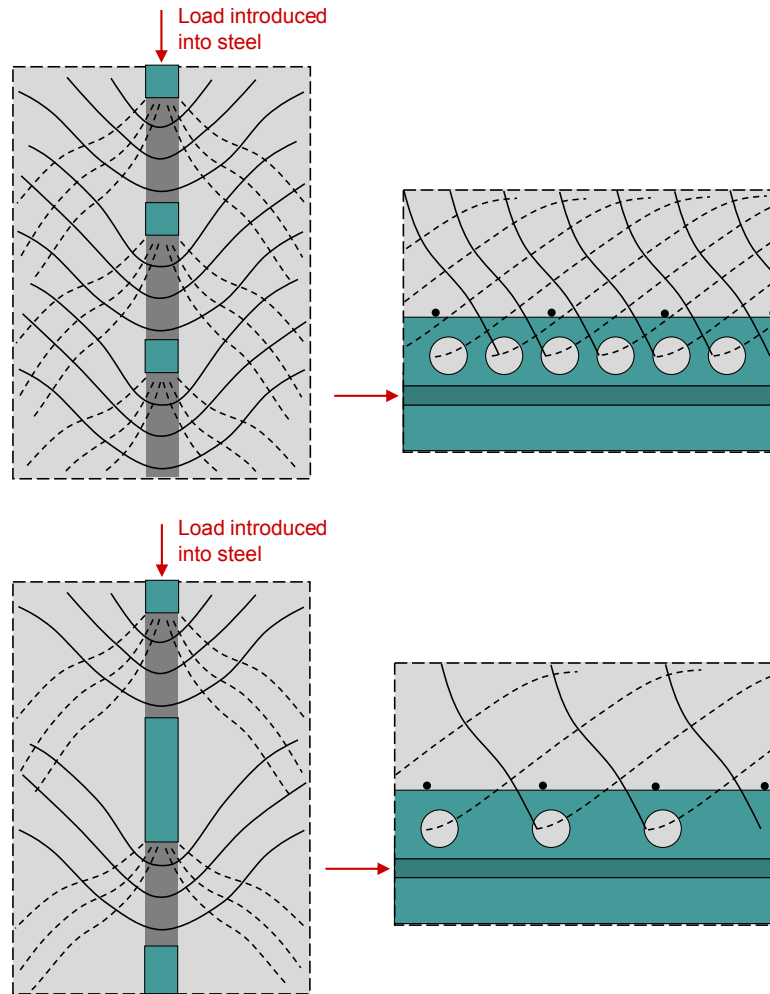


FIGURE 2.16: Stresses in grouped concrete dowel connectors and their intensification as connector spacing decreases.

### Load distribution over the connectors

Researchers (He et al., 2021; Zhang et al., 2017a; Morikawa et al., 1993; Ye and Luo, 1999; Zeng, Su, and Wu, 2008; Zhou et al., 2015) found an uneven load distribution in groups of connectors among the different layers of shear connectors. These experiments have been realised on different types of connectors, revealing that the uneven load distribution is a universal phenomenon, which is not dependent on the connector type.

He et al. (2021) performed push-out tests investigating the group behavior of rib-type composite dowel connectors. Strain results showed the uneven load distribution between the connector rows. The load is initially transferred by chemical adhesion at the steel-concrete interface. With the increase in the load, the chemical adhesion degraded, and the upper composite dowel connector was first activated. As the deduction of the adhesion and strains in the first composite dowel rises, the other composite dowels carry the transferred loads one by one. The transverse rebar in the connector exhibited large plastic bending-shear deformation after failure. This unevenness of load distribution among the group of connectors leads to a non-linear increase in the stiffness and strength of the CRCD connectors with the increase in the number.

In the experiments by Zhang et al. (2017a) on plug-in-type connectors, the results show uneven load distribution among multiple layers of CRCD shear connectors, as illustrated in Fig. 2.17. The internal forces in the perforated steel plate decrease progressively from the top layer to the bottom. Moreover, the relative slip between the perforated steel plate and the concrete is greater in the top and bottom layers than in the middle ones, a trend also reported by Li et al. (2018). Consequently, the top and bottom layers carry a significantly larger share of the load compared with the middle layers, consistent with the findings of Morikawa et al. (1993). When the load increases (from 400kN to 800kN), it can be observed that the distribution of loads is decreasing for the first layers and is increasing for the middle layers. This is due to a yielding of the first layers, thus a decrease of their stiffness, and the load is transferred to the stiffer following layers. In Fig. 2.17, when the slip between steel and concrete reaches 2mm, *i.e.*, more than 1900kN, the load distribution tends to evolve to a uniform distribution over all layers due to the yielding of all composite dowel connectors. The loading capability of the CRCD shear connector group equals approximately the summation of loads carried by all layers.

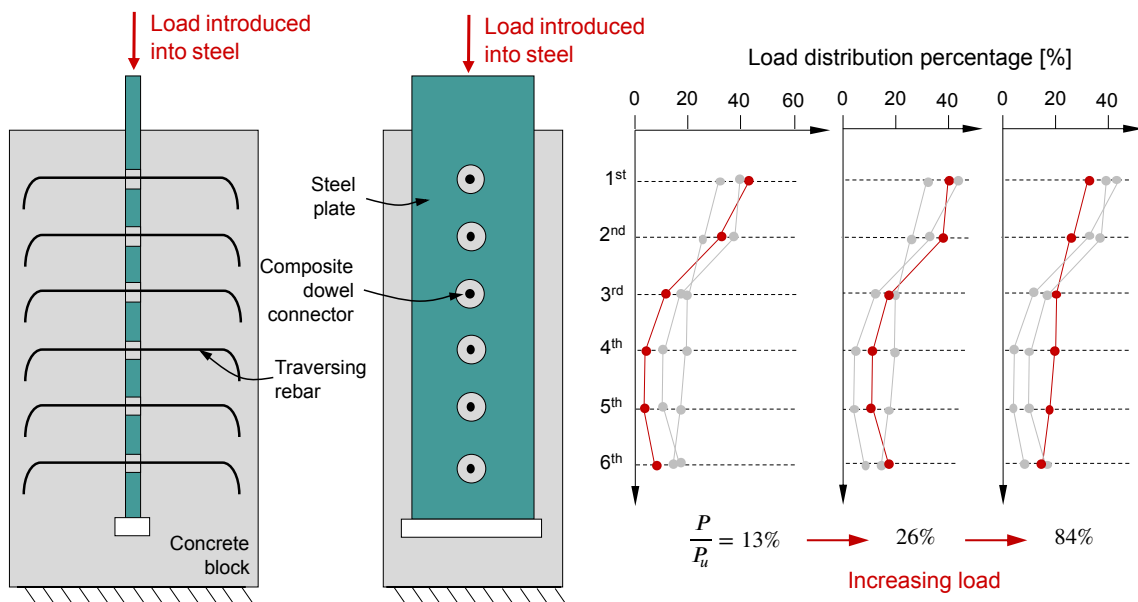


FIGURE 2.17: Distribution of loads between each connector considering an increasing load from 400kN to a relative slip between steel and concrete of 2mm. Experimental results from Zhang et al. (2017a) specimen G60-20.

Current design methods determine the required number of CRCD shear connectors by dividing the design load by the shear strength of a single connector, implicitly assuming equal load sharing among all connectors in the group. However, experimental results show that the connectors in the top layer carry loads exceeding their design shear strength, and their deformations surpass the allowable limits for individual connectors. According to Zhang et al. (2017b), such uneven load distribution can adversely affect both the mechanical performance and the durability of the CRCD connector group.

Hanswille, Illmann, and Dobelmann (2024) have studied the behavior of multiple-headed stud connectors in long sword connections and proved that the influences from the flexibility of the headed studs lead to a non-linear distribution of the longitudinal shear forces. This is critical for

the design, particularly in the serviceability limit state and the fatigue. The first studs are subjected to very high forces, and these high demands lead to the SLS and fatigue becoming the governing criteria for the design of long plate connectors. The authors also proved that the larger the number of studs and the stiffer the steel sword, the more pronounced this concentration becomes. With a high stud stiffness, the shear force gradient becomes very steep, making the first studs critical. At ULS, due to the large plastic deformation capacity of studs, shear forces can redistribute, allowing more studs to reach full design resistance. However, in SLS and fatigue, plastic redistribution cannot be used, and elastic becomes the governing limit state.

When considering the load introduction zone of compressive members, high loads need to be transferred from the steel element to the surrounding concrete over a short distance. Therefore, connectors with a high stiffness are required to transfer these loads, and a small displacement will be attained. A way to increase the transmission of the shear loads is to position multiple connectors in the load introduction zone. This can be realized by using multiple rows with several connectors in each row. As shown previously by Zhang et al. (2017a), when small displacements are considered, the first layers of the group of connectors support more than 70% of the total transferring load. Accordingly, Zhang et al. (2017b) investigated the optimal arrangement of connectors along the composite element. They found out that instead of increasing the number of connector layers, adding composite connectors in the top layer of the group of connectors is more effective in decreasing deformation. Due to the uneven load distribution between different layers of the composite connector, the top layer will always be the controlling layer for the design at the serviceability limit state.

### 2.5.1 Conclusion

The behavior of groups of shear connectors differs significantly from that of individual connectors due to stress interaction, confinement effects, and uneven load distribution. Increasing the number of shear connectors enhances the overall shear capacity and stiffness of the connection, but introduces stress overlapping between adjacent dowels, which can reduce the efficiency of each connector. An optimal spacing between perforations is therefore essential to avoid stress concentration and to ensure that each dowel develops its full load-bearing potential.

In groups arranged along multiple rows, an uneven load distribution is consistently observed at low load levels, with the top connectors carrying a larger proportion of the total shear force at small slips. As loading increases and the upper connectors begin to yield, part of the load is progressively transferred to the lower layers, leading to a more uniform distribution at larger deformations. This sequential activation results in a nonlinear relationship between the number of connectors and the total shear capacity, such that the overall resistance of the group is always lower than the simple sum of the individual connector capacities. The top layer of connectors is subjected to very high forces, such that SLS and fatigue become the governing design criteria for the group. Due to the high stiffness of the CRCD connectors, the shear force gradient along the group is very steep, rendering the first row of connectors critical. Once all connectors have yielded, the shear load becomes evenly distributed among the layers, and the group behaves as a fully mobilized composite system.

## 2.6 Synthesis and research gap

### 2.6.1 Summary of the state of the art

The literature reviewed in this chapter highlights several recurring themes that are essential for understanding load transfer in concrete-encased steel (CES) columns and for designing their load introduction zones.

First, the load introduction zone is recognised as a critical region in composite columns. Inadequate detailing of this region can significantly reduce composite action, leading to slip, insufficient shear transfer, and loss of stability. Different load paths (via the steel core, via the concrete encasement, or via a composite connection) generate distinct interface shear demands and time-dependent effects, all of which must be considered in design.

Second, when longitudinal shear demand exceeds the shear capacity provided by the natural steel–concrete bond, mechanical shear connectors become necessary. Current design provisions focus primarily on the ultimate resistance of these connectors and typically idealize the interface as rigid, using prescribed transfer lengths. This approach neglects the actual nonlinear load–slip behaviour of both bond and connectors and their interactions, as well as the role of connection stiffness at both service and ultimate limit states.

Third, high-strength concrete (HSC) exhibits a dense microstructure, higher compressive strength and stiffness, but presents a reduced ductility and increased brittleness compared with normal-strength concrete. These characteristics influence the development of plastic strains in the CES section.

Fourth, the bond at the steel–concrete interface arises from the combined action of chemical adhesion, mechanical interlock, and sliding friction. Experimental studies consistently show large scatter in adhesion resistance, with steel surface condition, area, and concrete strength identified as dominant parameters. As a result, design codes treat the bond very conservatively, often neglecting it or reducing it to a fixed friction value.

Fifth, circular reinforced composite dowel (CRCD) connectors derive their resistance from the combined action of the concrete dowel and the traversing rebar, confined by the surrounding concrete and steel. Rib-type connectors have been extensively studied in beam applications and bridge construction, whereas plug-in-type connectors—where the perforated element is deeply embedded in concrete—exhibit a different mechanical response due to stronger confinement and a larger interface area. Despite promising results in beams, joints, and piles, only limited research exists on plug-in-type CRCDs positioned on an H-shaped profile in composite columns.

Finally, groups of shear connectors behave differently from isolated connectors. Stress interaction and non-uniform load distribution lead to group effects, so that the resistance and deformation capacity of a group are not simply the sum of individual capacities. The spacing, arrangement, and stiffness of connectors within a group are therefore crucial design parameters.

### 2.6.2 Identified research gaps

Building on the summary above, several important gaps and unresolved issues are identified:

1. **Interaction between natural bond and mechanical connectors.** Current design standards prohibit combining natural bond and mechanical shear connectors in design, due to insufficient understanding of their interaction. Most experimental programmes on shear connectors rely on greased interfaces to suppress the bond, and therefore do not quantify the combined behaviour of bond and connectors in realistic CES columns.
2. **Plug-in CRCD connectors in CES columns.** While plug-in-type CRCDs have been investigated for composite joints, there is a lack of research on their use in CES columns with H-shaped steel profiles. In particular, the mechanical feasibility and performance of CRCD connectors placed on the flanges, or simultaneously on the web and flanges, remain undocumented.
3. **Behaviour in high-strength concrete.** The behaviour of CRCD connectors embedded in high-strength concrete, especially in fully encased H-shaped profiles, is not established. Existing studies on CRCD in HSC are sparse and do not provide a consistent basis for design in load introduction zones of CES columns.
4. **Stiffness and slip capacity of the shear connection.** Most available models and code provisions focus on ultimate resistance and adopt rigid–plastic assumptions for the connection. The stiffness and slip capacity of CRCD connectors, and of the combined bond–connector system, are not adequately characterised, even though they are fundamental for serviceability performance and for the effective mobilisation of composite action within a limited transfer length.
5. **Group effects for plug-in CRCDs on H-shaped steel profiles.** Group effects have been studied mainly for rib-type connectors and plug-in type connectors on steel plates. There is a limited understanding of how plug-in CRCD groups behave when arranged along the web and flanges of an H-shaped profile in a composite column configuration, including the distribution of shear forces between connectors and the influence of scale and spacing.
6. **Design models.** Existing analytical equations for CRCD connectors are not directly applicable to plug-in configurations in CES columns and generally neglect the contribution of the natural bond. Moreover, design expressions are rarely supported by a systematic reliability assessment in accordance with EN1990 (2002), particularly for connectors used in combination with friction.

These gaps motivate the experimental, numerical, and analytical investigations presented in the subsequent chapters. Chapter 3 addresses the lack of experimental data on bond and plug-in CRCD connectors using push-out tests, including configurations with connectors on the web and flanges. Chapter 4 develops and calibrates a three-dimensional finite element model to interpret the underlying load transfer mechanisms and to explore parameter ranges beyond the test matrix. Chapter 5 proposes semi-empirical design equations for stiffness, resistance, and slip capacity of CRCD connectors acting together with friction, and evaluates the reliability of the equation to estimate the shear resistance in line with EN1990 (2002).



## Chapter 3

# Experimental Investigations

### 3.1 Overview of test specimens

The performance and behaviour of the shear connectors were evaluated by means of a series of specific push-out tests, aimed at characterising the shear-slip response of different connector configurations. In this type of test, a steel profile is pushed relative to a reinforced concrete block, with a void at the bottom allowing the steel profile to slide within the concrete element. The test setup was designed in accordance with the push-out test provisions of EN1994-1-1 (2004) for steel–concrete connections, while accounting for the specific characteristics of concrete-encased steel (CES) sections. This setup isolates and highlights the behaviour of the shear connectors and the interfacial bond between steel and concrete.

Push-out tests are used to characterise the local shear transfer and load–slip behaviour of shear connectors. However, they do not reproduce the full three-dimensional stress state, bending effects, or eccentric load introduction that occur in real CES columns. In this thesis, push-out tests are used to obtain calibrated connector and interface properties, which form a necessary basis for subsequent studies on full-load introduction zones, but they are not a substitute for full-column tests. In push-out tests, the load is applied to the steel element and is then fully transferred to the concrete block through the shear connection system. In a real column, by contrast, the load may be introduced through the steel profile (see Chapter 2) and is then shared between the steel and the concrete so that both materials act compositely, rather than the load being fully transferred to the concrete.

The experimental testing campaign consists of 15 configurations of push-out tests, each series comprising three identical specimens according to EN1994-1-1 (2004), all series are summarized in Table 3.3. The studied parameters can be summarized in the following categories:

- **Interfacial bond:** Series A1, A2, and A3, evaluated the behavior of the pure bond resistance at the steel-concrete interface for concrete strength C50/60 (A1) and C80/95 (A2 and A3). Series A3 investigated a scale-up of the cross-section.
- **Single CRCD connector:** Series B1 and B2 evaluated the behavior of a single CRCD connector combined with the bond resistance for different concrete grades, C50/60 and C80/95, respectively.
- **Multiple CRCD connectors and distance between them:** Series C1, C2, C3, C4, and C5 evaluated the behavior of multiple CRCD connectors combined with the bond resistance

for different concrete grades, C50/60 (C1, C2, and C4) and C80/95 (C3 and C5), respectively. The center-to-center distance between the shear connectors was varied to observe the impact on the rows.

- **Scale-up and arrangement of shear connectors:** Series D1 and D2 evaluated the behavior of a 4 CRCD connector for a different arrangement of shear connectors with C80/95 concrete. D1 considers 2 rows of 2 connectors, while D2 considers 4 rows of 1 connector on the web.
- **Scale-up and CRCD connectors on the flanges:** Series E1 evaluated the behavior of 8 circular reinforced composite dowel connectors positioned on the flanges with C80/95 concrete.
- **Multiple connectors on the web and the flanges:** Series F1 (scale-up) evaluated the behavior of 4 CRCD connectors in two rows on the web and 8 CRCD connectors in two rows on the flanges with C80/95 concrete. Series F2 evaluated the behavior of 6 CRCD connectors in three rows on the web and 12 CRCD connectors in three rows on the flanges with C80/95 concrete.

Two categories can be identified depending on the geometry: (1) with a HEB 200 profile, and (2) with a HEA 360 profile. Uniformity is maintained across each category with respect to the geometries of the concrete block, steel profile, reinforcement bars, and negative formwork in Styropor.

Table 3.1 summarizes the main parameters for the specimens with an HEB 200 steel profile, and the detailed geometry is represented in Fig. 3.1.

TABLE 3.1: Overview of the tested configurations with a HEB 200.

Series	Concrete class	Nbre of connectors	Type of connection	Traversing rebar (mm)	Opening (mm)	Rows spacing (mm)
A1	C50/60	0	Pure bond	/	/	/
A2	C80/95	0	Pure bond	/	/	/
B1	C50/60	1	Single CRCD	$\phi 12$	$\phi 40$	/
B2	C80/95	1	Single CRCD	$\phi 12$	$\phi 40$	/
C1	C50/60	3	Rows CRCD web	$\phi 12$	$\phi 40$	100
C2	C50/60	3	Rows CRCD web	$\phi 12$	$\phi 40$	200
C3	C80/95	3	Rows CRCD web	$\phi 12$	$\phi 40$	200
C4	C50/60	4	Rows CRCD web	$\phi 12$	$\phi 40$	150
C5	C80/95	4	Rows CRCD web	$\phi 12$	$\phi 40$	150
F2	C80/95	18	CRCD web + flanges	$\phi 12$	$\phi 40$	100

All specimens encompass a concrete block with dimensions measuring 320 x 320 x 840mm, a centrally positioned steel profile (HEB 200) measuring 810mm in length, composed of steel grade S355. A steel cage, comprising eight longitudinal rebars with a diameter of 12mm and nine stirrups with a diameter of 10mm per 100mm, all constructed from steel grade B500B, is incorporated. The concrete cover is standardized at 20mm. A negative formwork in Styropor, exceeding

the cross-sectional dimensions of the steel profile by 10mm and with a thickness of 80mm, is employed. The connectors, uniformly designed as circular openings with a 40mm diameter in the web of the steel profile, are filled with concrete and penetrated by a 12mm steel rebar (B500B) bent at the ends for optimal anchorage.

For series B1, C1, C2, and C4, strain gauges were placed on the steel surface near the shear connector for one specimen of each series (Figure 3.8). The aim was to measure the strain distribution along the length of the steel profile, to assess the impact of the number and spacing of connectors, and to observe the strain distribution between the web and flange.

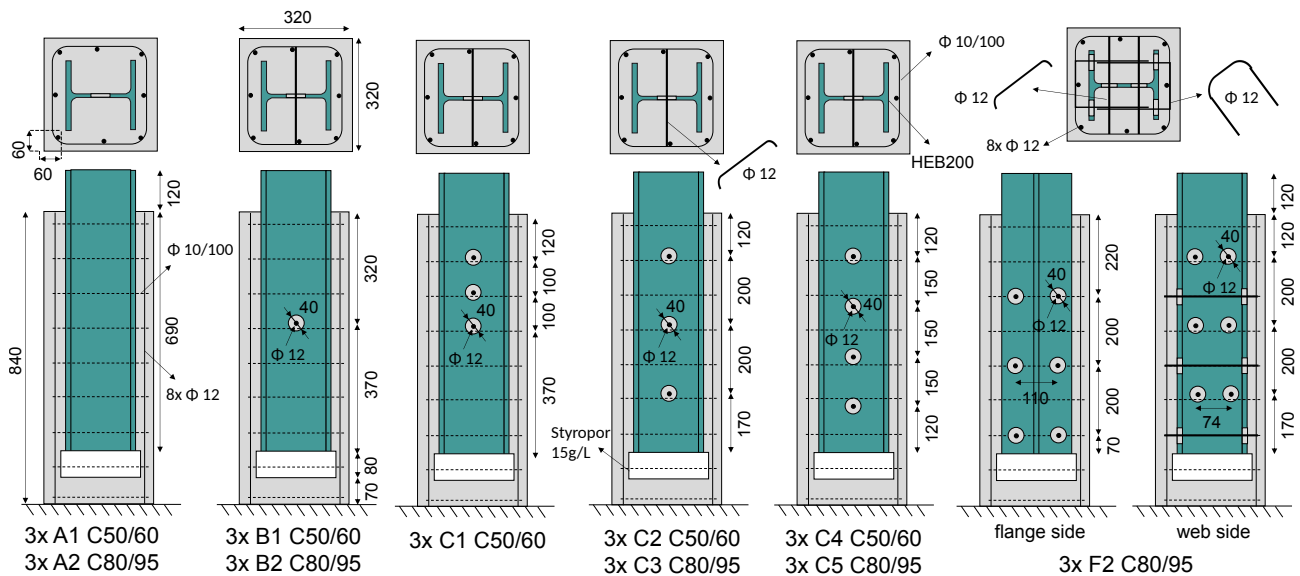


FIGURE 3.1: Description of the experimental specimens with HEB200.

The second category involves scaling up both the cross-section of the steel profile and the size of the shear connectors compared to the specimens utilizing an HEB 200 section. Table 3.2 provides an overview of the key parameters for the specimens incorporating a HEA 360 steel profile, with detailed geometry illustrated in Fig. 3.2.

TABLE 3.2: Overview of the tested configurations with a HEA 360.

Series	Concrete class	Nbre of connectors	Type of connection	Traversing rebar (mm)	Opening (mm)	Rows spacing (mm)
A3	C80/95	0	Pure bond	/	/	/
D1	C80/95	4	2 rows CRCD web	$\phi 20$	$\phi 60$	200
D2	C80/95	4	4 rows CRCD web	$\phi 20$	$\phi 60$	150
E1	C80/95	8	2 rows CRCD flanges	$\phi 16$	$\phi 50$	200
F1	C80/95	12	CRCD web + flanges	$\phi 20/\phi 16$	$\phi 60/\phi 50$	100

Each specimen consists of a concrete block measuring  $560 \times 540 \times 840$  mm, containing a centrally embedded HEA 360 steel section (length of 810 mm) made of S460 steel. A reinforcing steel cage is included, comprising eight longitudinal rebars with a diameter of 16 mm and nine stirrups of 10 mm diameter spaced at 100 mm intervals, all made from B500B steel. The concrete cover

is consistently maintained at 20 mm. A negative formwork made of Styropor is used, exceeding the steel profile's cross-sectional dimensions by 10 mm on all sides, with a uniform thickness of 80 mm. Shear connectors are formed by circular holes in the steel profile: 50 mm in diameter in the flanges and 60 mm in the web. These openings are filled with concrete and reinforced with a 16mm steel rebar in the flanges and 20 mm in the web, both bent at their ends to enhance anchorage. The 16 mm diameter for flange connectors was selected due to limitations in bending rebar to its diameter.

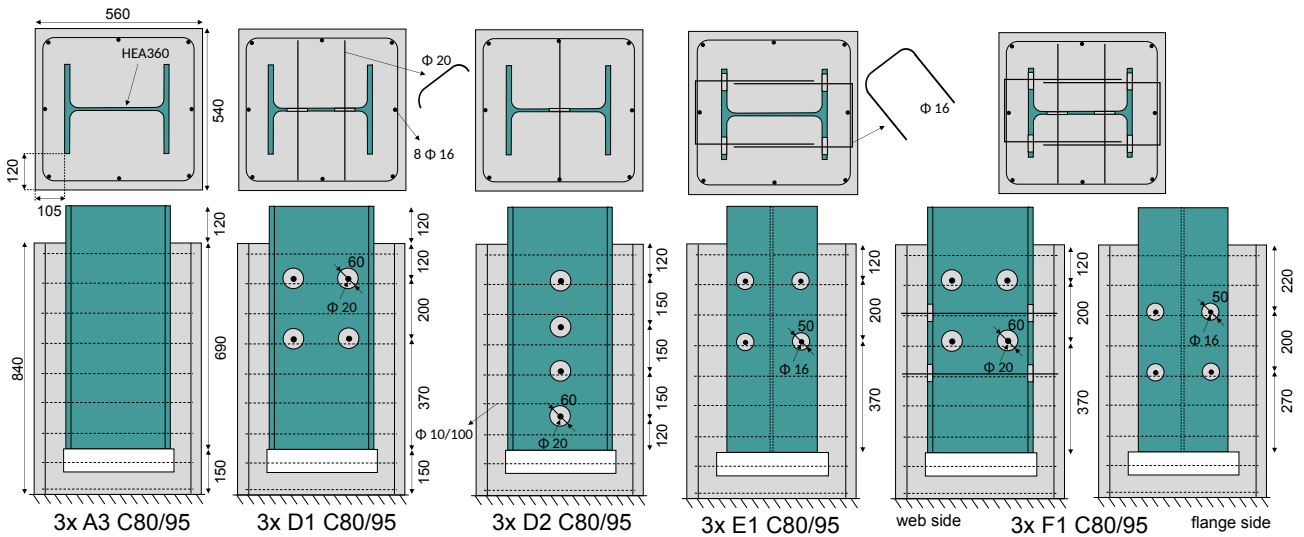


FIGURE 3.2: Description of the experimental specimens with HEA360.



## 3.2 Production of specimens

In total, 45 push-out specimens have been produced and tested. The production was realized in two main phases. The first phase, which comprises the series from A1 to C5 (excluding A3), was concreted in August/September 2023. The second phase, which includes series A3 and from D1 to F2, was produced in July 2024. The objective was to use the experimental and numerical results from the first campaign to design the second experimental phase.

The steel profiles were delivered by Ziemann Stahlbau and ArcelorMittal, respectively, for the first and second experimental campaigns. The surfaces were treated with sandblasting to remove the rust and ensure consistency in surface conditions. The quality of the sandblasting followed the category Sa 2<sup>1/2</sup>, very thorough blast-cleaning, of ISO8501-1 (1988).

The production of the specimens was executed by RAU Betonfertigteile, a company that realizes precast reinforced concrete elements and is able to deliver high-strength concrete C80/95. They have made the timber formworks, steel cage assembly and concreting of the specimens (Fig. 3.3).



FIGURE 3.3: Production of the specimens.

The first experimental campaign was divided into 3 concreting phases:

1. Concreting 1: 6 specimens (series A1 and B1) of concrete C50/60 on 21/08/2023;
2. Concreting 2: 9 specimens (series C1, C2 and C4) of concrete C50/60 on 25/08/2023;
3. Concreting 3: 12 specimens (series A2, B2, C3 and C5) of concrete C80/95 on 01/09/2023.

The second campaign, which comprises 18 specimens, was concreted in one phase on July 4, 2024.

No surface treatments such as oil, grease, or Teflon were applied to the steel profile surfaces. This decision aligns with real-world conditions on construction sites or in precast factories, where such treatments are typically absent. To be as realistic as possible, bond resistance should be

considered since it plays a significant role in transferring load from steel to the concrete at the interface in composite columns. Almost no rust was present at the steel profile surface.

The concreting process involved placing the specimens vertically in an inverted position, see Fig. 3.3a. The steel profile was stabilized and centered at the bottom using a Styropor with a density of 50 g/L (Fig. 3.3b), featuring an HE opening shape with a thickness of 120mm. At the top of the steel profile, a negative formwork made of Styropor with a density of 15 g/L (Fig. 3.3c) was glued and utilized as a void, allowing the steel profile to slide into the concrete block with almost no resistance. This negative formwork mirrored the cross-sectional shape of the steel profile with an additional 10 mm width.

For the concrete characterization, 3 cubes 150 mm are provided for each specimen for concrete C50/60 and 3 cubes 100 mm for concrete C80/95, which will be cured in the same conditions as the specimens (Figure 9). In addition, for each concreting, 6 cylinders 300x150 mm, 3 cubes 100 mm, 3 cubes 150 mm (except for C80/95), and 3 prisms 400x100x100 mm are cast and cured under water. During the transport time to Luxembourg, the specimens were wrapped in plastic foil to prevent them from drying out. Back in Luxembourg's laboratory, they were kept underwater. These concrete specimens will be tested after 28 days as reference values.

### 3.3 Materials

#### 3.3.1 Concrete

The different specimens have been concreted into four batches. Batches 1 and 2 were designed to achieve a concrete strength class C50/60, and batches 3 and 4 for a C80/95. The characteristics and compositions of the different concrete recipes are detailed in Table 3.4. The results on the shaking table test were 480 mm, 495 mm, 535 mm, and 535 mm for the batches 1, 2, 3, and 4, respectively.

TABLE 3.4: Description of the concrete composition.

Strength class	C50/60	C80/95
Cement	CEM II/A-LL 42.5R	CEM II/A-LL 42.5R
Aggregate	0/8	0/8
Exposition class	XD2, XC4, XF3, XA3	XD2, XC4, XF3, XA3
Consistency	F3	F4
W/C	0.4524	0.2458
Cement (kg/m <sup>3</sup> )	420	480
0-2 (kg/m <sup>3</sup> )	762	678
2-8 (kg/m <sup>3</sup> )	933	1017
Silica fumes (kg/m <sup>3</sup> )	/	45
FM (Superplasticizer) (kg/m <sup>3</sup> )	3.36	5.04
VZ (Retarder) (kg/m <sup>3</sup> )	1.26	0.96
Total water (kg/m <sup>3</sup> )	190	118
Mixed weight (kg/m <sup>3</sup> )	2309	2344

The specimens, for material characterization, underwent water curing and were tested after 28 days. The compressive strength was assessed using cylinders with dimensions of 150x300 mm  $f_{c,cylinder}$ , as well as cubes measuring 100 mm  $f_{c,cube,100}$  and 150 mm  $f_{c,cube,150}$  in length, following the specifications of EN12390-3 (2019). Additionally, the Young's modulus  $E_{c,0}$ , in accordance with EN12390-13 (2021), and tensile splitting strength  $f_{ct,sp}$ , following EN12390-6 (2023), were determined using cylinders measuring 150x300 mm. A 4-point bending test, in compliance with EN12390-5 (2019), was conducted on prisms measuring 400x100x100 mm to calculate the flexural strength  $f_{ct,fl}$ , which was then employed to derive the tensile strength. All results are summarized in Table 3.5.

TABLE 3.5: Summary of the concrete mechanical properties.

Batch	Sample number	$f_{c,cylinder}$ (MPa)	$E_{c,0}$ (GPa)	$f_{c,cube,100}$ (MPa)	$f_{c,cube,150}$ (MPa)	$f_{ct,sp}$ (MPa)	$f_{ct,fl}$ (MPa)
Batch 1 C50/60	1	51.8	N/A	53.1	57.2	4.2	5.8
	2	51.6	41.1	51.5	59.3	3.9	5.5
	3	52.8	40.7	51.9	57.6	4.1	5.8
Mean value		52.1	40.9	52.2	58.0	4.1	5.7
Mean density (kg/dm3)		2.26		2.31	2.33	2.29	2.28
Batch 2 C50/60	1	55.7	N/A	65.5	N/A	N/A	N/A
	2	56.3	42.7	64.2	N/A	N/A	N/A
	3	56.2	43.0	63.7	N/A	N/A	N/A
Mean value		56.1	42.9	64.5	N/A	N/A	N/A
Mean density (kg/dm3)		2.27		2.32	N/A	N/A	N/A
Batch 3 C80/95	1	92.6	N/A	78.4	N/A	7.2	10.6
	2	90.2	52.4	81.8	N/A	7.3	10.1
	3	87.3	51.0	55.9	N/A	7.1	10.1
Mean value		90.0	51.7	72.0	N/A	7.2	10.3
Mean density (kg/dm3)		2.35		2.35	N/A	2.37	2.36
Batch 4 C80/95	1	93.1	52.8	63.7	98.4	N/A	N/A
	2	92.0	53.1	84.9	93.9	N/A	N/A
	3	92.4	52.6	66.3	93.5	N/A	N/A
	4	90.9	N/A	N/A	N/A	N/A	N/A
Mean value		92.1	52.8	71.6	95.3	N/A	N/A
Mean density (kg/dm3)		2.31		2.38	2.37	N/A	N/A

Utilizing mean values, various parameters were derived to facilitate a comparative analysis of the compressive resistance relative to the shape and size of the concrete specimens. The results for each batch are presented in Table 3.6. The ratios were used to convert the concrete compressive strength on cubes, determined for each specimen, to a concrete compressive strength in a cylinder.

TABLE 3.6: Relationship between concrete compressive strength on cylinders and cubes.

Batches	Concrete shape and size ratios
Batch 1 C50/60	$f_{c,cylinder} = 0.898f_{c,cube,150}$
	$f_{c,cylinder} = 0.998f_{c,cube,100}$
Batch 2 C50/60	$f_{c,cylinder} = 0.870f_{c,cube,150}$
Batch 3 C80/95	$f_{c,cylinder} = 1.100f_{c,cube,100}$
Batch 4 C80/95	$f_{c,cylinder} = 0.966f_{c,cube,150}$
	$f_{c,cylinder} = 1.285f_{c,cube,100}$

### 3.3.2 Structural steel

The tensile strengths of the steel profiles were determined based on three different samples: top flange, web, and bottom flange. The tests were carried out at room temperature in accordance with ISO6892-1:2019 (2019) at the laboratory of the Luxembourg Institute of Science and Technology on July 6, 2023. The results can be found in Table 3.7.

TABLE 3.7: Mechanical properties of the steel profiles.

Steel section	Steel grade	Sample number	$R_{p0,2}$ (MPa)	$R_m$ (MPa)	$E_s$ (GPa)	$A$ (%)
HEB 200	S355	Top flange	375	529	207	32.5
		Web	389	537	205	29.5
		Bottom flange	380	529	207	30.5
Mean value			381	532	206	30.8
HEB 200	S460	Top flange	463	583	197	23.6
		Web	507	598	196	21.9
		Bottom flange	466	584	201	23.0
Mean value			479	588	198	22.9
HEA 360	S460	Top flange	527	599	213	21.7
		Web	495	584	192	19.3
		Bottom flange	526	600	198	19.8
Mean value			516	594	201	20.3

### 3.3.3 Steel reinforcement

For each reinforcement bar diameter, three tests were conducted to measure the tensile strength. The test was carried out at room temperature in accordance with ISO15630-1:2019 (2019) at the laboratory of the Luxembourg Institute of Science and Technology on July 6, 2023. The results can be found in Table 3.8 for the first phase and in Table 3.9 for the second phase, where the identification represents the nominal diameter of the rebar in mm.

TABLE 3.8: Mechanical properties of the reinforcement bars for the first phase.

Identification	$R_{p0,2}$ (MPa)	$R_m$ (MPa)	$E_s$ (GPa)	$A$ (%)
10-1	523	617	192	21.5
10-2	540	633	193	20.5
10-3	529	626	194	21.5
Mean value	531	625	193	21.2
12-1	528	649	202	27.5
12-2	533	653	202	26.5
12-3	528	648	201	26
Mean value	530	650	202	26.7

TABLE 3.9: Mechanical properties of the reinforcement bars for the second phase.

Identification	$R_{p0,2}$ (MPa)	$R_m$ (MPa)	$E_s$ (GPa)	$A$ (%)
10-1	591	615	252	/
10-2	591	617	220	13.5
10-3	584	608	212	16
Mean value	589	613	228	14.8
12-1	536	573	207	15.1
12-2	540	576	213	15.7
12-3	543	578	215	16.3
Mean value	540	576	212	15.7
16-1	504	606	272	25
16-2	507	611	244	21.6
16-3	508	610	271	24.3
Mean value	506	609	262	23.7
20-1	558	679	214	26.2
20-2	559	680	216	26.7
20-3	565	685	213	25.7
Mean value	561	682	214	26.2

### 3.4 Test setup

The push-out tests were conducted in the laboratories of the University of Luxembourg and the Bergische Universität Wuppertal. In Luxembourg, the specimens were tested on a horizontal 4MN hydraulic press, a configuration designed for rapid specimen set-up, facilitated by an overhead crane. The detailed set-up is described in Fig. 3.4.

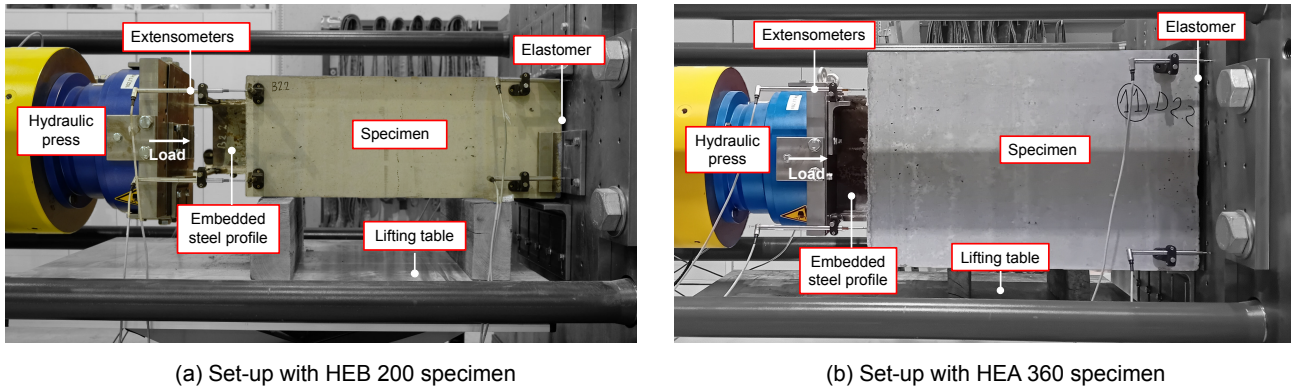


FIGURE 3.4: Test set-up in Luxembourg.

All series configurations were designed to obtain an ultimate predicted resistance of a maximum of 4MN and were tested in Luxembourg. However, after testing series A3, we obtained the adhesion strength at the steel-concrete interface. The updated FE simulations of series D1 and D2 were optimistic about the possibility of testing them in Luxembourg. Nonetheless, the peak load of series E1 and F1 was above or too close to the limit of the machine in Luxembourg.

The decision was taken to test them in the laboratory of the University of Wuppertal, where a vertical hydraulic press of 10MN capacity was available, see the set-up in Fig. 3.5.

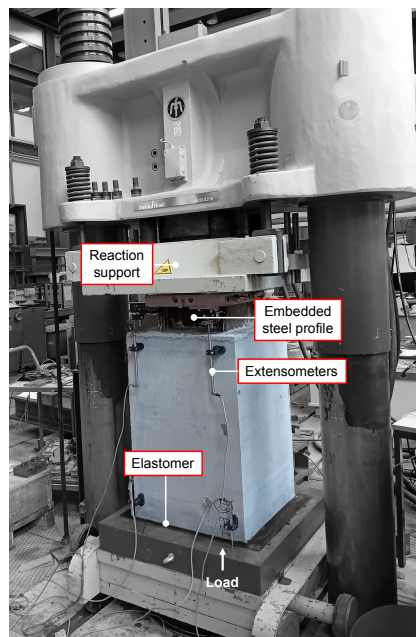


FIGURE 3.5: Test set-up in Wuppertal.

For all push-out specimens, to ensure uniform loading over the surface, a 5 mm-thick elastomer was interposed between the concrete block and the reaction support.

In Luxembourg, the procedural sequence involved the initial installation of the specimen on the lifting table through the overhead crane. Subsequently, the measuring equipment was affixed, and the load jack was positioned within 1cm of the steel profile. Following this, adjustments to the LVDTs were made, and the specimen was centered on both the load jack cylinder and the reaction frame. The final step entailed lowering the lifting table until the specimen was supported by the

steel components, at which point the load jack was advanced until it made contact with the steel profile.

In Wuppertal, the specimens were positioned and centered on a rolling table with a forklift. The table was then pushed into the hydraulic press. Finally, the LVDTs were installed and adjusted. The top of the machine served as the reaction support, and the load was applied from the hydraulic press located underground.

### 3.5 Instrumentation

The measured data were recorded and stored at a frequency of 1000 Hz in Luxembourg and 600 Hz in Wuppertal throughout the experimentation. The applied load was quantified using a load cell while simultaneously capturing the displacement in the axial direction and the transverse force exerted on the load jack.

#### 3.5.1 Extensometer

For each conducted test, we deployed 8 LVDTs as shown in Figure 3.6, produced by HBM, comprising 4 WA50 transducers to quantify the slip between the steel profile and the concrete block and 4 WA20 transducers to measure the deformation of the elastomer situated at the bottom of the concrete block. The experimental plan initially outlined loading the specimens until a relative displacement of 45 mm was achieved to observe complete shear failure of the connector. Consequently, displacement transducers with a 50 mm capacity were employed for recording relative displacements between the steel and concrete. Simultaneously, LVDTs with a 20 mm capacity were utilized to capture the deformation of the 5 mm-thick elastomer.

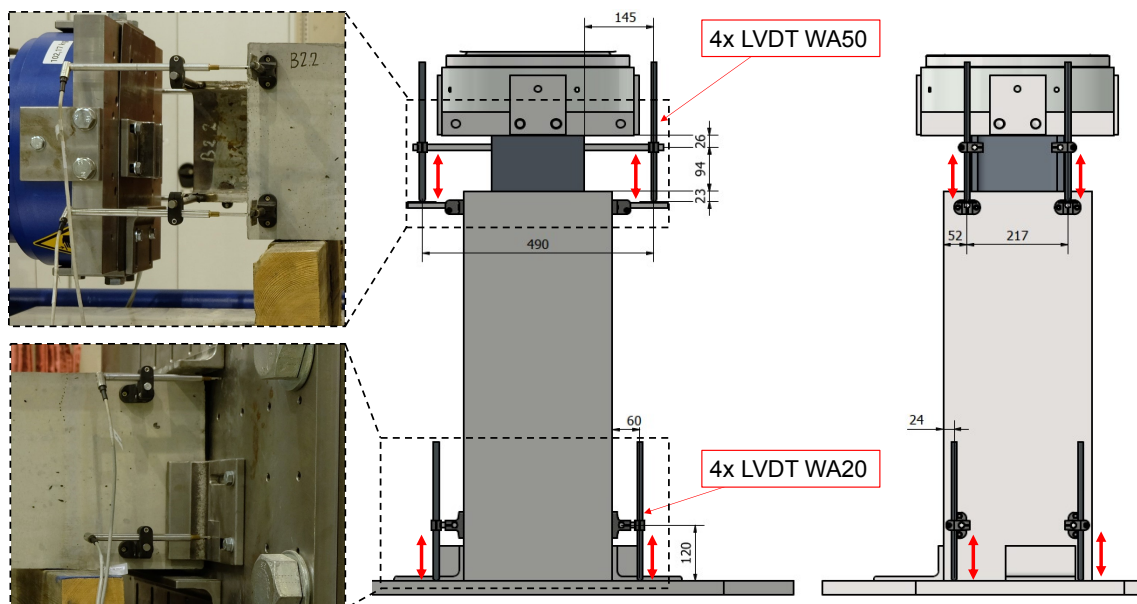


FIGURE 3.6: Positions of the displacement transducers.

To facilitate the measurement process, steel rods were welded onto the flanges of the steel profiles on the top side, providing attachment points for the LVDTs. The location of the LVDTs

is represented in Figure 3.7a for the specimen featuring a HEB 200 and in Figure 3.7b for the specimen with a HEA 360. Additionally, supports were screwed into the concrete to provide a stable base for the LVDT heads. On the bottom side, similar supports were affixed into the concrete, serving both as a foundation for the LVDTs and as points of application for reaction forces on the reaction frame.

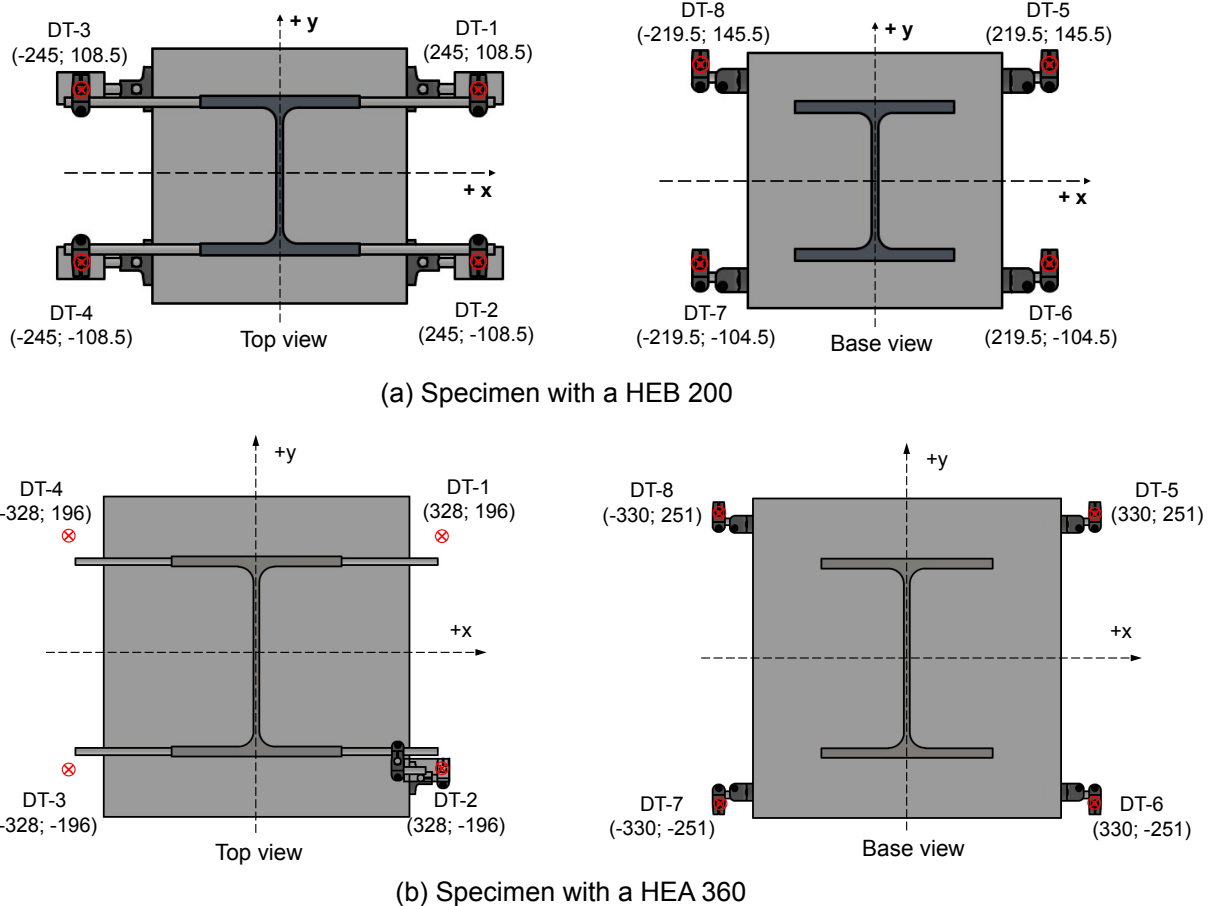


FIGURE 3.7: Coordinates of the LVDTs positions.

### 3.5.2 Strain gauges

Twenty-two strain gauges, specifically CEA-06-250UNA-120 from Micro Measurements, were positioned on the steel profile surface of four specimens: B1.3, C1.3, C2.3, and C4.3, as represented in Figure 3.8. For specimens B1.3, C1.3, and C4.3, strain gauges were exclusively placed on one side of the web, along the steel profile's length, surrounding the shear connectors. In the case of specimen C2.3, additional strain gauges were affixed to one flange. These sensors played a crucial role in evaluating strain distribution along the length of the steel profile, assessing the impact of the number and spacing of connectors, and observing strain distribution between the web and flange.

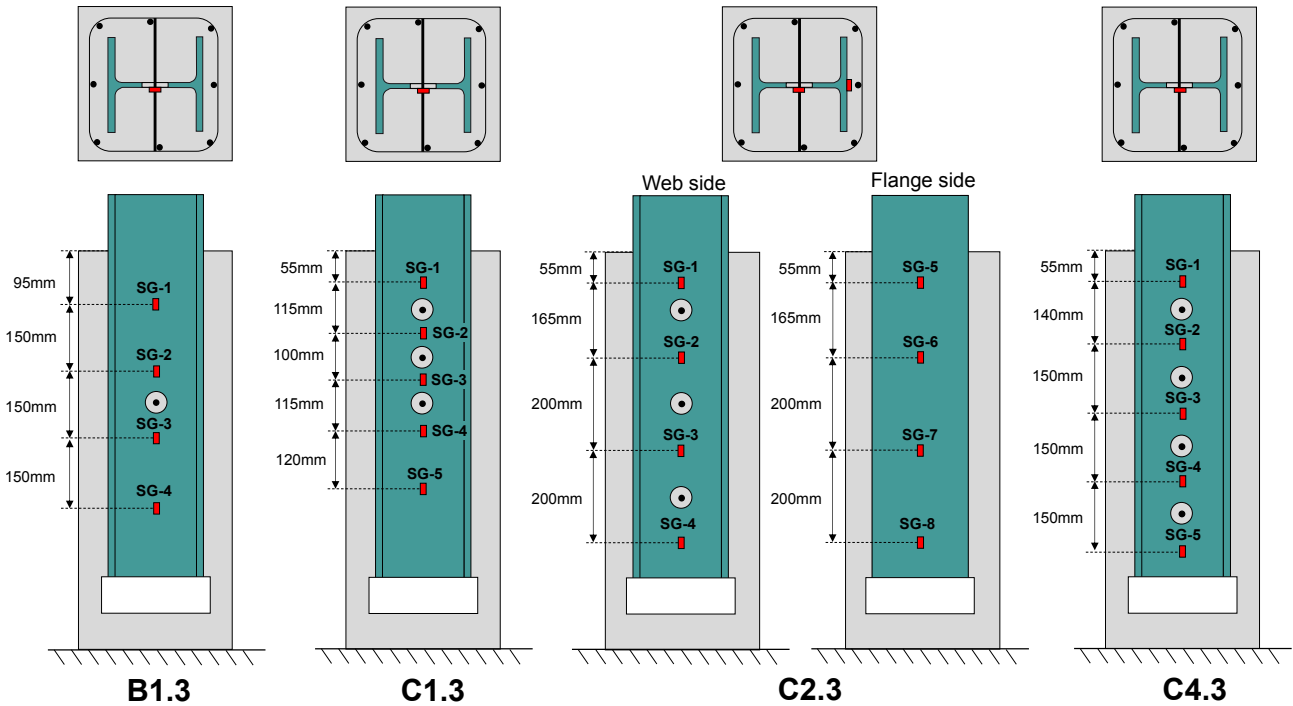


FIGURE 3.8: Positions of the strain gauges on series B1, C1, C2, and C4.

The installation of the strain gauges was a critical step. Placing the strain gauges directly on the steel surface would shear off the devices with the concrete slip on the steel surface. Since a displacement of 45 mm was imposed, it would have been difficult to find a protective system around the strain gauge to let it function through the all loading procedure.

Therefore, to accommodate the slip between the concrete and steel, which would otherwise shear off the strain gauges, notches with a 2 mm thickness were meticulously crafted for each strain gauge, see Fig. 3.9. Additionally, a channel was created along the steel profile to facilitate cable routing.

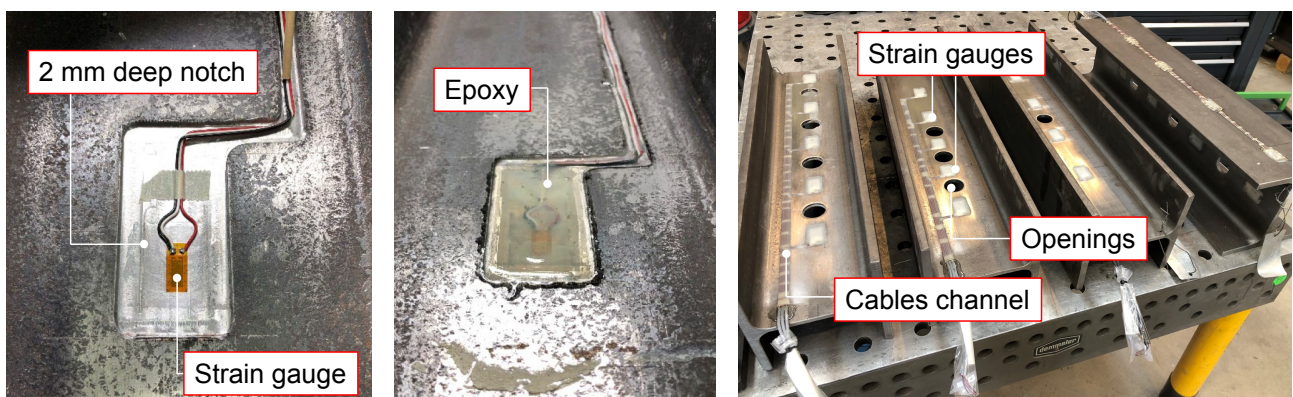


FIGURE 3.9: Details of the installation of the strain gauges.

Reduced tests were performed in the laboratory of the University of Luxembourg to determine the most appropriate procedure to attach the strain gauges and protect them in such a way that they could resist the 45 mm imposed slip between steel and concrete.

After multiple attempts, the best procedure was determined. The strain gauges were bonded into these notches using an M-Bond AI-10 epoxy, and the cables were glued into the channel. Then the gauge was protected using a Teflon film, and the opening and channel were filled with a 2-component epoxy glue. Finally, the surface was leveled using sandpaper, and the epoxy surface was covered with Teflon and tape. This meticulous preparation ensured the reliability of strain measurements despite the challenges posed by the dynamic interface between the concrete and steel during slip.

Before the concreting, the strain gauges were connected, and a pressure was applied to verify the proper functioning of the strain gauges. Special care was taken during the concreting to avoid any damage to the devices and the cables.

### 3.6 Loading procedure

The test initiation involved identifying initial cracks resulting from concrete shrinkage. Subsequently, the specimen was positioned on the press supports, and attachments for the supports and LVDTs were secured. The procedure continued with the centering of the specimen relative to the reaction frame and the load jack, followed by LVDT adjustment and calibration of the output data using a calibrated steel plate. The record system was then initialized, and security equipment positions were established. The test commenced thereafter. Upon test completion, instrumentation was dismantled, and cracks observed during specimen loading were recorded.

Conforming to the guidelines outlined in EN1994-1-1 (2004) Annex B, a minimum curing period of 28 days transpired between concreting and testing. For each push-out test, three cubes were cast with the same concrete batch and subjected to identical curing conditions as the specimens. These concrete cubes were loaded on the day of the respective push-out test. The general loading procedure (Figure 3.10) was as follows:

1. In displacement control:
  - (a) Loading to 50 kN at a speed of 0.1 mm/s, wait 60 seconds;
  - (b) Ramp force up to 40% and decrease to 5% of estimated failure load at a speed of 0.01 mm/s;
2. In force control:
  - (a) Cycling from 50% to 40% of ultimate load at a speed of 8 kN/s, repeat 24 times;
  - (b) Ramp force up to 40% and decrease to 5% of estimated failure load at a speed of 0.01 mm/s;
3. In displacement control:
  - (a) Relative move of 1 mm at a speed of 0.01 mm/s, wait 300 seconds;
  - (b) Repeat 5 times;
  - (c) Relative move of 2 mm at a speed of 0.02 mm/s, wait 60 seconds;
  - (d) Repeat 20 times.

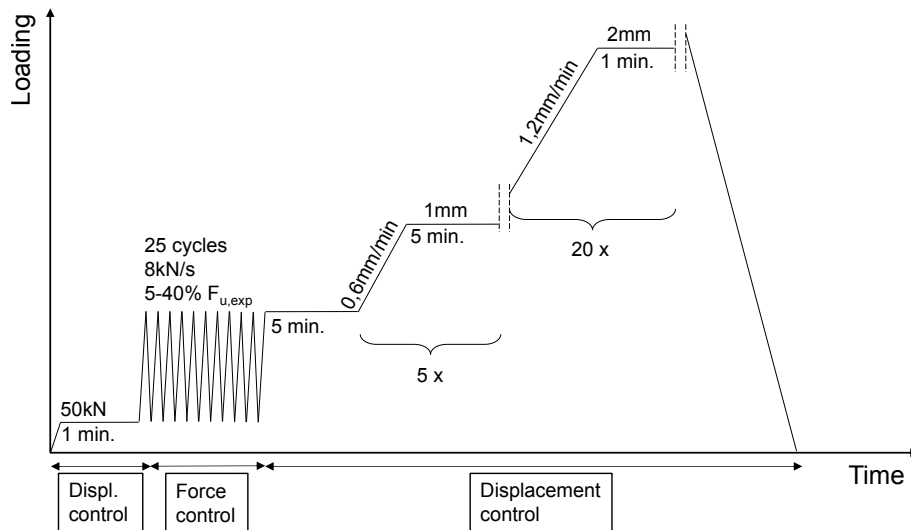


FIGURE 3.10: General loading procedure.

The ultimate resistance of the specimens is primarily governed by the adhesion resistance developed at the steel-concrete interface, characterized by a brittle and potentially unpredictable bond behavior. To mitigate any premature failure arising from potential issues during specimen manufacture, all tests were initiated in displacement mode. Following the guidelines outlined in EN 1994-1-1, the initial phase consisted of 25 cycles, with the first cycle conducted in displacement control and the subsequent 24 cycles in force control mode. A 5-minute pause followed, allowing for the measurement of concrete relaxation under imposed deformation. Subsequently, the test continued in displacement control until the connection failed or the conclusion of the loading procedure.

Throughout the procedure, the load was incrementally applied in 1 mm slip intervals, each followed by a 5-minute pause to account for relaxation effects, repeated five times. The ultimate load was anticipated within the initial 3 mm of displacement. Subsequently, the loading speed was accelerated, and concrete relaxation was reduced for the final 20 steps, culminating in a relative displacement of 45 mm.

The loading procedure varied for certain specimens. Series A1, A2, and A3, focusing solely on bond resistance, were loaded until a relative displacement of 25 mm. In these cases, after reaching the ultimate force, the bond resistance predominantly relied on friction, which stabilizes at near-constant values. For series involving high-strength concrete, a modification was introduced for one specimen per series (B2.2, C3.2, C5.2, D1.3, D2.3, E1.3, F1.3, and F2.1), see Figure 3.11. The objective was to assess the stiffness of the shear connector after reaching the ultimate load. Following 6 steps of applying 1 mm of displacement, the load was decreased to 5% of the anticipated ultimate load, and a 60-second pause ensued. Subsequently, the specimen was reloaded, and the general procedure continued. This unloading and reloading cycle facilitated the calculation of shear connector stiffness without considering adhesion resistance.

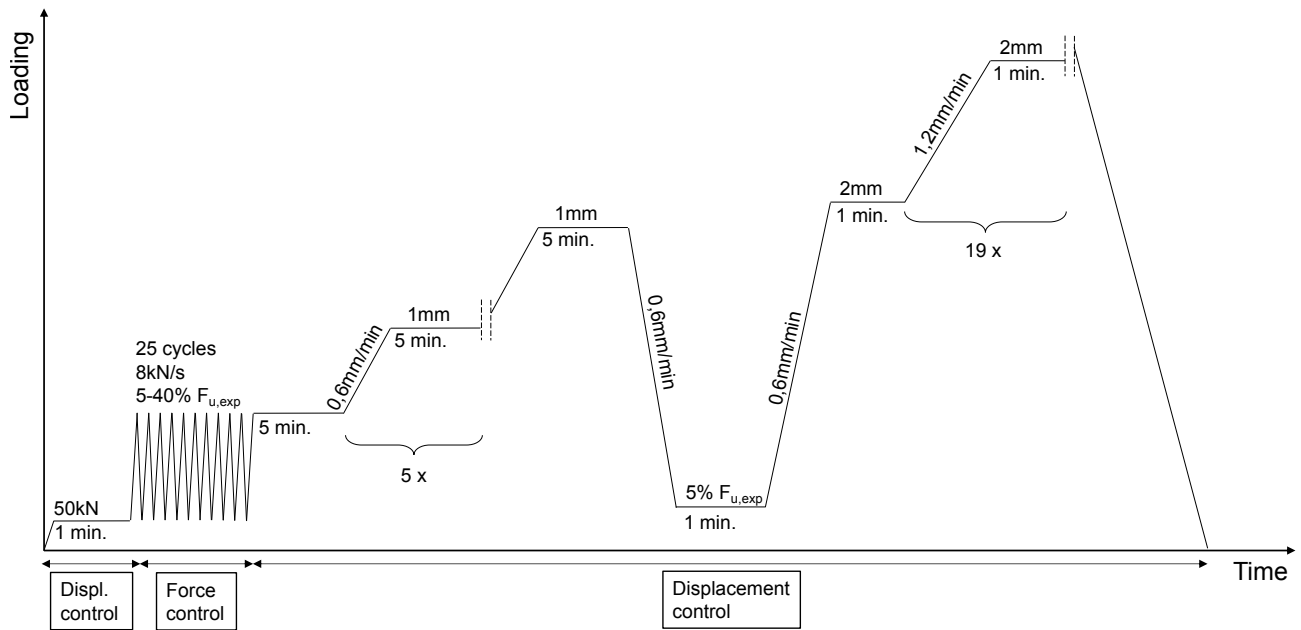


FIGURE 3.11: Loading procedure with recording of the stiffness of the shear connector(s).

### 3.7 Results and discussion

A total of 45 push-out tests were conducted, covering 15 distinct configurations. This section presents the experimental results and provides a discussion of their analysis. For clarity and to facilitate comparative studies, the test campaign has been organized into five thematic groups:

1. Steel–concrete interfacial bond;
2. Multiple connectors on the web and connector spacing;
3. Connector layout on the web and scale-up effects;
4. Shear connectors on the flanges and scale-up effects;
5. Combined web + flange connector configurations and scale-up effects.

#### 3.7.1 Steel-concrete interfacial bond

To investigate the behavior of the bond resistance at the steel-concrete interface, we tested three different configurations. The study focused on understanding the behavior of adhesion and friction developed at the steel-concrete interface for the specified configuration without any connector. Series A1 and A2, featuring the same geometry and considering a HEB 200, were designed to assess the impact of the concrete strength on the bond. While series A3, featuring a HEA 360, aims to observe the impact of increasing the section on the bond stresses with high-strength concrete. As explained by Chrzanowski et al. (2019), bond resistance depends on many parameters and is difficult to predict. Therefore, it was necessary to assess the contribution of the bond alone

to analyze the behavior of shear connectors combined with the bond in the following test series. Table 3.10 summarizes the geometrical and materials parameters in the three series.

TABLE 3.10: Description of the series relying only on bond resistance.

Series	Steel profile	Concrete section (mm <sup>2</sup> )	Mean concrete strength (MPa)	Concrete cover (mm)	Surface treatment
A1	HEB 200	320x320	58	60	Sandblasted
A2	HEB 200	320x320	102	60	Sandblasted
A3	HEA 360	560x540	108	120/105	Sandblasted

The anticipated resisting load for Series A1 was approximately 1000 kN. Consequently, the cyclic load for Series A1 was set within the range of 50 kN to 400 kN, equivalent to the 5-40% range stipulated by EN1994-1-1 Annex B.

Due to the considerable variability in bond resistance reported in the literature, predicting the ultimate resistance for series with high-strength concrete was challenging. To stay on the side of caution and not have too high cyclic loading that could damage the adhesion bond, the ultimate force was assumed to be the same as that for series A1, although it was acknowledged that the bond resistance would likely increase with the higher concrete grade.

To determine the resistance load of series A3, we considered the stresses developed in series A2 and applied them to the steel-concrete surface with the HEA 360. The anticipated resisting load was approximately 1900 kN. As per EN1994-1-1 (2004) Annex B, this would necessitate a cyclic load within the range of 90 kN to 720 kN. However, this cyclic load seems to be too high and destroyed the adhesion bond for specimen A3.1. Indeed, as observed in Fig. 3.12c, A3.1 does not present any peak load. The cyclic load was then decreased for the two other tests between 40 kN and 320 kN (resulting from the maximum load obtained in specimen A3.1).

### Load-slip behavior

Figures 3.12 illustrate the load–slip behavior for series A1, A2, and A3, which were tested without shear connectors. In these tests, resistance is provided solely by adhesion and friction, and no significant concrete relaxation effects are observed during the waiting pauses of the loading since there are no shear connectors.

In Figure 3.12b, after reaching the ultimate force, a cyclic behavior is observed in the load-curve diagram, tending to converge to the friction resistance value. The machine is in displacement control, and as the jack pushes forward at a certain speed, the force increases. After reaching a certain load, a failure occurs, leading to a jump in the relative slip between steel and concrete. Simultaneously, the applied load drops since the hydraulic jack encounters almost no resistance during this slip drop. The displacement of the jack continues, a new source of resistance is encountered, and the load increases again. This process repeats until around 13 mm of slip, 11 mm, and 7 mm for A2.1, A2.2, and A2.3, respectively. The brittleness of these failures could be explained by a rupture of a part of the adhesion bond. However, adhesion is slip-sensitive and may not be sustained until 13 mm of relative slip. The same behavior is observed in specimens A3.1 and A3.3.

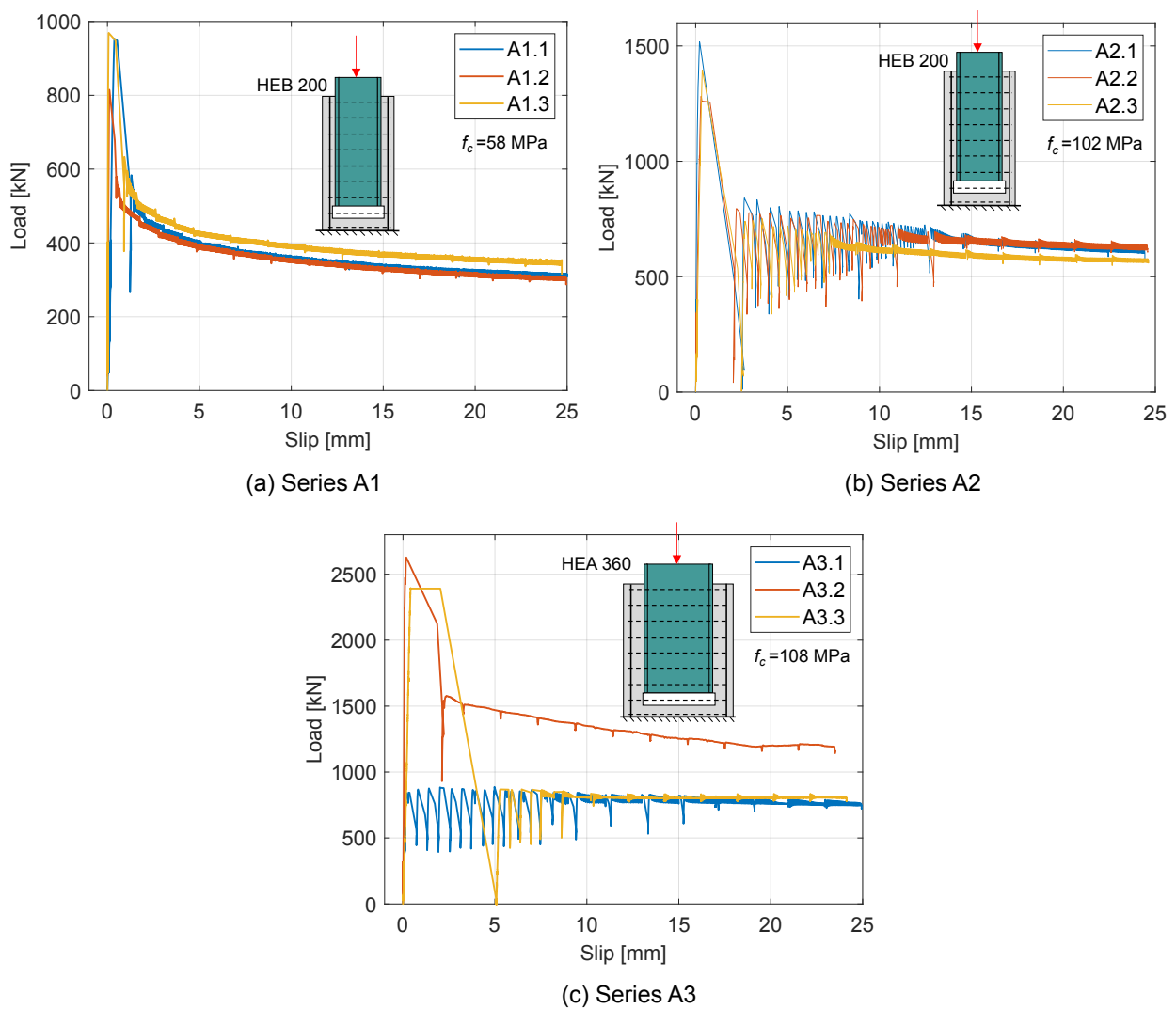


FIGURE 3.12: Load-slip curve for series A1, A2 and A3.

In Figure 3.12b, after reaching the ultimate force, a cyclic behavior is observed in the load-curve diagram, tending to converge to the friction resistance value. The machine is in displacement control, and as the jack pushes forward at a certain speed, the force increases. After reaching a certain load, a failure occurs, leading to a jump in the relative slip between steel and concrete. Simultaneously, the applied load drops since the hydraulic jack encounters almost no resistance during this slip drop. The displacement of the jack continues, a new source of resistance is encountered, and the load increases again. This process repeats until around 13 mm of slip, 11 mm, and 7 mm for A2.1, A2.2, and A2.3, respectively. The brittleness of these failures could be explained by a rupture of a part of the adhesion bond. However, adhesion is slip-sensitive and may not be sustained until 13 mm of relative slip. The same behavior is observed in specimens A3.1 and A3.3.

This behavior is analogous to stick-slip, a discontinuous and cyclic transition between two interfacial motion regimes (Berman, Ducker, and Israelachvili, 1996). In the stick phase, the two surfaces are mechanically locked. As the applied load increases, shear stresses accumulate while static friction prevents relative movement. The interface, therefore, experiences rising shear stresses with essentially zero slip. When the interfacial resistance is exceeded, the system enters

the slip phase: the interface suddenly debonds or unlocks, and rapid relative displacement occurs, see Fig. 3.13. During this event, friction typically drops from its static to its kinetic value, causing a sudden release of stored elastic energy (Zhang, 2006). This release was also clearly perceptible during the experiment, as each slip event generated a pronounced noise, characteristic of rapid interfacial debonding. The sequence can repeat until the damage at the interface becomes too large to sustain further stick-slip cycles. Indeed, local concrete damage at the surface is crushing the asperities, polishing the concrete surface, and these small particles act like a lubricant, reducing the coefficient of friction (Raous and Karray, 2009).

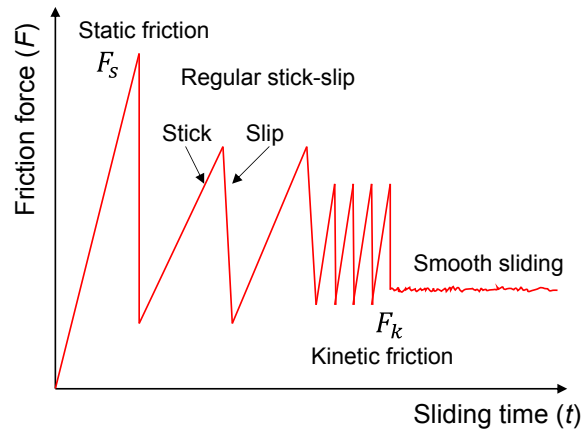


FIGURE 3.13: Stick-slip behavior.

Stick–slip generally occurs when: (1) static friction exceeds kinetic friction, promoting stress accumulation during sticking; (2) the driving system is stiff enough to store elastic energy during stick and release it rapidly at slip; and (3) friction is rate-dependent, a slowly loaded interface can suddenly transition from high static resistance to lower kinetic resistance, releasing stored energy abruptly (Gu et al., 1984).

These conditions are met in Series A2 and A3 at the steel–concrete interfaces involving high-strength concrete (HSC). Sandblasted steel surfaces exhibit significant roughness, which enhances mechanical interlock and static friction once chemical adhesion is lost. High-strength concrete also has a higher elastic modulus than normal-strength concrete, creating a stiffer load-transfer system. Its denser microstructure tends to be more brittle (fib, 2008), limiting distributed micro-cracking and promoting sudden interfacial slip events. After each slip, interfacial stress redistributes rapidly, and repeated stick–slip cycles may occur until the concrete surface becomes sufficiently damaged that the interface transitions toward continuous sliding governed by kinetic friction.

This behavior is clearly visible in Fig. 3.12, where the successive load drops diminish in amplitude and progressively converge toward a stable sliding-friction response.

Series A1 demonstrates an average ultimate shear resistance of 913 kN at a slip of 0.182 mm. The initial loading phase exhibits a purely linear response, with an average shear stiffness of 12215 kN/mm, although there is considerable scatter in stiffness values (see Table 3.11). Notably, shear stiffness is largely maintained until the peak load is reached. After reaching the ultimate shear resistance, the load drops abruptly due to bond failure and stabilizes at approximately 56% of the

peak load at a slip of 1.5 mm. This is followed by a gradual decline in load, reaching a steady state at about 36% of the maximum value, governed primarily by friction between the steel and concrete.

Series A2 exhibits a similar load–slip trend, with an average ultimate shear resistance of 1398 kN at a slip of 0.291 mm. The initial response is again purely linear, with an average shear stiffness of 8514 kN/mm and noticeable scatter (see Table 3.11). As with A1, no significant loss of stiffness occurs before the peak load. Following bond failure, the shear force drops abruptly and stabilizes at around 63% of the maximum load at 1.5 mm slip, then gradually decreases to a steady state at approximately 44% of the peak load due to frictional resistance.

Series A3, in contrast, displays a highly variable behavior among its specimens. Specimen A3.1, subjected to a different cyclic loading protocol, shows no adhesion contribution. Specimens A3.2 and A3.3 exhibit similar adhesion resistance but diverge in their frictional performance—A3.2 has significantly higher friction resistance than A3.3, which is similar in friction behavior to A3.1. Due to these inconsistencies, it is difficult to generalize the behavior of series A3 based on a combined load–slip response.

The coefficient of variation (CoV) in Table 3.11 is computed using the sample standard deviation. Across the three series, substantial scatter is observed in the measured stiffness, which is primarily attributed to the inherent variability of bond adhesion.

TABLE 3.11: Results for series relying only on the bond resistance.

Series	ID	$P_u$ (kN)	$s_u$ (mm)	$k_s$ (kN/mm)	$P(5mm)$ (kN)	$P(8mm)$ (kN)	$P(10mm)$ (kN)	$P(20mm)$ (kN)
A1	A1.1	954	0.378	2470	400	377	361	323
	A1.2	815	0.099	9942	389	368	352	314
	A1.3	969	0.068	24232	425	402	390	354
	Mean value	913	0.182	12215	405	382	368	330
CoV (%)	9.3	94.0	90.5	4.6	4.6	5.4	6.4	
A2	A2.1	1518	0.213	15841	786	750	735	628
	A2.2	1282	0.294	5572	758	738	713	642
	A2.3	1396	0.365	4129	721	637	615	577
	Mean value	1398	0.291	8514	755	708	688	616
CoV (%)	8.4	26.2	75.0	4.3	8.8	9.3	5.6	
A3	A3.1	840	0.188	6563	886	841	829	782
	A3.2	2627	0.168	22647	1469	1393	1349	1201
	A3.3	2394	0.410	5250	868	838	806	804
	Mean value	1954	0.255	11486	1074	1024	995	929
CoV (%)	49.7	52.6	84.3	31.8	31.2	30.9	25.4	

### Cyclic loading behavior

As explained at the beginning of this section, the EN1994-1-1 (2004) requires cyclic loading consisting of 25 cycles between 5% and 40% of the expected ultimate load. Figure 3.14 shows a zoomed-in

view of the load–slip curves for series A1, A2, and A3. It can be observed that these cycles are almost indistinguishable and remain within the elastic range.

A distinction can be made for specimen A1.1, which does not exhibit a clearly linear initial response. However, after the cyclic loading, the specimen still shows a strong linear behavior and was able to develop high shear resistance. The irregularity at the beginning of the curve could result from an error in the installation of the linear displacement sensors.

Specimen A3.1 exhibits a linear response during its first loading, but a shift can be observed in the subsequent cycles. These cycles remain elastic, although the maximum shear capacity of the bond appears to have been nearly reached. This may be attributed to an excessively high cyclic load that damaged the adhesive bond, or to fabrication issues leading to a pre-existing weakness in the interface.

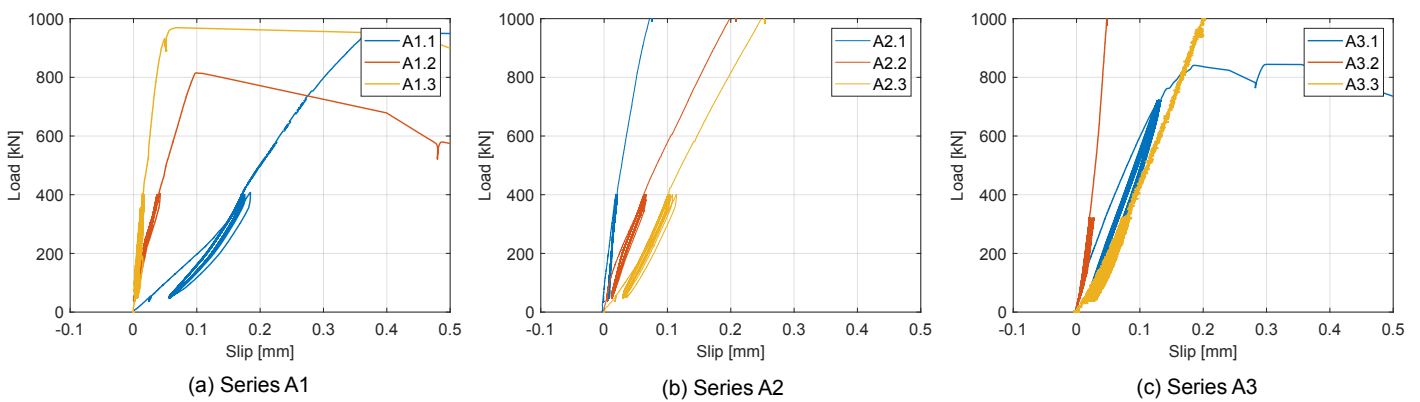


FIGURE 3.14: Cyclic loading for series A1, A2 and A3.

**Crack patterns**

Figure 3.15 presents the distribution of concrete cracks in Series A1, A2, and A3. Initially, some cracks were visible on the corners in the horizontal direction and longitudinally on the flange sides. Subsequently, these cracks progressively propagated downwards towards the unloaded end on the flange side. On the web sides, the cracks tended to slightly distribute horizontally. Meanwhile, on the flange sides, longitudinal cracks continued to develop, extending towards the total height of the concrete block. The cracks develop in series with a HEA360 (A3) are much more developed than with a HEB 200 (A1 and A2).

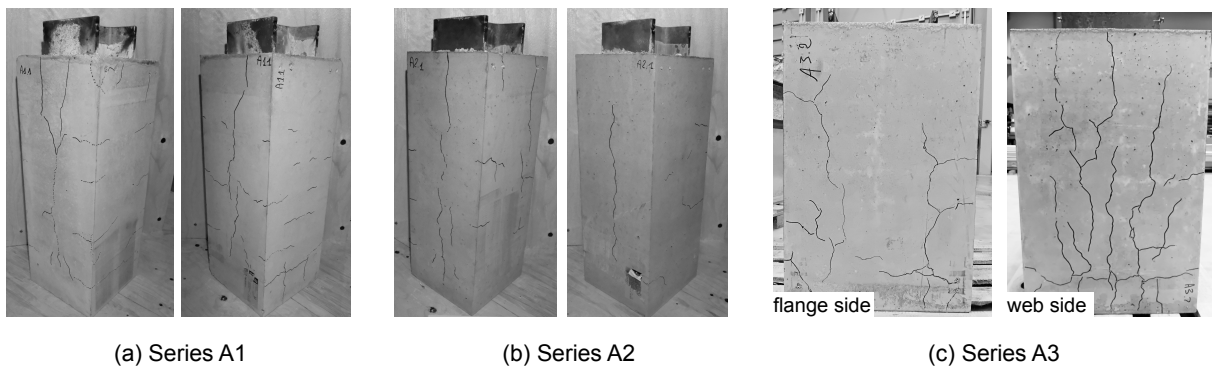


FIGURE 3.15: Crack patterns for series A1, A2 and A3.

## Discussion

Figure 3.16 presents the static load-slip curves of series A1 and A2, differing in their concrete grades, C50/65 and C80/95, respectively. Both series A1 and A2 exhibit similar load-slip behaviors characterized by a steep linear increase followed by a drop in load until a progressive decrease due to Coulomb friction degradation. Around 10 mm of slip for A1 and 15 mm for A2, a residual load directed by sliding friction is observed.

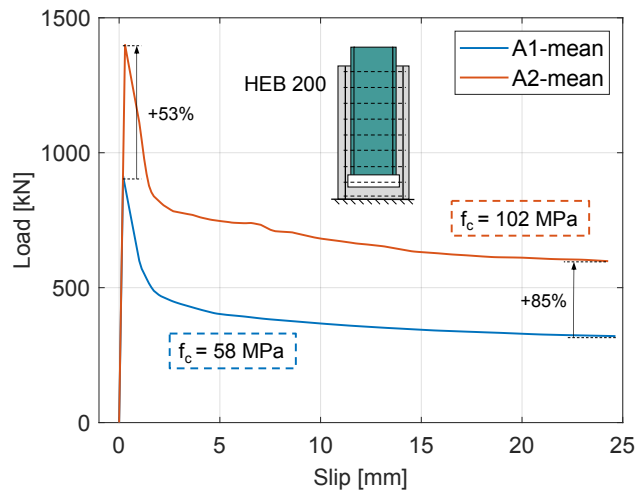


FIGURE 3.16: Impact of the concrete compressive strength on series relying on bond only with a HEB200.

Series A2 achieves a 53% higher peak load and an 85% higher residual strength than Series A1, attributed to the 76% increase in concrete strength.

Both series A1 and A2 show high variability in shear stiffness. On average, the lower concrete compressive strength in A1 results in a better shear stiffness, surpassing A2 by 43%.

As previously discussed, series A3 has a large scatter in the results, primarily due to a too-high initial cycling load in specimen A3.1. Table 3.12 summarizes the ultimate  $P_u$  and cyclic  $P_{cyclic}$  loads of series A2 and A3. It can be noticed, in Figure 3.17, that the cyclic load of series A2 was kept constant at 400 kN and approximately 29% of the ultimate load. On the other hand, in series A3, due to the early failure of adhesion during cyclic load in specimen A3.1, the cyclic load of specimens A3.2 and A3.3 was decreased to 320 kN, corresponding to 40% of the ultimate load of A3.1. This results in a cyclic load of only 12% of the ultimate load for specimens A3.2 and A3.3.

The ultimate load is mainly driven by adhesion, and the contact surface between steel and concrete plays an important role. As a result, series A3 has a higher peak resistance (+40%) than series A2 since the surfaces are respectively 1.265 and 0.794 m<sup>2</sup> (+59%).

Looking at the bond strength developed at the steel-concrete interface, it can be observed that series A3 developed slightly higher ultimate bond strength  $\tau_u$  (+13%) than series A2 (excluding specimen A3.1). Still, given the variability of adhesion resistance, the results are quite similar, with  $\tau_u$  between 1.61 and 2.08 MPa, and the residual strength  $\tau_r$  is also similar for both cross-sections, between 0.62 and 0.95 MPa. These differences can be influenced by the steel surface treatment, cross-section size, and the concrete cover of the steel profile (Wang et al., 2020).

The initial stiffness of adhesion between the different sections is higher (+35%) for HEA360 compared to HEB200, but a clear relationship cannot be established due to the high variability.

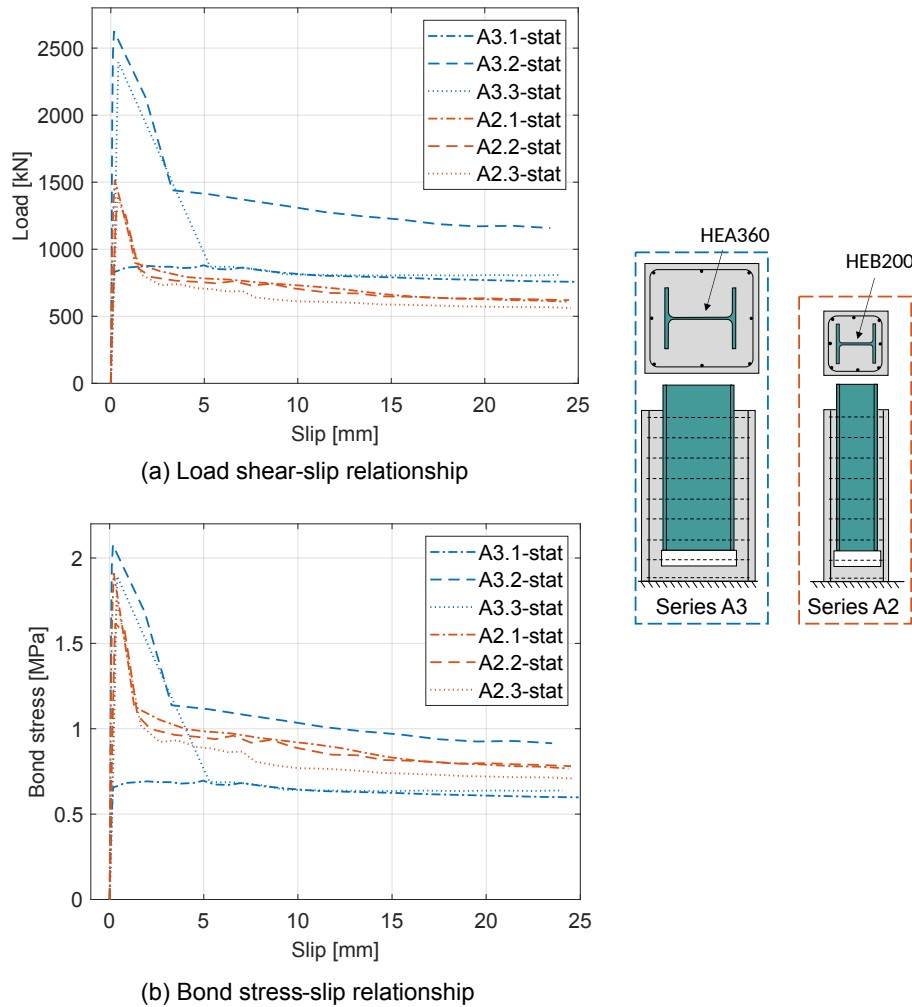


FIGURE 3.17: Influence of the cross-section size on bond resistance.

The load history is a key parameter governing the development of full steel-concrete adhesion. According to EN1994-1-1 (2004), a cyclic preloading between 5% and 40% of the expected ultimate load must be applied before monotonic loading to failure. However, defining an appropriate cyclic load amplitude is challenging without prior knowledge of the actual ultimate resistance.

Roeder (1985) reported that when the cyclic load remains below 40% of the ultimate resistance, the adhesive bond should not experience significant degradation. Nevertheless, in specimen A3.1, if the ultimate load had corresponded to the minimum value observed between A3.2 and A3.3, the applied cyclic load would have represented approximately 30% of the ultimate resistance—yet adhesion failure was observed. In contrast, series A1 and A2 exhibited a predominantly adhesive response, even though their cyclic load ratios ranged from 41-49% (A1) and 26-31% (A2).

Regarding the friction behavior observed in series A3, the results exhibit significant scatter, but no clear dependence on the load history is apparent. The same conclusion applies to series A1 and A2, where frictional resistance appears unaffected by the variation of the ratio of the initial cyclic loading to the ultimate load.

Similarly, no clear correlation can be established between loading history and initial stiffness. For instance, specimen A3.1—with a high cyclic-to-ultimate load ratio ( $P_{cyclic}/P_u = 86\%$  vs. 13% for A3.3)—still exhibited a higher initial stiffness than specimen A3.3.

Overall, these observations are derived from a limited number of tests, and the influence of long-term loading and cyclic load intensity on adhesion and frictional behavior requires further investigation.

TABLE 3.12: Summary of the series A2 and A3 comparing the section size impact on the bond resistance.

Specimen	$f_c$ (MPa)	$P_u$ (kN)	$P_{cyclic}$ (kN)	$P_{cyclic}/P_u$	$k_s$ (kN/mm)	$\tau_u$ (MPa)	$\tau_r$ (MPa)
A2.1	105	1518	400	26%	15841	1.91	0.79
A2.2	102	1282	400	31%	5572	1.61	0.81
A2.3	100	1396	400	29%	4129	1.76	0.73
A3.1	108	840	720	86%	6563	0.66	0.62
A3.2	108	2627	320	12%	22647	2.08	0.95
A3.3	108	2394	320	13%	5250	1.89	0.64

### 3.7.2 Multiple connectors on web and connectors spacing

In practice, it is likely that the natural bond developed at the steel-concrete interface is not strong enough to sustain the shear load required to reach the composite action. Moreover, as shown in the previous section, the contribution of adhesion can be important but is largely unreliable. While friction can be better evaluated, it still depends significantly on the steel surface treatment (Chrzanowski et al., 2019).

Therefore, in structural applications, mechanical shear connectors are generally added to the natural bond. Typically, in the literature, to evaluate the behavior of a shear connector solely, the steel surface is greased to limit the contribution of friction and adhesion. However, Chrzanowski (2019) showed that the contribution of the bond after greasing the surfaces was still non-negligible.

In this section, to evaluate the behavior of shear connectors in real-world conditions, we let the steel surface be without any treatment. This implies that we tested the combination of the shear connectors with the bond at the steel-concrete interface. The study focused on understanding the behavior of single and multi-connectors and investigating the impact of the distance between connector layers for different concrete compressive strengths. Series B1 and B2, featuring one connector with an opening in the web of 40 mm and a traversing rebar of 12 mm, were designed to assess the impact of a single connector with normal and high-strength concrete. Series C1 and C2, featuring 3 shear connectors with different center-to-center distances (100 mm and 200 mm, respectively) with normal-strength concrete, were evaluated to determine the impact of stress overlapping between the different layers. Indeed, Oguejiofor and Hosain (1994), Hosseinpour (2018), and Su et al. (2014) proves that the closer the shear connectors, the lower their individual resistance is. Series C3, having the same layout as series C2 but considering a high-strength concrete, aims to show the impact on concrete with 3 connectors. Series C4 and C5, featuring 4 shear connectors,

evaluated the impact of the concrete resistance with 4 connectors for normal- and high-strength concrete, respectively. Table 3.13 summarizes the differences between the configurations.

Specimens B1.3, C1.3, C2.3, and C4.3 were equipped with strain gauges to analyze the strain distribution along the length of the steel profile during the linear loading phase (before adhesion failure) and after reaching the peak load.

TABLE 3.13: Description of the series with multiple connectors on the web of HEB200.

Series	Number of connectors	Centre-to-centre distance (mm)	Mean concrete strength (MPa)
B1	1	/	60
B2	1	/	105
C1	3	100	63
C2	3	200	64
C3	3	200	104
C4	4	150	63
C5	4	150	104

Similar to series A1, the expected resisting load for series B1 was approximately the same, about 1000 kN. Thus, the cyclic load was set between 50 kN and 400 kN. Series C1, C2, and C4, featuring more connectors with the same concrete grades, were expected to reach a higher ultimate load of about 1200 kN. A cycling load between 60 kN and 480 kN was set.

The anticipated load-bearing capacity for series B2 was comparable to series A2, approximately 1300 kN for the weaker specimen. Following the test results of series B2, series C3 expected a peak load similar to B2 at approximately 1500 kN. And for series C5, the anticipated load was about 1600 kN. However, to keep a uniform loading procedure between specimens with normal- and high-strength concrete, we applied a cyclic load between 60 kN and 480 kN.

### Load-slip behavior

Figure 3.18 illustrates the load-slip behavior for series B1, B2, C1, C2, C3, C4 and C5.

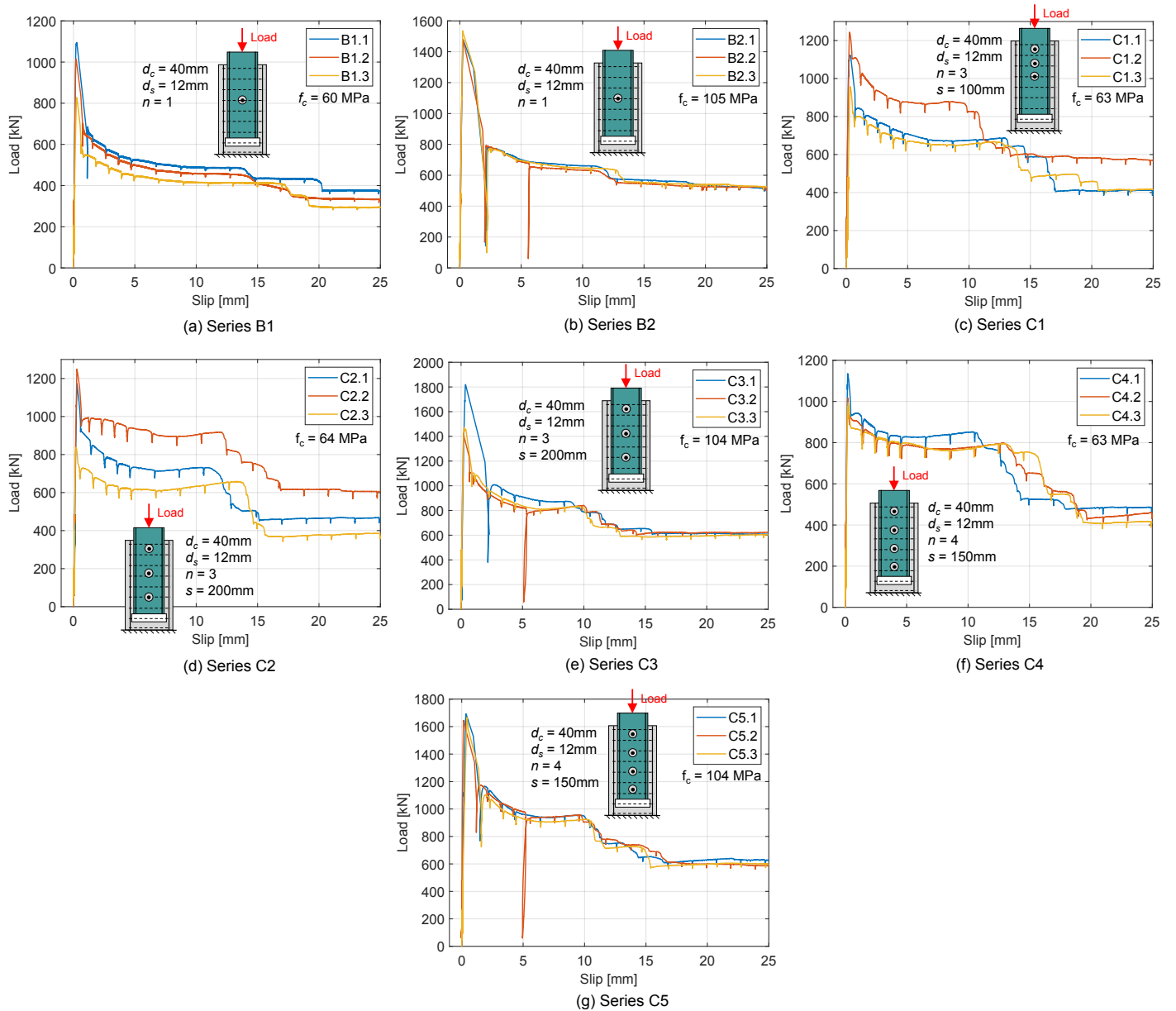


FIGURE 3.18: Load-slip curve for series B1, B2, C1, C2, C3, C4, and C5, featuring a HEB 200 section.

To consider the effect of concrete relaxation, Figure 3.19 shows the "static" load-slip curves for each series and the average of the three curves. All the results are summarized in Table 3.14. The construction of the "static" curves is shown in Fig. 3.20.

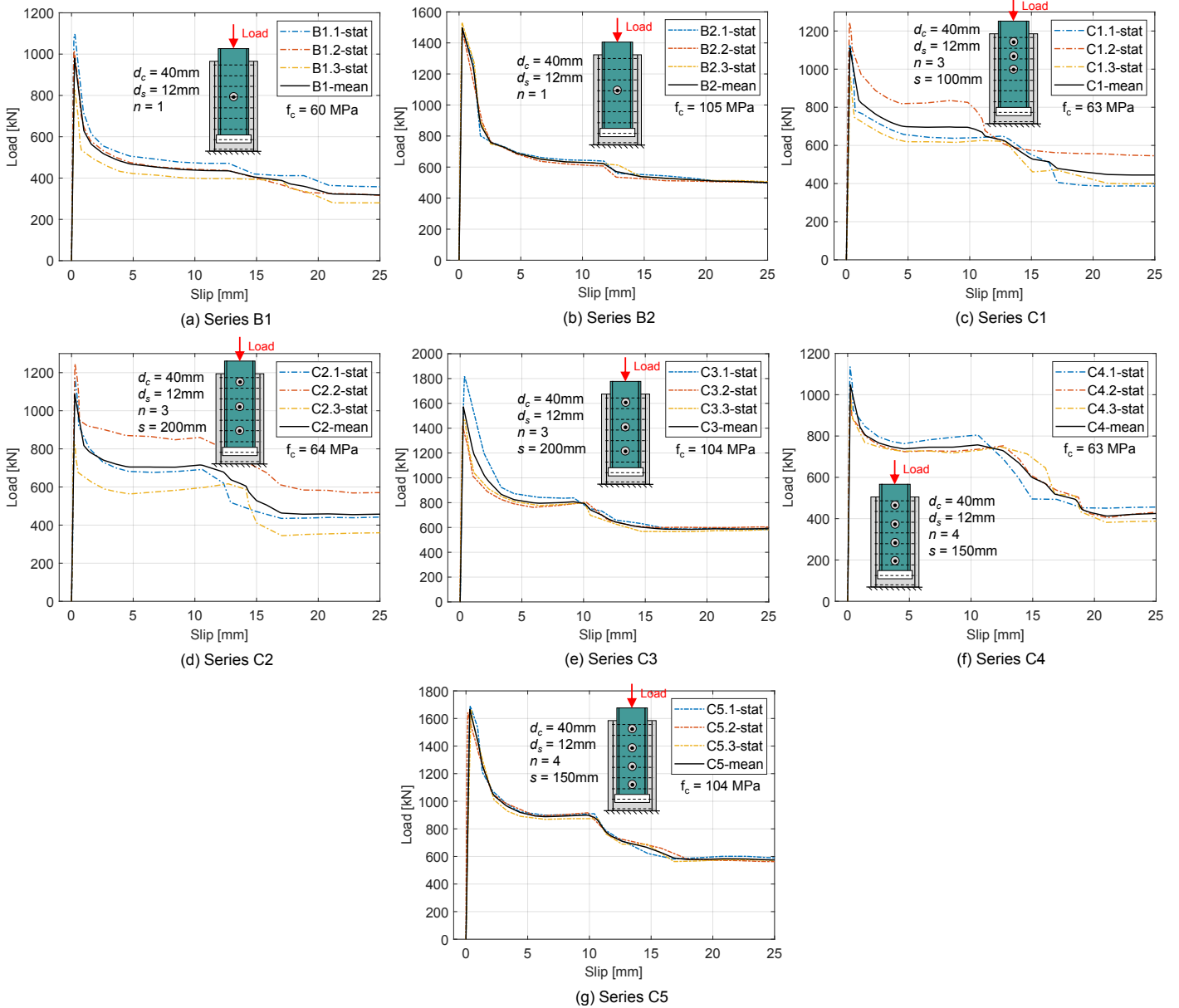


FIGURE 3.19: Static load-slip curve for series B1, B2, C1, C2, C3, C4, and C5, featuring a HEB 200 section.

The construction of Fig. 3.19 is represented in Fig. 3.20 for series C2. This has been developed by considering the lower values for each displacement increment. In this measurement, the deformation-controlled jack was maintained at a constant level, allowing observation of the influence of short-term relaxation. When a fixed deformation is imposed on concrete, the force required to maintain that deformation decreases over time. The physical cause is mainly creep, *i.e.*, time-dependent microstructural deformation. This phenomenon is primarily manifested by a lower bearing capacity. The impact of the concrete relaxation is between 5 and 7% for normal-strength concrete and between 4 and 5% for high-strength concrete.

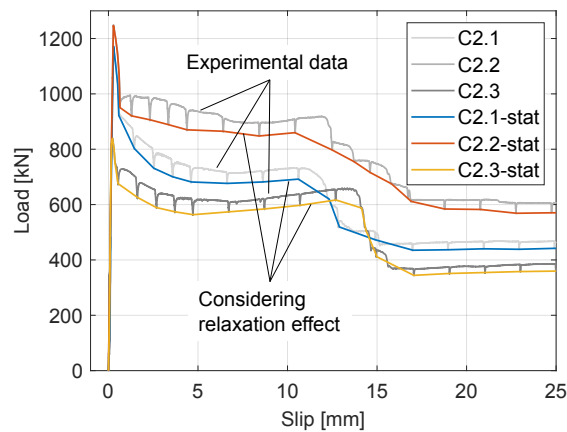


FIGURE 3.20: Construction of the "static" load-slip curve to consider the effect of concrete relaxation.

Based on the static shear-slip curves, we can build Figure 3.21, a typical load–slip curve for specimens with CRCD connectors can be defined. The response begins with a linear elastic phase, characterized by the stiffness ( $k_s$ ), which continues up to approximately 50% of the ultimate load. Beyond this point, the shear stiffness starts to degrade, leading to adhesion failure at the ultimate load  $P_u$ , corresponding to the slip  $s_u$ . For normal-strength concrete (NSC), slip values range from 0.17 to 0.29 mm, while for high-strength concrete (HSC), they range from 0.25 to 0.30 mm. Adhesion failure, which is brittle in nature, causes a sudden drop in load, stabilizing at  $P_s$  with a slip  $s_s$  of about 1.5 mm for NSC and 2.5 mm for HSC. This is followed by a progressive reduction in load, governed by the loss of Coulomb friction, until the initiation of the load plateau  $P_p$  at slip  $s_p$  (approximately 4–5 mm for NSC and around 6 mm for HSC). The plateau is controlled by both the resistance of the shear connector(s) and sliding friction, and it ends with CRCD failure at slip  $s_f$ . Connector failure typically occurs between 10–12 mm of slip for NSC and 8–11 mm for HSC. Not all connectors fail simultaneously, and failure may occur in steps; in such cases, the load stabilizes again at slip  $s_r$ , about 5–7 mm after  $s_f$ . Finally, the residual resistance of the connection is provided by the load  $P_r$ .

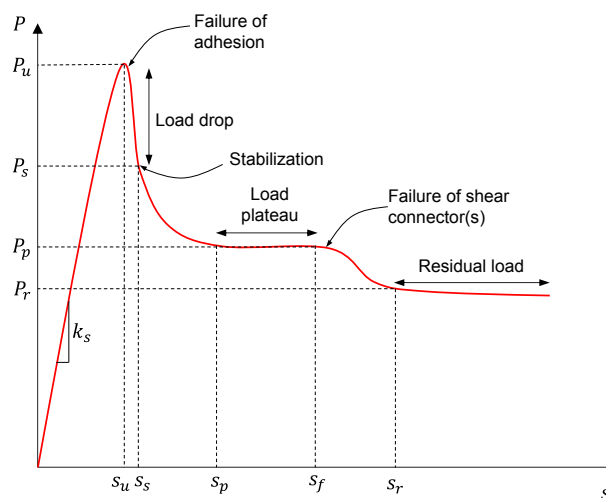


FIGURE 3.21: Typical load-slip curve.

Series B1 reached an average ultimate shear resistance of 979 kN at a slip of 0.244 mm. The initial phase showed purely linear behavior with an average shear stiffness of 5452 kN/mm. Almost no stiffness loss was recorded before the peak load. After reaching the maximum, the shear force dropped suddenly due to bond failure, stabilizing at about 60% of the peak load at a slip of 1.5 mm. Shear connector failure occurred at slips of 13 mm for B1.1 and B1.2, and 16 mm for B1.3. A progressive load decrease followed until reaching a steady state at about 33% of the maximum load, controlled by steel–concrete friction.

Series C1 exhibited an average ultimate shear resistance of 1109 kN at a slip of 0.287 mm. The initial loading phase was purely linear, with an average stiffness of 5307 kN/mm, and no notable loss of stiffness occurred until peak load. Beyond this point, the shear force dropped suddenly due to bond failure, stabilizing at about 77% of the ultimate load for a slip of 1.5 mm. Subsequently, the shear connectors failed at 9 mm of slip for C1.2, and at 12 mm for C1.1 and C1.3. A steady state was finally reached at around 42% of the maximum load, governed by friction.

Series C2 reached an average ultimate shear resistance of 1087 kN at a slip of 0.262 mm. The initial response was linear with an average stiffness of 4731 kN/mm, and minimal stiffness loss occurred before peak load. After reaching the maximum, a sudden drop in shear force due to bond failure stabilized at about 77% of the ultimate load for a slip of 1.5 mm. Connector failure occurred in stages: at 11 mm for C2.1, 12 mm for C2.2, and 13.5 mm for C2.3. The load then stabilized at about 45% of the maximum, mainly due to friction.

Series C4 reported an average ultimate shear resistance of 1049 kN at a slip of 0.223 mm. The initial phase was predominantly linear with an average stiffness of 6285 kN/mm. Minimal stiffness loss was observed up to peak load. Afterward, the shear force dropped suddenly due to bond failure, stabilizing at 82% of the ultimate load at a slip of 1.5 mm. A progressive increase followed until failure occurred at 10 mm for C4.1 and 13 mm for C4.2 and C4.3. Finally, the load stabilized at about 45% of the maximum, governed by friction.

Series B2 had a mean ultimate shear resistance of 1498 kN at a slip of 0.258 mm. The initial response was linear with an average stiffness of 7180 kN/mm. No significant stiffness loss was recorded before peak load. After maximum load, the shear force dropped suddenly due to bond failure, stabilizing at about 52% of the ultimate load at a slip of 2.5 mm. Connectors' failure occurred at 11 mm for B2.1 and B2.2, and at 13 mm for B2.3. A final steady state was reached up to 45 mm of slip, controlled by frictional resistance and connector shear friction.

After peak resistance, the adhesion bond nearly failed, and load transfer relied on the combined action of the reinforced composite dowel connector and steel–concrete friction. A sharp load drop, nearly down to 100 kN, reflected the brittle nature of adhesion failure. Under displacement control, once adhesion was lost, the steel was pushed rapidly into the concrete. The testing machine required time to reestablish contact with the steel section, explaining the initial load drop and its subsequent recovery.

Series C3 showed an average ultimate shear resistance of 1573 kN at a slip of 0.265 mm. Notably, C3.1 had about 25% higher resistance compared to the average of C3.2 and C3.3. The initial loading phase was linear with an average stiffness of 7955 kN/mm. Minimal stiffness loss was observed before peak load. Afterward, the shear force dropped suddenly due to bond failure,

stabilizing at about 61% of the ultimate load for a slip of 2.5 mm. Connector failures occurred in distinct steps starting between 8.7 and 9.9 mm of slip. Afterward, only friction resisted the applied load at about 41% of the maximum.

Series C5 achieved an average ultimate shear resistance of 1668 kN at a slip of 0.306 mm. The initial phase was purely linear with an average stiffness of 11803 kN/mm. A marked stiffness variation was observed in C5.2, which was 330% higher than the average of C5.1 and C5.3. Stiffness remained nearly constant until peak load. Afterward, a sudden drop due to bond failure stabilized at about 65% of the ultimate load for a slip of 2.5 mm. Connector failures occurred in steps starting between 9.6 and 10.1 mm of slip. After their failure, only friction resisted the applied load, reaching a steady state at about 36% of the maximum.

TABLE 3.14: Experimental results for series with multiple CRCD connectors on the web of HEB200.

Series	ID	$P_u$ (kN)	$s_u$ (mm)	$k_s$ (kN/mm)	$P(5mm)$ (kN)	$P(8mm)$ (kN)	$P(10mm)$ (kN)	$P(20mm)$ (kN)	$P(30mm)$ (kN)
B1	B1.1	1095	0.265	6152	503	481	473	385	354
	B1.2	1015	0.213	5962	471	448	442	327	321
	B1.3	827	0.254	4244	421	407	399	306	280
Mean value		979	0.244	5452	465	445	438	339	318
CoV (%)		14.0	11.2	19.3	8.9	8.3	8.5	12.1	11.6
B2	B2.1	1478	0.276	7314	682	652	644	518	487
	B2.2	1480	0.259	7116	665	625	613	507	490
	B2.3	1536	0.238	7110	681	641	628	514	503
Mean value		1498	0.258	7180	676	639	628	513	493
CoV (%)		2.2	7.4	1.6	1.4	2.1	2.5	1.1	1.7
C1	C1.1	1124	0.275	6571	651	639	638	388	385
	C1.2	1245	0.255	6395	820	829	809	556	550
	C1.3	958	0.331	2956	619	618	620	418	397
Mean value		1109	0.287	5307	697	695	689	454	444
CoV (%)		13.0	13.7	38.4	15.5	16.7	15.1	19.7	20.7
C2	C2.1	1174	0.283	4412	680	678	689	438	447
	C2.2	1249	0.280	4958	868	853	857	583	575
	C2.3	839	0.223	4823	566	580	591	352	359
Mean value		1087	0.262	4731	705	704	712	458	460
CoV (%)		20.1	12.9	6.0	21.6	19.7	18.9	25.5	23.6
C3	C3.1	1820	0.357	6453	858	838	765	592	568
	C3.2	1425	0.201	9136	775	778	791	599	604
	C3.3	1473	0.236	8276	798	785	721	571	580
Mean value		1573	0.265	7955	810	800	759	587	584
CoV (%)		13.7	30.9	17.2	5.3	4.1	4.7	2.5	3.1
C4	C4.1	1136	0.199	6604	769	790	802	451	472
	C4.2	1016	0.224	6962	725	727	733	413	444
	C4.3	994	0.245	5289	727	720	726	407	389
Mean value		1049	0.223	6285	740	746	754	424	435
CoV (%)		7.3	10.3	14.0	3.4	5.2	5.6	5.6	9.7
C5	C5.1	1693	0.341	6512	915	905	875	597	598
	C5.2	1644	0.156	24178	917	904	889	572	565
	C5.3	1667	0.422	4718	884	872	872	572	565
Mean value		1668	0.306	11803	905	894	879	580	576
CoV (%)		1.5	44.5	91.1	2.0	2.1	1.0	2.5	3.3

### Cyclic loading behavior

Figure 3.22 shows a detailed view of the shear–slip curves for series B1, B2, C1, C2, C3, C4, and C5. The 25 cyclic loadings prescribed by EN1994-1-1 (2004) demonstrate a predominantly elastic response, with minimal residual slip (about 0.02 mm) observed after unloading.

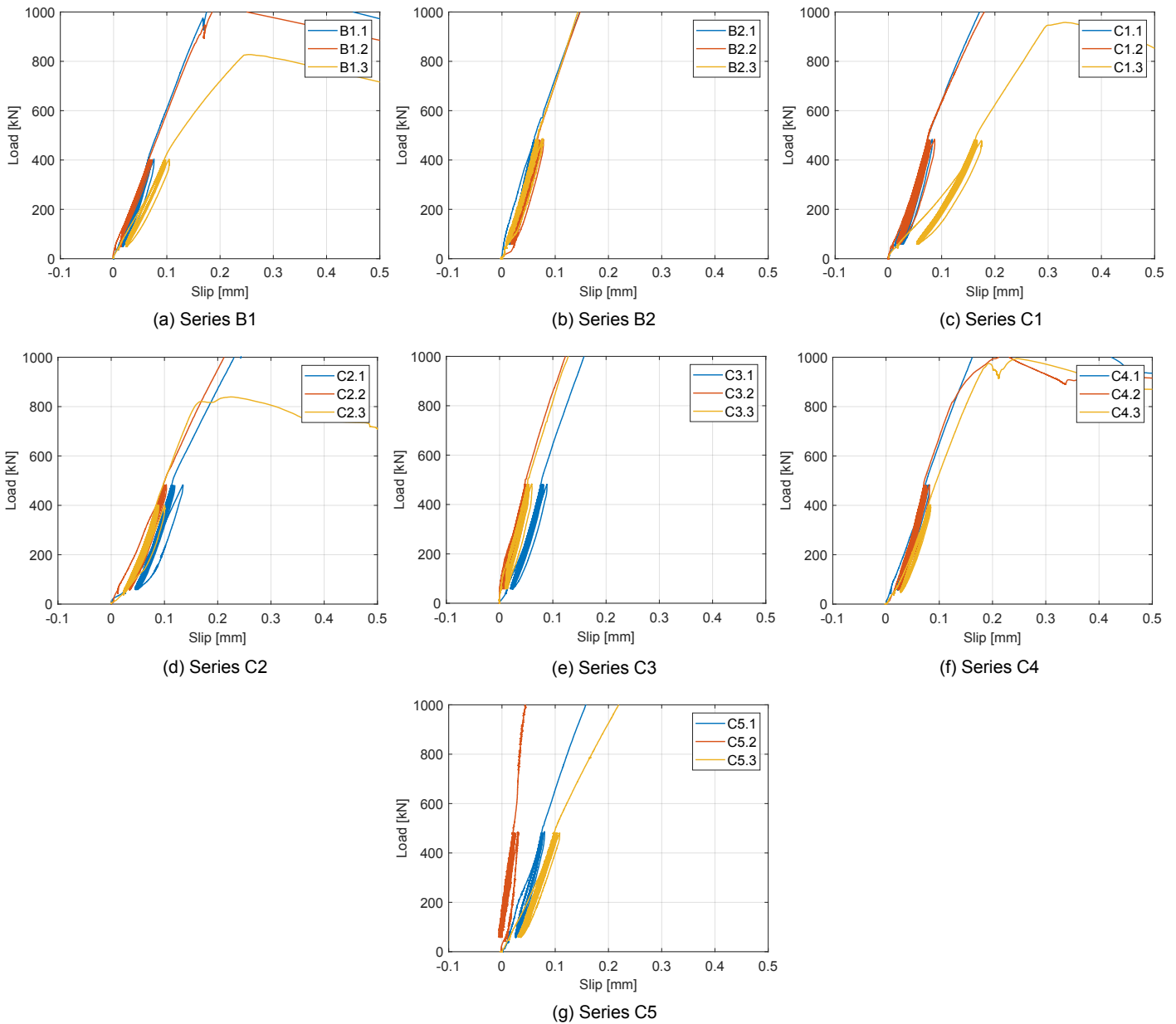


FIGURE 3.22: Cyclic loading for series B1, B2, C1, C2, C3, C4, and C5.

### Impact of the strain gauges

As explained previously, specimens B1.3, C1.3, C2.3, and C4.3 were instrumented with strain gauges in the web to measure strain distribution along the steel profile. Specimen C2.3 also had gauges on one flange. Installing these gauges altered the steel surface conditions: the epoxy used

to fill the gap for the cable and gauge had a different roughness than the sandblasted steel. Moreover, the epoxy had to be sanded to obtain a flat surface, further affecting the steel surface condition (Figure 3.23).

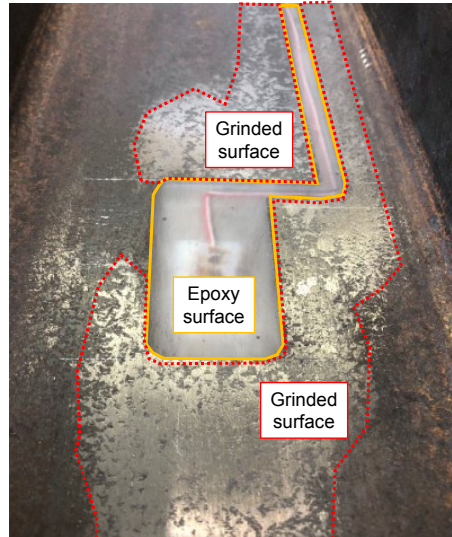


FIGURE 3.23: Representation of epoxy and sanded zones.

Consequently, B1.1 and B1.2 reached similar ultimate resistances, differing by only 8%, whereas B1.3 showed a 23% reduction compared to B1.2. Its sliding friction strength was also lower than that of the other two specimens. Similar trends were observed in series C1, C2, and C4. For series C1, specimen C1.3 deviated markedly, with a 24% lower maximum resistance than the average of C1.1 and C1.2. In series C2, specimen C2.3 showed the largest difference, with a 44% reduction compared to the average of C2.1 and C2.2. In series C4, the ultimate resistances were closer, with a maximum difference of 14% between C4.1 and C4.3. However, C4.3 exhibited a lower sliding friction, about 15% below the mean of C4.1 and C4.2.

These discrepancies can be partly attributed to a reduction of the friction coefficient in the epoxy- and sanding-affected zones. The epoxy covered 2–3% of the steel surface, while the sanded area accounted for 6–12%. Thus, although these modifications likely reduced friction resistance, they can only partially explain the reductions in shear resistance observed in the tests.

### Post-peak stiffness

For each series, we modified the loading procedure of one specimen and decreased the load after a certain slip to reload it again and capture the stiffness of the shear connectors.

Figure 3.24 shows the connector stiffness beyond 5 mm of slip. At 5.6 mm, the load was intentionally reduced to 60 kN, held for 60 s, and then reapplied, resulting in a residual difference of 22 kN in the final load. Between 60 and 550 kN, the response remained elastic with a stiffness of 9423 kN/mm, exceeding the average initial stiffness of the series (7180 kN/mm). After yielding, the stiffness decreased to 7405 kN/mm, still comparable to the initial stiffness.

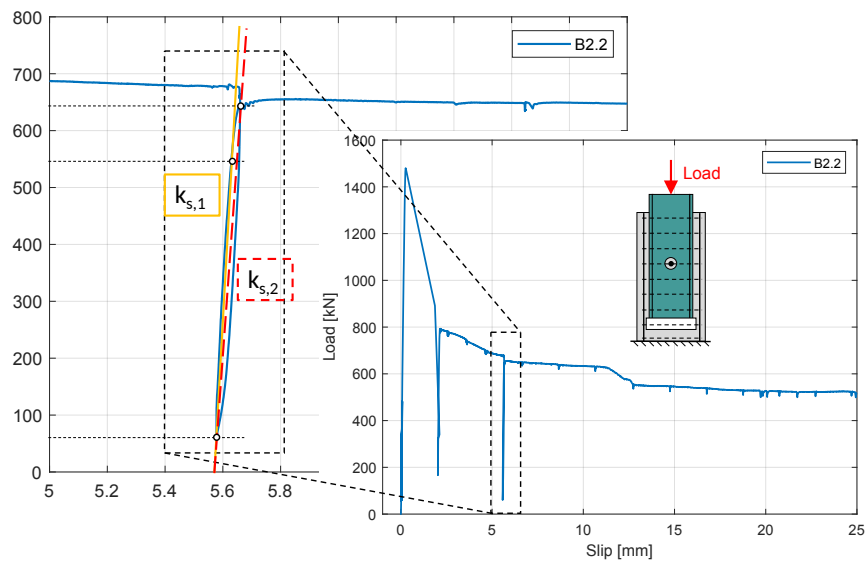


FIGURE 3.24: Post-peak stiffness of specimen B2.3.

Figure 3.25 exhibits similar behavior. At 5.3 mm of slip, the load was reduced to 60 kN, maintained for 60 s, and reloaded, producing a residual difference of 32 kN. The elastic range extended from 60 to 400 kN with a stiffness of 8293 kN/mm, slightly above the average initial stiffness of series C2 (7955 kN/mm). Beyond this range, the stiffness decreased to 2773 kN/mm until the connector yielded at about 850 kN.

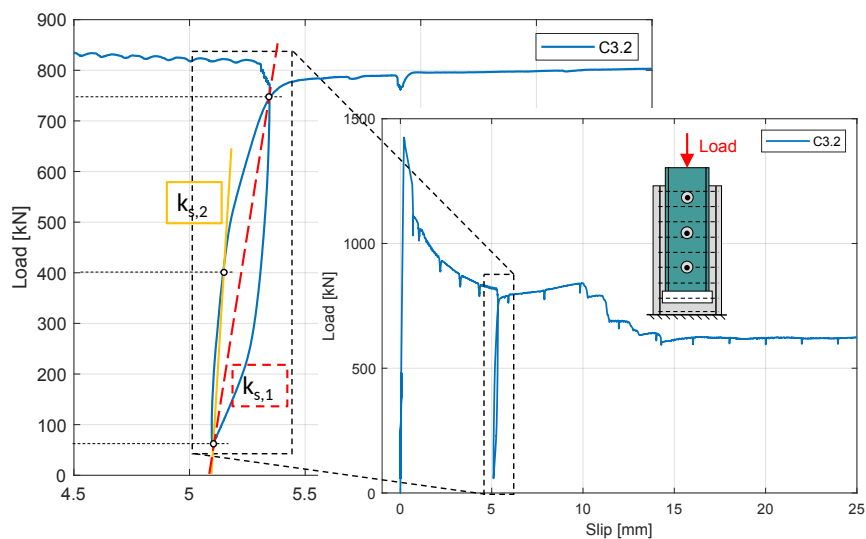


FIGURE 3.25: Post-peak stiffness of specimen C3.3.

Figure 3.26 highlights a different trend. At 5.2 mm of slip, the load was reduced to 60 kN, held for 60 s, and reloaded, resulting in a residual difference of 37 kN. Elastic behavior was observed between 60 and 400 kN with a stiffness of 17 000 kN/mm, significantly higher than the average initial stiffness of series C5 (11 803 kN/mm). Following this, the stiffness dropped to 3085 kN/mm until the connector yielded around 850 kN.

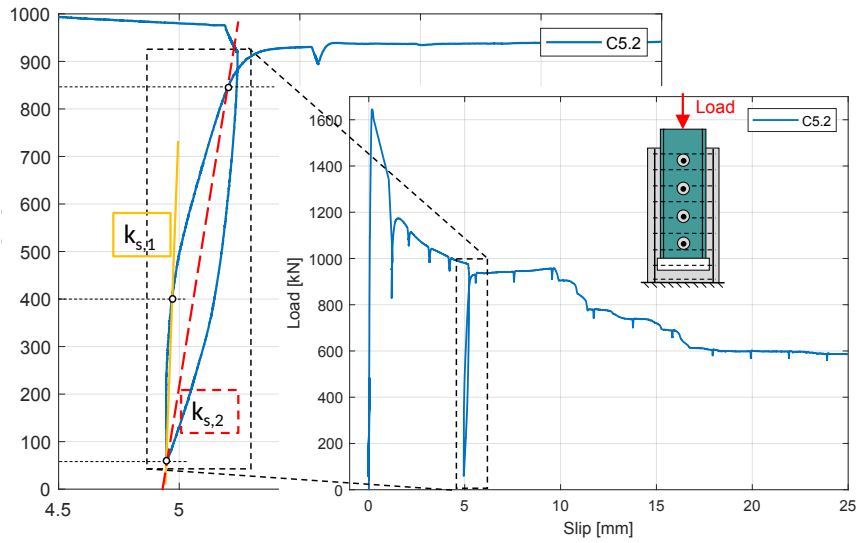


FIGURE 3.26: Post-peak stiffness of specimen C5.3.

### Crack patterns

The distribution of concrete cracks is depicted in Figure 3.27. Initially, cracks appeared on the corners in the transversal direction and longitudinally on the flange sides. Subsequently, these cracks progressed downward toward the unloaded end. On the web sides, cracks tended to distribute both transversally and longitudinally, particularly where the shear connectors were located. Longitudinal cracks on the flange sides continued to develop toward the total height of the concrete block, but were limited.

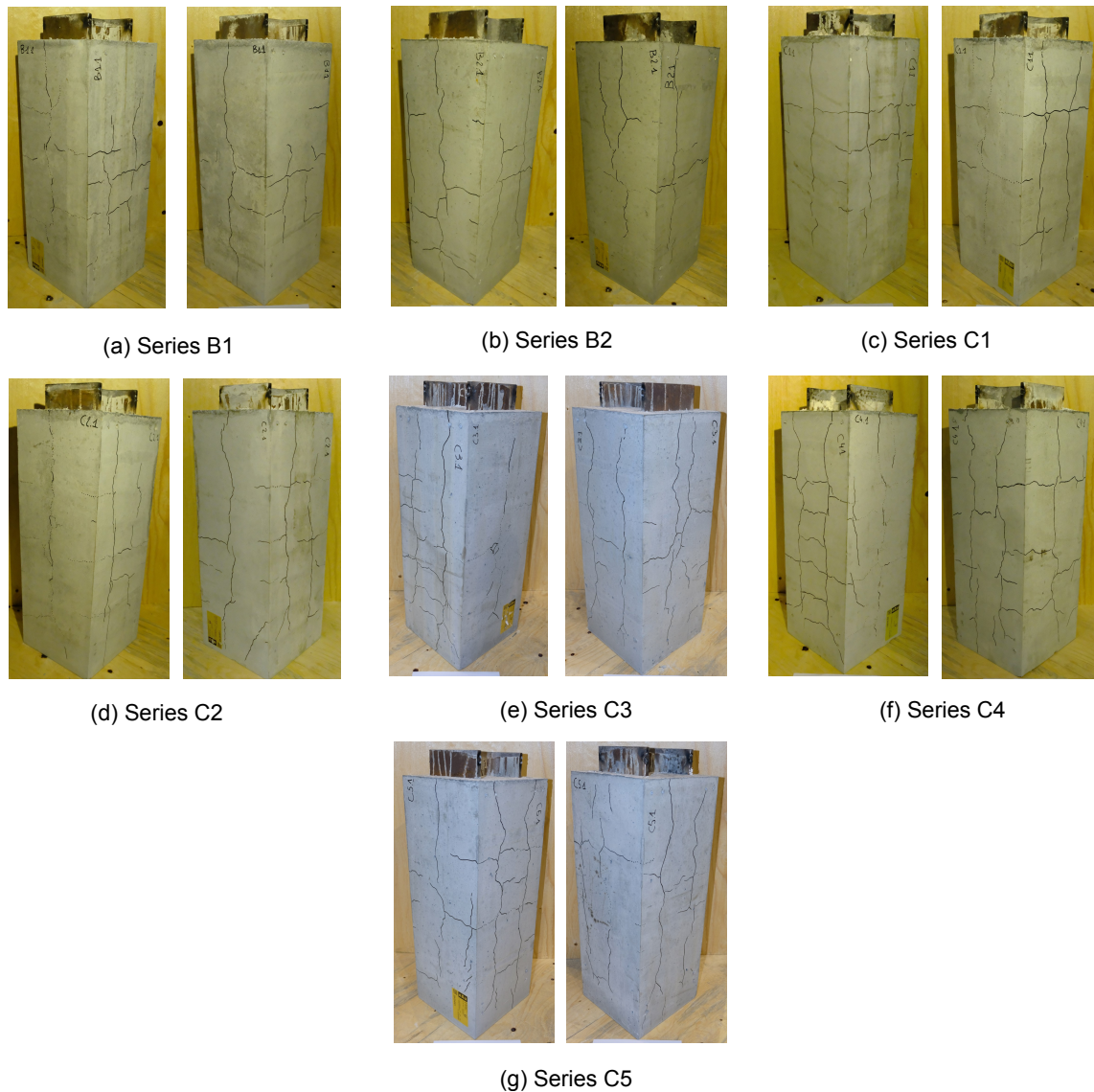


FIGURE 3.27: Crack patterns for series B1, B2, C1, C2, C3, C4 and C5.

### Shear connector failure

The inspection of the failure mode has been realized by opening one specimen of each series. In Figure 3.28, one can observe the failure details of specimen B1.3. The failure of the shear connector is primarily dictated by the rupture of the traversing rebar. With the displacement of the steel profile within the concrete block, the infill concrete in the opening is submitted to a large compressive force. As a result, the concrete matrix is crushed and reduced in volume. Through large hydrostatic pressure, the concrete compressive strength increases and can deform the traversing rebar. The high concentration stress leads to a local yielding of the steel web observed in the direction of the loading. Notably, an ovalization of the opening is observed in Figure 3.29, with a deviation of approximately 1-2 mm from the initial circular shape. This ovalization is accompanied by a local increase in the web thickness, consistent with the principles of Poisson's law.

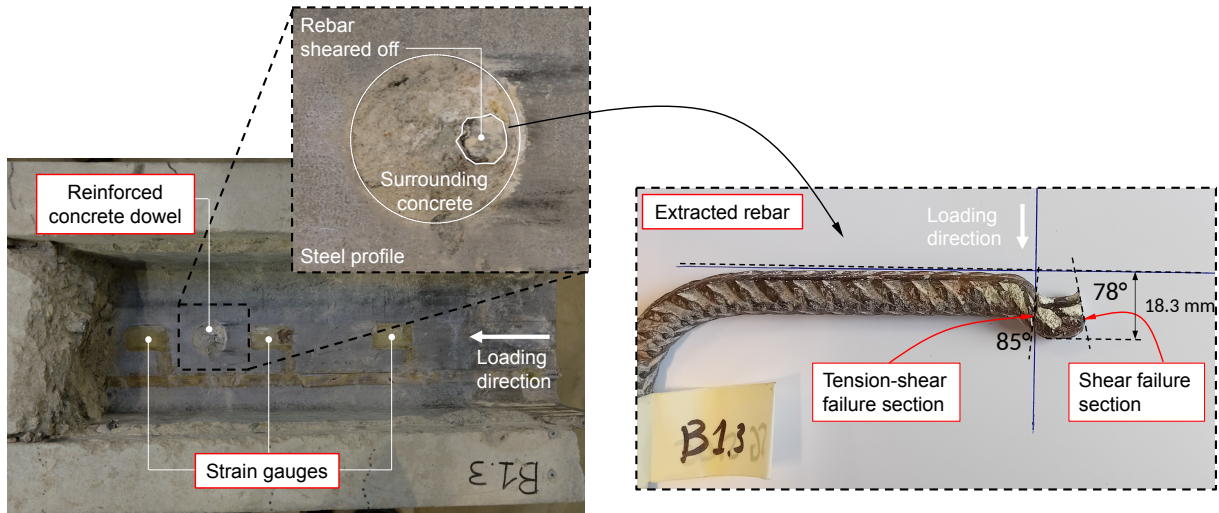


FIGURE 3.28: Failure mode of a CRCD connector.

The reinforcement bar undergoes significant deformation before localized failure occurs within the rebar. Two distinct modes of rupture have been identified: (1) a tension-shear failure occurring simultaneously on both sides of the web; (2) a two-step failure involving initial tension-shear failure on one side of the steel web, followed by flexural deformation of the remaining part of the traversing rebar, culminating in a pure shear failure at the edge of the steel profile's web.

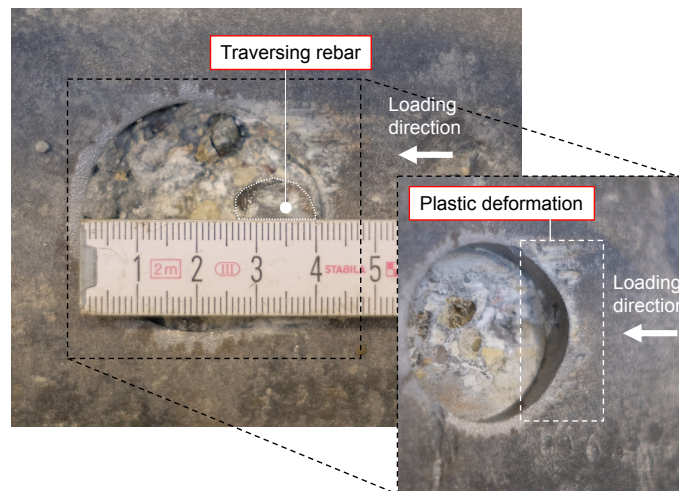


FIGURE 3.29: Plastic deformation of the steel web.

### Strains distribution

As shown in Figure 3.8, strain gauges were placed on the web of specimens B1.3, C1.3, C2.3, and C4.3. Additionally, specimen C2.3 was equipped with strain gauges on one flange to analyze the strain distribution across the section's perimeter. The positioning of the strain gauges was orchestrated to maintain approximately equal distances between them. It is pertinent to note that the number of strain gauges varies between 4 and 5, depending on the series, and their placement is not uniform in terms of distance from the shear connectors or the loading end.

**Strain distribution along the embedded length:** Figure 3.30 illustrates the strain distribution along the length of the steel profile relative to the ultimate load. The strains exhibit a non-uniform distribution along the embedded length of the steel profile, decreasing progressively from the loaded end to the unloaded end. With increasing applied load, a higher rate of strain increase is observed near the loaded end. The non-linear strain distribution is evident before reaching 50% of the ultimate load for all specimens.

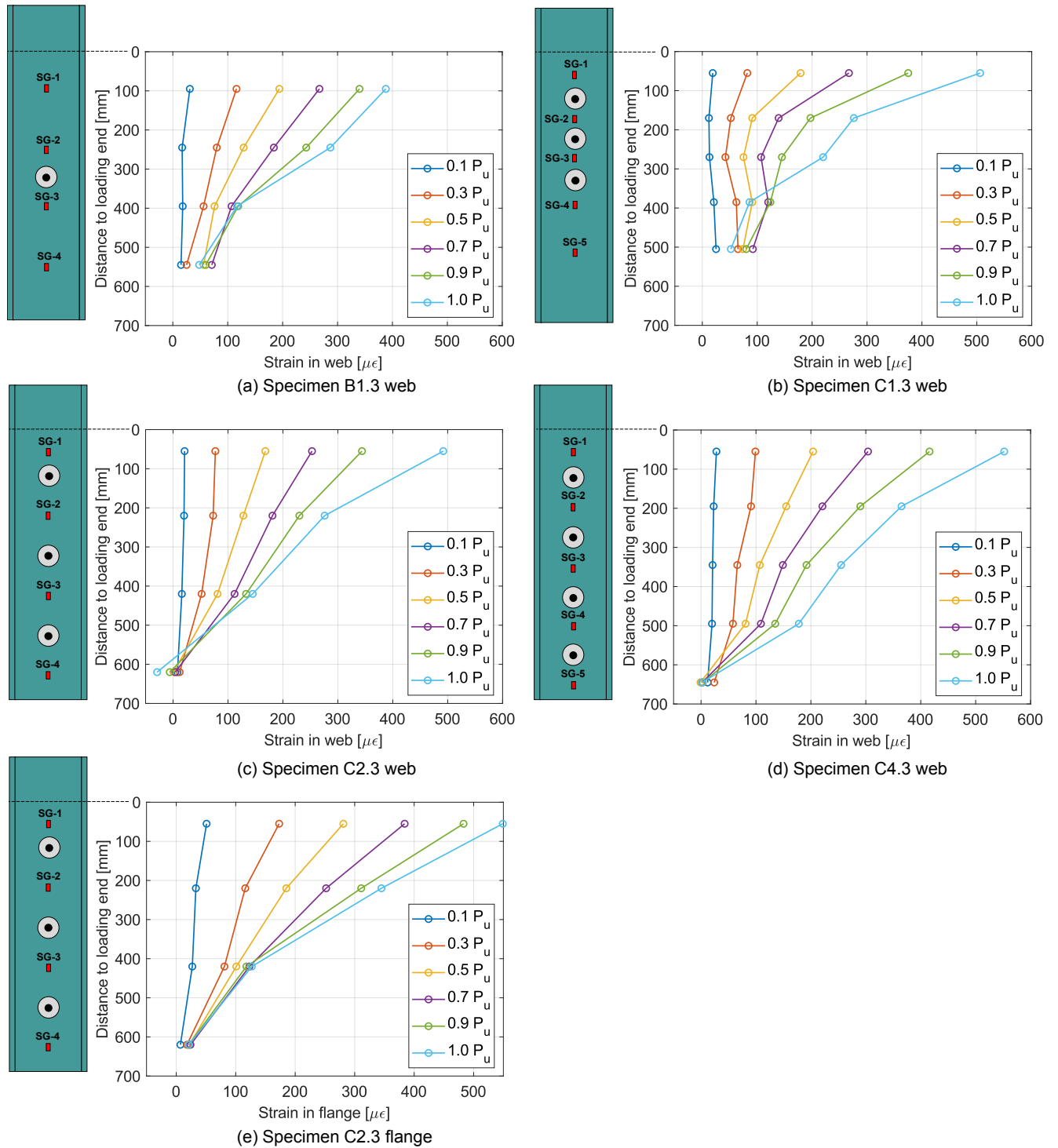


FIGURE 3.30: Comparison of strain distribution for different loading along the length.

As the applied load surpasses the 50% mark of the ultimate load  $P_u$ , bond deterioration initiates, leading to a redistribution of bond stress at the steel-concrete interface. This redistribution significantly impacts the strain distribution of the steel section. In the case of specimen C1.3, a notable difference in strains emerges around  $0.5 P_u$  between the first and second rows of strain gauges, intensifying as the applied load approaches ultimate resistance. This abrupt change in strains is attributed to the activation of the top shear connector.

For specimens B1.3, C2.3, and C4.3, where the distance between connectors is larger, the transition from almost linear to largely non-linear strain distribution is observed later, typically around  $0.7 P_u$ . This non-linear distribution further intensifies with increasing applied load. Strain gauges located after the shear connector(s) in the direction of the applied load in specimens B1.3 and C1.3 exhibit relatively low strain levels even with applied loads close to peak resistance. In contrast, at approximately the same location along the steel length, specimen C4.3 continues to experience higher strain levels due to the presence of a shear connector below the strain gauge. This observation suggests that shear connectors are activated before reaching the ultimate load, typically at around  $0.5-0.7 P_u$ .

**Strain distribution along the perimeter of the steel section:** In Figure 3.31, the strains manifest a non-uniform distribution along the section of the steel profile, indicating varying bond stresses along the embedded length and the perimeter of the steel section. Notably, higher strain levels are recorded on the flange side, particularly for the first and second rows of strain gauges in the direction of the applied load.

However, as the load increases from  $0.9 P_u$  to the ultimate load, the disparity in strain levels between the web and flange sides diminishes significantly. This phenomenon is attributed to the deterioration of bond strength with increasing load. Consequently, there is a lesser increase in strain on the flange side coupled with an enhanced transfer of shear load to shear connectors, resulting in a more substantial increase in strain on the web side.

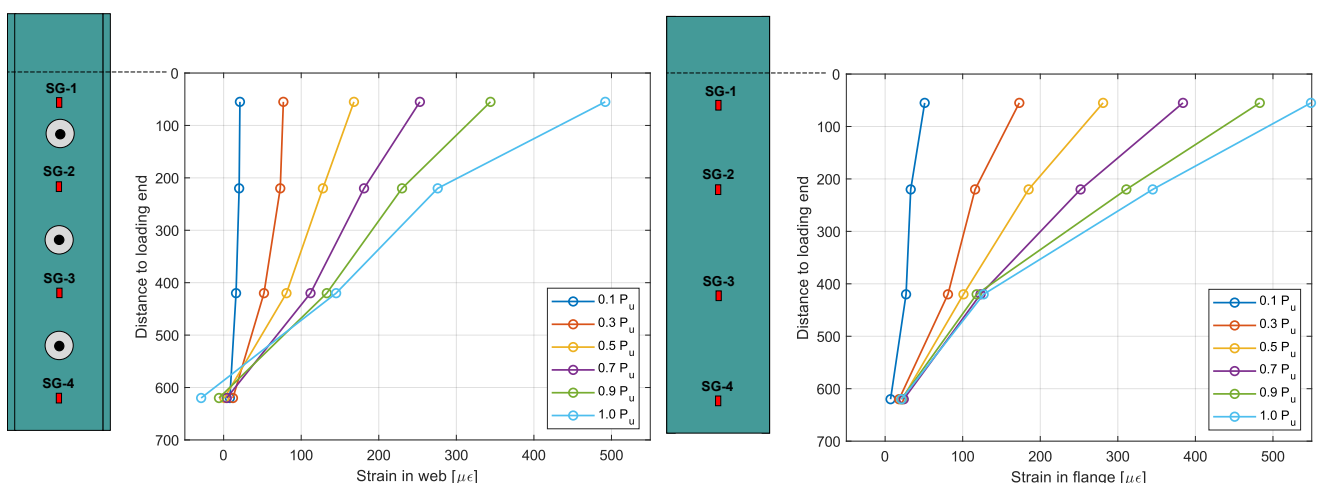


FIGURE 3.31: Comparison of strain distribution for different loading along the perimeter of specimen C2.3.

**Strain distribution in function of the relative slip:** Figure 3.32 presents the strain distribution in relation to the relative slip between steel and concrete for each strain gauge of every specimen. Considerable variations in strain levels are apparent among the different specimens, primarily contingent on the distance between the strain gauge and the shear connector. Following the failure of adhesion, the axial load is predominantly transferred from the steel to the surrounding concrete through the shear connectors and sliding friction. Consequently, localized stress concentrations in the direction of the applied load are observed around the shear connector. In simpler terms, proximity to the shear connector corresponds to higher strains.

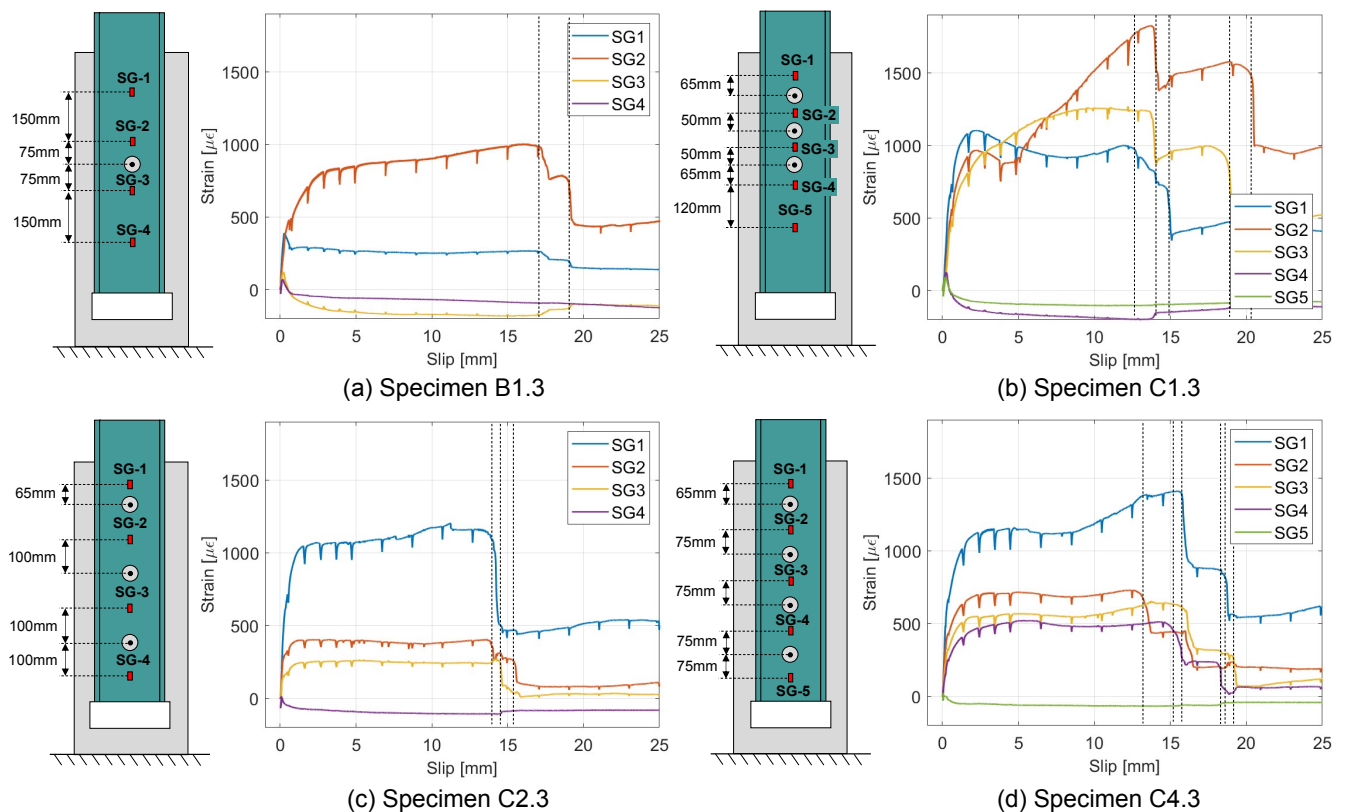


FIGURE 3.32: Comparison of strains distribution with the applied load for different strain gauge positions.

The failure of the reinforced composite dowel connector occurs in two modes: failure of the infill concrete dowel in combined compression and shear, and combined bending, tension, and shearing failure of the traversing rebar. Concrete dowel fails in shear, typically transpires shortly after reaching the ultimate load, within the range of 0.4 mm to 0.8 mm of relative slip. The traversing rebar may fail in one to two stages: initial plastic deformation due to combined tension and bending, followed by failure of the traversing rebar in shear on both sides of the web or only on one side, and finally, bending of the remaining part of the traversing rebar culminating in shear failure. Fig. 3.32 illustrates that, in specimen C2.3, only the first and last traversing rebars have failed simultaneously in shear on both sides of the web; all other rebars failed in two stages.

Previously established was the observation that the top row of strain gauges exhibits the highest strain levels and is the first to yield. However, in specimen C4.3, it is noteworthy that the shear connector in the first row is not the first to fail. Specifically, SG-2 shows a drop in strain

level before SG-1, indicating that the second connector failed before the first one in the direction of the applied load. In specimen C2.3, a simultaneous failure of the first and second connectors is observed, with the failure of the first shear connector occurring in one step, while the second one fails in two steps.

### Discussion

The influence of the number and distance between the shear connectors for normal-strength concrete is presented in Figure 3.33. We first observe that the peak load of series C1 and C2 is higher by 5% and 14%, respectively, when increasing the number of shear connectors from 1 to 3. After reaching the ultimate load, the load stabilizes around 75% of the maximum resistance for series C1 and C2 with 3 shear connectors, and only 58% for series B1 with one connector. This indicates a lower drop in force after the failure of the adhesion when increasing the number of connectors. Increasing the number of shear connectors from 1 to 3 results in a degradation of shear stiffness by 12% and 23% for series C1 and C2, respectively.

Following the drop in force, a progressive decrease in the load until 5 mm of relative slip for series C1 and C2 and 7 mm of slip for B1 is observed. This decrease is primarily due to the degradation of friction. A load plateau is then observed until the failure of the shear connectors occurs around 10 mm of slip for series C1 and C2, and 13 mm of slip for B1. Thus, increasing the number of connectors from 1 to 3 leads to a degradation of the slip capacity by 23%. The resistance of this plateau is respectively 57% and 63% higher than that of series B1 for series C1 and C2. The same behavior is observed after the failure of the connectors, where the sliding friction resistance is higher by 40% and 45% for series C1 and C2, respectively, compared to series B1 at 30 mm of slip. This difference can be explained by the larger friction provided by the sheared connectors of specimens C2 and C1 compared to B1.

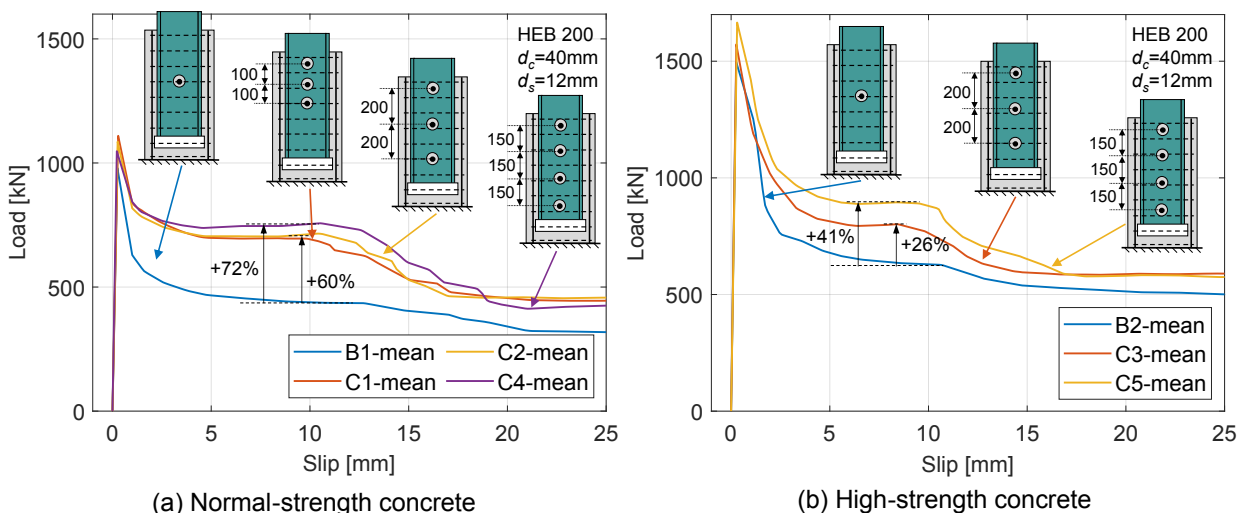


FIGURE 3.33: Impact of the number and distance of multiple CRCD connectors on the shear force.

In Series C1 and C2, both comprising three shear connectors, the only distinction is the center-to-center spacing. Increasing the spacing from 100 mm to 200 mm results in only a 3% increase

in plateau resistance, likely due to reduced overlap of the stress fields between connector layers; however, this influence is limited and becomes negligible for spacings greater than 100 mm. Accordingly, reducing the connector spacing up to 100 mm does not influence the overlapping of stresses significantly.

To further augment our analysis, we include series C4, characterized by four shear connectors spaced 150 mm apart. Comparative observations reveal that series C4 exhibits a lower peak resistance than C1 and C2 by 5% and 4%, respectively. However, it demonstrates a higher load plateau compared to C2 by 6% and C1 by 9%. Series C4 boasts a greater shear stiffness compared to C1, C2, and B1. The drop following the ultimate load is comparatively smaller for series C4, with a ratio  $P(1.5mm)/P_u = 82\%$ , in contrast to C1 and C2, which exhibit a ratio of around 75%. As demonstrated earlier, the augmentation in the number of shear connectors has been established to negatively impact slip capacity. Adding more shear connectors reduces slip capacity, likely due to placement imperfections: with more connectors, at least one rebar is more likely to be off-centre, reducing concrete cover and causing earlier rebar shear failure.

Figure 3.33b presents the static load-slip curves of specimens B1, C3, and C5 with a targeted concrete grade of C80/95 (+65% compared to  $f_c$  of C50/60). These specimens are equipped with 1, 3, and 4 shear connectors, respectively. The peak load of C5 with 4 shear connectors is 11% higher than that of B2 with 1 shear connector, and C3 with 3 shear connectors is 5% higher than B2. After the initial load drop, all specimens exhibit a progressive decrease until the plateau phase begins at 7 mm of slip for series B2, and 6 mm for series C3 and C5. The plateau concludes when the shear connector(s) start to fail, occurring at 10.5 mm of slip for B2, 8.5 mm for C3, and 9.5 mm for C5. The resistance of the C5 plateau is 41% higher than that of B2, and the series C3 plateau is 26% higher than B2. Additionally, the residual resistance of series C3 and C5 is 13% higher than B2. Considerable variability in the shear stiffness of series C5 is observed compared to series B2 and C3. Nevertheless, on average, increasing the number of shear connectors leads to an increase in shear stiffness.

The impact of concrete grade on one shear connector is illustrated in Figure 3.34a for C50/60 and C80/95 concrete. Series B2 exhibited significantly higher peak, plateau, and residual loads compared to series B1. Specifically, peak, plateau, and residual loads were, respectively, 53%, 38%, and 46% higher. Series B2 also demonstrated 32% greater shear stiffness than series B1.

In terms of slip behavior, series B2 showed a gradual decrease after the initial drop until reaching 5.5 mm of slip, whereas series B1 exhibited a similar trend but up to 4.5 mm of slip. Both series then entered a plateau phase, with series B2 concluding at 10.5 mm of slip and series B1 at 12.5 mm, ultimately resulting in shear connector failure. Thus, using higher compressive strength concrete led to higher peak, plateau, and residual loads, although with a loss of the connectors' ductility.

Regarding failure modes, series B1 specimens failed in shear in two stages, while series B2 specimens uniformly exhibited a single-step failure mechanism where the traversing rebar sheared concurrently on both sides, indicating a distinct failure pattern compared to series B1.

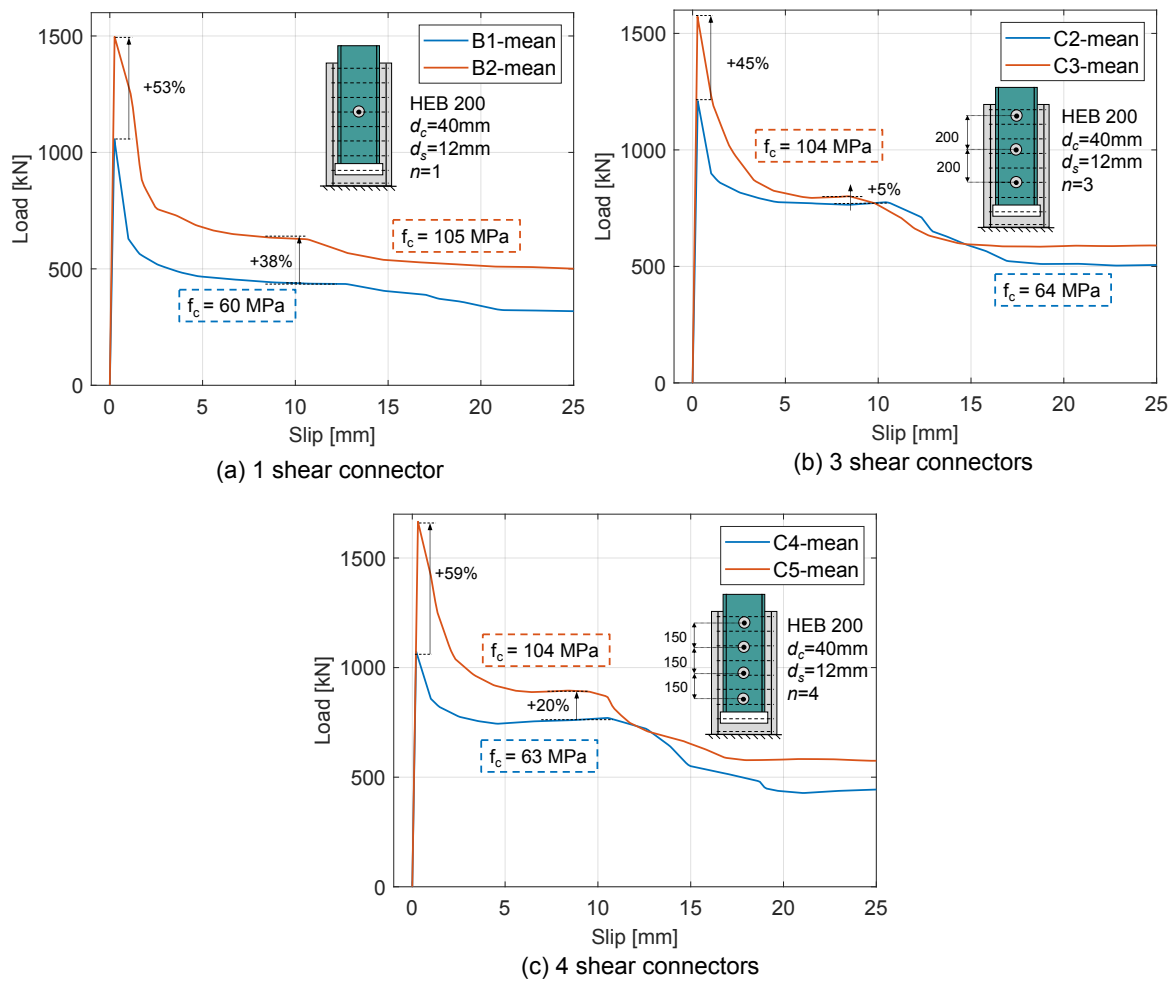


FIGURE 3.34: Comparison of the shear force-slip curves with the concrete grade.

Figure 3.34b illustrates the static load-slip curves from series C2 and C3, utilizing concrete compressive strength  $f_c = 63\text{MPa}$  and  $f_c = 104\text{MPa}$ , respectively. Series C3 showed higher peak ( $P_u$ ), plateau ( $P_p$ ), and residual ( $P_r$ ) loads compared to series C2, with peak and residual loads approximately 45% and 14% higher, and plateau load 5% higher. Series C3 also demonstrated 68% greater shear stiffness than series C2.

In terms of slip behavior, series C3 exhibited a gradual decrease after the drop until reaching 5 mm of slip, whereas series C2 showed a similar trend but up to 4 mm of slip. Both series then entered a plateau phase, concluding at 8.5 mm of slip for series C3 and 10.5 mm for series C2, resulting in shear connector failure. Thus, employing higher compressive strength concrete led to higher peak and residual loads, albeit with a slightly shorter plateau duration and a slightly higher load plateau.

Figure 3.34c depicts the static load-slip curves from series C4 and C5, using concrete classes C50/65 and C80/95 respectively. Series C5 exhibited elevated peak, plateau, and residual loads compared to series C4, with peak and plateau loads approximately 59% and 20% higher, and residual load 32% higher. Series C5 also showed significantly higher shear stiffness (11803 kN/mm) compared to series C4 (6285 kN/mm). In terms of slip behavior, series C5 displayed a gradual decrease post-drop until reaching 5.5 mm of slip, while series C4 showed a similar trend but up to

3.5 mm of slip. Both series then entered a plateau phase, concluding at 9.5 mm of slip for series C5 and 11 mm for series C4, resulting in shear connector failure. Thus, employing higher compressive strength concrete resulted in higher peak, plateau, and residual loads, albeit with a shorter plateau duration. However, it is noted that series C5 exhibited greater data scatter.

### 3.7.3 Shear connectors layout on web and scale-up

This experimental series investigates the effect of scaling up the composite cross-section while keeping the embedded length constant, as well as the use of larger shear connectors. In previous tests, the influence of the number of connectors and their spacing was examined. Here, two configurations with the same number of connectors but different layouts are presented.

Both series consist of a HEA 360 steel section embedded in a  $540 \times 560$  mm C80/95 reinforced concrete block, with 60 mm diameter openings in the web traversed by 20 mm diameter reinforcing bars:

- Series D1: 4 shear connectors arranged in two rows, with horizontal and vertical spacing of 200 mm;
- Series D2: 4 shear connectors arranged in four rows, with spacing of 150 mm.

The anticipated resistance for each series was approximately 2700 kN. According to EN1994-1-1 (2004) Annex B, this corresponds to a cyclic load range between 1080 kN and 135 kN.

#### Load-slip behavior

Figures 3.35a and b present the shear-slip curves for the specimens of series D1 and D2. While Figures 3.35c and d illustrate the static shear-slip curves, representing the effect of concrete relaxation, along with the mean curve derived from the three specimens of each series. After the peak load is reached, the shear connectors are activated, and the influence of the jack speed is determined to be approximately 5%. For this measurement, the deformation-controlled jack was kept constant, and the influence of the short-term concrete relaxation was observed. This phenomenon is mainly translated by a lower bearing capacity.

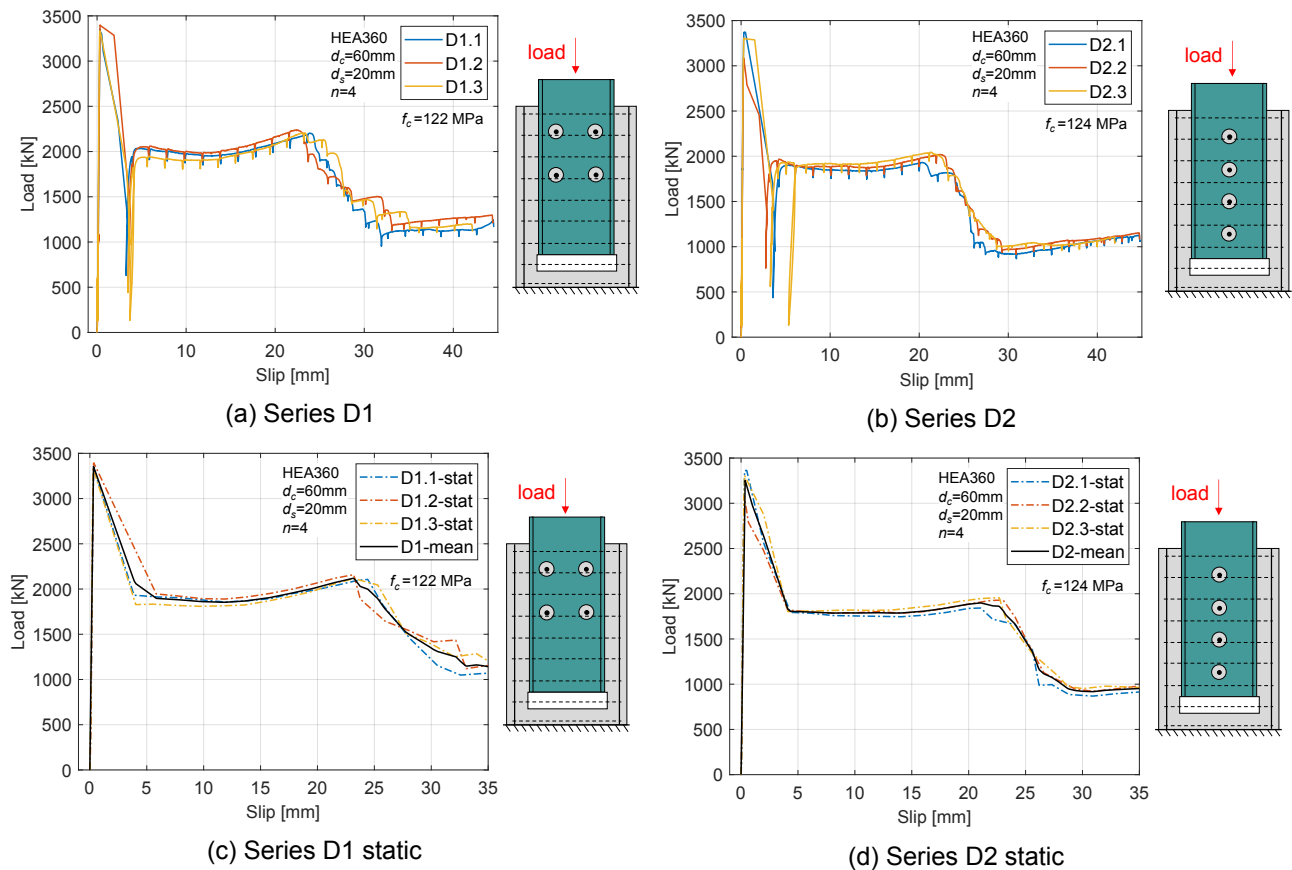


FIGURE 3.35: Load-slip and static load-slip curves for Series D1 and D2.

Series D1 reached an average ultimate shear resistance of 3362 kN at a slip of 0.322 mm, while series D2 reached 3254 kN at 0.311 mm (Table 3.15). Both series exhibit an initially linear response, with average shear stiffnesses of 9925 kN/mm (D1) and 11831 kN/mm (D2). This stiffness is maintained up to the peak load, after which it drops abruptly and stabilizes at about 60% of the maximum resistance in both cases. Subsequently, yielding of the shear connectors leads to a slight increase in shear force, until the failure of the shear connectors between 22.5 mm and 24 mm for D1, and between 20.3 mm and 22.5 mm for D2.

Beyond the ultimate resistance, the adhesion bond almost completely fails, and shear transfer is governed by the CRCD connectors together with steel-concrete friction. For all specimens, the load decreases by about 1350 kN (D1) and 1330 kN (D2), stabilizing at slips of 4–5 mm. The load then remains stable until the first shear connector failures occur. These are observed at slips of 24.0 mm, 22.6 mm, and 23.3 mm for D1.1, D1.2, and D1.3, and at 20.3 mm, 21.3 mm, and 22.5 mm for D2.1, D2.2, and D2.3. Connector failures progress stepwise until final slips of 32.0 mm, 33.0 mm, and 35.0 mm for D1 specimens, and 27.5 mm, 29.4 mm, and 28.8 mm for D2 specimens. After the complete failure of the connectors, friction alone resists the applied load.

TABLE 3.15: Experimental results for series with multiple CRCD connectors on the web of HEA360.

Series	ID	$P_u$ (kN)	$s_u$ (mm)	$k_s$ (kN/mm)	$P(5mm)$ (kN)	$P(8mm)$ (kN)	$P(10mm)$ (kN)	$P(20mm)$ (kN)	$P(30mm)$ (kN)
D1	D1.1	3353	0.321	9366	1921	1901	1878	1996	1221
	D1.2	3399	0.338	9442	2166	1919	1893	2068	1429
	D1.3	3334	0.307	10967	1830	1816	1809	1994	1392
Mean value		3362	0.322	9925	1972	1879	1860	2019	1347
CoV (%)		1.0	4.8	9.1	8.8	2.9	2.4	2.1	8.2
D2	D2.1	3371	0.342	12126	1992	1759	1754	1837	876
	D2.2	3084	0.282	10936	1897	1785	1789	1886	908
	D2.3	3307	0.308	12432	1820	1814	1818	1929	951
Mean value		3254	0.311	11831	1903	1786	1787	1884	912
CoV (%)		4.6	9.7	6.7	4.5	1.5	1.8	2.4	4.1

### Cyclic loading behavior

Figure 3.36 presents a zoomed-in view of the shear–slip curves for series D1 and D2. The 25 loading cycles prescribed by EN1994-1-1 (2004) exhibit an elastic behavior, remaining within the linear range of the response. The specimens show negligible residual slip (about 0.03mm) after unloading, confirming that no significant damage occurred during the cyclic loading phase and that the adhesive bond maintained its integrity prior to monotonic loading.

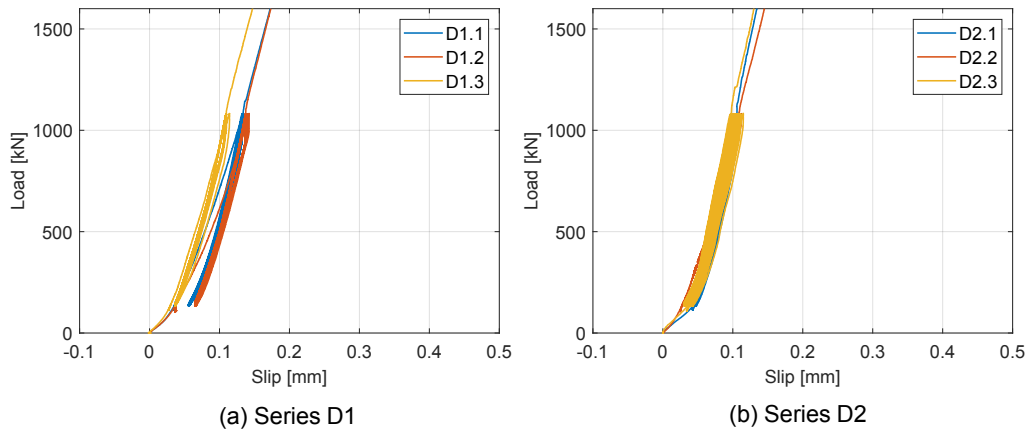


FIGURE 3.36: Cyclic loading for series D1, and D2.

### Post-peak stiffness

Figure 3.37 presents a detailed view of the load–slip response of specimen D1.1, highlighting the connector stiffness after peak load. At a relative slip of 4 mm, the load was reduced to 130 kN, held for 60 seconds, and then reloaded. The reloading branch exhibits an elastic response with a stiffness  $k_{s,1} = 6347$  kN/mm. This stiffness is 36% lower than the average initial stiffness of the series (9925 kN/mm). In addition, a secant stiffness of  $k_{s,2} = 3368$  kN/mm can be defined

between the origin and the point where the stiffness begins to decrease significantly at a load of 1700 kN.

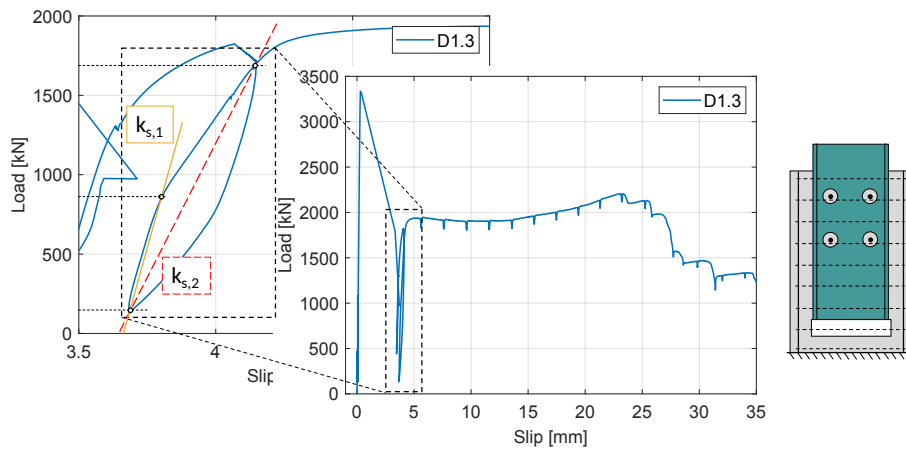


FIGURE 3.37: Post-peak stiffness of specimen D1.3.

Similarly, Figure 3.38 illustrates the load–slip curve of specimen D2.1. At a relative slip of 6 mm, the load was reduced to 130 kN, held for 60 seconds, and then reloaded. In this case, a secant stiffness of  $k_{s,2} = 2346$  kN/mm is obtained between the origin and the point of noticeable stiffness reduction at 1750 kN. Almost no elastic was noticed in this specimen. The secant stiffness was about 5 times lower than the average initial stiffness of the series at 11831 kN/mm.

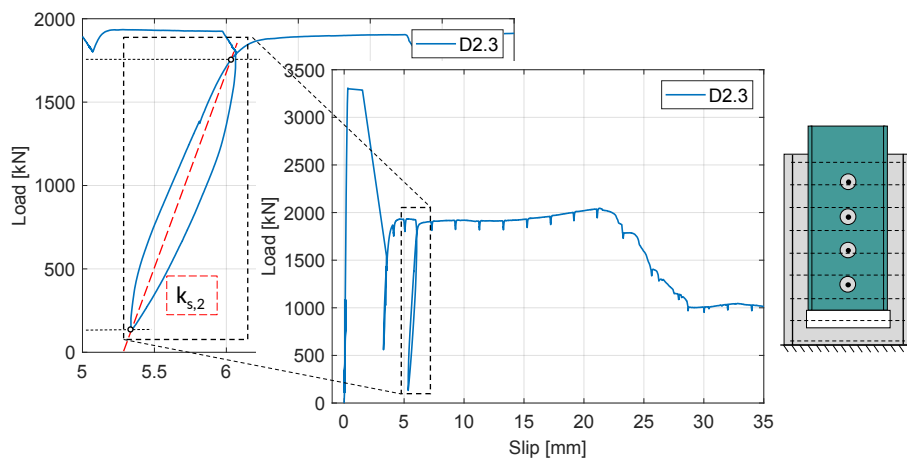


FIGURE 3.38: Post-peak stiffness of specimen D2.3.

### Crack patterns

The distribution of concrete cracks is presented in Figure 3.39 for Series D1 and D2. On the web side, the cracks are mainly distributed in the areas around the shear connectors. On the flange side, they are mainly distributed longitudinally due to the expansion of the shear connectors.

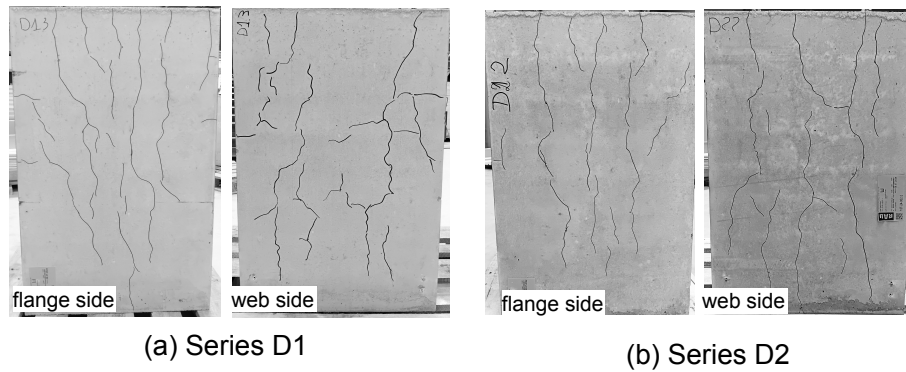


FIGURE 3.39: Crack patterns for Series D1 and D2.

### Shear connector failure

Figure 3.40 shows the failure mode of the 20 mm traversing rebar located in one of the openings of specimen D1.2. The failure mode observed in the remaining connectors is analogous, including those in series D2. Pronounced deformation of the steel web is visible in the load direction in the vicinity of the traversing rebar.

Because the shear resistance of the 20 mm traversing rebar exceeded that of the 10 mm steel web, the web experienced substantial ovalization. The traversing rebar exhibited the same failure pattern previously identified for the 12 mm traversing rebars embedded in normal-strength concrete.

As load increased, the high-strength concrete crushed and compacted, reducing its volume. The resulting confinement forced the infill concrete to deform the steel web until the rebar reached its deformation limit and began to bend. Ultimately, the traversing rebar failed through a combined tensile–shear mechanism on one side of the web, while the remaining portion bent and subsequently failed in shear.

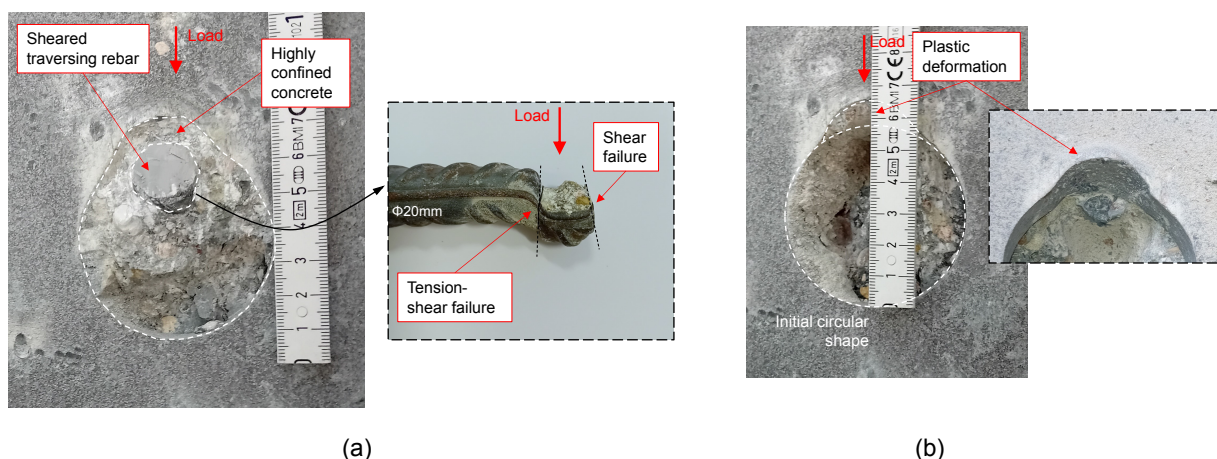


FIGURE 3.40: Shear connector failure for Series D1.

### Discussion

Series D1 and D2 were designed with identical geometries, cross-sections, number of CRCD connectors, and concrete strength. The key variable between them is the arrangement of the shear

connectors: series D1 features four connectors arranged in two vertical rows of two, while series D2 aligns all four in a single vertical row.

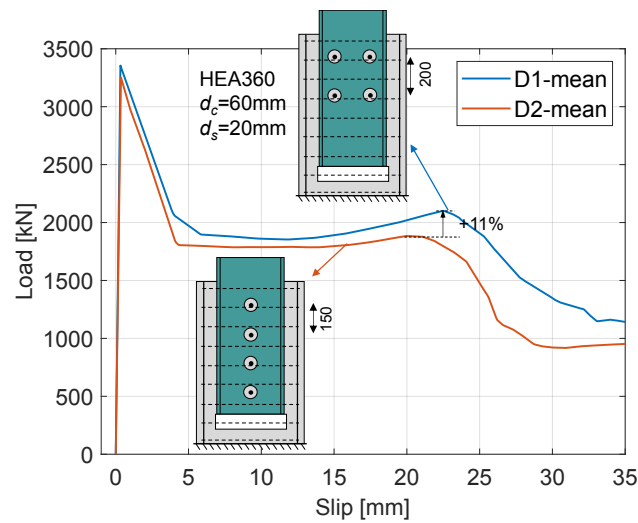


FIGURE 3.41: Analysis of Series D1 and D2.

Comparative analysis reveals that series D2 exhibits 20% higher initial stiffness than D1. However, as shown in Figure 3.41, series D1 surpasses D2 in both peak load (+3%) and plateau load (+11%). The average slip capacity of series D1 also exceeds that of series D2 by 2 mm, though this is influenced by an early failure in specimen D2.1. When excluding this specimen, both series demonstrate comparable slip capacities.

The important ductile plateau observed in both series is primarily attributed to the concrete cover between the traversing rebar and the edge of the web opening. As this infill concrete crushes under load, volume reduction in the concrete leads to enhanced slip capacity. Although the theoretical infill concrete thickness is only 20 mm (distance between the traversing rebar and the web opening, slip capacities reach 22–24 mm. This discrepancy can be explained by: (1) partial preservation of confined concrete between the steel profiles, (2) rebar deformation contributing additional slip, and (3) ovalization of the 60 mm steel opening due to deformation of the 10 mm thick web by the 20 mm rebar, adding approximately 5 mm of slip.

### 3.7.4 Shear connectors on flanges and scale-up

Positioning shear connectors on the web is the conventional solution, mainly because welding headed studs on the inner surface of flanges is not possible, and placing them on the outer surface complicates reinforcement cage arrangement. In addition, the reduced concrete cover on the flange side limits the possible stud size.

With CRCD shear connectors, the only constraint for flange placement is the bending diameter of the rebars relative to the concrete cover. This provides greater flexibility in connector arrangement. Since an H-shaped steel profile has two flanges for one web, it is possible to place up to twice as many connectors over the same embedded length on the flanges, improving the load transfer in the load introduction zone.

Series E1 consisted of a HEA 360 section with eight flange openings of 50 mm diameter, each traversed by U-shaped 16 mm rebar. Larger rebars could not be used due to the bending radius restrictions imposed by the concrete cover. This series aimed to evaluate the feasibility and performance of CRCD connectors placed on the flanges.

Since this was the first series tested at the University of Wuppertal, calibration adjustments were necessary. In specimens E1.1 and E1.2, the displacement sensor of the hydraulic press was not sensitive enough to capture stress relaxation during the waiting phases, resulting in significant force fluctuations while maintaining constant displacement. For specimen E1.3, the sensor calibration was refined, which substantially reduced this noise.

### Load-slip behavior

Figure 3.42a presents the shear-slip curves for the specimens of series E1. While Figure 3.42b illustrates the static shear-slip curves, representing the effect of concrete relaxation, along with the mean curve derived from the three specimens of each series. The influence of the jack speed is about 8% and is characterized mainly by a reduced shear load.

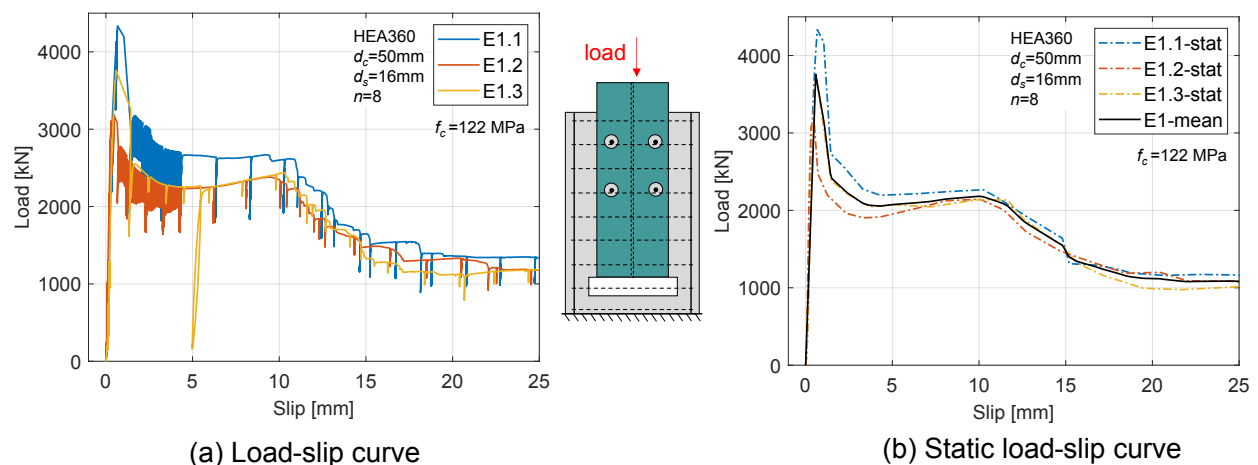


FIGURE 3.42: Load-slip and static load-slip curves for Series E1.

A noticeable scatter in ultimate resistance was observed among the three specimens. After adhesion failure, specimens E1.2 and E1.3 showed a plateau-like response similar to E1.1. Series E1 reached an average ultimate shear resistance of 3759 kN at a slip of 0.582 mm (Table 3.16). The initial loading phase was linear, with an average shear stiffness of 8541 kN/mm, which remained almost unchanged until the ultimate load. Beyond this point, stiffness dropped sharply and stabilized at about 59% of the ultimate resistance. A slight load increase followed due to the yielding of the shear connectors, with secondary peaks between 20.3 and 22.5 mm.

Once the adhesion bond failed, shear resistance was carried by the reinforced composite dowel action and steel–concrete friction. The load dropped by about 1200–1500 kN and stabilized at 1–1.5 mm of slip. It then remained nearly constant up to 3–4 mm, marking the onset of plateau behavior, before progressively increasing until the first connector failures at 9.3 mm, 9.4 mm, and 10.3 mm for E1.1–E1.3. Connector failures occurred in stages, extending to 18.3 mm, 22.3 mm, and 17.2 mm, after which only friction resisted the applied load.

TABLE 3.16: Experimental results for series with multiple CRCD connectors on the flanges of HEA360.

Series	ID	$P_u$ (kN)	$s_u$ (mm)	$k_s$ (kN/mm)	$P(5mm)$ (kN)	$P(8mm)$ (kN)	$P(10mm)$ (kN)	$P(20mm)$ (kN)	$P(30mm)$ (kN)
E1	E1.1	4335	0.674	7797	2399	2341	2344	1222	1218
	E1.2	3183	0.478	10681	2072	2210	2217	1268	1077
	E1.3	3759	0.593	7146	2040	2137	2218	969	1032
Mean value		3759	0.582	8541	2170	2229	2260	1153	1109
CoV (%)		15.3	16.9	22.0	9.1	4.6	3.2	14.0	8.8

### Cyclic loading behavior

A similar behavior to the previous tests can be observed in Figure 3.43, which presents the response of specimen E1 under cyclic loading. The load–slip curve exhibits a linear response, indicating that the adhesive bond remained intact and that no significant damage occurred during the cycling phase.

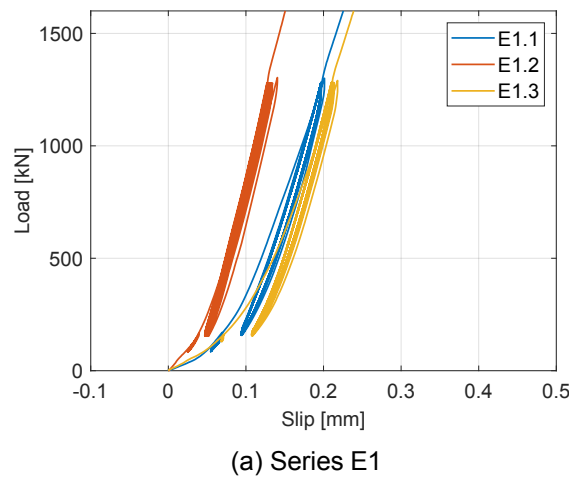


FIGURE 3.43: Cyclic loading for series E1.

### Post-peak stiffness

Figure 3.44 shows the load–slip curve of specimen E1.1, highlighting connector stiffness after the peak load. At a slip of 5.4 mm, the load was reduced to 150 kN, held for 60 seconds, and then reloaded. The reloading exhibited an elastic response with a stiffness of  $k_{s,1} = 7001$  kN/mm. This stiffness is 18% lower than the initial stiffness (8541 kN/mm). A second stiffness,  $k_{s,2} = 4293$  kN/mm, was identified between the initial loading point and the onset of significant stiffness reduction at 1975 kN.

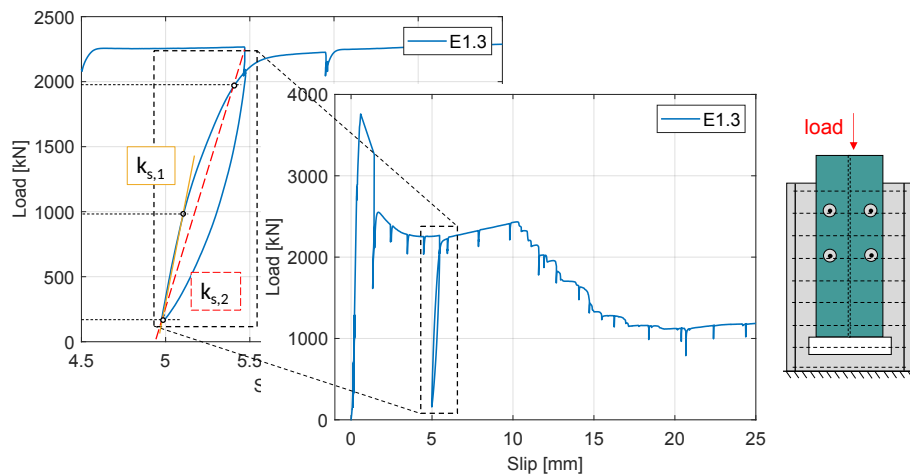


FIGURE 3.44: Post-peak stiffness for Series E1.

### Crack patterns

The distribution of concrete cracks is presented in Figure 3.45. On the web side, the cracks are limited to the edges. On the flange side, they are mainly distributed at the location of the shear connectors longitudinally and transversally.

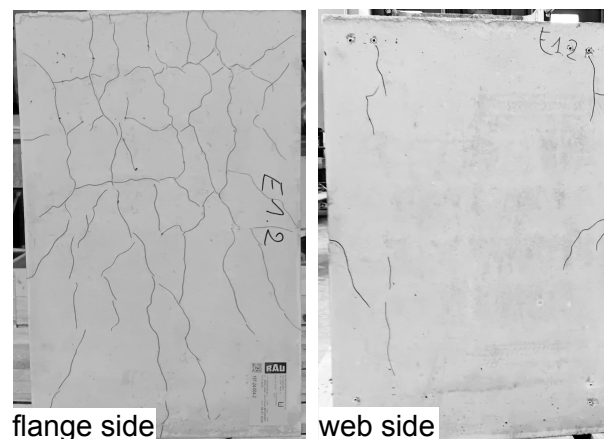


FIGURE 3.45: Crack patterns for Series E1.

### Shear connector failure

Figure 3.46 illustrates the failure mode of a traversing rebar located in the flange of one connector from series E1. The 16 mm traversing rebar was sheared on both sides of the 17.5 mm–thick flange. During sectioning, the remaining portion of the rebar embedded within the flange was lost.

No significant plastic deformation was observed. The segment located outside the flange (right side) failed first through a combined tension–shear mechanism, followed by failure of the segment on the interior side. After the initial failure, the remaining portion of the rebar bent and ultimately failed in shear.

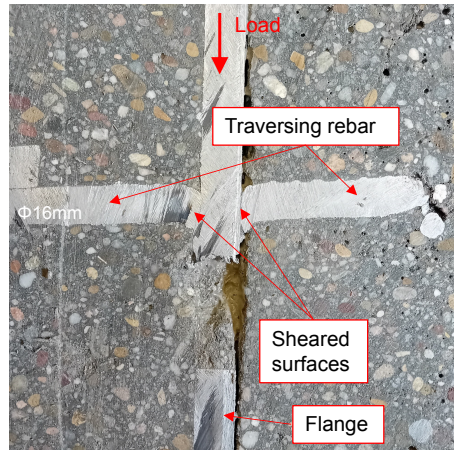


FIGURE 3.46: Shear connector failure for Series E1.

### Discussion

Series E1 incorporated eight CRCD connectors in 50 mm flange openings, each crossed by a 16 mm U-shaped rebar. Owing to the 105 mm concrete cover on the flange, straight rebars could not be used, making the bent configuration necessary.

The maximum allowable rebar diameter was governed by bending radius requirements: four times the bar diameter for  $< 20$  mm and seven times for  $\geq 20$  mm, which limited the rebar size to 16 mm. Push-out tests confirmed the feasibility of using CRCD connectors on flanges, offering a practical alternative where headed studs are difficult to install due to limited cover or reinforcement congestion.

Although the theoretical concrete infill between the opening and traversing rebar is 17 mm, the observed slip capacity was only 10–12 mm. This reduction is attributed to two factors: (1) the lack of plastic deformation in the 15 mm thick flange, and (2) the higher confinement of the concrete dowel, which restricts the traversing rebar from crushing and deforming the surrounding concrete.

### 3.7.5 Shear connectors on the web + flanges and scale-up

Series F1 and F2 represented the logical next step in the experimental program. After conducting numerous tests with CRCD connectors placed on the web and validating the feasibility of their application on the flanges, the investigation was extended to specimens with CRCD connectors installed on both the web and the flanges. These series were carried out with high-strength concrete (C80/95) and two distinct geometric configurations.

Series F1 consisted of a HEA 360 steel profile embedded in a  $560 \times 540$  mm reinforced concrete section. The specimen incorporated 12 CRCD connectors with 60 mm opening diameter and 20 mm traversing rebars on the web, as well as connectors with 50 mm opening diameter and 16 mm traversing rebars on the flanges. Series F1 can be regarded as a combination of series D1 and E1.

Series F2 consisted of an HEB 200 steel profile embedded in a  $320 \times 320$  mm reinforced concrete section, with 18 CRCD connectors featuring 40 mm opening diameter and 12 mm traversing rebars.

The expected ultimate resistance of series F1 was approximately 3600 kN. According to EN1994-1-1 (2004) Annex B, this would require a cyclic loading range between 1440 kN and 1800 kN. Since there was a significant risk that the hydraulic press at the University of Luxembourg would not be able to reach this ultimate load, series F1 was tested at the Laboratory of the University of Wuppertal.

For series F2, the expected ultimate resistance was approximately 2400 kN. In this case, the hydraulic press in Luxembourg was sufficient, and the tests were therefore conducted at the University of Luxembourg. The required cyclic loading range, as per EN 1994-1-1 Annex B, was between 120 kN and 960 kN.

**Load-slip behavior**

Figures 3.47a and b show the shear-slip curves of series F1 and F2, while Figures 3.47c and d present the corresponding static curves, including the effect of concrete relaxation and the mean response of each series. The influence of the relaxation is depicted by a lower shear resistance of 3% for series F1 and a 6% for F2.

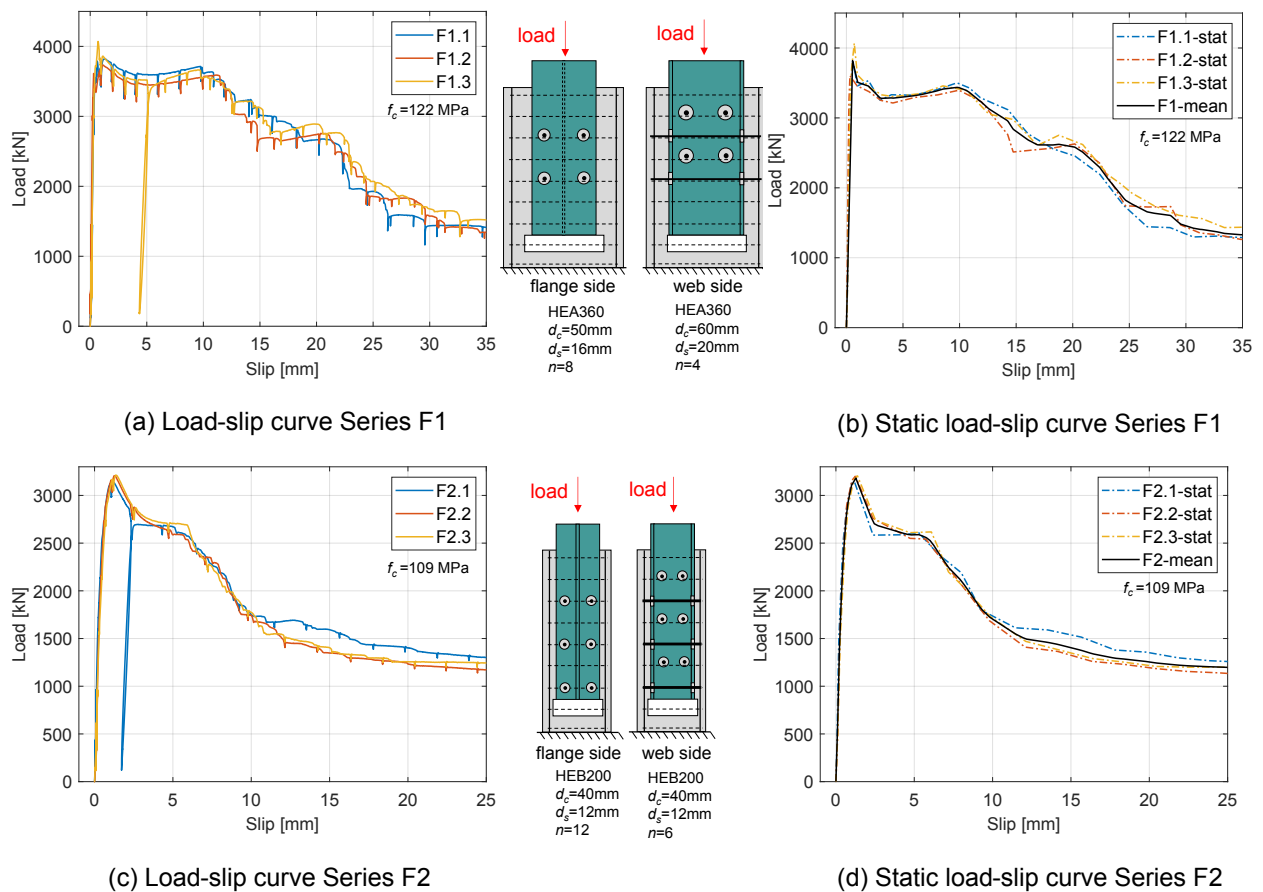


FIGURE 3.47: Load-slip and static load-slip curves for Series F1 and F2.

Series F1 reached an average ultimate shear resistance of 3874 kN at a slip of 1.020 mm (Table 3.17). The initial loading phase was linear, with an average shear stiffness of 11226 kN/mm, which remained nearly constant up to the ultimate load. Beyond this point, stiffness dropped abruptly

and stabilized at about 91% of the ultimate resistance, followed by a slight increase in load due to connector yielding, with secondary peaks between 9.7 and 11.3 mm. After the adhesive layer failed, resistance was carried by the concrete dowel action and steel–concrete friction. The load decreased by 200–500 kN, then recovered gradually until the first connector failures at 9.7 mm, 11.3 mm, and 9.6 mm for specimens F1.1–F1.3. Failure progressed in stages until slips of 29.8–32.9 mm, after which only friction resisted the load.

Series F2 reached an average ultimate shear resistance of 3185 kN at a slip of 1.269 mm (Table 3.17). The response was linear initially, with an average stiffness of 6215 kN/mm, constant up to 50% of the ultimate load and then gradually decreasing, with strong deterioration near 90%. After the peak load, shear resistance dropped slightly due to bond failure and stabilized at about 85% of the ultimate for slips of 2.5–3.5 mm. The subsequent failure of the adhesive layer transferred resistance to dowel action and friction, with a load drop of about 450 kN. Connector failures began at slips of 4.8–5.8 mm and progressed until 19.0–20.5 mm, after which only friction resisted the applied load.

TABLE 3.17: Experimental results for series with multiple CRCD connectors on the web and the flanges.

Series	ID	$P_u$ (kN)	$s_u$ (mm)	$k_s$ (kN/mm)	$P(5mm)$ (kN)	$P(8mm)$ (kN)	$P(10mm)$ (kN)	$P(20mm)$ (kN)	$P(30mm)$ (kN)
F1	F1.1	3820	1.232	9363	3328	3404	3486	2464	1339
	F1.2	3732	1.136	14810	3250	3327	3391	2622	1438
	F1.3	4069	0.692	9507	3320	3427	3410	2674	1592
Mean value		3874	1.020	11226	3299	3386	3429	2587	1456
CoV (%)		4.5	28.2	27.6	1.3	1.5	1.5	4.2	8.8
F2	F2.1	3136	1.203	7801	2603	2189	1735	1351	1230
	F2.2	3207	1.269	5727	2547	2066	1662	1194	1095
	F2.3	3213	1.355	5116	2611	2063	1713	1217	1179
Mean value		3185	1.276	6215	2587	2106	1703	1254	1168
CoV (%)		1.3	6.0	22.6	1.3	3.4	2.2	6.8	5.8

### Cyclic loading behavior

Figure 3.48 illustrates the zoom-in shear–slip curves for series F1 and F2. The specimens exhibit a response comparable to that observed in the previous tests, with the cyclic loadings producing a stable and linear behavior. The load–slip relationship remains within the elastic range, confirming that the adhesive bond preserved its integrity throughout the cycling phase.

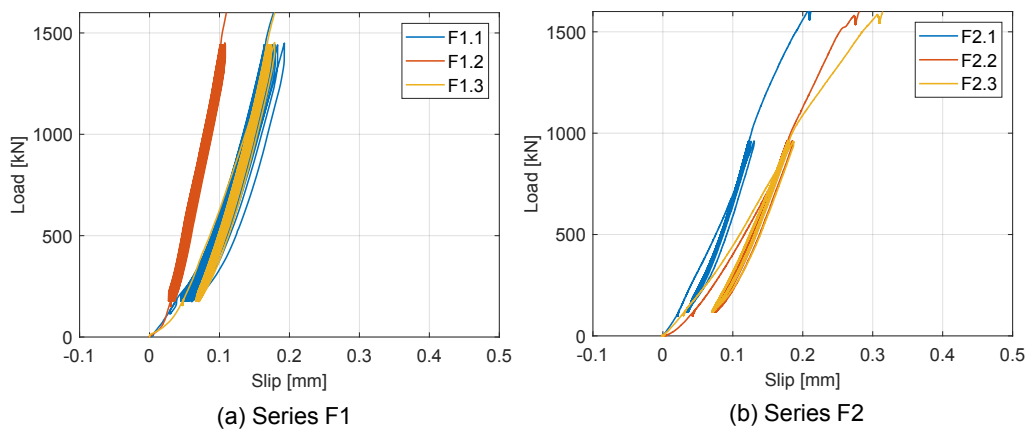


FIGURE 3.48: Cyclic loading for series F1, and F2.

### Post-peak stiffness

Figure 3.49 shows the load–slip curve of specimen F1.1, highlighting the connector stiffness after the peak load. At a slip of 5 mm, the load was reduced to 190 kN, held for 60 seconds, and then reloaded. The reloading exhibited an elastic behavior with a stiffness of  $k_{s,1} = 5704$  kN/mm, which is half of the initial stiffness (11226 kN/mm). A second stiffness,  $k_{s,2} = 3893$  kN/mm, can be identified between the initial loading point and the onset of significant stiffness degradation at a load of 3109 kN.

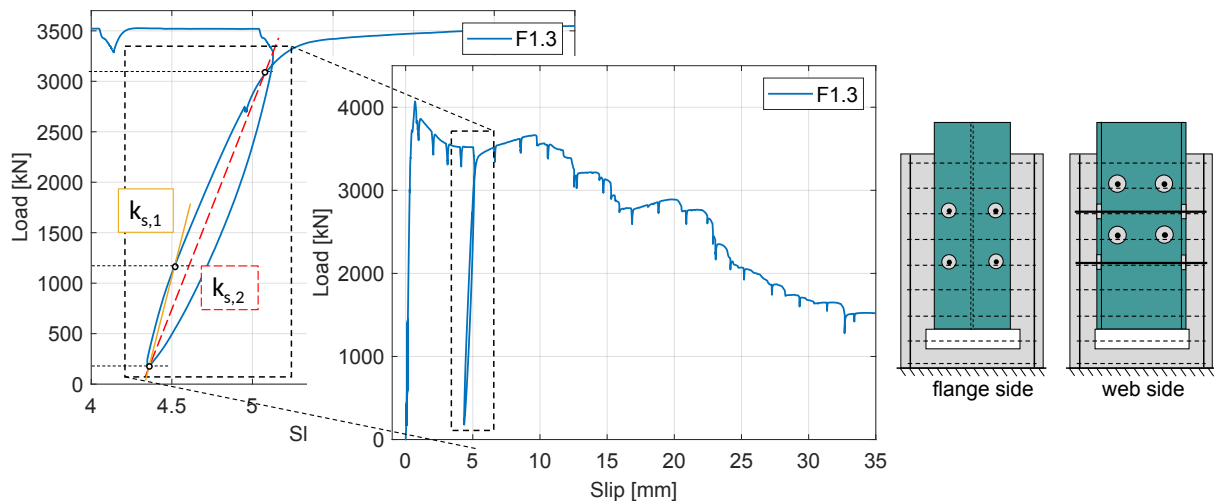


FIGURE 3.49: Post-peak stiffness for series F1.

Figure 3.50 also presents the load–slip curve of specimen F2.1. At a slip of 2.3 mm, the load was reduced to 130 kN, held for 60 seconds, and subsequently reloaded. A quasi-elastic response was observed between 130 kN and approximately 2400 kN, corresponding to a stiffness of 4096 kN/mm, corresponding to 64% of the initial stiffness (6215 kN/mm). Beyond this range, the stiffness decreased markedly.

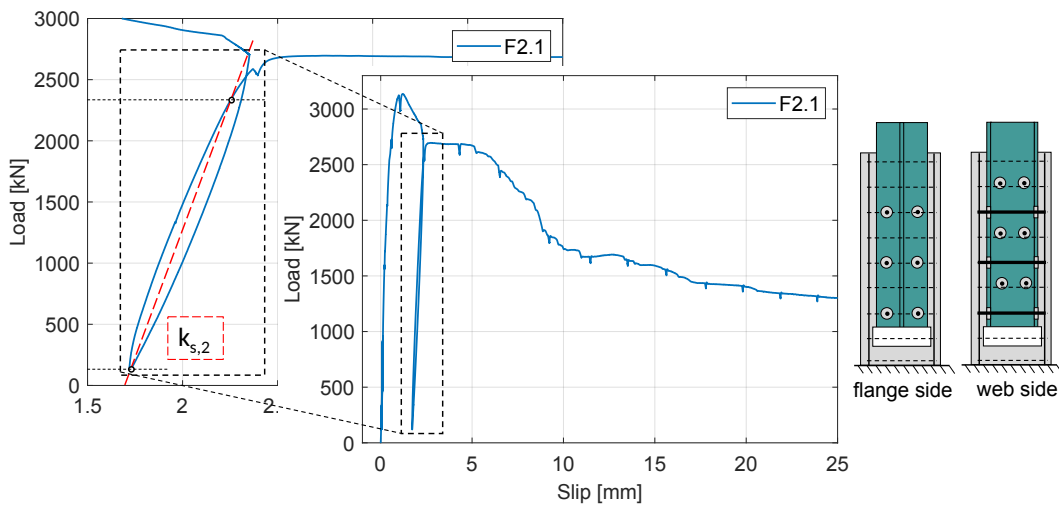


FIGURE 3.50: Post-peak stiffness for Series F2.

**Crack patterns**

Figure 3.51 shows the distribution of concrete cracks for series F1 and F2, which are mainly concentrated around the shear connectors. On the web side, where the connectors are deeply embedded, the cracks are predominantly longitudinal. On the flange side, the connectors are located closer to the concrete edge, leading to a higher density of both longitudinal and transverse cracks. In specimen F2.2, the concrete cover spalled, exposing the stirrups. This was the result of the dilation of the concrete dowel and a close position of the connector to the concrete edge. No loss of shear resistance was noticed in the load-slip curve compared to the two other specimens.

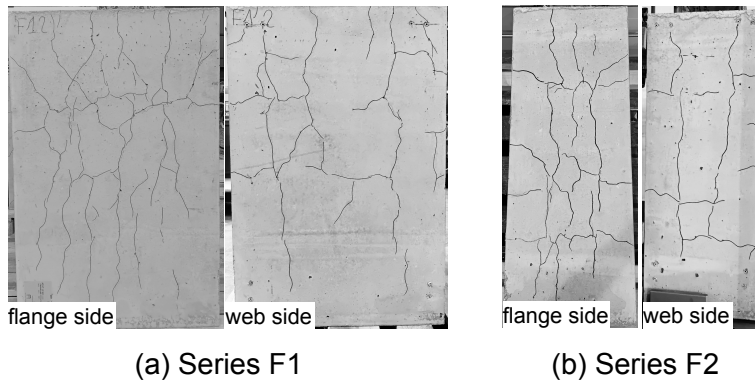


FIGURE 3.51: Crack patterns for Series F1 and F2.

**Shear connector failure**

Specimens F2.3 and F1.1 were sectioned using a circular saw. Figure 3.52 shows the sectioned specimen F2.3, which includes CRCD connectors located both on the web and the flanges. This specimen features 40 mm circular openings with 12 mm traversing rebars. In the web region, the rebars exhibit shear failure on both sides, occurring in one or two stages—similar to specimens from series C3 and C5, which used the same concrete grade. A comparable failure pattern is observed in the flange region.

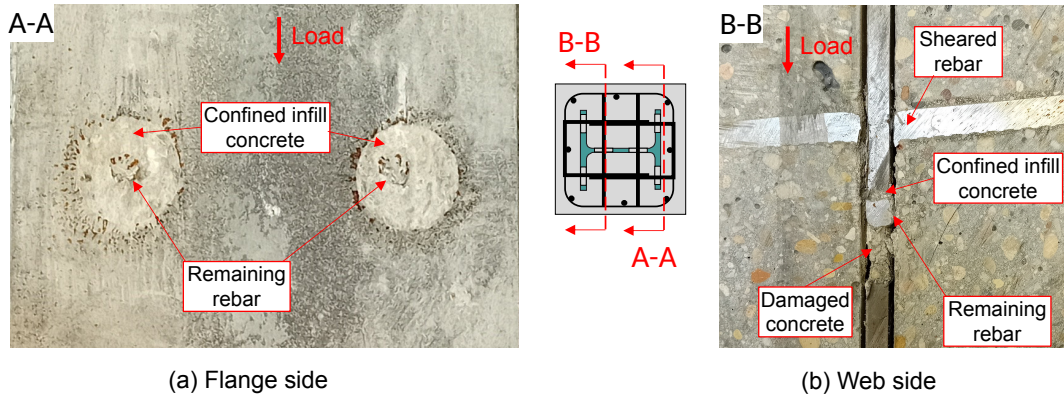


FIGURE 3.52: Shear connector failure for series F2.

Figure 3.52 also reveals that the rebars in the web were not perfectly horizontally aligned. Their deformed shape indicates a two-step failure mechanism: (1) an initial tensile-shear failure on one side, and (2) followed by bending of the remaining section and final shear failure at the opposite steel edge.

Within the opening, remnants of highly confined concrete remain between the traversing rebar and the steel web, while damaged concrete is visible at the bottom of the opening. Additionally, significant gaps are present along the web edges, caused by the cutting process separating the steel–concrete interface.

In contrast, the remaining portions of the traversing rebars in the flanges are not located near the upper edge of the opening, unlike those in the web. This can be attributed to two main factors: (1) the flange rebars were not precisely centered during fabrication; and (2) the increased flange thickness creates a larger concrete dowel between the rebar and steel, which is more confined under load. This increased concrete confinement hinders the rebar’s ability to damage the surrounding concrete, leading to earlier failure compared to the web region. This explains why series F2 shows a lower slip capacity than series C3 and C5. In the flanges, rebar failure occurs around 6 mm of slip, whereas in the web, failure occurs later—between 12 mm and 15 mm.

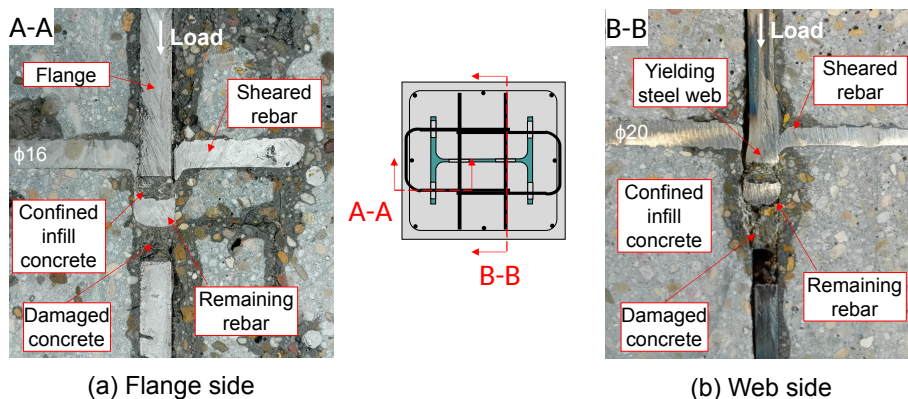


FIGURE 3.53: Shear connector failure for series F1.

Figure 3.53 presents the sectioned specimen F1.1, which includes CRCD connectors on both the web and flanges. It features 60 mm circular openings with 20 mm rebars in the web and 50

mm openings with 16 mm rebars in the flanges. The same failure modes were observed in series E1, D1, and D2.

As in series F2, the flange connectors show bending of the rebar followed by shear failure on both sides of the steel element. A highly confined concrete zone is observed between the steel profile and rebar, with limited concrete crushing. This behavior is again attributed to the thicker steel flange, which creates a more confined concrete dowel, reducing the rebar's ability to damage the surrounding concrete and resulting in earlier failure for flange-mounted connectors.

In the web, a similar failure sequence is observed. However, significant deformation of the steel web is also evident, along with larger deformation of the infill concrete dowel compared to the flange region. In this case, the shear resistance of the 20 mm traversing rebar exceeded that of the 10 mm thick steel web. Initially, the rebar crushed the infill concrete, increasing confinement until the concrete dowel's strength surpassed the web's bearing capacity. As a result, the steel web began to deform under the concentrated stresses. Eventually, the rebar experienced excessive stress, leading to bending and final shear failure on both sides of the steel section.

## Discussion

This study evaluated CRCD connector performance on both web and flanges for two configurations with high-strength concrete ( $f_c = 109\text{-}122$  MPa): (1) HEB200: 60 mm concrete cover; connectors with 40 mm openings and 12 mm rebars, and (2) HEA360: 105 mm concrete cover; connectors with 60 mm/20 mm (web) and 50 mm/16 mm (flange).

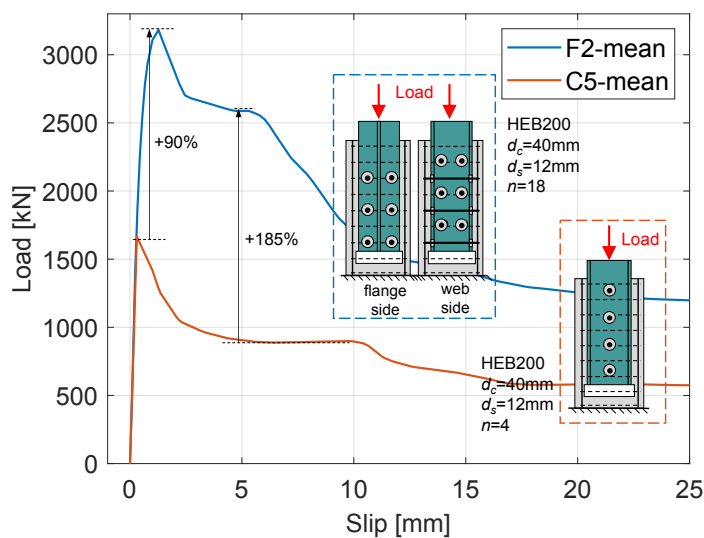


FIGURE 3.54: Analysis of Series F2 and C5.

In Series F2 (HEB200), the inclusion of additional shear connectors significantly altered the load-slip response compared to series C5 (prior study), see Fig. 3.54. Series C5 exhibited a 38% post-peak load drop due to adhesion failure, while series F2 showed only a 16% drop, maintaining a stable plateau post-adhesion failure. This performance is attributed to the increased density of CRCD connectors, which reduces the relative contribution of adhesion and enhances the mechanical resistance from the outset. As these connectors are mobilized at low slip values, they

contribute substantially to the overall shear resistance at the ultimate load. Consequently, series F2 achieves high initial stiffness and avoids brittle failure mechanisms, a desirable trait for serviceability design. Series F2 presents a 90% increase in ultimate resistance and 185% increase in plateau resistance for 3.5 times more connectors compared to series C5. However, due to the limited slip capacity of the connectors positioned on the flanges, series F2 has a reduced slip capacity of 4.5 mm compared to series C5. These results confirm the practical applicability of CRCD connectors on the flanges, even with minimal concrete cover (60 mm), complying with the limits defined in EN1994-1-1 (2004).

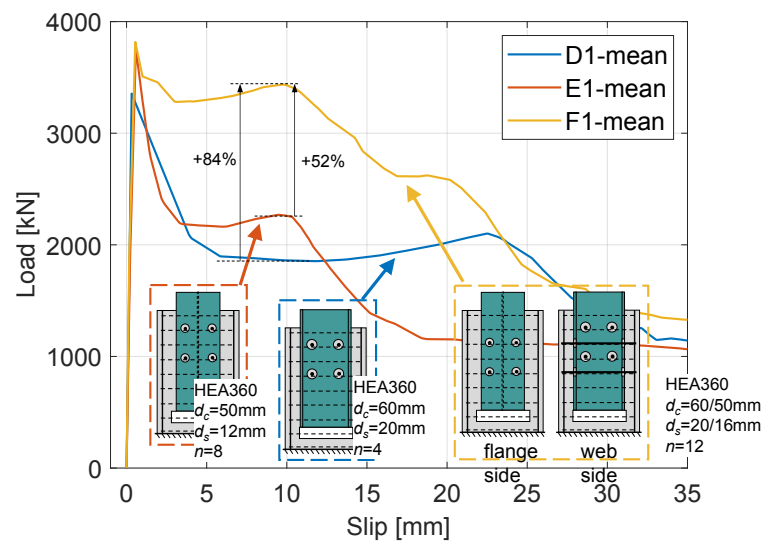


FIGURE 3.55: Analysis of Series F1, D1 and E1.

Series F1 combines the configurations of series D1 (web) and E1 (flange), using 4 CRCD connectors on the web and 8 on the flanges, arranged in four alternating layers, see Figure 3.55. Its load-slip behavior is not a simple sum of the individual series. The peak load is close to E1 (+3%), exceeding D1 by 15%, and a small post-peak drop of 9% follows—attributed to adhesion loss.

Subsequently, a plateau phase is observed, which terminates at a slip of 10 mm, consistent with Series E1. At  $s = 10$  mm, the plateau shear resistance of Series F1 exceeds that of Series E1 by 52% and that of Series D1 by 84%. The earlier termination of the plateau is attributed to the reduced concrete infill between the flange reinforcement and the steel section, combined with the increased confinement provided by the thicker flanges. This confinement limits the slip capacity of the flange dowels, causing them to govern the global failure.

This suggests that the design of series F1 is not optimal. While D1 reaches its maximum plateau resistance at 23 mm and E1 at 10 mm, the web connectors in F1 are underutilized. For applications where high slip capacity is critical, it is preferable to design CRCD connectors on both web and flanges with similar slip capacities, ensuring balanced utilization and maximizing the overall performance. This design of the slip capacity is developed in Chapter 5.

### 3.8 Summary and conclusions

This chapter presented an experimental programme of 45 monotonic push-out tests on concrete-encased steel sections with HEB 200 and HEA 360 steel sections normal- and high-strength concrete, and different arrangements of circular reinforced composite dowel (CRCD) connectors. The test matrix comprised pure-bond specimens, single and multiple CRCD connectors on the web, connectors on the flanges, and combined web+flange layouts, with systematic variation of connector number, spacing, opening diameter, and rebar diameter.

The results confirm that natural bond at the steel–concrete interface can mobilise an important shear resistance, but that the contribution of adhesion has a high variability. CRCD connectors significantly increase the peak and plateau shear resistance compared to pure-bond specimens. For web-only configurations, resistance and stiffness increase with rebar diameter and opening diameter, while maintaining large slip capacities. In contrast, flange-only configurations develop higher initial stiffness and plateau resistance for the same number of connector layers, but their slip capacity is reduced.

The combined web+flange configurations achieve the highest plateau resistances within the investigated range by exploiting both the efficient load transfer of flange connectors and the additional shear paths provided by web connectors. For the same embedded length, these mixed layouts provide substantially higher shear transfer than web-only or flange-only arrangements. However, the ultimate slip is often governed by the less ductile response of the flange connectors, so that web connectors may remain partially underutilized unless the connector geometry and layout are specifically tuned to balance the slip capacities of web and flange connectors.

Different failure modes of the CRCD shear connectors were identified and can be classified into four main categories:

**Mode I:**

- Pronounced crushing and volume reduction of the infill concrete in the opening;
- Traversing rebar exhibiting a combined bending–tension–shear failure;
- Limited plastic deformation of the surrounding steel profile.

**Mode II:**

- Moderate crushing and volume reduction of the infill concrete;
- Traversing rebar with limited bending deformation and a tensile-shear failure;
- Limited plastic deformation of the steel profile.

**Mode III:**

- Minor crushing and damage of the infill concrete;
- Traversing rebar showing limited bending and a predominantly shear-type failure;

- No plastic deformation of the steel profile.

#### Mode IV:

- Pronounced crushing and volume reduction of the infill concrete;
- Traversing rebar with limited bending deformation and a tensile-shear failure;
- Significant plastic deformation of the steel profile in the vicinity of the opening.

Table 3.18 summarises the governing failure mode identified for each series. In each series, one specimen was opened after testing to allow detailed observation of the internal damage patterns.

TABLE 3.18: Summary of the main failure modes for each series.

Series	$f_c$ (MPa)	Connector position	$n$	$t$ (mm)	$d_c$ (mm)	$d_s$ (mm)	Main failure
B1	60	web	1	9	40	12	Mode I
B2	105	web	1	9	40	12	Mode II
C1	63	web	3	9	40	12	Mode I
C2	64	web	3	9	40	12	Mode I
C3	104	web	3	9	40	12	Mode II
C4	63	web	4	9	40	12	Mode I
C5	104	web	4	9	40	12	Mode II
D1	122	web	4	10	60	20	Mode IV
D2	124	web	4	10	60	20	Mode IV
E1	122	flg	8	17.5	50	16	Mode III
F1	122	web	4	10	60	20	Mode II
		flg	8	17.5	50	16	Mode III
F2	109	web	6	9	40	12	Mode IV
		flg	12	15	40	12	Mode III

The experimental results are limited to HEB 200 and HEA 360 profiles, concrete compressive strength between C50/60 and C80/95, the investigated ranges of opening and rebar diameters, sandblasted steel surfaces category Sa 2<sup>1/2</sup>, and monotonic quasi-static loading. Within this domain of validity, the test data provide a consistent basis for calibrating and validating a three-dimensional finite element model and for developing semi-empirical design expressions for CRCD connectors acting together with the bond. The following chapter builds on the experimental database to establish and validate a numerical model that reproduces the observed load–slip response and failure mechanisms and enables a broader parametric study of connector geometry and layout.



## Chapter 4

# Numerical Investigations

### 4.1 Finite element model

The finite element (FE) model is deliberately calibrated to the experimental campaign. Its primary role is to interpret the load-transfer mechanisms and to explore parametric variations within the experimentally tested domain, rather than to provide blind predictions for arbitrary geometries or loading conditions. The model is therefore an interpretive tool, and its use outside the calibration range should be regarded as qualitative only.

#### 4.1.1 General

Three-dimensional push-out tests were simulated using ABAQUS/EXPLICIT (Dassault, 2014) to investigate the failure behavior of the CRCD connectors and the interaction between the shear connector and the steel–concrete bond interface. The finite element model was validated against the experimental results and subsequently used for an extended parametric study. The use of the Explicit solver was necessary for several reasons: (1) severe nonlinear contact at the steel–concrete interface, including sliding, separation, and progressive loss of adhesion; (2) significant crushing and localized deformation of the concrete in the steel openings, leading to large element distortions; and (3) strong material nonlinearities, including concrete softening and damage, as well as shear and ductile damage in the traversing rebar.

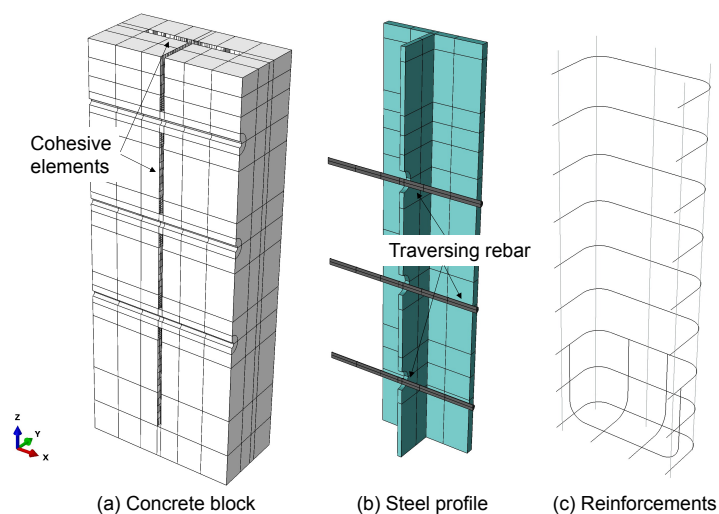


FIGURE 4.1: Description of the finite element model.

A unique model has been developed for all specimens, taking into account the material and geometrical differences of each series. It corresponds to half of the push-out test, considering the symmetry of the geometry (see Figure 4.1). This assumption is validated in section 4.3.1. The failure mode has been observed to be asymmetric along the web; therefore, a quarter model does not accurately represent the real failure mode. Only series E1 was modeled as a quarter push-out, as it included CRCD connectors only on the flanges.

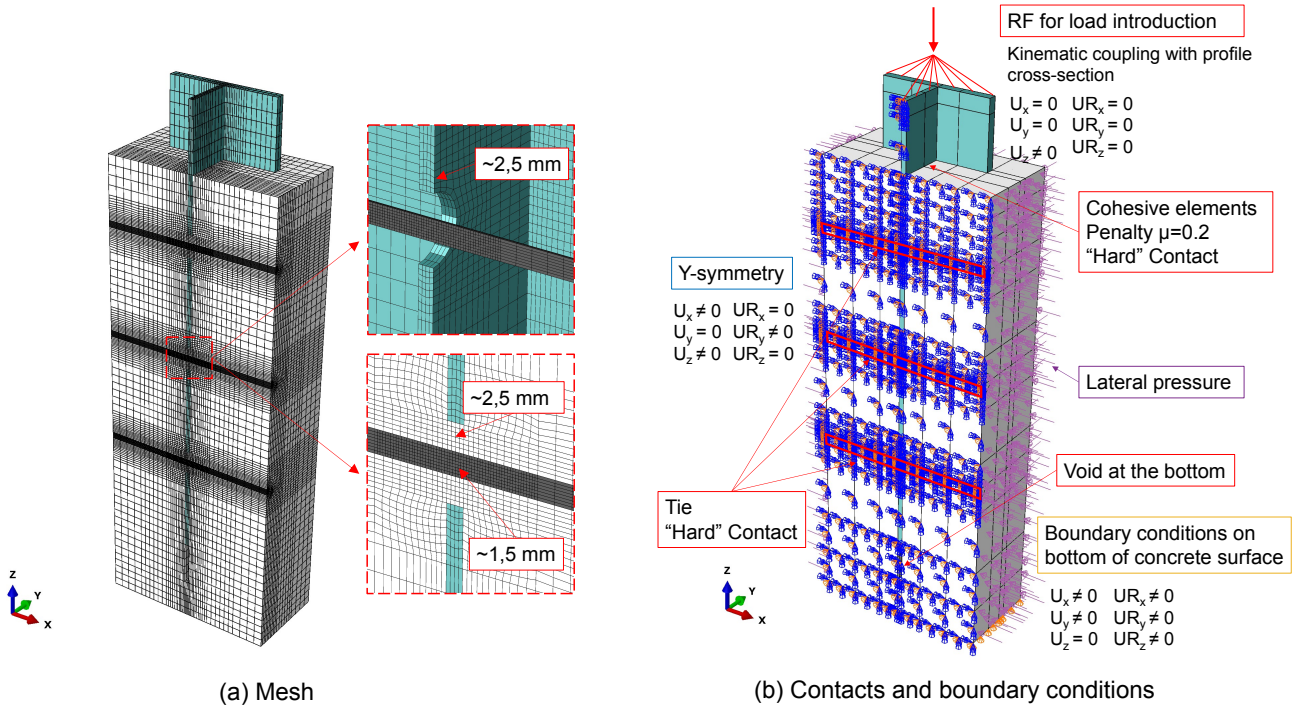


FIGURE 4.2: Mesh, boundary conditions, and contacts of the numerical model.

The concrete is modeled using the Concrete Damage Plasticity (CDP) model, as detailed in section 4.1.2. The steel of the traversing rebar integrated a trilinear stress-strain curve with ductile and shear damage. The steel profile and the reinforcement were simulated, respectively, using bilinear and elasto-perfectly plastic stress-strain curves. The concrete block, steel profile, and traversing rebar(s) were built using solid reduced integration elements C3D8R. Stirrups and longitudinal rebar were modeled by beam element B31. As shown in Figure 4.2, a symmetrical condition ( $U_y = UR_x = UR_z = 0$ ) was used to consider the half model, vertical displacement was blocked at the bottom of the concrete block ( $U_z = 0$ ), and the top of the steel profile was constrained in all directions except vertically ( $U_x = U_y = UR_x = UR_y = UR_z = 0$ ) where the load is applied as a smooth displacement with a speed of 1 mm/s. The minimum mesh sizes of concrete block, steel profile, and perforated rebars were 2.5, 2.5, and 1.5 mm, respectively.

General contact interactions were defined at two interfaces: (i) between the steel profile and the concrete block, and (ii) between the traversing rebar and the surrounding concrete. The normal contact behaviour was modelled using a pressure-overclosure relationship with a hard-contact formulation, which is standard for solid elements and prevents interpenetration. The tangential behaviour followed a Coulomb friction law implemented through a penalty formulation. The experiments showed that sliding friction contributes significantly to the post-peak response.

However, as demonstrated by Chrzanowski (2019), frictional behaviour in numerical simulations cannot be reproduced solely by prescribing a Coulomb friction model. In reality, micro-interlocking, which occurs due to the irregular surface of the steel profile, cannot be reproduced with the Coulomb friction model. Additionally, concrete shrinkage during curing reduces the concrete volume, generating lateral pressure on the steel profile. Various imperfections—such as slight misalignment of the steel profile, fabrication tolerances, deviations in reinforcement cage positioning, or imperfect specimen centring in the hydraulic press—introduce unintentional eccentricities. These effects create residual horizontal forces that activate friction at the steel–concrete interface. Since numerical models are geometrically perfect and do not naturally include these imperfections or the effects of shrinkage, an artificial lateral pressure was applied to the concrete surface to replicate these conditions.

To reproduce the friction behaviour observed in the tests, it was therefore necessary to identify appropriate values for the friction coefficient  $\mu$  and the lateral pressure  $p$ . The frictional resistance arising from interface roughness, shrinkage, and imperfections, is given by  $P_{\text{frict,rough}} = \mu p A_b$  (Fig. 4.3a), where  $A_b$  is the steel–concrete contact area.

Accordingly, increasing  $\mu$  increases  $P_{\text{frict,rough}}$ . However, CRCD connectors placed on the web and flanges also generate compressive struts, which in turn produce an additional friction component  $P_{\text{frict,CRCD}}$  along these surfaces, see Fig. 4.3c. For specimens with few connectors, this additional contribution is minor relative to  $P_{\text{frict,rough}}$ . With many connectors, it becomes significant.

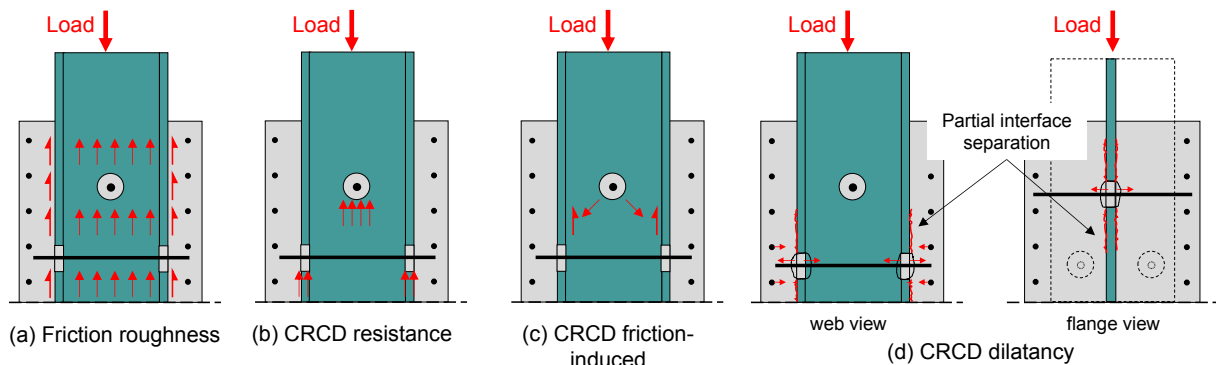


FIGURE 4.3: Shear forces components when considering CRCD connectors with friction.

When the CRCD connectors are loaded, lateral dilatancy of the concrete dowel induces transverse compressive stresses. These stresses mobilize confinement through the stirrups and can increase the normal pressure at the steel surface, thereby enhancing frictional resistance (Fig. 4.3d). Simultaneously, the same dilatancy can cause local separation of the steel–concrete interface in the vicinity of the shear connector, which reduces the effective contact area and may decrease the friction contribution. This coupled mechanism has been investigated in detail by Zou et al. (2020), Zou et al. (2021), Zhao et al. (2018), and Tan, Fang, and Xiong (2022). Accordingly, CRCD connectors can both (1) generate additional friction via strut action and confinement induced by dilatancy and (2) reduce interface friction due to partial separation of the steel–concrete interface.

Through iterative trial simulations, the parameters  $\mu$  and  $p$  were calibrated to reproduce the push-out test responses. Figure 4.4 reports the final calibrated values for specimens in series B1 to

F2 (HEB200 profiles with opening 40 mm and traversing rebar 12 mm) and decomposes the shear resistance into the principal transfer mechanisms as a function of the number of connectors.

With increasing connector number, the frictional resistance associated with surface roughness,  $P_{\text{frict,rough}}$ , decreases slightly, as the effective steel–concrete contact area is reduced. Conversely, the connector contribution,  $P_{\text{CRCD}}$ , increases. The total resistance,  $P_{\text{CRCD+frict}}$ , comprises the connector contribution and all interface-friction components, including friction from roughness, shrinkage, and initial imperfections, as well as additional friction mobilized by CRCD-induced confinement (due to dowel dilatancy) and by CRCD-induced compressive strut action. It also accounts for the reduction in interface friction caused by partial opening of the steel–concrete interface around the connector. Hence,  $P_{\text{CRCD+frict}}$  represents the aggregated friction contributions together with the connector resistance.

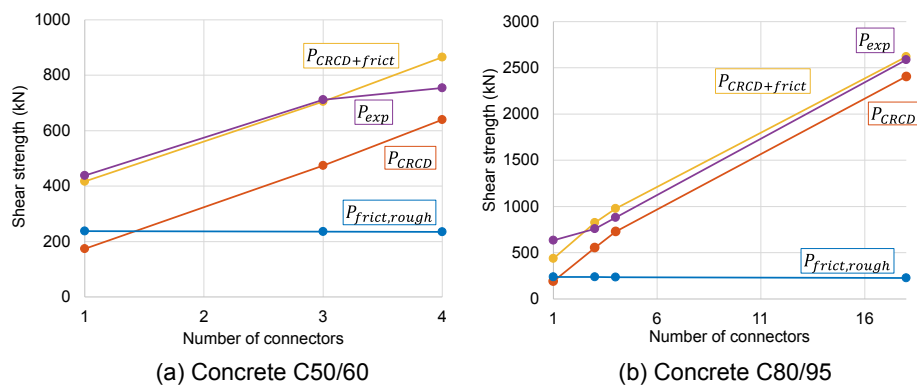


FIGURE 4.4: Shear strength of the different components in function of the number of connectors for concrete compressive strength C50/60 and C80/95.

The calibration yielded  $\mu = 0.2$  and a lateral pressure  $p = 1.5$  MPa. Increasing  $\mu$  produces excessive friction for specimens with many connectors, while increasing  $p$  results in excessive friction for specimens with few connectors. The combination of  $p = 1.5$  MPa and  $\mu = 0.2$  corresponds to a shear strength of 0.3 MPa—matching the maximum allowable value for fully encased members according to EN1994-1-1 (2004). This approach effectively captures the sliding friction observed experimentally, see section 4.2. In Fig. 4.4, the FE results for the specimens with one connector for C80/95 (series B2) show limited agreement with the experimental results. This discrepancy is discussed in detail in Section 4.2.

The same friction coefficient and lateral pressure values were also applied to specimens with a HEA 360 profile, for which the numerical results showed very good agreement with the corresponding push-out tests.

In the specimens with HEB 200 profiles, the traversing rebars were fully tied to the surrounding concrete. For specimens incorporating CRCD connectors on the web of a HEA 360 profile, a friction coefficient of 0.5 was assigned at the interface between the traversing rebar in the opening and the surrounding concrete, following the recommendations of Braun, Obiala, and Odenbreit (2017). The ends of the rebars were tied to represent the anchorage conditions observed in the experiments. For the CRCD connectors positioned on the flanges, the real geometry of the traversing rebar was simplified by straight rebars for an easier mesh implementation. To reproduce the behavior observed in the experiments with this modeling simplification, a friction coefficient of 0.3

was numerically calibrated, and the rebar ends were again tied to the concrete to represent the U-shape on the edge of the concrete, see Fig. 4.5.

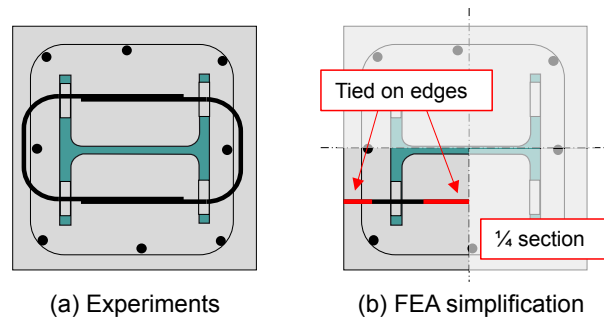


FIGURE 4.5: Simplification of the FE model for an easier mesh.

Cohesive elements were introduced to simulate the adhesive interaction between the steel and concrete surfaces. This was achieved by generating an offset mesh with a zero-thickness cohesive layer on the surface of the concrete block in contact with the steel profile. The offset mesh was modeled using COH3D8 elements, and a surface-to-surface tie constraint was applied between the cohesive layer and the steel profile to ensure connection continuity. Finally, the reinforcing bars were embedded in the concrete block to define the interaction constraint.

#### 4.1.2 Materials modeling

##### Concrete

The concrete was simulated using the CDP model, as realized by recent studies (Liu et al., 2023; Pavlović et al., 2013; Wang, Liu, and Xin, 2021; Wang, Chen, and Liu, 2022). The CDP is the recommended material law for reinforced concrete due to its plasticity-based nature, where the modeled material loses its stiffness as damage progresses. The compressive stress-strain curve of concrete (Figure 4.6a) was defined according to Liu et al., 2023, *i.e.*, a linear behavior is considered, from point A to B, before 40% of the cylinder compressive strength, with a slope corresponding to the modulus of elasticity of the concrete  $E_c$ . This is followed by a parabolic curve, from point B to C, expressed by Eq. 4.1 until the strain  $\varepsilon_{c1}$ . Since high crushing strains appear in the opening of the steel profile, it is essential to consider softening behavior to not overestimate the concrete crushing strength. Therefore, the curve is extended, from point C to D, according to Eq. 4.1 for strains after  $\varepsilon_{c1}$ .

$$\sigma_c(\varepsilon) = \begin{cases} f_{cm} \frac{n\bar{\xi} - \bar{\xi}^2}{1 + (n-2)\bar{\xi}} & \text{for } 0 < \varepsilon \leq \varepsilon_{c1} \\ f_{cm} \frac{\bar{\xi}}{2(\bar{\xi}-1)^2 + \bar{\xi}} & \text{for } \varepsilon > \varepsilon_{c1} \end{cases} \quad (4.1)$$

where the symbols  $n$  and  $\bar{\xi}$  are expressed as  $n = \varepsilon_{c1} E_c / f_{cm}$  and  $\bar{\xi} = \varepsilon / \varepsilon_{c1}$ , respectively. The strain at the ultimate concrete compressive strength depends on the concrete compressive strength class and is taken to, as defined in Model Code (2013),  $\varepsilon_{c1} = 0.0026$  for C50/60 and  $\varepsilon_{c1} = 0.0028$  for C80/95. The modulus of elasticity of the concrete  $E_c$  is also defined according to Model Code (2013).

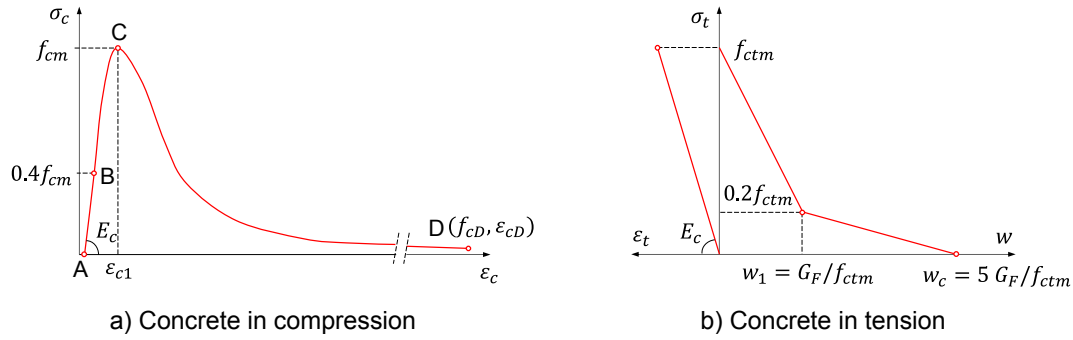


FIGURE 4.6: Stress-strain curves for the concrete under (a) compression, and (b) tension.

The tensile stress-strain curve is defined according to Model Code (2013) as a function of crack opening and tensile stress, see Figure 4.6b. Tensile stress increases linearly along with the modulus of elasticity, up to the peak value  $f_{ctm}$ . After this point, stress degrades linearly up to  $0.2f_{ctm}$  and the crack opening  $w_1 = G_F/f_{ctm}$ , where  $G_F$  is the fracture energy. Finally, the curve evolved linearly to zero stress and a crack opening  $w_c = 5 G_F/f_{ctm}$ . A function of the concrete compressive strength determines the fracture energy and the tensile strength,  $G_F = 73 f_{cm}^{0.18}$  and  $f_{ctm} = 0.3 (f_{cm} - 8)^{2/3}$  for concrete strength classes lower than or equal to C50/60 and  $f_{ctm} = 2.12 \ln(1 + 0.1f_{cm})$  for classes higher than C50/60.

Damage evolution laws in ABAQUS were defined for concrete in compression and tension. The damage parameters were given by  $d_c = 1 - \sigma_c/f_{cm}$  and  $d_t = 1 - \sigma_t/f_{ctm}$  as defined in Dassault (2014).

The parameters of the CDP model were chosen as follows: flow potential eccentricity  $\epsilon = 0.1$ , and biaxial/uniaxial compressive strength ratio  $f_{b0}/f_{c0} = 1.16$  were set as recommended by Dassault (2014). The dilation angle  $\psi = 15^\circ$  was iteratively calibrated to match push-out test results. The ratio of the second stress invariant on the tensile meridian to that on the compressive meridian was taken as  $K_c = 0.67$ , as recommended by Braun (2018), Fang et al. (2023), Gu et al. (2025), Le Minh et al. (2021), and Zhang et al. (2019). The viscosity coefficient was set to 0.001.

### Traversing rebar

The traversing rebar definition is critical since it determines the failure of the shear connector. Ductile and shear damage were introduced to model the failure process of the steel rebar. The stress-strain relationship was represented by a trilinear curve, as shown in Figure 4.7a. The elastic modulus  $E_s$ , yield strength  $f_y$ , yielding phase strain  $\epsilon_{sh}$  and ultimate strength  $f_u$ , and strain  $\epsilon_u$  were deduced from material tests. The ductile damage model was implemented based on Pavlović et al. (2013) where the equivalent plastic strain at the onset of damage  $\bar{\epsilon}_0^{pl}$  is defined as a function of the stress triaxiality according to Eq. 4.2. The damage evolution law and uniaxial plastic strain at the onset of damage  $\epsilon_n^{pl}$  have been extracted from experimental results of standard tensile tests.

$$\bar{\epsilon}_0^{pl} = \epsilon_n^{pl} e^{-1.5(\theta - \frac{1}{3})} \quad (4.2)$$

The shear damage model was implemented according to Dassault (2014). The shear stress ratio was chosen as recommended to  $\theta_s = 1.732$ , and the equivalent plastic strain at the onset of damage  $\bar{\varepsilon}_0^{pl}$  was numerically determined to fit the failure model of the experimental tests since no shear tests of the rebars were provided. An exponential law described the damage evolution with a parameter of 0.7 and a displacement at failure  $\bar{u}_f^{pl} = 10 \bar{\varepsilon}_0^{pl} L_{ch}$ , where  $L_{ch} = 1.5$  mm is the characteristic length of the finite element.

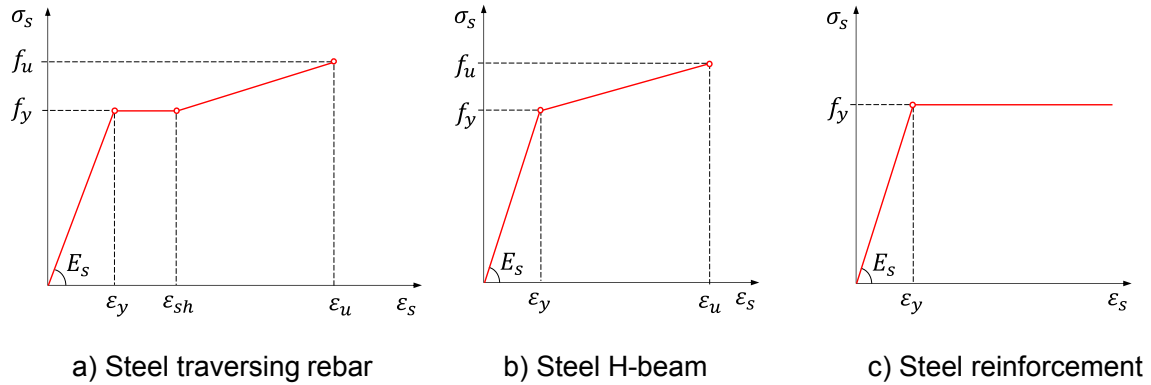


FIGURE 4.7: Stress-strain curves for steel: (a) traversing rebar, (b) structural steel, and (c) reinforcement.

### Structural steel

A bilinear stress–strain relationship was adopted to idealize the behavior of the steel section, as illustrated in Figure 4.7b, using the material properties presented in Chapter 2. The elastic modulus  $E_s$ , yield strength  $f_y$ , ultimate strength  $f_u$ , and ultimate strain  $\varepsilon_u$  were obtained from the material test results.

In the push-out tests with a 20 mm traversing rebar, significant deformation of the steel web was observed. To account for the associated loss of stiffness, a ductile damage model was incorporated into the steel material definition in ABAQUS. The damage parameters were calibrated using data from the steel tensile tests.

### Reinforcement

The reinforcements were idealized by an elastic-perfectly plastic curve (Figure 4.7c) with the values presented in Chapter 2. The elastic modulus  $E_s$ , yield strength  $f_y$ , ultimate strength  $f_u$ , and strain  $\varepsilon_u$  were deduced from material tests.

### Cohesive layer

The element-based cohesive behavior, defined as a zero-thickness cohesive element, was used to model the adhesion bond. A linear elastic traction-separation law adopts the stress-displacement relationship of the cohesion. The quadratic nominal stress criterion defined the damage initiation point. An exponential damage evolution of the cohesive material has been defined to reproduce the progressive decrease of the interfacial shear strength observed during the experiments (Figure

4.8). The adhesion is largely dependent on the steel surface conditions and the concrete compressive strength. Accordingly, three sets of interface parameters have been defined: (1) for concrete class C50/60 (batches 1 and 2) with the first delivery of steel beams sandblasted by Ziemann; (2) for C80/95 concrete (batch 3) with beams sandblasted by Ziemann; and (3) for C80/95 concrete (batch 4) with beams sandblasted by ArcelorMittal. The interface parameters adopted in the traction-separation model were determined based on experimental data (series A1, A2, and A3), as listed in Table 4.1 for the different concretes.

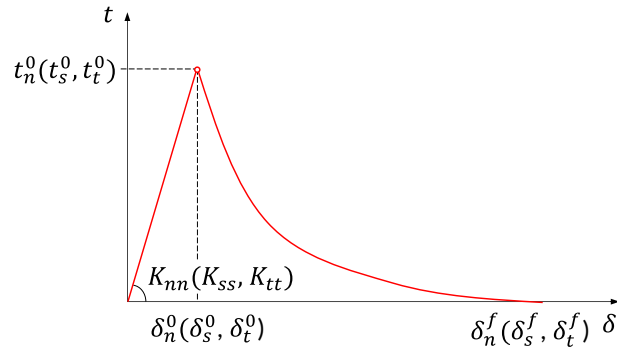


FIGURE 4.8: Stress-strain curves for adhesion bond.

TABLE 4.1: Mechanical properties of adhesion at the steel–concrete interface.

Parameters	C50/60 batch 1+2	C80/95 batch 3	C80/95 batch 4
Normal elastic stiffness $K_{nn}$ (MPa/mm)	1	1	1
Shear elastic stiffness $K_{ss}, K_{tt}$ (MPa/mm)	20	30	30
Nominal stress normal direction $t_{nn}$ (MPa)	1	1	1
Nominal stress shear direction $t_{ss}, t_{tt}$ (MPa)	0.8	1.4	1.8
Exponential parameter	4	3	5
Displacement at failure (mm)	8	7	3

## 4.2 Model validation

To assess the validity of the finite elements model, we observed the differences between the FE results and the experiments, considering the failure mode of the shear connector, the ultimate shear resistance, and the plateau shear resistance at 2 mm, 4 mm, 8 mm, 10 mm, and 15 mm. Series A1, A2, and A3 were used to calibrate both the stiffness and ultimate strength of the adhesion component and are not represented in this model validation, whose objective is to reproduce the behaviour of the CRCD connectors combined with the bond.

Table 4.2 presents the results from the FE analysis and the error compared to the experimental tests for the ultimate strength  $P_u$  and slip  $s_u$ , the stiffness  $k_s$ , and the shear resistance  $P$  at 2 mm, 4 mm, 8 mm, 10 mm, and 15 mm of slip. The difference between the FE model and the experimental results is less than 8% for the ultimate resistance (mean value is 3%) and less than 12% for the plateau load (mean value is 4%), except for the numerical model of series B2, which has poor performance compared to the experimental results. The mean value of the error between the FE

model and the experiment for the stiffness is 17%, which is related to the scatter of the adhesion behavior. A large scatter in the ultimate slip between the FEA and the experiments can be noticed, which can be mainly explained by the scatter of adhesion behavior. The extended dataset includes variations in concrete and steel section dimensions, connector size, number, and placement of connectors, and concrete compressive strength, confirming the robustness of the model across different configurations.

TABLE 4.2: Results from the finite element analysis and the error compared to the experimental tests.

	$P_u$		$s_u$		$k_s$		$P(2mm)$		$P(4mm)$		$P(8mm)$		$P(10mm)$		$P(15mm)$	
	(kN)	$\Delta$	(mm)	$\Delta$	(kN/mm)	$\Delta$	(kN)	$\Delta$	(kN)	$\Delta$	(kN)	$\Delta$	(kN)	$\Delta$	(kN)	$\Delta$
B1	974	1%	0.250	3%	5704	5%	612	12%	452	6%	396	11%	404	10%		
B2	1496	0%	0.381	48%	5918	18%	883	5%	560	21%	397	38%	411	37%		
C1	1071	3%	0.333	16%	5714	8%	769	2%	660	7%	671	3%	685	3%		
C2	1081	1%	0.371	42%	5878	24%	787	3%	672	6%	675	4%	710	5%		
C3	1615	3%	0.479	81%	5888	26%	1093	8%	821	2%	739	8%				
C4	1136	8%	0.414	86%	5587	11%	870	11%	772	4%	830	11%	844	10%		
C5	1675	0%	0.513	68%	5798	51%	1202	9%	957	2%	941	6%	947	5%		
D1	3248	3%	0.553	72%	9515	4%	2737	1%	2254	10%	1739	7%	1736	7%	1880	1%
D2	3239	0%	0.647	108%	9416	20%	2789	6%	2312	9%	1795	1%	1706	5%	1791	0%
E1	3550	6%	0.500	14%	9921	16%	2268	2%	2202	7%	2307	8%	2214	1%		
F1	4129	7%	0.738	28%	9597	15%	3636	6%	3492	6%	3268	3%	3540	3%		
F2	3090	3%	1.469	15%	5471	12%	2909	1%	2628	0%	2111	1%				

Figure 4.9 compares the force-displacement curves of the FE models to the experimental results. The overall trends of the shear force-slip response from FE models conform well to the experimental curves.

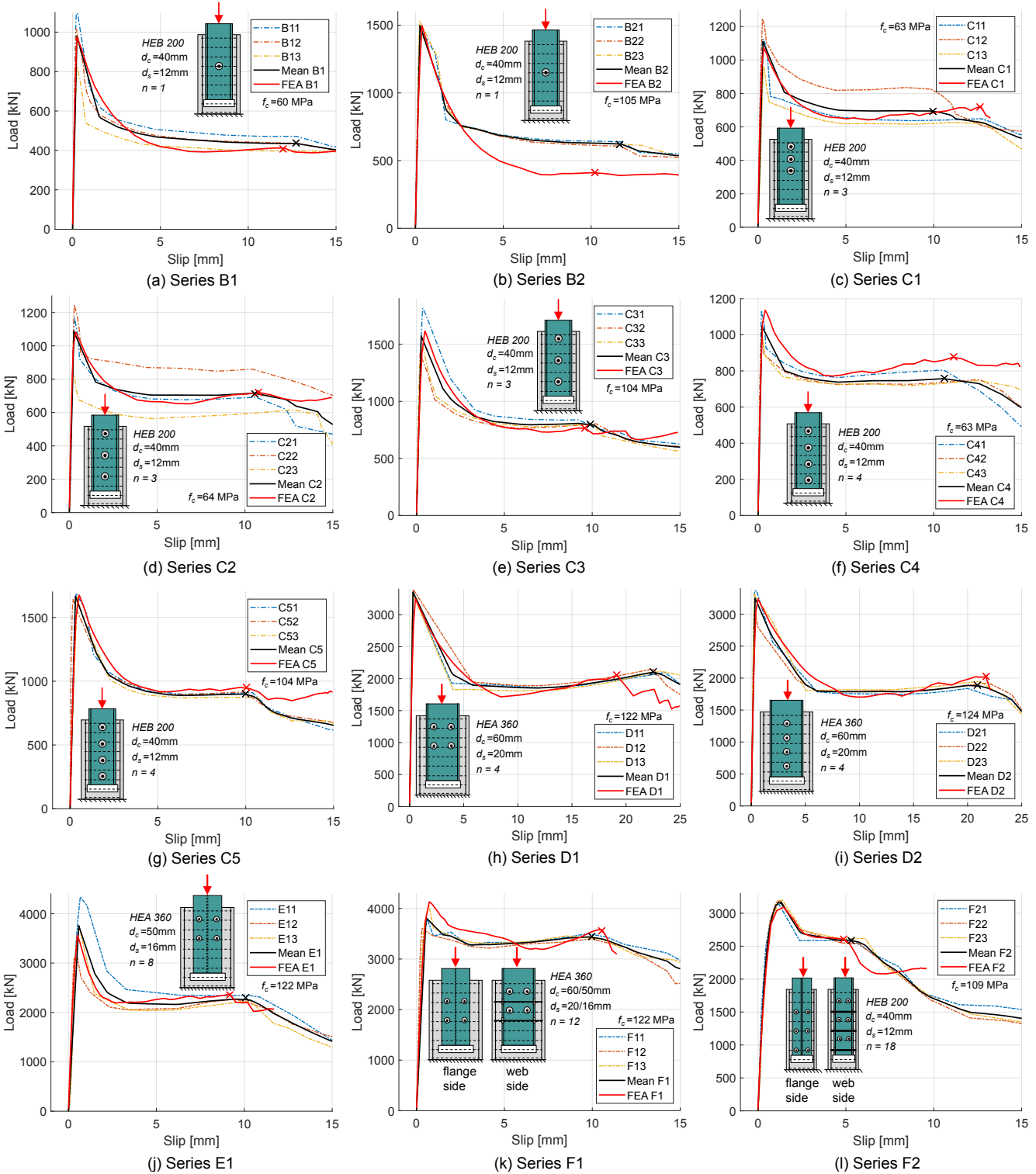


FIGURE 4.9: Comparison of the experimental and the FEA shear-slip curves for all Series.

The current ABAQUS model accounts only for kinetic friction. Consequently, it cannot reproduce the high experimental resistance observed in configurations governed by static friction, such as A2 or B2. Indeed, the poor performance of the FE model for series B2 can be better understood by comparing the experimental behaviors of series A2 and B2, see Fig. 4.10. Series B2 is identical

to series A2 except for the addition of a CRCD connector. When examining their load–slip curves, the plateau resistance of series A2 appears higher than that of B2, even though B2 includes a shear connector. This counterintuitive result arises from the stick–slip behavior described in section 3.7.1, which increases the frictional resistance in series A2.

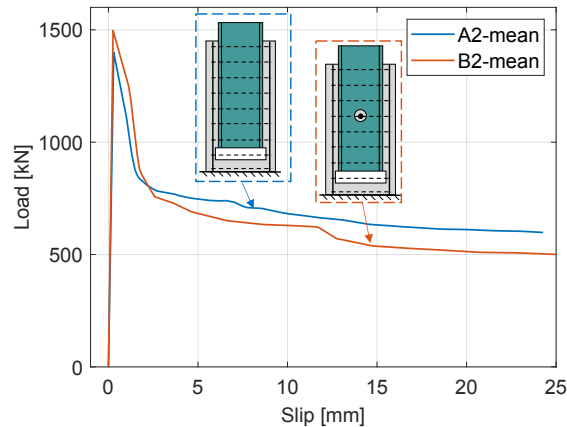


FIGURE 4.10: Comparison between the average of Series A2, without shear connector, and B2, with a shear connector.

In series B2, loading the CRCD connector causes the concrete dowel to expand, locally separating the steel–concrete interface and reducing friction. The additional shear resistance provided by the connector does not compensate for this loss, leading to a lower plateau resistance than in A2. Because B2 contains only one connector, the affected area is small, allowing part of the static friction to remain active. As a result, B2 still benefits from limited stick–slip behavior.

By contrast, series C3 and C5—containing multiple CRCD connectors along the web—experience greater overall interface separation, which markedly reduces frictional resistance. This explains why series B2 shows an unusually high plateau load compared with configurations where multiple connectors drive the response toward a kinetic frictional resistance.

When connectors are introduced, their local expansion partially detaches the interface. A single connector affects only a small zone, while multiple connectors increase the detached area and drive the response toward pure sliding friction. In those cases, the plateau load is governed by the connector shear capacity combined with the sliding friction.

Therefore, the ABAQUS model fails to capture the response of series B2 because it lacks a representation of static-friction effects, which dominate that configuration. Adjusting the model to match B2 would be impractical, as real structures and this study rely on multiple connectors rather than isolated ones.

Figure 4.11 compares the observed failure modes between the FE simulations and the cut specimens: (a) 12mm traversing rebar positioned on the web of a HEB 200, (b) 16mm traversing rebar positioned on the flange of a HEA 360, and (c) 20mm traversing rebar positioned on the web of a HEA 360. Both analyses reveal a two-step failure process of the traversing rebar consistent with the experiments: (1) tensile–shear failure on one side of the steel element, accompanied by bending of the remaining rebar, followed by (2) shear fracture of the traversing rebar on the opposite side.

The bending deformation of the rebar is also accurately captured by the FE model, corresponding to the experimental observations.

Overall, these results demonstrate that the calibrated FE model reliably reproduces the shear transfer mechanisms of CRCD connectors and can be confidently used to investigate their mechanical behavior

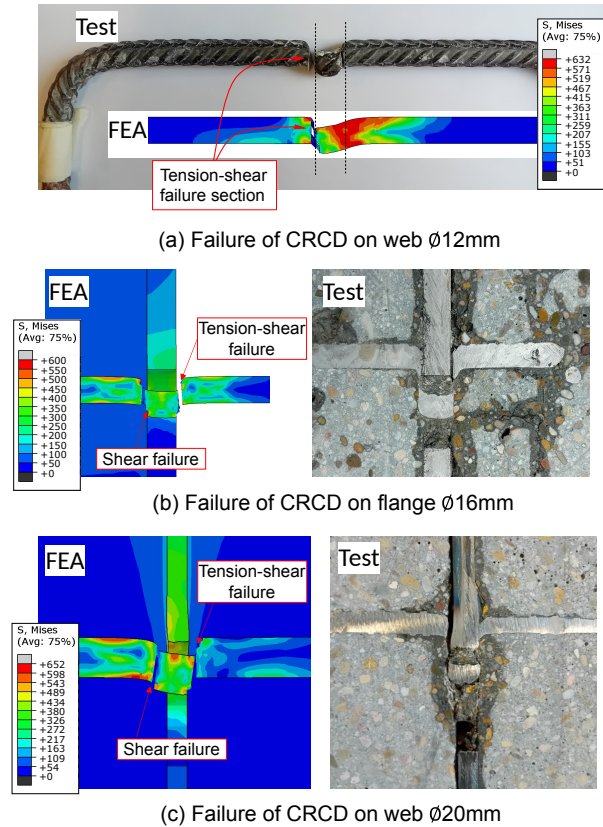


FIGURE 4.11: Comparison of the experimental and the FEA failure modes.

### 4.3 Model sensitivity

In this section, the sensitivity of the finite element (FE) model to various parameters is investigated. The objective is to demonstrate how the key parameters influencing the behavior of CRCD connectors were selected to achieve good agreement with the experimental results. Numerous simulations were conducted in ABAQUS; however, this section summarizes only the most relevant findings for series C2.

The results in Figures 4.12, 4.15, 4.14, 4.16, and 4.17 compare the experimental results with the numerical results for the different scenarios. To better observe the impact of the studied parameters, the adhesion bond was not included in the numerical simulations.

It was not possible to obtain a single model that perfectly reproduced the behavior of all test series. Therefore, some compromises were made to develop a model that provides the best overall fit across all series. The results presented here correspond to this optimized model. A single FE model was developed, while certain parameters were adapted depending on the materials used and geometries of the specimen:

- The mesh size, boundary conditions, and steel-concrete interface parameters were kept constant for all models.
- Two concrete strength classes were considered: C50/60 and C80/95. A single constitutive law for concrete was employed, with parameters adjusted according to the respective strength class.
- Four types of material laws were considered for the steel of traversing rebars:  $\phi 12$  mm hot-rolled,  $\phi 12$  mm cold-formed,  $\phi 16$  mm hot-rolled, and  $\phi 20$  mm hot-rolled. The parameters were defined based on the tensile test results of each rebar type.
- Two steel profile grades were used: S355 and S460. The FE model accounted for the corresponding material differences.
- The cohesive behavior was found to be sensitive to both the steel surface treatment and the concrete strength class. Consequently, three distinct sets of parameters were developed for the cohesive zone model, as explained in section 4.1.
- The interaction between the traversing rebar and the surrounding concrete varied depending on the specimen type. For the HEB 200 specimens, the rebar was tied to the surrounding concrete. For CRCD connectors located on the web of HEA 360 profiles, a friction coefficient of  $\mu = 0.5$  was applied. For connectors placed on the flanges of HEA 360 profiles, the rebar edges were tied, while a friction coefficient of  $\mu = 0.3$  was assigned to the middle portion. These variations were introduced to account for simplifications in the modeling of the push-out tests and to better reproduce the experimental shear-slip curves. For example, the U-shaped traversing rebars in the openings of the flanges were modeled as simple straight bars.

### 4.3.1 General

#### Symmetric model

Figure 4.12a compares the full and half push-out models. The two configurations exhibit almost identical behavior, with the only notable difference being that failure of the CRCD connectors in the full model occurs at a slip approximately 1 mm later than in the half model. This confirms that using a symmetric half model is a valid assumption, enabling a significant reduction in computational time without compromising accuracy.

#### Mesh size

The mesh size of the concrete dowel and the traversing rebar in the CRCD connectors is among the most critical parameters. Figure 4.12b illustrates the influence of varying the concrete mesh size within the steel opening. A pronounced effect is observed on both the shear-slip response and the failure mode. The softening branch of the concrete stress-strain relationship is also sensitive to the concrete element size in this region due to the extensive crushing of the concrete matrix. An

optimized concrete mesh size of approximately 2.3 mm was selected as a balance between computational efficiency and result accuracy, providing six concrete elements between the traversing rebar and the steel opening (for a 40 mm opening).

Figure 4.12c shows the influence of the mesh size of the traversing rebar. The shear-slip response is largely unaffected by mesh refinement; however, the mesh size has a noticeable effect on the shear failure mode of the rebar. A mesh size of 1.5 mm provided the best agreement with the experimentally observed failure shape and accurately reproduced the measured slip capacity.

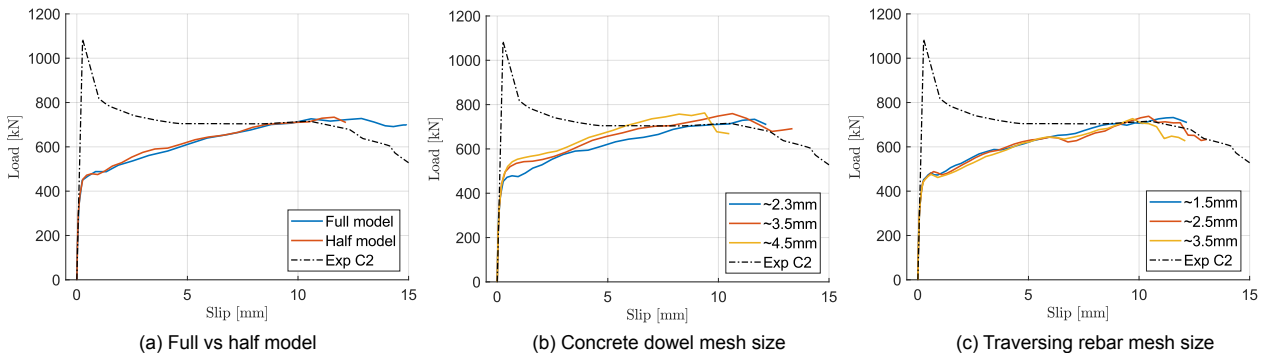


FIGURE 4.12: Impact of the half model assumption and the mesh size in the most critical elements: concrete dowel and traversing rebar.

### Quasi-static loading and mass scaling

The prescribed loading rate in ABAQUS was set to 1 mm/s. To ensure that the quasi-static assumption remains valid, the evolution of the kinetic energy (ALLKE) and the internal energy (ALLIE) was monitored over the entire analysis (see Fig. 4.13a). The details for all other simulations are given in Annex A. For quasi-static simulations, the ratio ALLKE/ALLIE is typically required to remain below about 5–10 %. In all analyses performed in this study, this ratio remained below 5 % for the whole duration of the loading, indicating that inertial effects are negligible and that the quasi-static assumption is satisfied.

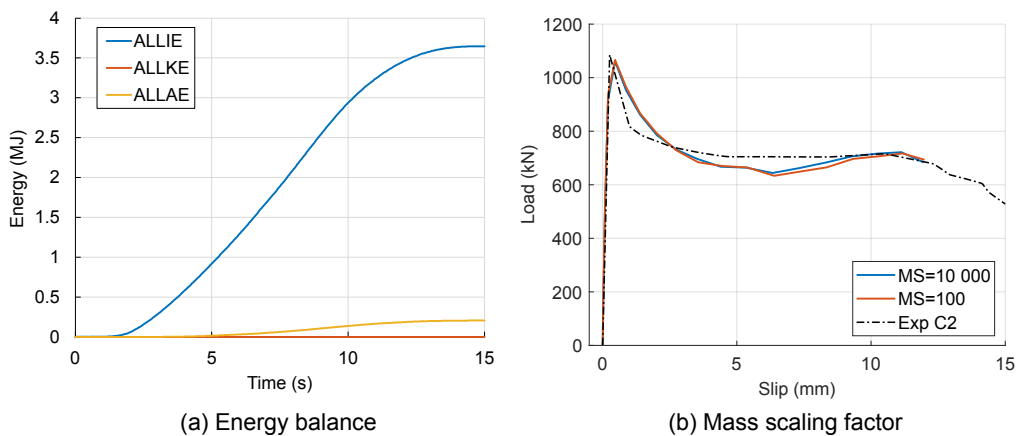


FIGURE 4.13: Comparison for series C2 between: (a) the internal (ALLIE), kinetic (ALLKE), and artificial (ALLAE) energies; (b) the mass scaling factors.

A fixed mass scaling factor of 10 000 was applied in all simulations, which is approximately equivalent to a loading-rate scaling factor of 100. The objective of the mass scaling is to increase the stable time increment and thereby reduce the number of increments required, without significantly affecting the mechanical response. The influence of mass scaling on the solution was assessed by comparing the artificial energy (ALLAE) with the internal energy (ALLIE), as shown in Fig. 4.13a. For a well-behaved explicit quasi-static analysis, the artificial energy should remain small compared to the internal energy, typically below 5–10 %. In all simulations, the ratio ALLAE/ALLIE remained below 8 %, indicating that numerical artifacts (such as hourglass control and contact stabilization) do not dominate the response.

To further verify the validity of the chosen mass scaling factor, a dedicated sensitivity analysis was carried out (see Fig. 4.13b), in which several simulations with different fixed mass scaling factors were performed. The comparison of the global load-slip curve shows only minor differences between the analyzed cases. This confirms that the selected mass scaling factor does not significantly influence the numerical results and can be considered acceptable for the present quasi-static analyses.

### 4.3.2 Interaction

#### Steel–concrete interface

The friction at the steel–concrete interface in the FE model was defined as Coulomb friction, where the frictional force depends on the normal pressure and the friction coefficient. Figure 4.14a presents the results obtained for different friction coefficients. Due to the large contact area between steel and concrete, friction plays a key role in the global response. A friction coefficient of  $\mu = 0.2$  was found to provide the best agreement across all series.

#### Traversing rebar–concrete interface

The interface conditions between the traversing rebar and the surrounding concrete are illustrated in Figure 4.14b, considering either a tie constraint or a frictional contact with  $\mu = 0.5$ . In the experimental specimens, the traversing rebars were bent at their edges, and no slip was observed when the specimens were loaded. In contrast, the numerical model used straight rebars, leading to some relative slip when frictional contact was applied. Consequently, a tied connection between the traversing rebar and the surrounding concrete was adopted in the FE model to reproduce the observed experimental behavior.

#### Lateral pressure

As previously discussed, frictional behavior comprises two components: (1) Coulomb friction, which requires a normal force to be activated, and (2) micro-interlocking, which arises from the roughness of the steel surface. In ABAQUS, it is not straightforward to model the frictional effects caused by surface roughness. To account for this phenomenon—as well as for imperfections and shrinkage-induced horizontal stresses—a lateral pressure was applied to the concrete surfaces. Figure 4.14c illustrates the parameters considered to represent these effects. A lateral pressure

of 1.5 MPa applied to the concrete surfaces provided the best correlation with the experimental results across all series.

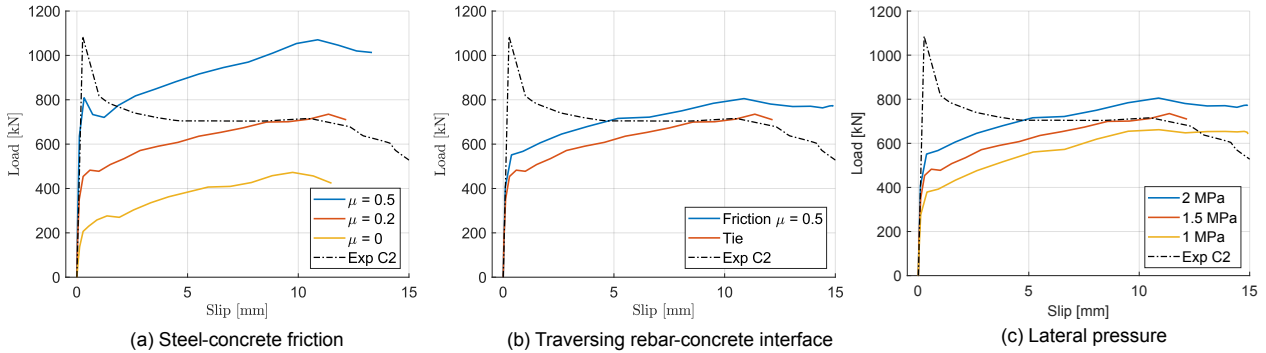


FIGURE 4.14: Influence of different parameters impacting the steel-concrete interaction.

### 4.3.3 Concrete block

#### CDP model parameters

The definition of the parameters in the Concrete Damage Plasticity (CDP) model is one of the most critical aspects of the FE analysis, as it significantly influences both the failure mode of the traversing rebar and the overall shear–slip response. The dilation angle was numerically calibrated, as shown in Figure 4.15a, while the parameters  $K_c$  and  $f_{b0}/f_{c0}$  were selected based on recommendations from the literature and the ABAQUS User Guide (Dassault, 2014) (see Figures 4.15b and c).

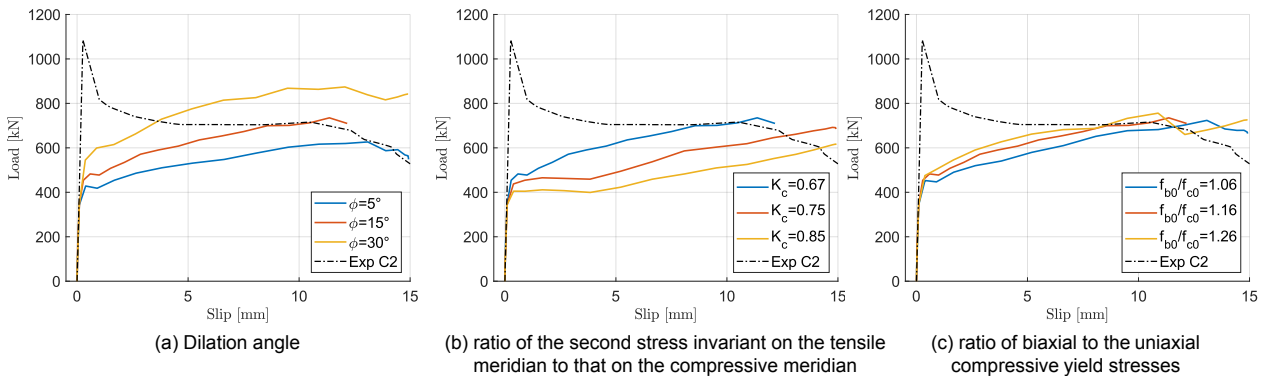


FIGURE 4.15: Impact of the parameters from the CDP model.

#### Concrete compressive and tensile strength

As illustrated in Figure 4.16, the FE model exhibited limited sensitivity to variations in the concrete compressive and tensile strengths. Although these parameters influence the structural response, their impact is minor compared to that of the CDP model parameters.

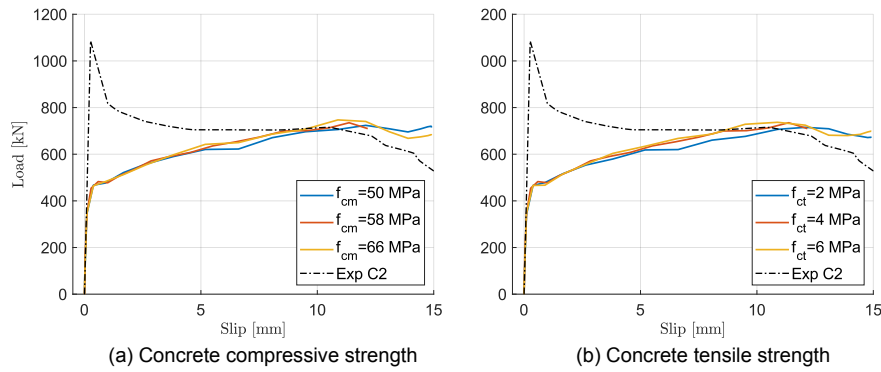


FIGURE 4.16: Influence of the concrete compressive and tensile strength.

#### 4.3.4 Traversing rebar

The material parameters of the traversing rebar in ABAQUS were defined based on the results of the tensile tests on coupons. The failure behavior was initially modeled using ductile damage. However, during the push-out tests, the traversing rebar failed under a combined action of tension and shear. To accurately reproduce this behavior, a shear damage model was implemented and numerically calibrated against the experimental results. Figures 4.17a and b present the results obtained for the fracture strain and the displacement at failure associated with the shear damage model. A fracture strain of 0.08 was found to effectively capture the failure mode across all series with a 12 mm diameter rebar, with the displacement at failure defined as ten times the fracture strain multiplied by the element size.

The parameters for the ductile damage model were derived directly from the tensile test results. As shown in Figure 4.17c, the displacement at failure had no significant influence on the shear–slip response; therefore, the values obtained from the tests were adopted.

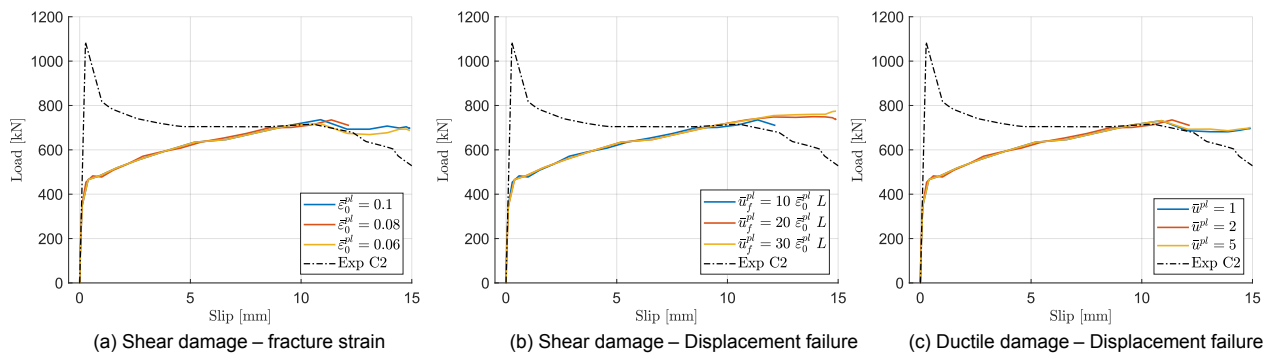


FIGURE 4.17: Impact of the parameters for the shear and ductile damage for metals.

#### 4.3.5 Cohesive layer

The cohesive behavior was calibrated using the specimens without connectors, *i.e.*, series A1, A2, and A3. Figures 4.18a and b illustrate the influence of the shear stresses  $t_{ss}$  and  $t_{tt}$  as well as the corresponding shear stiffness values  $K_{ss}$  and  $K_{tt}$ , in comparison with the experimental shear–slip curves. The softening behavior of the interface was modeled using an exponential degradation

evolution, and the sensitivity of the response to these parameters is shown in Figures 4.18c and d. The final set of parameters was selected to achieve the best overall agreement across all series.

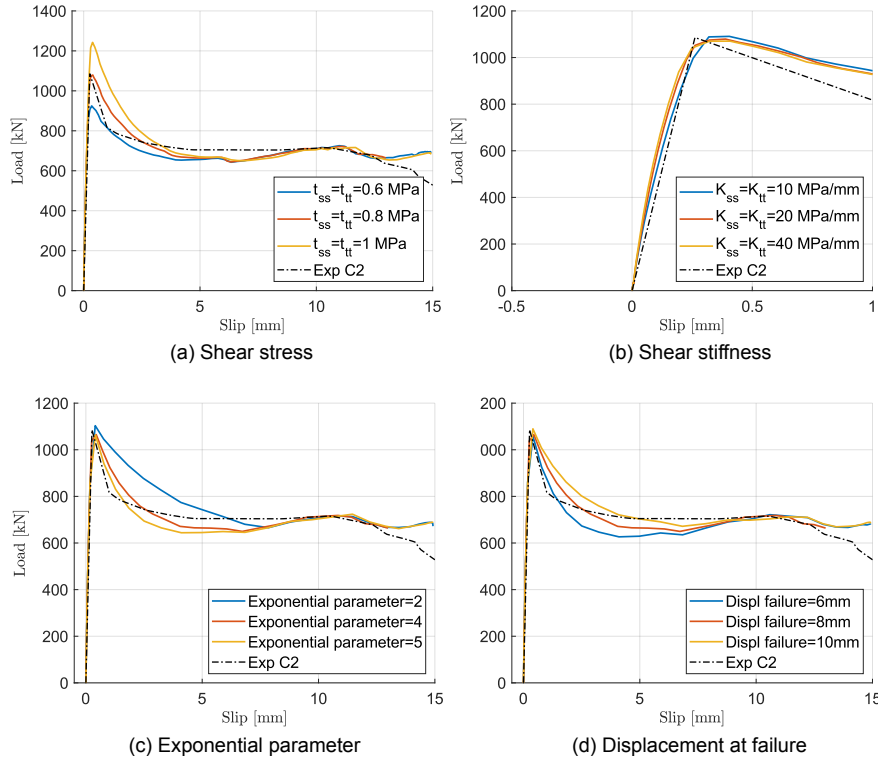


FIGURE 4.18: Impact of the parameters of the cohesive behavior.

## 4.4 Numerical analysis

### 4.4.1 Decomposition of the shear resistance components

In Figure 4.19, we decompose the numerical model of series C2 with 3 CRCD connectors and concrete compressive strength class of C50/60 into three different models: (1) modeling only the shear connectors without any bond resistance; (2) modeling the CRCD connectors with the friction; and (3) modeling the CRCD connectors with the friction and the adhesion. Different phases can be identified in Figure 4.19: (1) In phase 1, the initial stiffness is mainly driven by the stiffness of the adhesion layer and the ultimate load is mainly driven by bond (adhesion and friction) but the shear connectors are already activated and account for 20% of the resistance; (2) In phase 2, with further slip, the adhesion fails and is fully destroyed at around 4 mm of slip. Bond resistance is only provided by friction; (3) In phase 3, the resistance provided by the connectors increases. The shear connectors account for 54% and 64% of the total resistance at, respectively, 4 mm and 8 mm of slip; (4) In phase 4, the connector failed in shear at about 11 mm of slip and contributed to 66% of the shear resistance. The remaining shear resistance is provided by the friction between the steel and concrete interfaces and from the sheared surface of the connectors at the openings in the steel web.

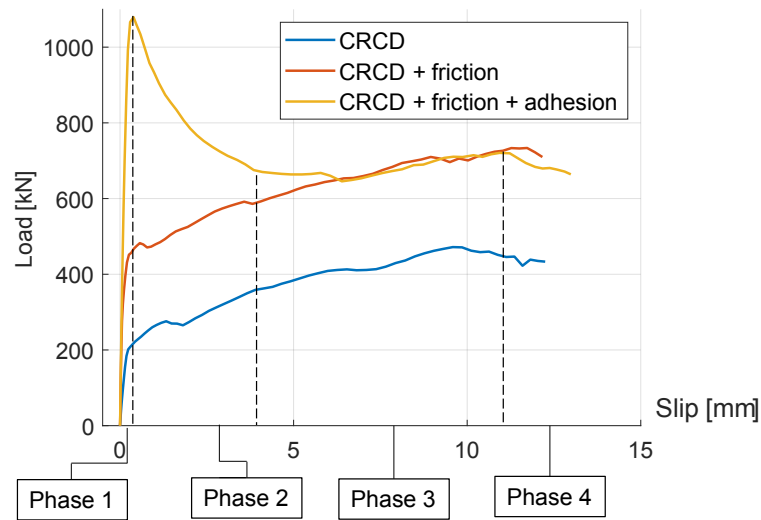


FIGURE 4.19: Decomposition of the load shear-slip curve in the different shear components for Series C2.

Considering series C3, we can realize the same analysis for concrete compressive strength class C80/95. The shear connectors contribute a bit less (17%) to the ultimate resistance. The peak load is dominated at 68% by the adhesion for C80/95, while it was 57% for concrete class C50/60. In phase 2, the CRCD connectors represent about half of the shear resistance. However, the CRCD connectors represent a more significant part of the shear resistance of phase 3, with a contribution of 70% and 74% at, respectively, 8 mm and 10 mm of slip.

This analysis was realized for all configurations, and the results are presented in Fig. 4.20.

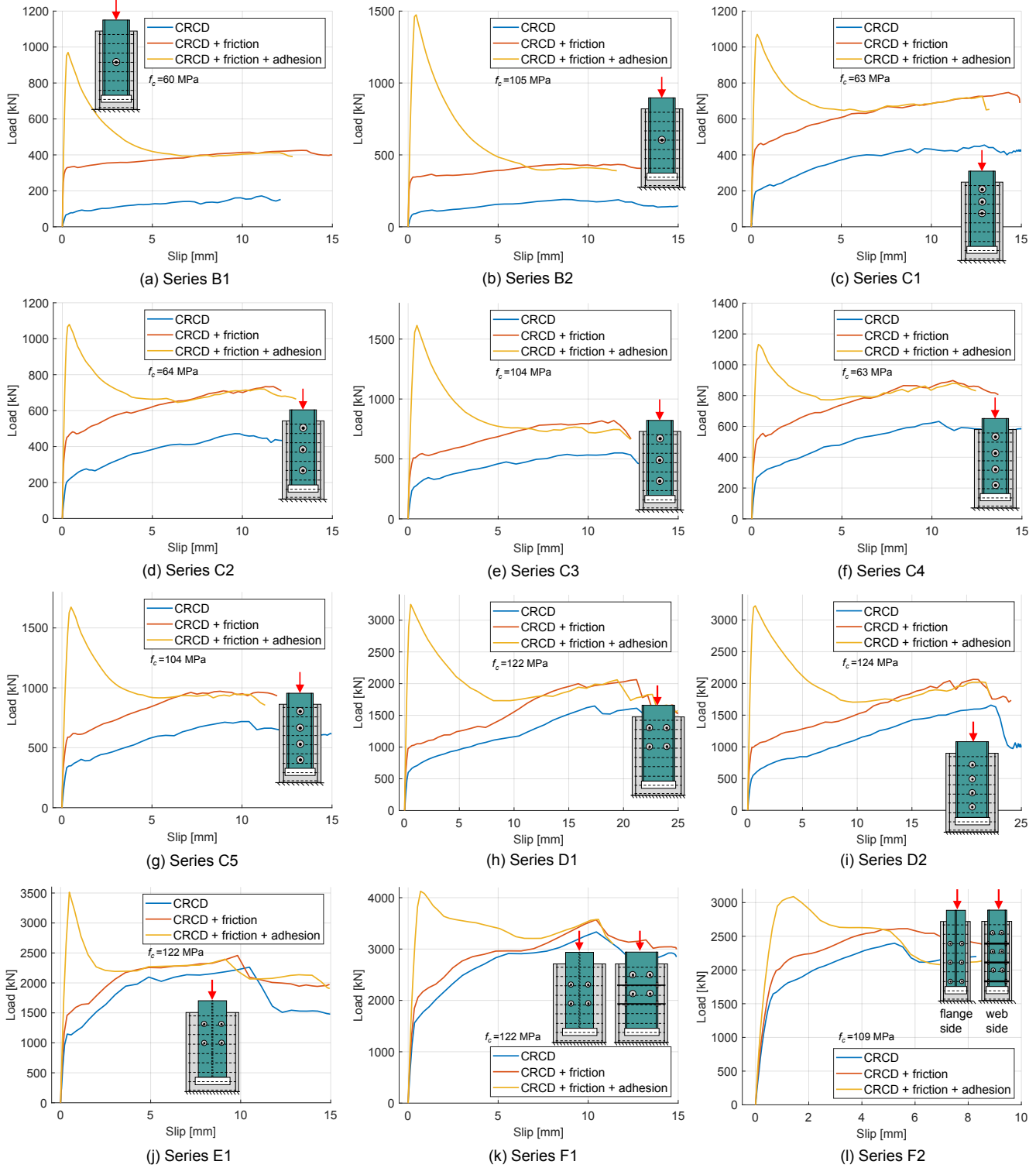


FIGURE 4.20: Decomposition of the load shear-slip curve in the different shear components for all Series.

#### 4.4.2 Analysis of the adhesion interface

Figure 4.21 illustrates the distribution of adhesion bond stresses in series C3 with three shear connectors and a HEB 200. A large non-uniform distribution of adhesion stress along the contact surface between steel and concrete is noticeable, as confirmed by the strain gauge results in Chapter 3. The distribution of adhesion stress is also strongly influenced by the presence of the shear connectors, mainly on the web. Indeed, the strain compatibility is affected by the higher local shear stiffness of the shear connectors. This results in a discontinuous shear flow at the position of the CRCD connectors, proving the activation of the shear connectors at the early loading stage. At the ultimate load, the adhesion stress is almost uniformly distributed and higher than 2 MPa along the steel-concrete interface.

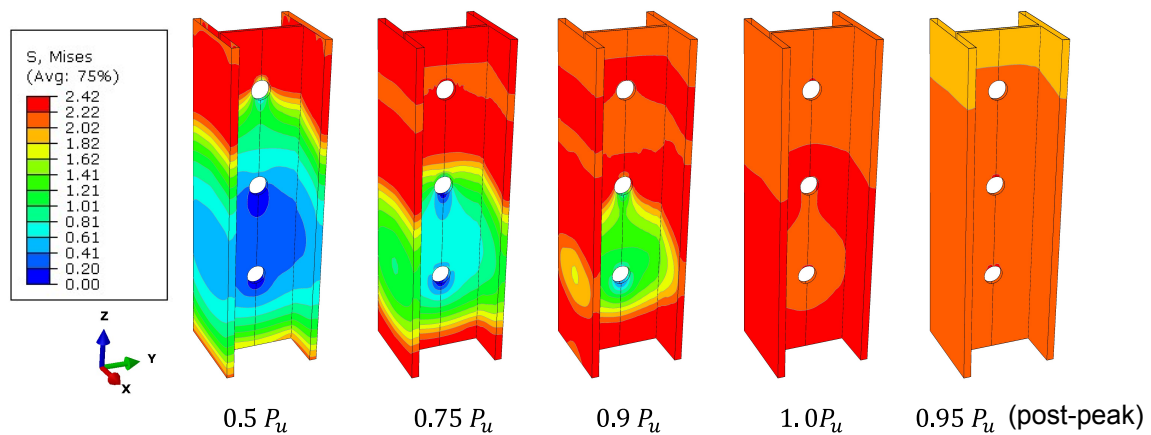


FIGURE 4.21: Distribution of the bond stress for different loading in series C3.

Figure 4.22 represents the degradation of the adhesion layer at the steel-concrete interface for series C3 for different loading relative to the ultimate load. We can observe that before 50% of the peak load, there is almost no damage to the adhesion layer. With the increase in the load, the adhesion layer degrades starting from the loaded end to the supported end. At the position of the connectors, a stress concentration is observed, and adhesion layer degradation becomes uniform. At the ultimate load, the adhesion layer is not entirely destroyed. After 95% of the ultimate load (post-peak), the adhesion is totally damaged, a sudden drop in the shear resistance can be noticed, and the shear transfer is only realized through friction and the CRCDs.

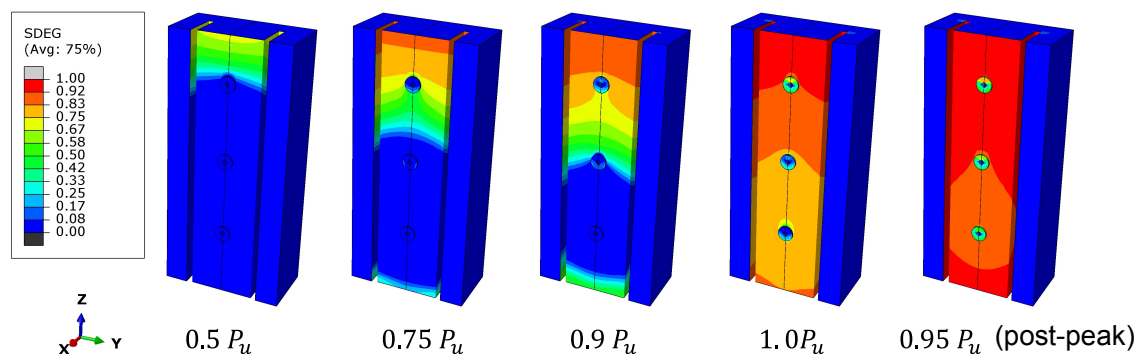


FIGURE 4.22: Distribution of the stiffness degradation for different loading in series C3.

### 4.4.3 Analysis of the traversing rebar failure

Figure 4.23 analyzes the failure mechanism of the shear connectors for series C3. The following steps are observed during the numerical simulation: (1) at the ultimate load (slip= $s_u$ ) the shear connector is activated, the infill concrete between the web and traversing rebar is under compression and the rebar is taking the tension; (2) at a slip of 5 mm, high compression stresses are observed in the infill concrete and it starts to reduce in volume; (3) after 8 mm of slip, there is high confinement of the infill concrete leading to a state of hydrostatic pressure provided by the traversing rebar, web and surrounding concrete; the infill concrete is completely crushed and cannot reduce in volume anymore. As a result, the traversing rebar starts to bend due to the high-stress concentration; (4) finally, at 10 mm of slip, a rupture of the traversing rebar is observed due to a shear-tensile failure on one side of the web, indicating the end of the simulation.

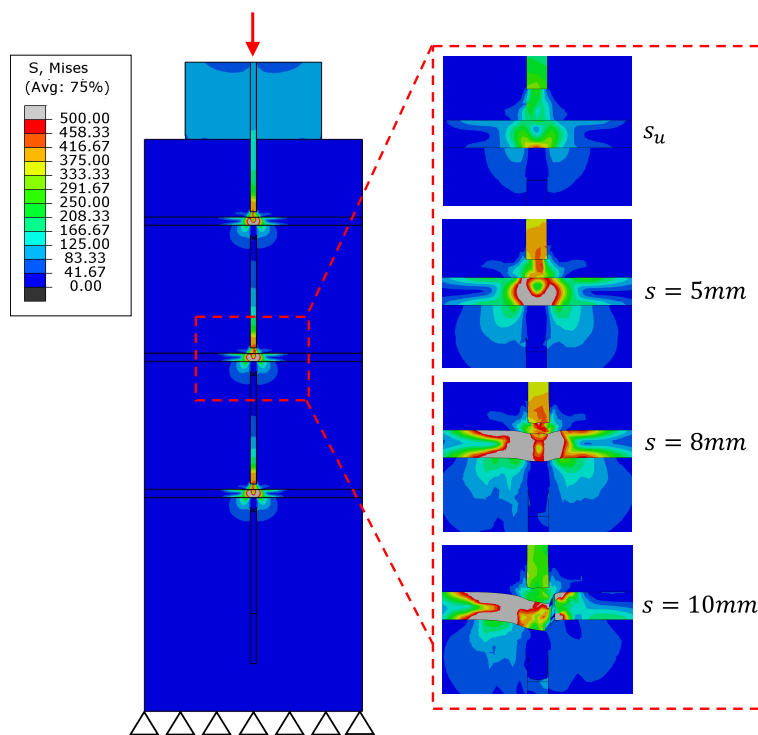


FIGURE 4.23: Failure mechanism of the traversing rebar in series C3.

During the experimental tests, it was found that the shear connectors did not break at the same time and, through strain gauges, it was possible to establish that it was not necessarily the first CRCD that broke first. However, experimental tests are not perfect in terms of geometry; it is possible that a traversing rebar is not perfectly positioned at the center of the opening, which would impact the slip when this connector fails. On the opposite side, the geometry of the numerical models is perfect, and the traversing rebar is perfectly in the center. In this situation, a similar pattern was identified: the traversing rebar is not failing at the same slip; it is not necessary that the first CRCD connector that fails first, and the tensile-shear failure can be located on one side of the web or the other, or even at the same time on both sides of the web.

#### 4.4.4 Analysis of the stress distribution along the traversing rebar

Figure 4.24 shows the distribution of Von Mises and shear stress along the traversing rebar for the first CRCD connector in series C2 (featuring 3 CRCD connectors in a HEB 200). No significant deformation is observed in the rebar until the load reaches  $0.9 P_u$ , with  $P_u$  the ultimate shear resistance of the shear connectors. At this point, the steel bar begins to yield at a stress of approximately 530 MPa. As loading continues, the rebar undergoes bending and strain hardening, ultimately reaching the maximum shear force  $P_u$  at a peak stress of 610 MPa. This deformation causes stress to increase along a large portion of the traversing rebar.

In the Von Mises stress distribution, two prominent peaks appear and reach their maximum at  $P_u$ . These peaks are located approximately  $\pm 6.5$  mm from the center of the rebar, which corresponds to about 2 mm from the edges of the steel web. A similar pattern is observed in the shear stress distribution, where the peaks align with those of the Von Mises stress, reaching a maximum shear stress of 350 MPa at  $P_u$ .

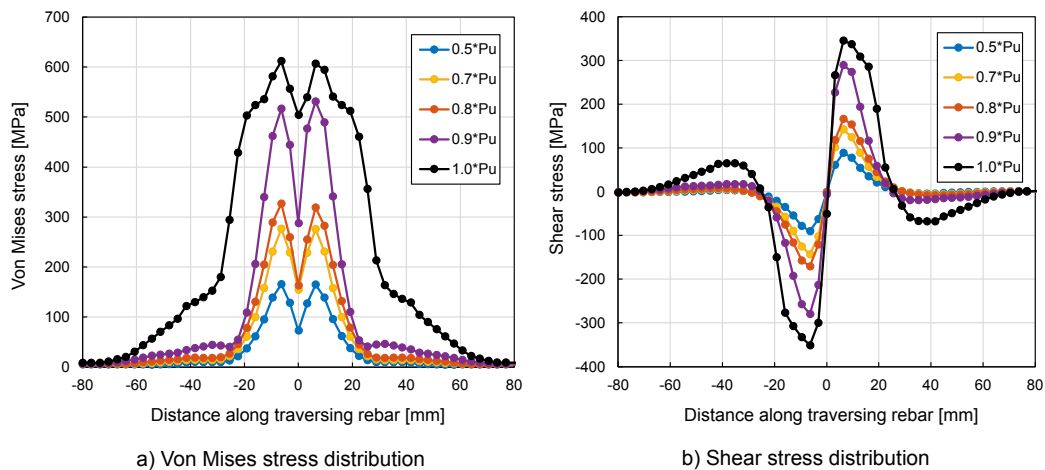


FIGURE 4.24: Von Mises and shear stress of the traversing rebar for Series C2.

#### 4.4.5 Study of the position of the reinforcement in the opening

The position of the traversing rebar in the opening of the CRCD connector is one of the main difficult parameters to control during the concreting of this kind of shear connector. During the experimental tests, great care has been taken to ensure the rebars were centered within the opening. However, a perfect alignment was not possible due to potential movement of the reinforcement cage where the traversing rebar is attached, or when the concrete was dropped in the framework, leading to potential movement of the traversing rebar.

For these reasons, we wanted to investigate the impact of a change in the vertical position of the rebar in the opening. The reference is a specimen with three centered-positioned rebars for each concrete compressive class (C50/60 and C80/95), similar to series C2 and C3, respectively, with an opening 40 mm in diameter and a rebar 12 mm. We studied two other positions: (1) with the three rebars at the top of the opening, and (2) with the three rebar at the bottom. To keep a proper mesh size, uniform to the reference, a 7 mm concrete cover was kept between the rebar

and the edge opening. This means that the center of the rebar was shifted up in (1) and down in (2) by 7 mm.

Figure 4.25 shows the results for (a) normal-strength concrete and (b) high-strength concrete. For normal-strength concrete, placing the rebar closer to the top of the opening reduces both slip capacity and ultimate shear resistance, although it increases the initial shear stiffness. This behaviour can be explained as follows: when the rebar is positioned close to the edge of the opening and aligned with the load direction, the volume of concrete available to be crushed and displaced is reduced. As a result, the concrete infill is more confined, which prevents the traversing rebar from developing a full bending–tension–shear failure. Instead, the failure becomes predominantly tension–shear governed, leading to a reduction in ultimate capacity. The slip capacity is therefore directly related to the amount of concrete available to be crushed and displaced.

Compared with a centrally positioned rebar, placing the rebar at the top results in a 10% reduction in strength and an approximately 5 mm reduction in slip capacity. Conversely, positioning the rebar at the bottom of the opening yields a similar load capacity to the reference case but increases slip capacity to 5.5 mm.

Similar trends are observed for high-strength concrete. (1) A rebar positioned at the top shows a 12% reduction in shear strength and a 4 mm lower slip capacity compared with the reference configuration, while (2) a rebar placed at the bottom maintains the same shear resistance but exhibits a 6.5 mm increase in slip capacity.

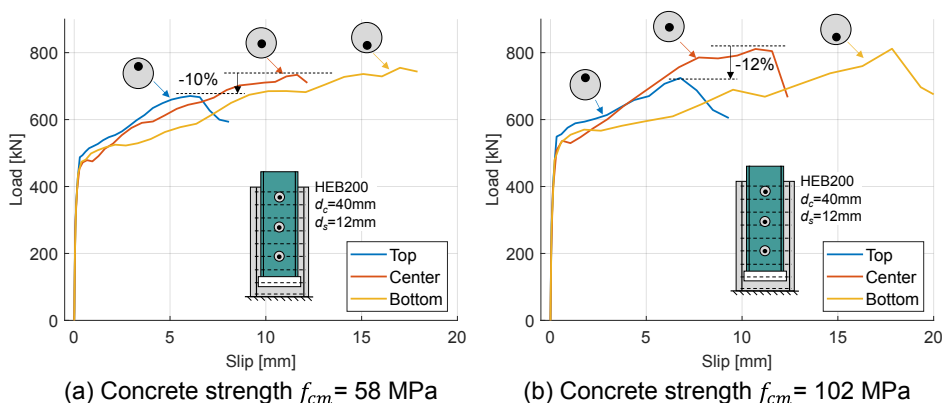


FIGURE 4.25: Impact of the position of the traversing rebar in the opening.

## 4.5 Parametric study

The previous section shows that modeling the entire experiment—including both the bond interface and the shear connectors—gives the same result as adding up the outcomes of the separate models. This means that even though the steel–concrete bond and the CRCD connectors interact, their behaviors can still be analyzed independently.

The adhesion behavior of concrete-encased H-shaped steel sections has been investigated by Chrzanowski et al. (2019), Huang et al. (2021), and Wang et al. (2019). However, the influence of key parameters governing the performance of CRCD connectors installed on the web and/or flanges of H-shaped steel profiles has received limited attention. Using the FE model calibrated

in Section 4.1, a parametric study is therefore conducted. Unless otherwise specified, a HEB 200 section encased in a square concrete section of  $320 \times 320 \text{ mm}^2$  with three rows of shear connectors and concrete compressive strengths  $f_c = 58$  and  $102 \text{ MPa}$  is considered. Accounting for both the resistance provided by the CRCD connectors and the friction at the steel–concrete interface, the following parameters are varied:

- **Traversing rebar diameter:** Opening diameter  $d_c = 40 \text{ mm}$  and three traversing rebar diameters  $d_s = 12, 16, 20 \text{ mm}$ .
- **Opening diameter:** Traversing rebar diameter  $d_s = 12 \text{ mm}$  and three opening diameters  $d_c = 40, 50, 65 \text{ mm}$ .
- **Traversing rebar steel grade:** Two opening/rebar diameter combinations,  $(d_c/d_s) = 65/20 \text{ mm}$  and  $40/12 \text{ mm}$ , and two steel grades with yield strengths  $f_y = 500$  and  $700 \text{ MPa}$ .
- **Web and flange thickness:** For the web, two thicknesses  $t_w = 9$  and  $20 \text{ mm}$  are considered with three opening/rebar combinations  $(d_c/d_s) = 65/20, 50/16,$  and  $40/12 \text{ mm}$ . For the flanges, connectors are placed only on the flanges, with  $(d_c/d_s) = 40/12 \text{ mm}$  and three flange thicknesses  $t_f = 10, 15, 20 \text{ mm}$ .
- **Concrete compressive strength:** For all previously described configurations, the concrete compressive strength is varied with  $f_c = 58$  and  $102 \text{ MPa}$ .
- **Concrete cover:** Connectors are placed on the flanges (three rows; 12 connectors in total), and three concrete cross-section dimensions with width  $b$  and height  $h$  are studied:  $b = h = 320, 380, 440 \text{ mm}$ .
- **Connectors layout:** Two cross-section configurations are examined:
  1. HEB 200 with a  $320 \times 320 \text{ mm}^2$  concrete section and connectors  $(d_c/d_s) = 40/12 \text{ mm}$  placed on the flanges and/or the web.
  2. HEA 360 with a  $540 \times 520 \text{ mm}^2$  concrete section and connectors  $(d_c/d_s) = 60/20 \text{ mm}$  placed on the flanges and/or the web.

#### 4.5.1 Impact of the traversing rebar diameter

Figure 4.26 presents the impact of the increase in the traversing rebar diameter on the shear resistance at different slip levels for normal- and high-strength concrete. It should be noted that the opening diameter was kept constant at  $40 \text{ mm}$ . It can be observed for both concrete compressive strength classes that the shear resistance increases almost linearly with the increase of the rebar diameter, slip lower than or equal to  $5 \text{ mm}$ . For higher slip levels (from  $8 \text{ mm}$  to ultimate load), the increase of the shear resistance was nonlinear, increasing faster from  $16$  to  $20 \text{ mm}$  than from  $12$  to  $16 \text{ mm}$ , and almost linear with the area of the traversing rebar's cross-section. This evolution is explained by the fact that first, the traversing rebar brings confinement to the infill concrete, and second, when the concrete cannot reduce in volume, the traversing rebar deforms and enhances the resistance of the connection. Increasing the traversing rebar diameter from  $12 \text{ mm}$  to  $16 \text{ mm}$

improves shear resistance by 12% and 9% for NSC and HSC, respectively, and from 16 mm to 20 mm by 28% and 24% for NSC and HSC, respectively. Finally, the traversing rebar fails in shear, which is proportional to the traversing rebar cross-section area.

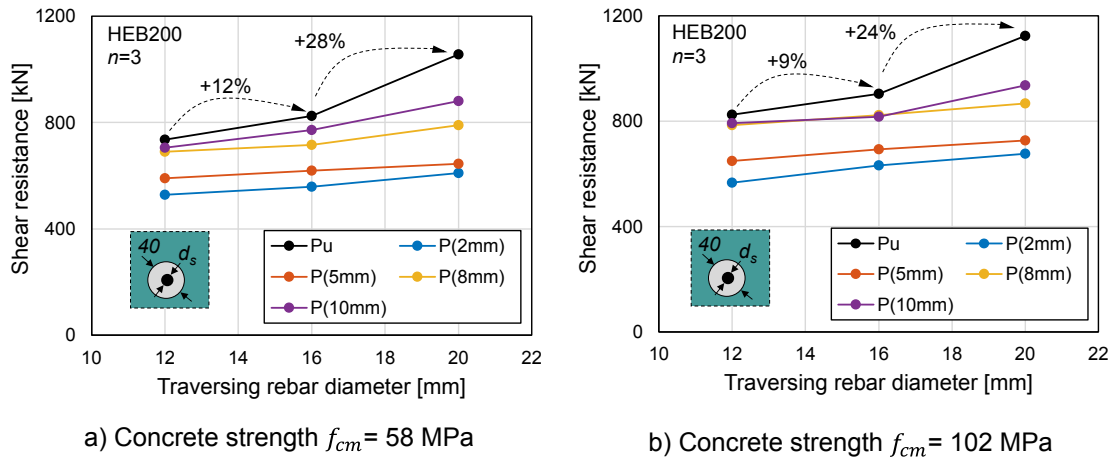


FIGURE 4.26: Impact of the traversing rebar diameter.

With the increase in the rebar diameter, the slip capacity also increases due to two phenomena: (1) the traversing rebar resistance to shear is stronger and the bar is able to resist more to the highly confined concrete, creating more space and reducing the concrete infill volume; (2) at a certain level the traversing rebar is stronger than the steel element and the steel web yield and an ovalization of the circular opening starts increasing the slip capacity. It is critical to consider the bearing resistance of the steel web in the design of the CRCD connectors.

#### 4.5.2 Impact of the opening diameter

In Figure 4.27, we kept the traversing rebar diameter constant at 12 mm, and we varied the opening diameter for the two different compressive strength classes of concrete. It can be noticed that an increase in the opening diameter increases the shear resistance for all slip levels. The increase in shear resistance is almost linear. The increase in the opening diameter results mainly in a change in the traversing rebar failure. With a larger opening, the traversing rebar has more capacity to deform. Thus, the failure mode goes from a shear-dominated failure mode to more bending deformation capacity, resulting in a bending-tensile-shear failure. Increasing the opening diameter from 40 mm to 50 mm improves shear resistance by 21% and 31% for NSC and HSC, respectively, and from 50 mm to 65 mm by 28% for both concrete compressive strength classes.

The slip capacity also increases with the increase in the opening diameter since it provides more distance between the traversing and the steel opening. This gives more space for volume reduction of the infill concrete, improving the ductile plateau.

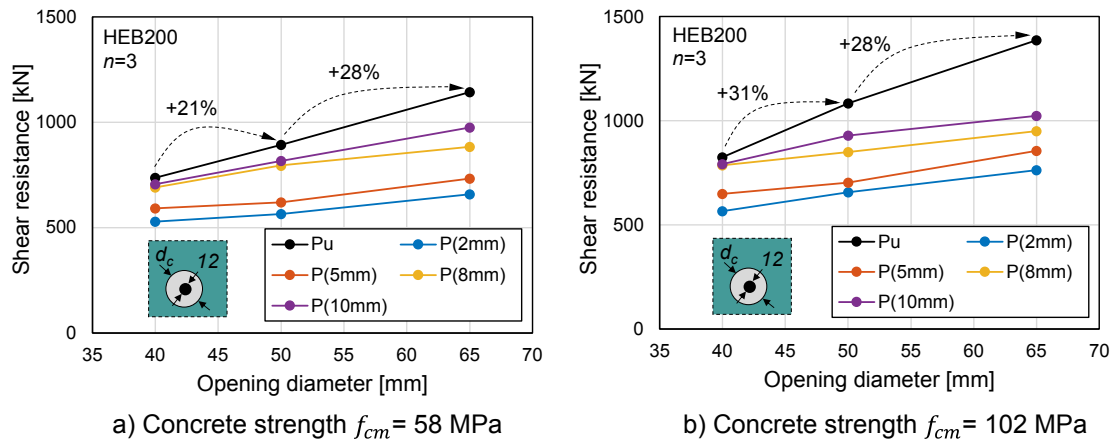


FIGURE 4.27: Impact of the opening diameter.

### 4.5.3 Impact of the traversing rebar steel grade

Figure 4.28 presents the evolution of the ultimate shear resistance with different traversing rebar steel grades for two configurations  $d_s/d_c = 12/40$  (mm) and  $20/65$  (mm), and for concrete classes C50/60 and C80/95. Steel grade has a limited impact on shear strength and only influences the ultimate resistance due to its higher yield strength. For a smaller rebar 12 mm in a 40 mm opening, increasing the steel yield strength from 500 MPa to 700 MPa, improves shear resistance by 7% and 11% for NSC and HSC, respectively. While for bigger rebar 20 mm in a 65 mm opening, this increase is 4% for NSC and null for HSC. The impact of the steel yield strength for higher rebar diameter is mainly due to the early yielding of the steel web, limiting the ultimate capacity of the CRCD connector.

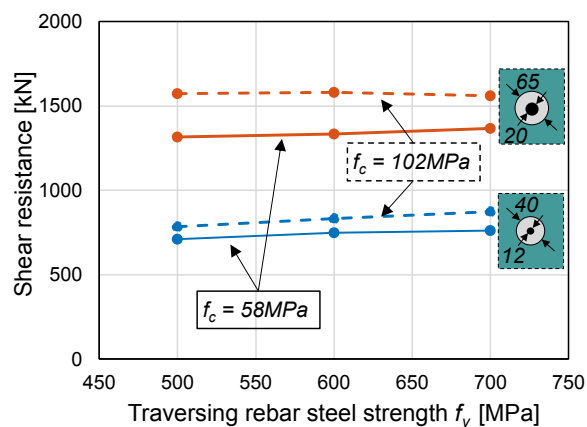


FIGURE 4.28: Impact of the steel grade of the traversing rebar.

### 4.5.4 Impact of the web and flange thickness

Figure 4.29 illustrates the influence of web thickness  $t_w$  on the shear resistance of the CRCD connector for various concrete classes and different configurations of traversing rebar and opening diameters: (1)  $d_s/d_c = 12/40$ , (2)  $16/50$ , and (3)  $20/65$ . Two web thicknesses were considered: 9 mm and 20 mm.

An increase in web thickness has a negative effect on slip capacity across all configurations and concrete compressive strength classes. When the web thickness is increased from 9 mm to 20 mm, a reduction in slip capacity of approximately 6 to 11 mm is observed. This is attributed to the larger concrete dowel infill between the traversing rebar and the steel profile, which increases confinement of the concrete. This greater confinement hinders the movement of the traversing rebar, leads to less concrete damage, and ultimately reduces the slip capacity.

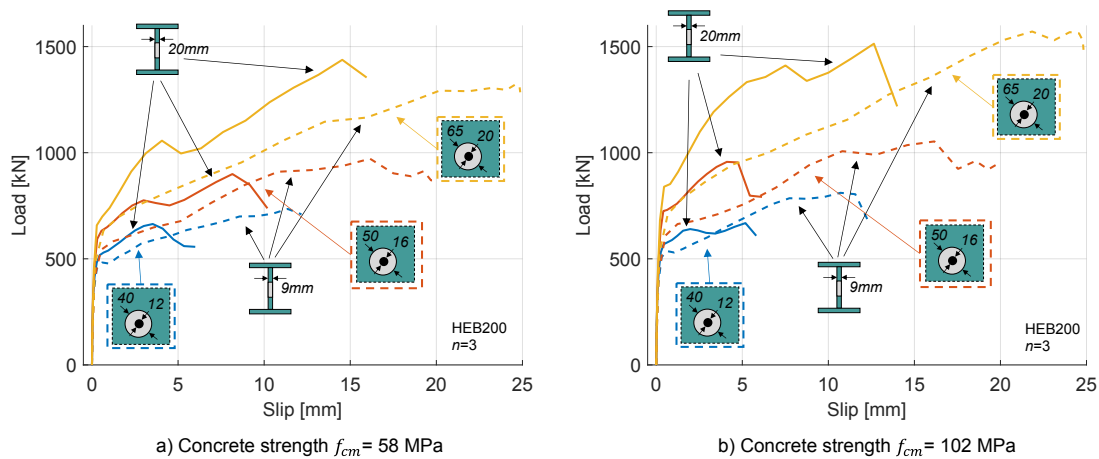


FIGURE 4.29: Impact of the thickness of the web.

Moreover, increasing the web thickness also reduces the ultimate shear resistance of the CRCD connector. For all configurations, a thickness increase from 9 mm to 20 mm results in a reduction of ultimate shear capacity ranging from 5% to 19%. This reduction is due to the stronger concrete dowel, which limits damage to the concrete matrix and prevents sufficient deformation of the traversing rebar. As a result, the failure mode shifts from a combined bending-tensile-shear failure to a predominantly shear failure, which has a lower ultimate shear capacity.

An exception occurs with the 60 mm opening and 20 mm rebar in normal-strength concrete. For the 9 mm web, shear failure was mainly due to ovalization of the steel element rather than failure of the rebar itself. By increasing the web thickness, the steel element becomes more resistant to deformation, allowing the connection to achieve its full shear capacity. This highlights the importance of designing the CRCD connector with adequate resistance in the steel element.

Improving the web thickness of the steel element also brings more shear capacity at low slip. At 2 mm of slip, a 20 mm thickness has between 13% to 26% higher shear capacity compared to a 9 mm thickness for all configurations and all concrete classes. This is particularly interesting for compressive elements where low slips are met, and a stiff connection improves the stress distribution between the two materials composing the composite connection.

Figure 4.30 illustrates the influence of the flange thickness  $t_f$  on the shear resistance for two different concrete strength classes. The analysis considers 12 CRCD connectors 40/12 positioned on the flanges of a HEB200 profile. The reference configuration, with  $t_f = 15$  mm, was calibrated based on experimental results, and two additional configurations with  $t_f = 10$  mm and  $t_f = 20$  mm were evaluated.

For normal-strength concrete (Figure 4.30a), increasing the flange thickness primarily affects the slip capacity. When increasing the thickness from 10 mm to 15 mm, the slip capacity decreases by approximately 3 mm, and from 15 mm to 20 mm, it decreases by a further 4.3 mm. The overall shear resistance shows a slight reduction of about 3.5% when increasing  $t_f$  from 10 mm to 20 mm. The main advantage of a thicker flange is the improvement in shear resistance at low slip levels (slip < 4 mm). The initial stiffness also increases significantly with flange thickness: for  $t_f = 10$  mm,  $k_s = 2306$  kN/mm; increasing to 15 mm results in a 51% increase, and to 20 mm, a 76% increase compared to the 10 mm case.

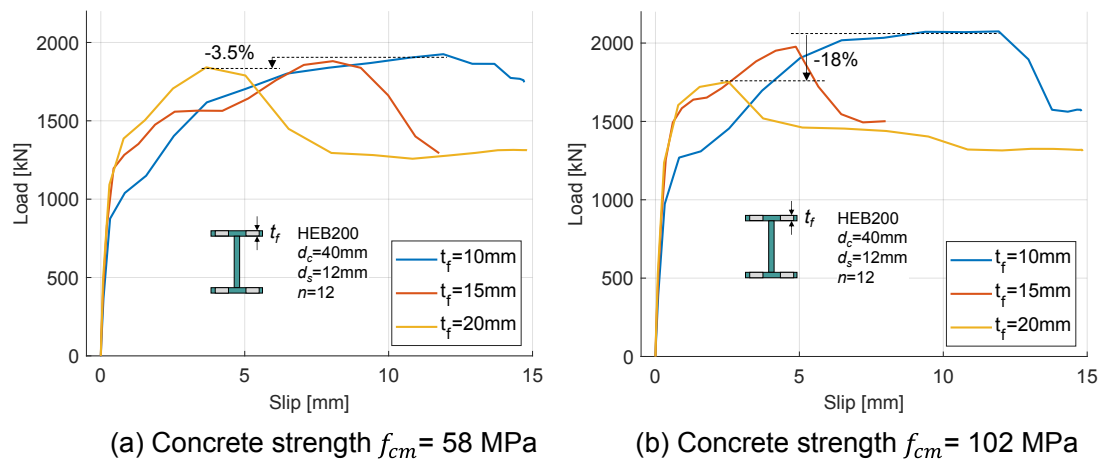


FIGURE 4.30: Impact of the thickness of the flanges.

For high-strength concrete (Figure 4.30b), a similar trend is observed: increasing the flange thickness leads to a reduction in slip capacity. The slip decreases by approximately 7 mm when  $t_f$  increases from 10 mm to 15 mm, and by 2.5 mm from 15 mm to 20 mm. However, in this case, the shear capacity decreases more noticeably with increasing flange thickness, with a reduction of up to 18% between  $t_f = 10$  mm and  $t_f = 20$  mm. The stiffness follows the same pattern as for normal-strength concrete: for  $t_f = 10$  mm,  $k_s = 2973$  kN/mm; increasing to 15 mm yields a 37% increase, and to 20 mm, a 63% increase relative to the 10 mm configuration.

#### 4.5.5 Impact of the concrete compressive strength

Increasing the concrete compressive strength from  $f_c = 58$  MPa to 102 MPa generally results in higher shear bearing capacity and reduced slip capacity. However, the extent of this impact depends on several parameters:

- **Web thickness:** The influence of concrete class on shear resistance diminishes with increased web thickness. For a thicker web (20 mm), the effect of higher concrete strength on shear capacity is minimal (between 1% and 5%). In contrast, with a thinner web (9 mm), the improvement in shear capacity is more pronounced: 12%, 9%, and 20% for configurations  $d_s/d_c = 12/40$ ,  $16/50$ , and  $20/65$ , respectively.
- **Opening diameter:** The benefit of increasing the concrete compressive strength becomes more significant with larger web openings. For a constant 12 mm traversing rebar, increasing

the concrete strength yields a 12% gain in shear capacity for 40 mm, and a 21% gain for 50 mm, and 65 mm openings. The positive influence of high-strength concrete becomes more evident as the size of the opening increases, likely due to more extensive engagement of the concrete infill in the load transfer mechanism.

- **Rebar diameter:** For a constant opening diameter, increasing the concrete compressive strength class continues to improve shear capacity, but the gains diminish as the rebar diameter increases. For a 40 mm opening, the increase in concrete strength leads to a 12% improvement for a 12 mm rebar, 10% for a 16 mm rebar, and only 6% for a 20 mm rebar. This is attributed to the reduction in the relative volume of infill concrete as the rebar occupies more space. With less concrete available to participate in load transfer, the contribution of the concrete dowel is reduced.
- **Traversing rebar yield strength:** The benefit of higher concrete strength also depends on the yield strength of the traversing rebar. For configuration  $d_s/d_c = 12/40$ , increasing concrete strength leads to shear capacity gains of 10%, 11%, and 15% for S500, S600, and S700 rebars, respectively. These gains occur because higher-strength rebars can better damage the surrounding concrete and achieve a more efficient failure mode. However, for configuration 20/65, the benefit decreases with increasing rebar strength: 20% for S500, 18% for S600, and 14% for S700. In this case, the 20 mm rebar is already sufficiently strong to fully engage the infill concrete, and the limiting factor becomes the steel web. Thus, increasing only the rebar strength no longer significantly improves the overall shear capacity.

#### 4.5.6 Impact of the concrete cover

Figure 4.31 illustrates the influence of the concrete cover in the width  $b$  (Figures 4.31a and 4.31b) and in the height  $h$  (Figures 4.31c and 4.31d) for the two concrete strength classes, considering 12 shear connectors positioned on the flanges. A reference configuration, corresponding to the minimum concrete cover specified in EN1994-1-1 (2004), was adopted with a base dimension  $b = 320$  mm and a height  $h = 320$  mm.

In Figures 4.31a and 4.31b, the base dimension was increased to  $b = 380$  mm and  $b = 440$  mm, respectively. No significant influence was observed on either the shear resistance or the slip capacity. Similarly, in Figures 4.31c and 4.31d, the height was increased to  $h = 380$  mm and  $h = 440$  mm, respectively. For high-strength concrete, no noticeable variation in shear resistance or slip capacity was observed. However, for normal-strength concrete, an increase in the shear peak of approximately 10% was recorded when the height increased from  $h = 320$  mm to  $h = 380$  mm, and a further 1.5% increase from  $h = 380$  mm to  $h = 440$  mm.

These results indicate the existence of a threshold concrete cover required for shear connectors positioned near the concrete edge to fully develop their strength. For high-strength concrete, a cover corresponding to  $h = 320$  mm is sufficient, whereas for normal-strength concrete, a minimum height of  $h = 380$  mm is necessary to achieve the full shear capacity of the connectors.



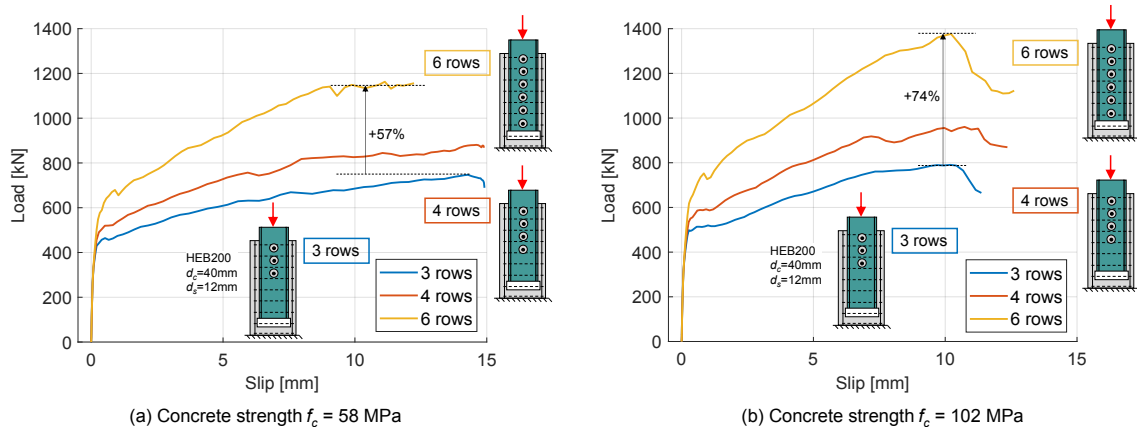


FIGURE 4.32: Comparison of different configurations with one row of CRCD connectors on the web.

Figure 4.33 illustrates the effect of increasing the number of connectors with two CRCDs per row, considering configurations with 2, 3, and 4 rows. In this setup, doubling the number of connectors from 4 to 8 leads to a 71% increase in shear resistance for both normal- and high-strength concrete. However, increasing the concrete grade by 76% results in only a marginal improvement in ultimate shear resistance, ranging from 1% to 3% across all configurations. A similar trend is observed for slip capacity, with a reduction of approximately 2 mm when using high-strength concrete compared to normal-strength concrete.

Comparing Figures 4.32 and 4.33, it can be seen that for normal-strength concrete, arranging two connectors per row improves the shear capacity by 2% and 6% for configurations with 4 and 6 connectors, respectively. In contrast, for high-strength concrete, the opposite trend is observed: a decrease in shear capacity of 6% and 10% for 4 and 6 connectors, respectively, when changing from one connector per row to two.

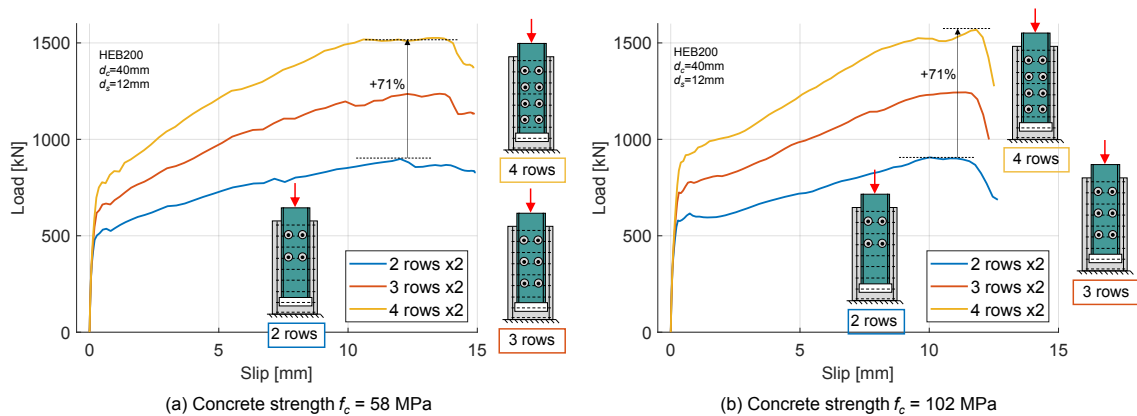


FIGURE 4.33: Comparison of different configurations with one row of CRCD connectors on the web.

Figure 4.34, featuring larger steel sections HEA360, compares layouts with two and three connectors, respectively. The objective is to identify the optimal arrangement of connectors. For the two-connector layouts, almost no difference is observed up to a slip of 16 mm. Beyond this point,

the specimen with two layers fails approximately 2 mm earlier than the one with a single layer, although their ultimate resistances are comparable. For the three-connector case (Figure 4.34b), the response is similar up to 14 mm of slip. Afterward, the specimen with three connectors in a single row exhibits a markedly lower resistance—up to 300 kN less—than the layout with three layers of one connector each. This reduction is attributed to concrete failure above the connectors near the edge of the block.

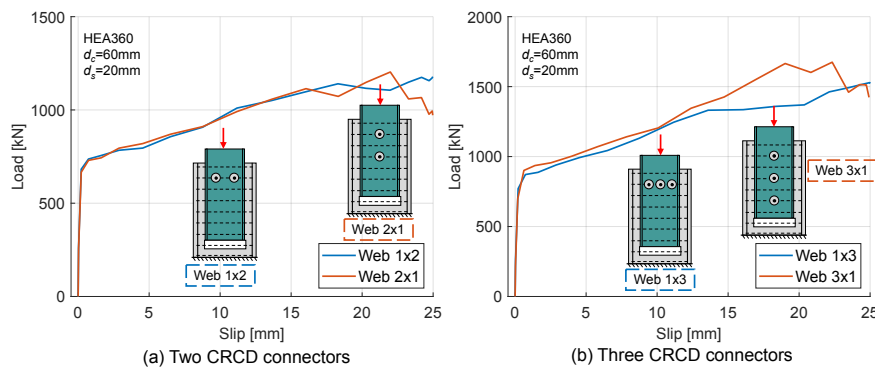


FIGURE 4.34: Influence of the layout for connectors on the web.

### Connectors on flanges

Figure 4.35 presents an evaluation of different configurations with CRCDs positioned on the flanges of an H-shaped steel profile, considering 1 to 3 rows of connectors, each row containing 4 connectors. Increasing the number of connectors from 4 to 8 and from 4 to 12 enhances the shear resistance by 66% and 135%, respectively, for normal-strength concrete, and by 70% and 145%, respectively, for high-strength concrete. Increasing the concrete strength has a negligible impact on the ultimate shear resistance (ranging from 0% to 4%), but it reduces the slip capacity by approximately 3 to 4 mm.

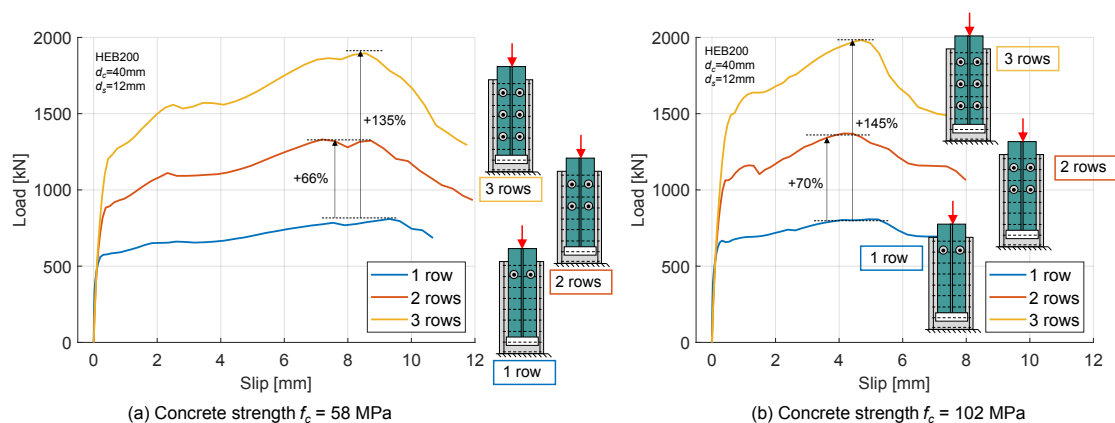


FIGURE 4.35: Comparison of different configurations with CRCD connectors on the flanges.

**Connectors on web & flanges**

Figure 4.36 compares three different arrangements of four CRCD connectors. For normal-strength concrete, the differences between the configurations are relatively minor. The configuration with connectors positioned on the flanges exhibits higher shear resistance for relative slips below 3 mm. However, its ultimate resistance and slip capacity are lower than those of the configuration with two rows of two connectors on the web by 11% and 2.5 mm, respectively.

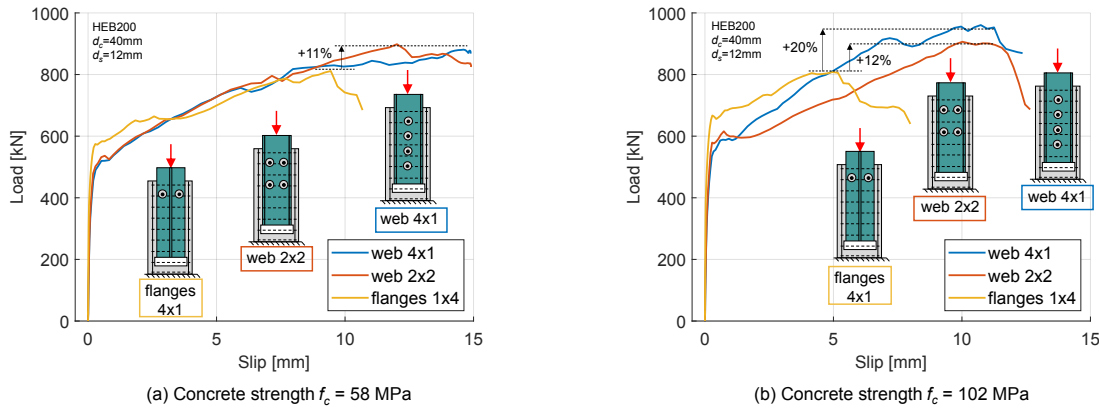


FIGURE 4.36: Comparison of different configurations with 4 CRCD connectors.

For high-strength concrete, the differences are more pronounced. The configuration with connectors on the flanges achieves better shear resistance for slips below 5 mm, but its slip capacity is reduced by approximately 5 mm compared to the web configurations. In terms of ultimate shear resistance, the 2x2 configuration on the web outperforms the flange configuration by 12%, while the 4x1 configuration achieves an even greater improvement of 20%.

Figure 4.37 presents three different 4 configurations: (1) six shear connectors positioned on the web, (2) twelve connectors positioned on the flanges, and (3) a combination of configurations (1) and (2). Since the configuration with connectors on the flanges exhibits a lower slip capacity, it governs the maximum performance of configuration (3) for both concrete grades.

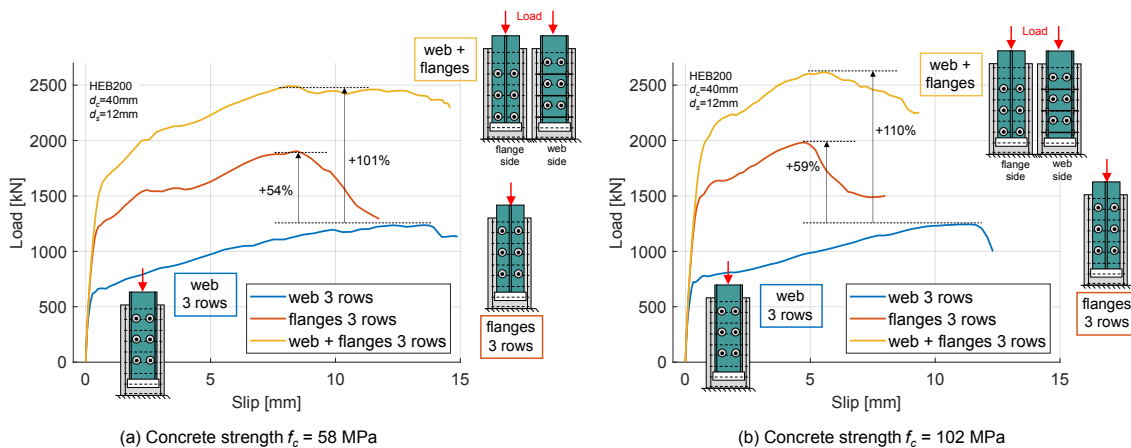


FIGURE 4.37: Comparison of CRCD on web, on flanges, and combined for a constant embedded length.

Due to the possibility of installing more connectors on the flanges within the same space compared to the web, configuration (2) achieves a higher ultimate shear resistance, by 54% and 59% for normal- and high-strength concrete, respectively, despite the reduced slip capacity. Combining configurations (1) and (2) further enhances the shear resistance by 101% and 110% compared to configuration (1) alone, for normal- and high-strength concrete, respectively.

Increasing the concrete grade slightly improves the ultimate shear resistance by about 5% for configurations with connectors on both the web and flanges, while reducing the slip capacity by approximately 2.5 mm.

Figure 4.38a and b also compare different layouts using 12 and 4 connectors, respectively. In Figure 4.38a, three 12-connector arrangements are examined: (1) Flange layout: 3 layers of 4 connectors on the flanges; (2) Web layout: 4 layers of 3 connectors on the web; and (3) Mixed layout: 2 layers of 4 connectors on the flanges and 2 layers of 2 connectors on the web. The web-only configuration shows the lowest shear resistance throughout the curve but offers a higher slip capacity (+7 mm compared to (1) and +5 mm compared to (3)). The flange-only configuration provides the highest initial stiffness (+26% relative to (1)) and an early peak at 6 mm of slip, but its strength is limited by cracking at the flange edge due to the reduced concrete cover. The mixed configuration combines both effects, achieving the highest shear resistance ( $\approx 4500$  kN) with shear-slip behavior intermediate between layouts (1) and (2).

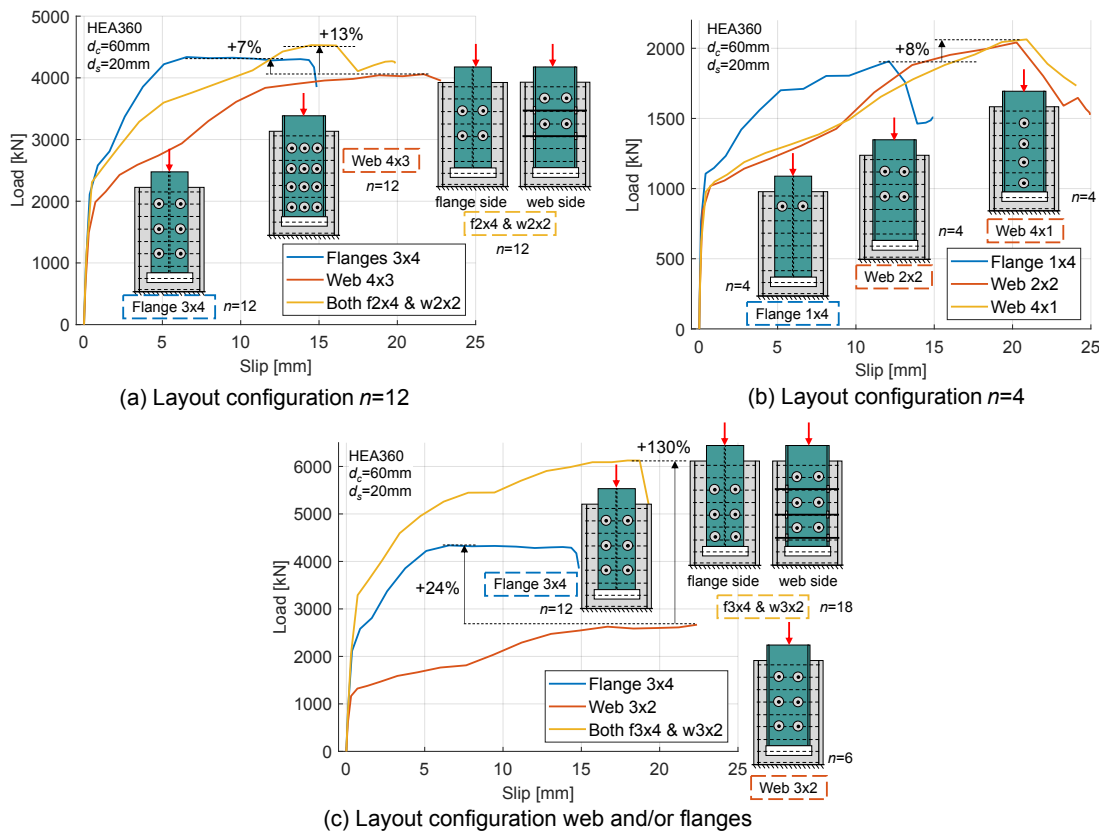


FIGURE 4.38: Comparison of different configurations with one row of CRCD connectors on the web.

In Figure 4.38b, configuration (1) places 4 connectors in one row on the flanges, while configurations (2) and (3) use 2 and 4 rows on the web. The two web configurations behave almost identically. Compared to them, the flange arrangement provides higher stiffness (+52%), higher resistance at low slip (< 12 mm, +31% up to 400 kN), but lower ultimate resistance (−8%) and slip capacity (7 mm).

Figure 4.38c compares: (1) 3 rows of 4 connectors on the flanges, (2) 3 rows of 2 connectors on the web, (3) the combination of (1) and (2). The combined layout benefits from both systems: the early shear strength of the flange connectors and the extended slip capacity of the web connectors. Its peak resistance is not limited by edge cracking because part of the shear force is redirected to the web. This configuration shows slip capacities up to 22 mm and ultimately fails due to flange connector rupture at 19 mm of slip. Compared to (1), it provides 24% higher strength before 5 mm of slip and achieves a greater peak resistance. Overall, for the same embedded length, combining flange and web connectors increases shear transfer capacity by 41% and 130% compared to flange-only and web-only layouts, respectively.

#### 4.5.8 Conclusions from the parametric study

Based on the calibrated FE model, a parametric study was carried out considering the response of the CRCDC connectors and the friction at the steel-concrete interface. Within the investigated ranges, the main conclusions are:

- **Connector geometry governs the response more than material grades.** The shear resistance and slip capacity are primarily controlled by the traversing rebar diameter  $d_s$ , the opening diameter  $d_c$ , and the thickness  $t$  of the steel element. In contrast, increasing the steel strength of the traversing rebar has only a modest influence on ultimate resistance.
- **Increasing  $d_s$  and  $d_c$  increases both resistance and ductility, up to web/flange bearing limits.** Larger rebars and larger openings enhance shear resistance and extend the ductile plateau, because the bar can mobilise more confinement and damage a larger volume of infill concrete. However, beyond a certain size combination, the governing failure shifts towards yielding and local diametral bearing of the steel web/flange, so the resistance of the steel element becomes a design constraint.
- **Concrete resistance and steel thickness improve stiffness but penalize slip capacity.** Higher concrete strength and thicker webs/flanges increase initial stiffness and shear resistance at small slip, but reduce slip capacity and can even reduce ultimate resistance once confinement of the concrete dowel becomes too strong.
- **Connector layout on web and flanges mainly boosts resistance; ductility is governed by the flanges connectors.** For the same embedded length, pure web layouts show the lowest resistance but the largest slip capacities, while flange-only layouts provide the highest initial stiffness and high resistance at small slip, but their slip capacity is limited. This is mainly the result of the thicker steel flanges compared to the web and the capacity of placing more connectors on the flanges for the same embedded length. Mixed web+flange arrangements

exploit the high early strength of flange connectors and the additional shear paths via the web, leading to the highest total shear transfer (up to about 40–130% increase for the same embedded length compared to flange-only and web-only layouts for HEA 360). However, the ultimate slip is often still controlled by the flange connectors, so web connectors can remain underutilized unless the geometry is deliberately tuned to align the slip capacities of web and flange connectors.

Overall, the parametric study shows that the behaviour of plug-in CRCD connectors is largely governed by a few geometric parameters, and that both resistance and slip capacity can be deliberately tuned. This justifies the use of geometry-based terms in the semi-empirical resistance and slip capacity equations developed in Chapter 5 and clarifies the limitations associated with very thick steel elements and high concrete strengths.



## Chapter 5

# Semi-Empirical Model

This chapter shows first that existing analytical equations from the literature cannot adequately reproduce the behavior of CRCD shear connectors arranged in groups on H-shaped steel profiles. This motivates the development of a dedicated semi-empirical model for CRCD groups combined with friction in the studied configuration.

A semi-empirical equation is therefore proposed to predict the resistance of a group of CRCD connectors, including the contribution of friction at the steel–concrete interface. A complementary expression is introduced to estimate the initial stiffness of the connection; this stiffness model is more tentative and should be used with caution. Stiffness remains a key parameter, as it governs the load–slip response in the service range and the distribution of forces within the load introduction zone. In addition, a simplified equation is proposed to provide only an order-of-magnitude estimate of the slip capacity, which can be used to optimize the geometry of the connectors positioned on the web and the flanges.

The resistance and stiffness formulations are evaluated statistically to quantify their accuracy and to derive corresponding partial safety factors. The chapter concludes with a discussion of the limitations and validity range of the proposed equations, and with design considerations for load introduction zones. Throughout, it is emphasized that the models developed here have clear limits of applicability and should not be used outside the parameter range covered by the underlying experimental and numerical data.

### 5.1 Existing analytical models

Various equations have been developed to predict the resistance of CRCD connectors, as described in Table 5.1. Two categories can be highlighted from this table: equations for rib-type and plug-in-type CRCD connectors. This distinction arises because equations developed for rib-type connectors perform poorly in predicting the resistance of plug-in-type connectors. Indeed, plug-in-type connectors are deeply embedded in the concrete block, which allows the connector to develop its full strength. In contrast, rib-type connectors are commonly used for composite beams and are positioned in the concrete slab, which often leads to premature failure of the concrete slab before the full strength of the connector has been reached.

Equations developed for rib-type CRCD connectors by Oguejiofor and Hosain (1994), Al-Darzi, Chen, and Liu (2007), Vianna et al. (2008), Ahn et al. (2010), and Verissimo et al. (2007) consider discontinuous steel ribs perforated with multiple CRCD connectors. In addition to the

strength of the concrete dowel and transverse reinforcement, these authors take into account the load-bearing capacity of the end-strip, which transfers compression to the concrete. On the other hand, Ushijima et al. (2001) and Zheng et al. (2016b) investigated continuous steel strips perforated with CRCD connectors and used Styrofoam to eliminate the end-bearing effect of the steel strip in their experiments. Therefore, their equations consider only the resistance provided by the concrete dowel and the traversing rebar.

TABLE 5.1: Analytical equations to predict the resistance of rib-type and plug-in-type CRCD connectors.

Reference	Equation to predict CRCD connector resistance
<b>Equations to predict the resistance of rib-type shear connectors</b>	
Oguejiofor and Hosain (1994)	$P_u = 4.5 h t f_c + 3.31 n d_c^2 \sqrt{f_c} + 0.91 A_{s,s} f_{s,s}$ (5.1)
Al-Darzi, Chen, and Liu (2007)	$P_u = 255.31 \cdot 10^3 + 7.62 \cdot 10^{-1} h t f_c - 7.59 \cdot 10^{-4} A_{s,s} f_{s,s} + 2.53 n A_c \sqrt{f_c}$ (5.2)
Vianna et al. (2008)	$P_u = \begin{cases} 152.9 \cdot 10^3 + 3.21 h t f_c - 0.86 n A_c \sqrt{f_c} & \text{for } f_c \leq 30\text{MPa} \\ 31.8 \cdot 10^3 + 1.9 h t f_c + 0.53 A_{s,s} f_{s,s} - 0.6 \cdot 10^{-3} n A_c \sqrt{f_c} & \text{for } f_c > 30\text{MPa} \end{cases}$ (5.3)
Ahn et al. (2010)	$P_u = 3.14 h t f_c + 1.21 A_{s,s} f_{s,s} + 7.58 n A_c \sqrt{f_c}$ (5.4)
Verissimo et al. (2007)	$P_u = 4.04 \frac{h}{b} h t f_c + 2.37 n d^2 \sqrt{f_c} + 0.16 A_c \sqrt{f_c} + 31.85 \cdot 10^6 \frac{A_{s,s}}{A_c}$ (5.5)
Ushijima et al. (2001)	$\begin{cases} P_u = 1.45 ((d_c^2 - d_s^2) 1.25 f_c + d_s^2 f_{s,t}) - 26.1 \cdot 10^3 \\ 51 < (d_c^2 - d_s^2) 1.25 f_c + d_s^2 f_{s,t} < 488 \end{cases}$ (5.6)
Zheng et al. (2016b)	$P_u = 6.69 \left( \frac{A_{s,t}}{A_{s,t} + A_c} \right)^{2/3} A_c f_c + 1.58 A_{s,t} f_{s,t}$ (5.7)
<b>Equations to predict the resistance of plug-in-type shear connectors</b>	
Su, Yang, and Bradford (2016)	$P_u = \begin{cases} A_c \tau_c + A_{s,t} f_{s,t} & \text{for } A_{s,t} (\beta A_{s,t} f_{u,t} - f_{s,t}) \leq A_c \tau_c \\ \beta A_{s,t} f_{u,t} & \text{for } A_{s,t} (\beta A_{s,t} f_{u,t} - f_{s,t}) > A_c \tau_c \end{cases}$ (5.8)
He et al. (2016)	$P_u = (-0.0275 f_c + 0.342 \sqrt{f_c} - 0.573) A_b + 1.325 A_c f_c + 2.09 A_{s,t} f_{s,t}$ (5.9)
He, Fang, and Mosallam (2017)	$P_u = 0.045 A_b \sqrt{f_c} + 1.325 A_c f_c + 2.09 A_{s,t} f_{s,t}$ (5.10)
Wang et al. (2014)	$P_u = 4.98 A_c \sqrt{f_c} + 2.55 A_{s,t} f_{s,t} + 0.65 A_{s,s} f_{s,s}$ (5.11)
Zhao et al. (2018)	$P_u = 0.65 (A_{s,s} f_{s,s} + A_{s,t} f_{s,t}) + 1.12 (5.512 d_s^2 - 0.0028 d_s^4) n \sqrt{f_c f_{s,t}}$ (5.12)
Tan, Fang, and Xiong (2022)	$P_u = (0.03 \rho_s + 0.031) \frac{f_c}{0.057 f_c + 1} A_b + 2.1 \sqrt{\frac{t}{d_c}} (A_c f_c + 1.55 A_{s,t} f_{s,t})$ (5.13)

Plug-in-type CRCD connectors can be classified depending on whether they consider the bonding effects or not. Su, Yang, and Bradford (2016) developed their equation considering experiments that neglected the bond resistance between the steel plate surface and the surrounding concrete. However, He et al. (2016), He, Fang, and Mosallam (2017), Wang et al. (2014), Zhao et al. (2018), and Tan, Fang, and Xiong (2022) conducted experiments with both types of steel surface conditions to include the bond resistance in the resistance of the global connection.

In Paoletti and Schäfer (2023), a dataset comprising 55 specimens with plug-in CRCD connectors was compiled from experimental studies available in the literature (Wang et al., 2022; Li et al., 2018; Zhao et al., 2018; Wang et al., 2014; He et al., 2016; He, Fang, and Mosallam, 2017; Su et al.,

2014; Tan, Fang, and Xiong, 2022; Di et al., 2018). The study demonstrated that the equations developed for plug-in-type CRCD connectors provided reliable predictions of test resistances. However, all the push-out tests considered CRCD connectors attached to a steel plate embedded into the concrete. Only one experimental program investigated CRCD connectors positioned on the web of an H-shaped steel profile. In that case, the analytical predictions significantly underestimated the experimentally measured resistance. This discrepancy can mainly be attributed to the higher contribution of the bond component relative to the connector resistance when CRCD connectors are installed on an H-shaped steel profile rather than on a flat steel plate. The study, therefore, emphasized the need for a new analytical formulation capable of accurately predicting the resistance of CRCD connectors positioned on the web and/or flanges of H-shaped steel profiles.

## 5.2 Proposed semi-empirical model

In Section 4.1, it is shown that the resistance contributed by the interfacial bond and by the CRCD connectors can be treated as separate components. This separation enables the formulation of two distinct predictive equations: one for the interfacial bond resistance and one for the CRCD connector resistance. Because the adhesion component of the bond is brittle and unreliable, only the initial stiffness and the sliding friction are incorporated into the semi-empirical model. In contrast, the shear load-slip response of the CRCD connectors is characterized by a lower initial stiffness but substantial strain hardening up to failure. When combined, these two behaviours can be idealized using an elastic-perfectly plastic model (Fig. 5.1), in which the plastic plateau resistance  $P_p$  reflects the combined effects of sliding friction and the CRCD connectors and is considered as the ultimate resistance of the semi-empirical model.

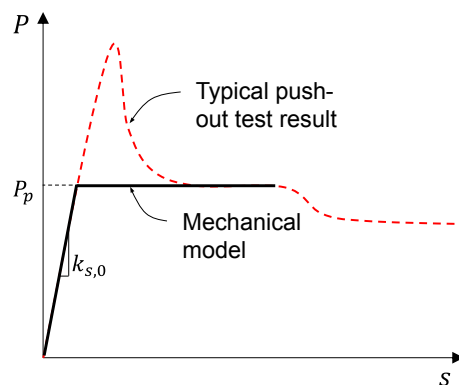


FIGURE 5.1: Semi-empirical model for predicting the shear resistance of CRCD connectors combined with bond, compared to a typical shear-slip curve from tests (see Chapter 3).

The model is described as semi-empirical because it couples established mechanical principles—such as the shear resistance of steel rebars—with curve fitting to achieve close agreement with the experimental results. The plateau resistance  $P_p$  is predicted using Eq. 5.14, which sums the contribution of the CRCD connectors,  $P_{\text{CRCD}}$ , and the frictional resistance at the steel-concrete interface,

$P_{friction}$ . The connector resistance is further separated into the concrete dowel contribution,  $P_c$ , and the traversing rebar contribution,  $P_s$ :

$$P_p = P_{CRCD} + P_{friction} = P_c + P_s + P_{friction} \quad (5.14)$$

A key feature of the proposed model is that it accounts for the actual connection stiffness rather than assuming a fully rigid interface. An equation is therefore developed to predict the stiffness  $k_s$ , governed primarily by adhesion at the steel-concrete interface. A statistical evaluation of both prediction equations is carried out in Section 5.3 following Annex D of EN1990 (2002).

To provide an overview of the chapter, Fig. 5.2 summarizes the workflow used to develop the model. As noted previously, two equations are proposed: one predicting the connection stiffness  $k_{s,pred}$  (Section 5.2.1), and another predicting the plateau resistance  $P_{p,pred}$ . The latter combines the resistance provided by the CRCD connectors,  $P_{CRCD}$  (Section 5.2.3), and the frictional resistance,  $P_{friction}$  (Section 5.2.2).

The equation for  $P_{CRCD}$  begins by considering the group effect, since the resistance of a group of connectors is lower than the sum of their individual resistances. This reduction is accounted for through the coefficient  $\varphi$ . The contributions of the concrete dowel and the traversing rebar are then determined based on experimental observations. The resistance of the steel element against diametral pressure is evaluated using the method for bolted connections described in EN1993-1-8 (2005). The influence of the steel element thickness on the failure mode is incorporated through the reduction factor  $\beta$ . Finally, the equation distinguishes between CRCD connectors located in the web and in the flanges, as their geometrical characteristics may differ.

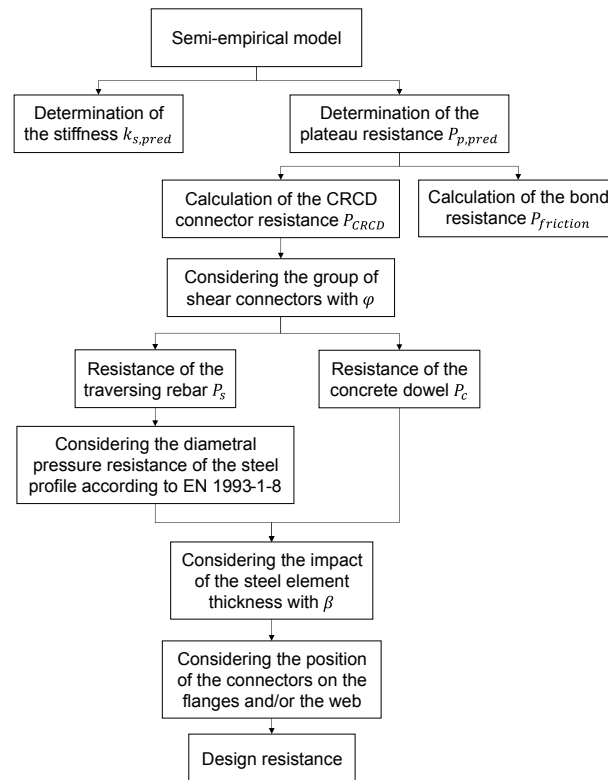


FIGURE 5.2: Procedure to determine the stiffness and the plateau resistance according to the proposed semi-empirical model.

### 5.2.1 Evaluation of the stiffness

The stiffness of the shear-slip curve is determined based on the initial stiffness measured during the push-out tests. In total, 45 experimental tests were analyzed, resulting in 45 corresponding stiffness values. From the literature review (Chrzanowski et al., 2019; Wang et al., 2019; Huang et al., 2021) and the experiments, it is known that adhesion exhibits high stiffness but fails in a brittle manner. The adhesion behavior mainly depends on the concrete strength grade, the interfacial area, and the steel surface conditions.

The stiffness of the shear connectors at 5mm of slip between steel and concrete is significantly lower than that of the adhesion at the initial loading, except for series B2, adhesion bond presents a stiffness  $1.5\times$  to  $5\times$  higher than the shear connectors, see Chapter 3. Hence, the contribution of the shear connectors to the initial stiffness is considered negligible, especially at the initial loading. To verify this assumption, Fig. 5.3 presents the stiffness of all experiments plotted against the number of connectors. If the CRCD connectors are contributing to the initial stiffness, an increase in the stiffness should be observed when we increase the number of connectors. As shown, no clear correlation can be identified.

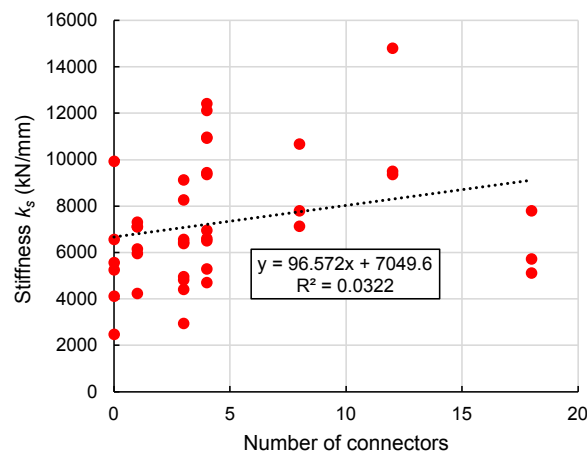


FIGURE 5.3: Variation of stiffness with the number of connectors.

As previously mentioned, adhesion bond is not a reliable shear transfer mechanism, and a large scatter in the results can be observed. In the experimental program, parameters influencing adhesion were kept as constant as possible; therefore, all steel surfaces were sandblasted to ensure comparable interface conditions. Even with this surface treatment, the surface roughness and the presence of potential rust can lead to a high variation in the steel surface quality. The only two parameters that varied across the tests were the concrete strength and the embedded interfacial surface area between steel and concrete, by changing the cross-section and keeping the embedded length constant. It was observed in Chapter 3 that increasing the concrete strength or enlarging the cross-section leads to higher stiffness.

By expressing the stiffness as a function of the product of the concrete compressive strength  $f_c$  and the embedded surface area  $A_b$ , the results can be plotted as shown in Fig. 5.4. Specimens with  $k_s > 15000$  kN/mm were treated as outliers and excluded. This threshold corresponds to twice the mean stiffness of the dataset and results in the removal of four specimens. The data

can be reasonably fitted by a linear trend line with a coefficient of determination of  $R^2 = 0.54$ . An increase in stiffness is observed with increasing concrete compressive strength and embedded surface area. However, this statement is based on a constant embedded length. It is possible that the increase in stiffness is primarily caused by the larger cross-section rather than the greater embedded length. Additional test configurations are needed to clarify this effect.

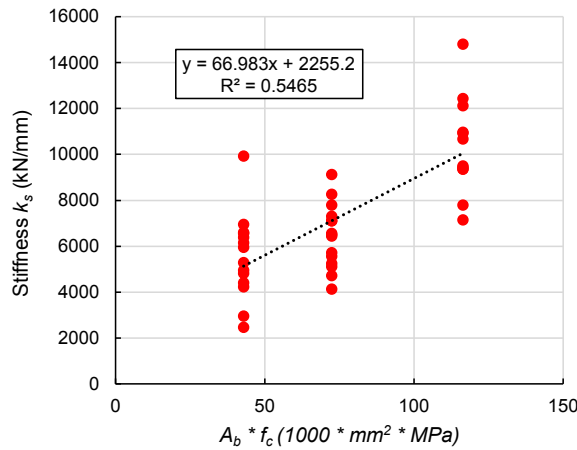


FIGURE 5.4: Variation of the stiffness with the product of the concrete compressive strength and the embedded surface.

A simplified expression to predict the initial stiffness is proposed as follows for an embedded length of 690mm:

$$k_{s,\text{pred}} = 0.07 f_c A_b + 2255 \quad (5.15)$$

where  $A_b$  is the embedded surface area between steel and concrete minus the are of the openings of the shear connectors.

However, this equation does not consider the values for  $A_b f_c$  lower than 43 000 mm<sup>2</sup>MPa. In this situation, with the surface contact falling to zero, the stiffness should be null. To make the equation more general, we introduce Eq. 5.16 given the initial stiffness in N/mm where  $A_b$  is the embedded surface in mm<sup>2</sup> and  $f_c$  is the concrete compressive strength in MPa.

$$k_{s,\text{pred}} = \eta f_c A_b \quad (5.16)$$

Proposed for: HE 200 to HE 360 sections; C50/60–C80/95 concrete; 690 mm embedded length; sandblasted steel surfaces; monotonic push-out loading.

Calibrated against 41 push-out tests described in Chapter 3.

The parameter  $\eta$  will be expressed in 1/mm and will be calibrated to best-fit the slope as the "least squares". Excluding the outliers with  $k_s > 15\,000$  kN/mm, parameter  $\eta$  should be equal to  $0.094 \text{ mm}^{-1}$ .

This equation yields a mean ratio of  $k_{\text{pred}}/k_{\text{exp}} = 0.94$  with a coefficient of variation of 37%, including the outliers. The relatively large scatter is attributed to the inherent variability of adhesion behavior. As this equation is only a preliminary expression, additional tests are required to

calibrate and validate a more reliable formulation. It should therefore be used solely to obtain a rough estimate of the stiffness.

### 5.2.2 Determination of the interfacial friction resistance

From Chrzanowski et al. (2019) and Goralski and Hegger (2006), we know that the friction developed at the interface between steel and concrete depends on many parameters. In this study, we tried to keep the parameters as constant as possible between the different series. Only the concrete compressive strength and the cross-sections of the steel profile have been changed.

The interfacial bond between steel and concrete primarily consists of two components: (1) adhesion, which provides high initial stiffness but is brittle and highly sensitive to slip, and (2) friction, which combines sliding friction and surface roughness friction.

The overall bond behavior is influenced by several parameters, such as the steel surface treatment, concrete compressive strength, interfacial contact area, and confinement conditions (see Chapter 2). Given the unstable and unreliable nature of adhesion, especially under cyclic or high-slip conditions, its peak contribution is excluded from the present analytical model. Therefore, only the frictional component is considered as the shear resistance of the bond.

To compute the shear force provided by the friction, the residual shear strength  $\tau_r$  acting between the steel and concrete surfaces is first evaluated. This frictional resistance arises from two main mechanisms: (1) the surface roughness friction, activated even in the absence of normal stress, and (2) the Coulomb friction, which depends on the normal compressive forces acting at the steel–concrete interface.

The normal forces contributing to the Coulomb friction are primarily generated by the confinement of the reinforcement stirrups and originate from several sources:

- concrete shrinkage, which induces compressive pressure on the steel profile;
- fabrication and loading imperfections, which may introduce additional horizontal forces;
- compressive struts of the shear connectors, apply local pressure on the steel element;
- dilation of the concrete dowel in the connectors, producing perpendicular pressure due to the confinement effect of the stirrups.

Other phenomena, such as the lateral dilation of the concrete dowel due to the displacement of the steel beam into the concrete block, tend to separate the steel–concrete interface, thereby reducing the effective frictional contact, see Fig. 4.3. Shear connectors positioned on the flanges with a limited concrete cover can amplify this separation, further decreasing the frictional contribution at the interface.

These opposing effects—an increase in normal pressure due to dilatancy-induced confinement and CRCD compressive strut action, versus a reduction in contact caused by dilatancy-driven interface opening—are strongly coupled and difficult to isolate experimentally. Accordingly, they are treated as a combined mechanism in this study. For example, increasing the number of connectors amplifies the frictional contribution by raising the compressive stresses associated with connector strut action. In parallel, expansion of the concrete dowel promotes partial opening of

the steel–concrete interface, which offsets part of the frictional gain by reducing effective contact. The same expansion, however, also mobilizes greater active confinement from the stirrups. The resulting response, therefore, reflects a nontrivial balance between friction mobilization and interface separation.

The finite element (FE) model developed in ABAQUS was validated against 33 experimental specimens (series A1, A2, and A3 were used to determine the adhesion parameters, and series B2 was not validated with the FE model). In this model, it was only possible to explicitly represent the Coulomb friction induced by (1) the expansion of the concrete around the connectors and (2) the compressive struts from the connectors, resulting in pressure on the flanges. To account for these effects, the friction coefficient at the steel–concrete interface was numerically calibrated to  $\mu = 0.2$ .

Other factors influencing the interfacial friction, such as fabrication imperfections, concrete shrinkage, and steel surface roughness, could not be modeled directly. To represent their combined influence, an artificial uniform lateral pressure  $p$  of 1.5 MPa was applied to the external surfaces of the concrete in all simulation series. This approach allowed for a more realistic representation of the friction at the steel-concrete interface and ensured better agreement with experimental observations.

Therefore, the contribution from friction was simplified by the Eq. 5.31, where  $\tau_r = \mu p$ , with  $\mu = 0.2$  and  $p = 1.5\text{MPa}$ . This corresponds to a bond strength  $\tau_r = 0.3\text{MPa}$ , similar to the design value given in EN1994-1-1 (2004) for a fully concrete encased steel section. The assumption of a uniform bond strength  $\tau_r$  is consistent with approaches adopted in previous studies (Chrzanowski et al., 2019; Roeder, 1985). They have shown that, despite the inherently non-uniform nature of bond stresses along the embedded length, the use of an equivalent uniform bond stress provides a reasonable approximation of the average transfer mechanism between steel and concrete.

$$P_{friction} = \tau_r A_b \quad (5.17)$$

where  $\tau_r = 0.3$  for sandblasted steel surface Sa 2<sup>1/2</sup> and  $A_b$  is the area of the H-shaped steel section embedded in the concrete minus the area of the openings for the shear connectors.

### 5.2.3 Calculation of the resistance of CRCD connectors

The ultimate shear resistance of a single CRCD connector,  $P_{CRCD,1}$ , is usually expressed in the literature as the sum of the contributions from the concrete dowel,  $P_{c,1}$ , and the traversing rebar,  $P_{s,1}$ :

$$P_{CRCD,1} = P_{c,1} + P_{s,1} \quad (5.18)$$

#### Considering the group of shear connectors

Shear connectors are never used alone, and a group of connectors is generally required. In this situation, it will be necessary to account for the number of connectors positioned on the web,

$n_w$ , and on the flanges,  $n_f$ . The geometry of the shear connectors on the web and flanges can be different, thus it is required to consider these differences in Eq. 5.19.

$$P_{CRCD,exp} \approx P_{CRCD,n} = n_w(P_{c,w} + P_{s,w}) + n_f(P_{c,f} + P_{s,f}) \quad (5.19)$$

where  $P_{CRCD,exp}$  is the experimental resistance of the group of  $n$  connectors and  $P_{CRCD,n}$  is the approximation resistance of the CRCD group.

As demonstrated experimentally by Tan, Fang, and Xiong (2022), the shear resistance of a group of CRCD connectors is systematically lower than the sum of the resistances of the individual connectors. Their results showed that the reduction of the individual shear strength within a group follows a decreasing trend that depends on the number of connectors. This behavior is also observed in the push-out tests conducted in the present study.

To quantify this reduction, we introduce the parameter  $\varphi$ , defined as the ratio between the shear resistance of one connector within a group and the shear resistance of an individual connector (Eq. 5.20). Thus,  $\varphi = 1$  corresponds to no loss of strength, while  $\varphi < 1$  indicates a reduction due to group effects.

$$\varphi = \frac{P_{CRCD,n}/n}{P_{CRCD,1}} \quad (5.20)$$

To evaluate the evolution of  $\varphi$  as a function of the number of connectors  $n$ , we selected all specimens sharing the same connector geometry (40 mm opening diameter and 12 mm traversing rebar) and the same steel profile (HEB200). These include series B1 to C5 and F2, covering two concrete compressive strengths and configurations with 1, 3, 4, and 18 connectors. Table 5.2 reports the selected specimens together with the group and individual connector resistances.

To isolate only the contribution of the CRCD connectors, the results of the calibrated FE model were used to remove the effects of adhesion and friction. For the configuration with 18 connectors with normal-strength concrete, no test was performed; therefore, its value stems solely from the FE model. Series B1 and B2, each containing a single connector, were used as reference values for computing  $\varphi$ .

TABLE 5.2: Specimen considered to evaluation the parameter  $\varphi$ .

Series	Concrete strength	$n$	$P_{CRCD,n}$	$P_{CRCD,n}/n$	$\varphi$
B1	C50/60	1	173	173	1
C2	C50/60	3	474	158	0.91
C4	C50/60	4	640	160	0.92
F2bis <sup>1</sup>	C50/60	18	2492	138	0.80
B2	C80/95	1	191	191	1
C3	C80/95	3	554	185	0.97
C4	C80/95	4	728	182	0.95
F2	C80/95	18	2619	145	0.76

<sup>1</sup>This series was not calibrated from a dedicated experiment.

Based on these data (Table 5.2), Figure 5.5 shows the evolution of  $\varphi$  with the total number of connectors  $n = n_f + n_w$ . The reduction follows a smooth decreasing trend that is well approximated by a logarithmic relationship (Eq. 5.21), with a coefficient of determination  $R^2 = 0.90$ .

$$\varphi = 1.0179 - 0.077 \ln(n_f + n_w) \quad (5.21)$$

This logarithmic evolution highlights that the largest loss in individual shear resistance occurs when increasing the number of connectors from 1 to approximately 5 (up to about 10% reduction). Beyond this point, adding more connectors leads to additional loss of resistance, but at a significantly slower rate. For example, increasing from 5 to 18 connectors produces a reduction of similar magnitude (also about 10%), indicating that the group effect tends to stabilize for large connector numbers, supported by Tan, Fang, and Xiong (2022).

To enforce the physically intuitive condition  $\varphi = 1$  when only one connector is present ( $n = 1$ ) since  $\ln(1) = 0$ , Eq. 5.21 can be rewritten as:

$$\varphi = 1 - 0.077 \ln(n_f + n_w) \quad (5.22)$$

This modified form preserves the fitted curve while ensuring the correct behaviour for  $n = 1$ .

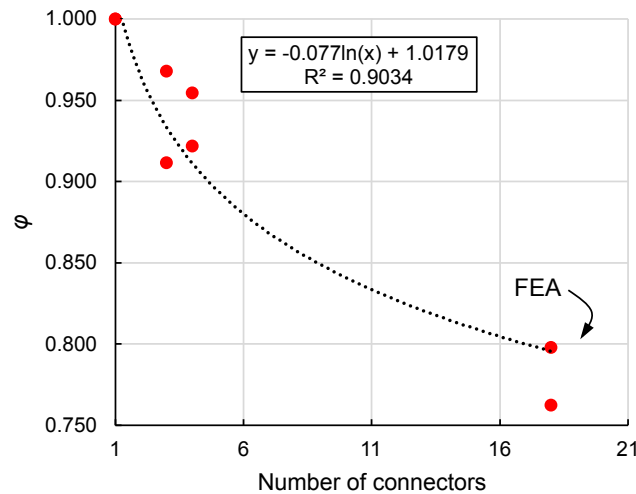


FIGURE 5.5: Coefficient  $\varphi$  in function of the number of connectors

### Determining the strength components

The traversing rebar within the web opening experiences a combination of tension, bending, and shear, ultimately failing in shear. Its contribution to the connection's load-bearing capacity can be expressed as (He et al., 2016; Braun, 2018):

$$P_{s,1} = 2 \frac{f_s}{\sqrt{3}} A_s \quad (5.23)$$

where  $A_s = \pi d_s^2 / 4$  is the cross-sectional area of the traversing rebar, multiplied by 2 to account for the two sheared sections on either side of the web, and  $f_s$  is the yield strength of the traversing rebar.

The contribution of the concrete dowel is more complex to characterize. During the push-out test, the infill concrete within the web opening is sheared early on both edges of the steel element, typically before a slip of 3 mm, while the ultimate resistance of the CRCD connector is reached at approximately 10 mm of slip for series B1 to C5. As a result, it cannot be assumed that the resistance of the CRCD connector is simply the sum of the resistances of the concrete dowel and the traversing rebar, see Fig. 5.6. At ultimate load, the infill concrete between the rebar and the web is crushed and highly confined. This crushed concrete and the traversing rebar interact in a composite manner, working together to provide the ultimate resistance of the CRCD connector.

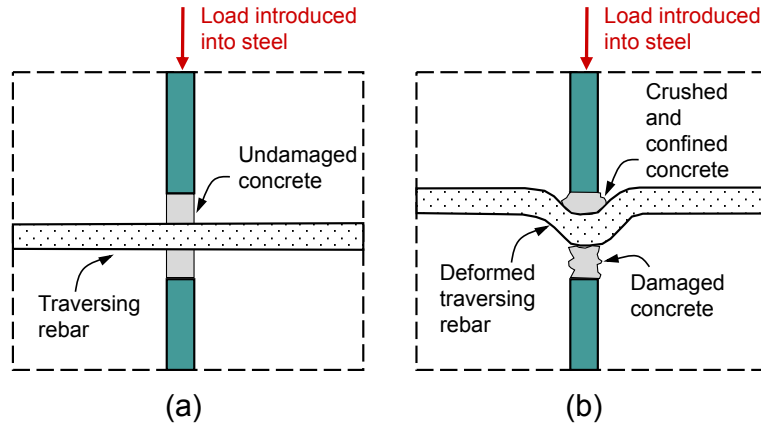


FIGURE 5.6: Representation of the resisting components in a CRCD connector: (a) undeformed situation stated in an additive model; (b) real situation stated in a composite model.

To simplify the empirical model, we assume that the concrete contribution is equal to the difference between the composite resistance of the concrete dowel and traversing rebar (determined experimentally), minus the resistance of the traversing rebar alone (determined analytically). This relationship is expressed in the following equation:

$$P_{c,1} = P_{CRCD,1} - P_{s,1} = \frac{P_{CRCD,n}}{n \varphi} - P_{s,1} \quad (5.24)$$

Experimental results for CRCD connectors placed on the web of HEB200 profiles (series B1 to C5) show that a 61% increase in concrete compressive strength leads to only a 2–12% increase in shear capacity. This suggests a different failure mode between normal- and high-strength concrete. In normal-strength concrete, the traversing rebar experienced important bending deformation, failing in a combined tension-bending-shear failure, while in high-strength concrete, the rebar cannot deform sufficiently to crush the concrete, leading to failure primarily in tension-shear. To reflect this reduced concrete contribution, an effective concrete strength is introduced through a reduction coefficient  $\alpha$ . The concrete dowel resistance is then expressed as

$$P_{c,1} = \frac{P_{CRCD,n}}{n \varphi} - P_{s,1} = \frac{A_c f_c}{\alpha} \quad (5.25)$$

$$\alpha = \frac{A_c f_c}{\frac{P_{CRCD,n}}{n \varphi} - P_{s,1}} \quad (5.26)$$

where

$$A_c = \frac{\pi}{4} (d_c^2 - d_s^2)$$

To establish the evolution of the parameter  $\alpha$ , we selected all experimental specimens sharing the same connector geometry (steel element thickness of 9 mm, opening diameter of 40 mm, and traversing rebar of 12 mm) and the same steel profile (HEB 200). These correspond to series B1 to C5, covering two concrete compressive strengths and configurations with 1, 3, and 4 connectors.

To isolate only the contribution of the CRCD connectors, the calibrated FE model was used to remove the effects of adhesion and friction from the measured resistances. The resulting values of  $\alpha$  are plotted in Figure 5.7 as a function of  $f_c$ . A linear regression fitted to these data yields

$$\alpha = 0.0054 f_c + 0.3085, \quad R^2 = 0.89$$

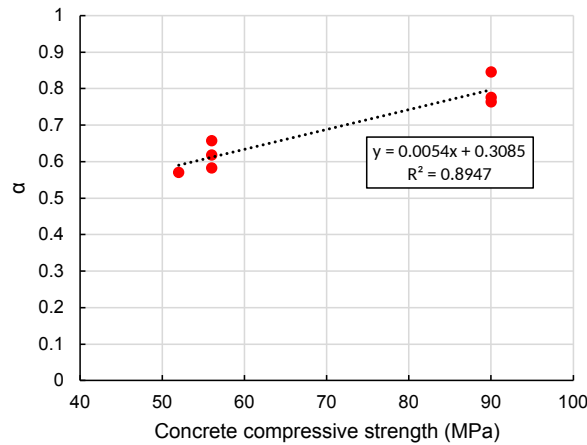


FIGURE 5.7: Coefficient  $\alpha$  as a function of the concrete compressive strength.

Finally, combining the contributions of the concrete dowel and the rebar shear resistance gives the expression for the capacity of a group of CRCD connectors:

$$P_{CRCD,n} = n \varphi (P_{c,1} + P_{s,1}) = (n_f + n_w) \varphi \left( \frac{A_c f_c}{\alpha} + 2 \frac{f_s}{\sqrt{3}} A_s \right) \quad (5.27)$$

with

$$\varphi = 1 - 0.077 \ln(n_f + n_w), \quad \alpha = 0.0054 f_c + 0.3085$$

### Considering the resistance of the steel profile

It has been noticed, in the experiments with a large traversing rebar (20mm) and a thin steel thickness (10mm), that the steel web was experiencing significant plastic deformation. This phenomenon is similar to the diametral pressure failure of steel plates in bolted connections.

To consider this limitation, we will include the worst-case scenario where the traversing rebar would be positioned at the top of the opening and directly in contact with the steel profile. In this situation, according to EN1993-1-8 (2005), the resistance  $P_{s,1}$  should be the minimum of the

resistance of the traversing rebar in shear and the resistance of the plate to diametral pressure (Eq. 5.28).

$$P_{s,1} = \min \left\{ \begin{array}{l} 2 \frac{f_s}{\sqrt{3}} A_s \\ k_1 \alpha_b f_u d t \end{array} \right\} \quad (5.28)$$

with  $\alpha_b$  and  $k_1$  defined in EN1993-1-8 (2005).

### Adding the impact of the steel element thickness

It has been demonstrated in both the literature review and the parametric study that the thickness of the steel element significantly influences the shear strength of the connector.

For a constant opening diameter, when using a relatively small traversing rebar (12 mm or 16 mm), a larger steel thickness (15 mm or 20 mm) provides stronger concrete confinement, resulting in a more resistant concrete dowel, see Fig. 5.8a. In this case, the rebar struggles to damage the concrete dowel and primarily fails through a tension–shear rupture. Conversely, for smaller steel thicknesses (9 mm or 10 mm), the rebar can more easily damage the concrete dowel and undergoes greater deformation, leading to a bending–tension–shear rupture (Fig. 5.8b), which typically results in a higher slip capacity and shear strength.

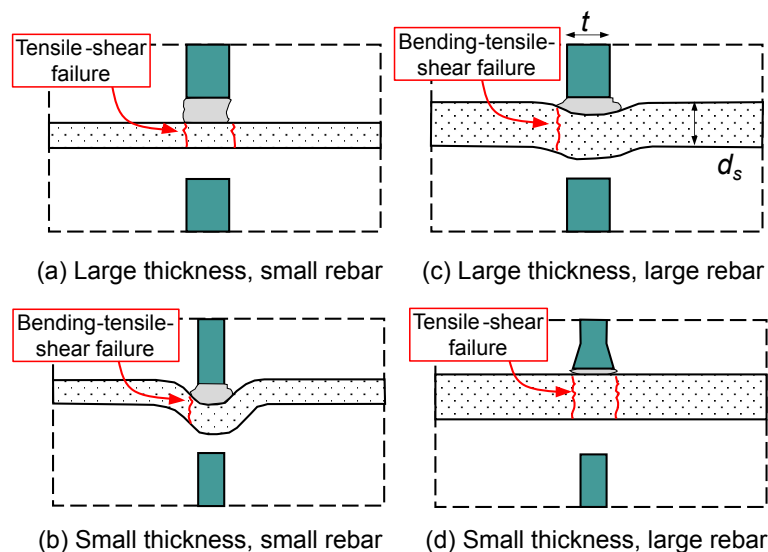


FIGURE 5.8: Impact of the thickness of the steel element and the traversing rebar on the failure mode.

However, this behavior changes for larger traversing rebars (20 mm). With smaller steel thicknesses (9 mm or 10 mm), the shear strength of the rebar exceeds that of the concrete dowel, causing the rebar to crush the concrete with minimal deformation before failing in a tension–shear rupture (Fig. 5.8d), potentially accompanied by significant yielding of the steel element. In contrast, with larger steel thicknesses (15 mm or 20 mm), both the concrete dowel and steel element have sufficient resistance compared to the rebar’s shear strength. The rebar progressively damages the confined concrete until the confinement is so great that the rebar deforms, ultimately failing in a bending–tension–shear rupture, as shown in Fig. 5.8c.

These observations indicate that the relationship between the ratio of the traversing rebar diameter to the steel-element thickness and the shear strength of CRCD connectors is inherently non-linear. This relation exhibits two minima: one at low ratios  $d_s/t$ , where small rebar crosses relatively thick steel, and another at high ratios  $d_s/t$ , where large rebar passes through thin steel. Between these two extremes lies a maximum corresponding to the most favorable failure mechanism—namely, bending–tension–shear failure of the traversing rebar—which occurs when either a small rebar is combined with a small steel thickness element or a large rebar with a large steel thickness element.

To capture this behavior, we introduce a coefficient  $\beta$ , applied to  $P_{CRCD,n}$ , to obtain an improved approximation of the experimental resistance  $P_{CRCD,exp}$  according to:

$$P_{CRCD,exp} \approx P_{CRCD,n,2} = \beta P_{CRCD,n}, \quad (5.29)$$

where  $P_{CRCD,n,2}$  denotes the refined prediction of the connector resistance.

To quantify the influence of the steel element thickness, all results from the FE analyses performed in this study (38 configurations in total) were considered, see Table B.1. Based on the previous observations, the function  $\beta$  is expected to follow a parabolic trend,  $\beta = ax^2 + bx + c$ , with  $a < 0$ , where  $x$  is a function of  $d_s/t$ . To determine  $\beta$ , Eq. 5.29 is reformulated in terms of the ratio  $\sqrt{d_s/t}$ :

$$\frac{P_{CRCD,n,2}}{P_{CRCD,n} \sqrt{d_s/t}} = \frac{\beta}{\sqrt{d_s/t}} = f\left(\sqrt{d_s/t}\right). \quad (5.30)$$

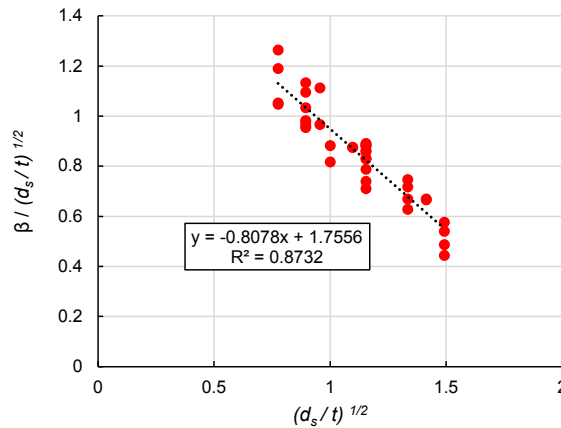


FIGURE 5.9: Ratio  $\beta / \sqrt{d_s/t}$  in function of the ratio  $\sqrt{d_s/t}$ .

Figure 5.9, derived from Eq. 5.30, shows a clear linear correlation between  $\beta / \sqrt{d_s/t}$  and  $\sqrt{d_s/t}$ , with a coefficient of determination  $R^2 = 0.87$ . Consequently,  $\beta$  may be expressed by the following second-order relationship:

$$\begin{aligned} \frac{\beta}{\sqrt{d_s/t}} &= 1.7556 - 0.8078 \sqrt{d_s/t}, \\ \beta &= 1.7556 \sqrt{d_s/t} - 0.8078 \frac{d_s}{t}. \end{aligned} \quad (5.31)$$

Using the definition of  $\beta$ , the improved prediction of the shear resistance of CRCD connectors becomes:

$$P_{CRCD,n,2} = P_{CRCD,n} \left( 1.7556 \sqrt{d_s/t} - 0.8078 \frac{d_s}{t} \right). \quad (5.32)$$

In some experimental configurations, connectors were placed on both the web and the flanges. Because hot-rolled H-sections have different thicknesses in these regions, their corresponding failure mechanisms also differ. Since the flanges are thicker than the web, the governing failure mode for combined configurations (web + flanges) was generally dictated by the CRCD connectors installed in the flanges. As a result, the web connectors did not reach their full shear capacity, limiting the overall response. To account for this effect, the parameter  $\beta$  is taken as the minimum of  $\sqrt{d_{sw}/t_w}$  and  $\sqrt{d_{sf}/t_f}$ .

### Considering shear connectors on the web and the flanges

The previous developments hold when the shear connectors have identical geometries in terms of traversing rebar, opening diameter, and thickness of the steel element. However, hot-rolled H-shaped steel profiles generally have different thicknesses in the web and the flanges. When CRCD connectors are installed on both components, their geometric parameters may therefore differ. It is also possible to use different numbers of shear connectors on the web and on the flanges. Equation 5.33 accounts for these differences by separating the contribution of connectors placed on the web and on the flanges.

$$P_{CRCD,n,2} = \varphi \beta (n_w P_{CRCD,1,w} + n_f P_{CRCD,1,f}) \quad (5.33)$$

Introducing the detailed expressions of the shear connectors' capacities leads to Eq. 5.34:

$$P_{CRCD,n,2} = \varphi \beta (n_w (P_{c,1,w} + P_{s,1,w}) + n_f (P_{c,1,f} + P_{s,1,f})) \quad (5.34)$$

with

$$\begin{aligned} P_{c,1,w} &= \frac{A_{c,w} f_c}{\alpha}, \\ P_{s,1,w} &= \min(1.155 A_{s,w} f_{s,w}; k_1 \alpha_b f_u d_{s,w} t_w), \\ P_{c,1,f} &= \frac{A_{c,f} f_c}{\alpha}, \\ P_{s,1,f} &= \min(1.155 A_{s,f} f_{s,f}; k_1 \alpha_b f_u d_{s,f} t_f), \\ \varphi &= 1 - 0.077 \ln(n_w + n_f), \\ \beta &= 1.7556 \sqrt{d_s/t} - 0.8078 (d_s/t), \\ d_s/t &= \min\left(\frac{d_{s,w}}{t_w}, \frac{d_{s,f}}{t_f}\right), \\ \alpha &= 0.0054 f_c + 0.3085. \end{aligned} \quad (5.35)$$

The performance of Eq. 5.34 for predicting the resistance of multiple shear connectors placed on the web and/or the flanges was evaluated against the numerical results of 38 configurations developed for the parametric study, see Annex B.1. Figure 5.10 compares the predicted resistances with the FE results, excluding bond contribution. The dotted line represents the regression fit of the predictions against the FE results ( $R^2 = 0.98$ ), while the solid line denotes the 1:1 reference. The fitted line is nearly indistinguishable from the diagonal, and the high coefficient of determination confirms the strong predictive performance of the proposed analytical model. The average ratio  $P_{CRCD,pred}/P_{CRCD,FEA} = 0.94$  with a coefficient of variation of 7%.

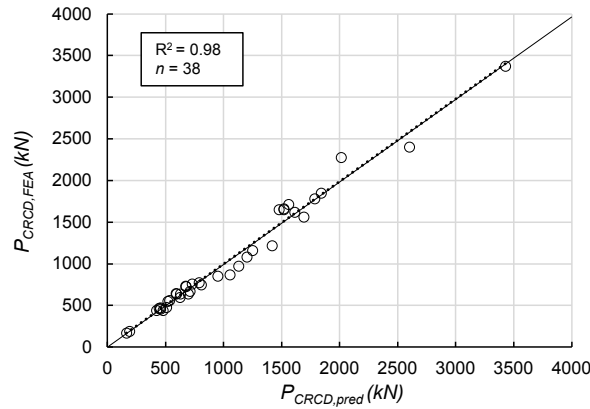


FIGURE 5.10: Comparison of the shear resistance prediction for CRCD connectors with the results from FEA.

#### 5.2.4 Prediction of the resistance for CRCD connectors combined with friction

The ultimate shear resistance of a group of CRCD connectors, considering the friction resistance between steel and concrete, can be determined by the combination of Eq. 5.31 and 5.34 to produce Eq. 5.36.

$$\begin{aligned} P_p &= P_{friction} + P_{CRCD,n,2} \\ &= \tau_r A_b + \varphi \beta (n_w (P_{c,1,w} + P_{s,1,w}) + n_f (P_{c,1,f} + P_{s,1,f})), \end{aligned} \quad (5.36)$$

with  $\tau_r = 0.3$  for sandblasted steel surface.

Valid for: HE 200 to HE 360 sections; C50/60–C80/95 concrete;  $d_c = 40\text{--}60$  mm;  $d_s = 12\text{--}20$  mm; 690 mm embedded length; sandblasted steel surfaces; monotonic push-out loading.

Calibrated against 36 push-out tests described in Chapter 3.

Fig. 5.11 summarizes the results from the developed equation, combining the resistance of the CRCD connectors with the friction, compared to the experimental results for each specimen (36 experiments). The resistance of the experiments was measured at the plateau load (before the failure of the shear connectors). The predictions are on the  $x$ -axis and the test results on the  $y$ -axis; the diagonal line represents a perfect prediction of the test result. The average ratio  $P_{p,pred}/P_{p,exp} = 0.98$  with a coefficient of variation of 12%.

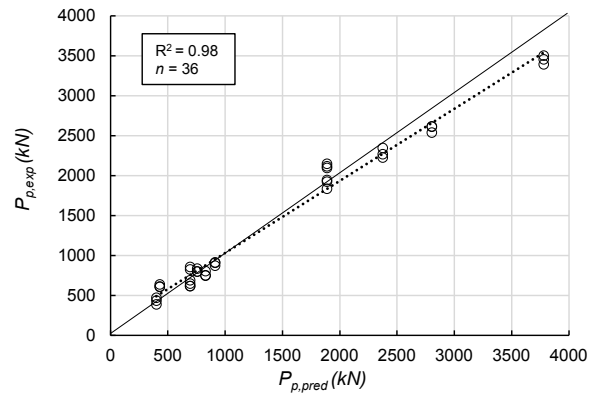


FIGURE 5.11: Comparison of the shear resistance prediction, for CRC connectors combined with the bond, with the results from experiments.

Fig. 5.12 compares the results from the developed semi-empirical model to the experimental results and the mean of the series. The resistance of the plateau is based on the Eq. 5.36 and the initial stiffness is based on the Eq. 5.16. Annex B.2 compares the performance of the prediction equations to the experiment results for the plateau resistance and the stiffness.

As expected, Eq. 5.36 does not perform well for series B2. Since the equation was calibrated using the finite element model—and the FE model did not accurately capture the behaviour of series B2 (see Chapter 3)—the resulting prediction equation is unable to reproduce the experimental response of this series. When series B2 is excluded, however, the semi-empirical model predicts the resistance of the shear connectors combined with friction with a mean error of approximately 7% relative to the experimental results. For the stiffness prediction, the average deviation between the model and the experimental values across the 45 tests is about 20%.

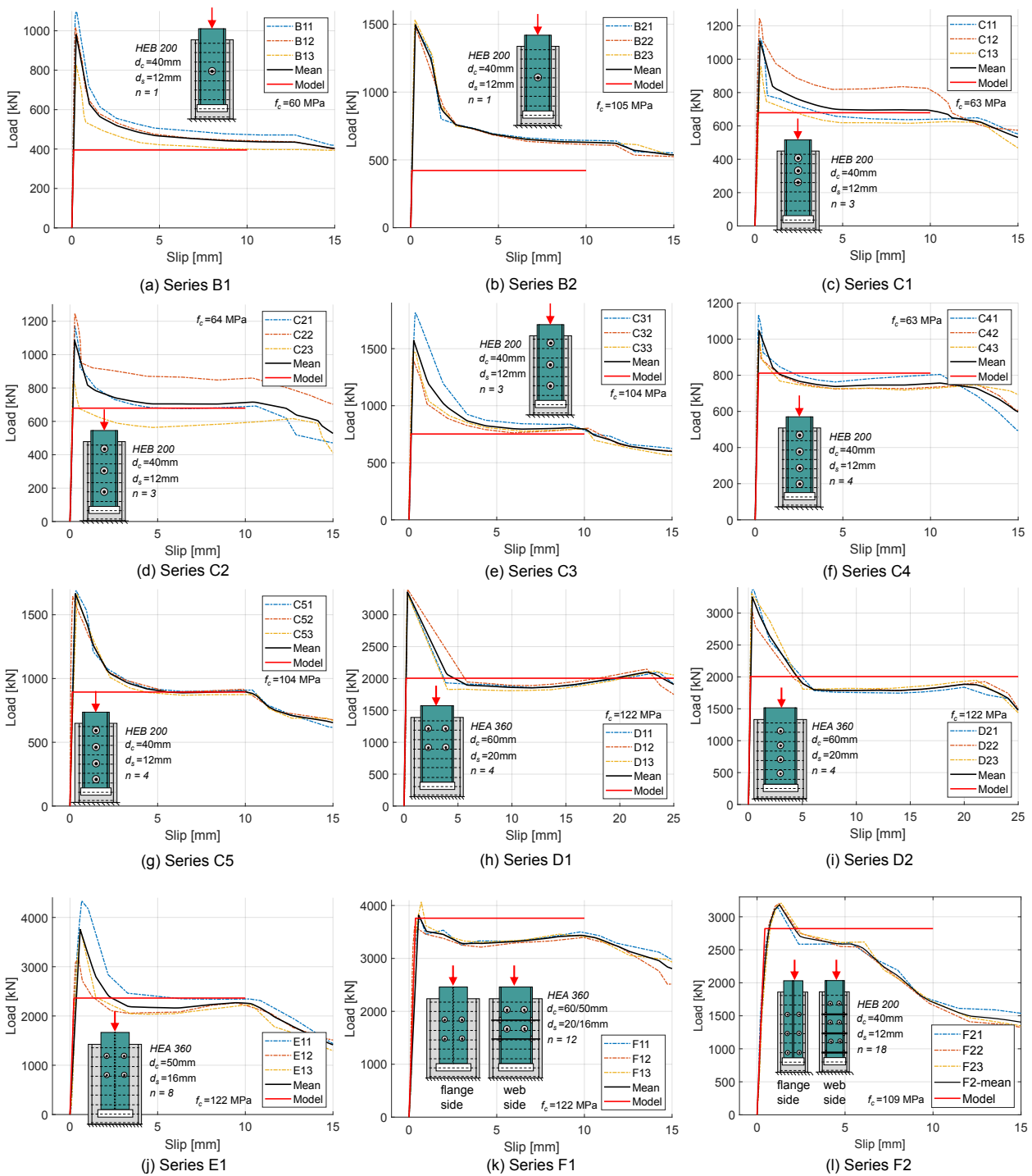


FIGURE 5.12: Comparison of the developed semi-empirical model with the experimental results.

### 5.2.5 Prediction of the slip capacity of the shear connectors

One of the main advantages of CRCD connectors is that their slip capacity can be designed. Depending on the configuration, both the concrete and steel sections can be optimized for the global behavior of the composite column. In particular, the opening size and the traversing reinforcement diameter have a significant influence on the slip capacity of the connection. The designer

can therefore adjust these parameters to obtain the level of ductility required for the structural scenario. Moreover, the geometry of the connectors can be adapted depending on their position on the web and the flanges, so they achieve the same slip capacity related to the different thicknesses of the steel element.

Based on the parametric study from Chapter 4, several qualitative trends can be identified:

1. Increasing the concrete compressive strength reduces the slip capacity because the reinforcing bar does not have sufficient strength to damage a denser concrete matrix.
2. Increasing the thickness of the steel element also reduces the slip capacity. A thicker steel plate creates a more confined concrete dowel, again limiting the ability of the rebar to damage the concrete.
3. Increasing the distance between the rebar and the steel element, *i.e.*, increasing the infill concrete thickness ( $d_c - d_s$ ), increases the slip capacity because a larger concrete volume can be progressively damaged.
4. Increasing the rebar diameter increases the slip capacity because a larger bar has greater strength to induce damage in the concrete and reduces its volume.

These observations lead to the development of a relationship linking the slip capacity  $s$  to the governing parameters, expressed in Eq. 5.37:

$$s \propto \frac{(d_c - d_s) d_s}{f_c t} \quad (5.37)$$

Considering that the flanges and the web have different thicknesses, when shear connectors are placed on both the web and the flange, the ductility of the connection is governed by the connector that fails first. Consequently, the governing ratio is the minimum of  $(d_{c,w} - d_{s,w}) d_{s,w} / (f_c t_w)$  and  $(d_{c,f} - d_{s,f}) d_{s,f} / (f_c t_f)$ .

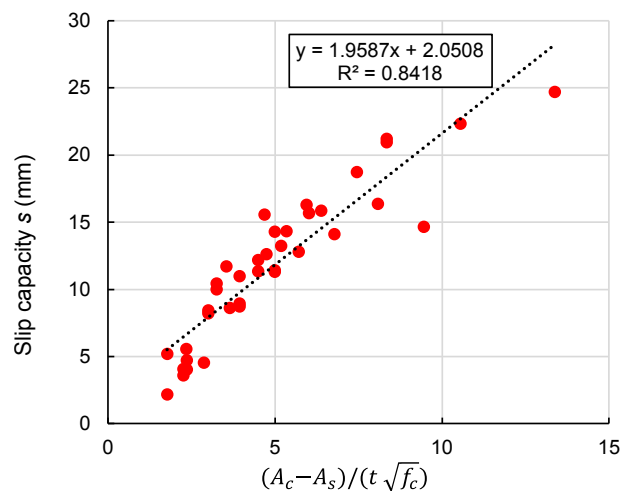


FIGURE 5.13: Evaluation of the slip capacity  $s$  with the geometrical parameters of the CRCD connectors.

Using all available FE specimens from Table B.1, the data were plotted to evaluate the validity of this relationship (Fig. 5.13). After several iterations, it became apparent that a more accurate

formulation involves the square root of the concrete compressive strength rather than the strength itself. Ultimately, we obtained the following predictive equation for the slip capacity  $s_{pred}$  in mm, which shows a strong correlation with the numerical results ( $R^2 = 0.84$ ):

$$s_{pred} = 1.96 \frac{(d_c - d_s) d_s}{\sqrt{f_c} t} + 2 \quad (5.38)$$

Proposed for: HE 200 to HE 360 sections; C50/60–C80/95 concrete;  $d_c = 40$ – $65$  mm;  $d_s = 12$ – $20$  mm;  $t_w = 9$ – $20$  mm;  $t_f = 10$ – $20$  mm; 690 mm embedded length; sandblasted steel surfaces; monotonic push-out loading.

Calibrated against 38 numerical simulations described in Chapter 4.

The average ratio of  $s_{pred}/s_{FEA} = 1.09$  with a coefficient of variation of 32%.

This equation is derived under the assumptions that the traversing rebars are located at the center of their respective openings and are sufficiently anchored in the concrete to avoid slip at the interface between the rebar and surrounding concrete. It is a preliminary expression to estimate the ductility of the connectors, established solely based on FE simulations. Additional experimental tests are required to calibrate and validate a more reliable formulation. For now, the equation should be used primarily to design the geometry of connectors placed on the web and on the flange, ensuring they achieve approximately the same slip capacity.

### 5.3 Statistical evaluation of the proposed semi-empirical model

In the semi-empirical model, two equations have been developed to predict the ultimate resistance of the shear connectors combined with the friction at the steel-concrete surface and estimate the stiffness. Eq. 5.36 predicted the resistance of the CRCD connectors and the friction with good accuracy, but were distributed around the diagonal line; the estimations did not perfectly match the test results. Eq. 5.16 gives an estimation of the stiffness with quite low accuracy, mainly due to the variability of the adhesion behaviors. Therefore, a statistical evaluation of both equations was performed based on the procedure defined in EN1990 (2002) Annex D to establish partial safety factors for the utilization of Eq. 5.39 and 5.40.

$$r_{t,p} = \tau_r A_b + \varphi \beta (n_w (P_{c,1,w} + P_{s,1,w}) + n_f (P_{c,1,f} + P_{s,1,f})) \quad (5.39)$$

$$r_{t,k_s} = 0.094 f_c A_b \quad (5.40)$$

The database consists of 45 push-out tests, where 36 have CRCD shear connectors, and three identical tests have been realized for each configuration. Table 5.3 summarizes the minimum and maximum values of the basic variables.

TABLE 5.3: Limits of the basic variables  $X_i$  in the representative test database.

Property	Min	Max
(Nominal) diameter of the traversing rebar in the web $d_{s,w}$ (mm)	12	20
(Nominal) diameter of the traversing rebar in the flange $d_{s,f}$ (mm)	12	16
(Nominal) diameter of the opening in the web $d_{c,w}$ (mm)	40	60
(Nominal) diameter of the opening in the web $d_{c,f}$ (mm)	40	50
(Nominal) thickness of the web $t_w$ (mm)	9	10
(Nominal) thickness of the flange $t_f$ (mm)	15	17.5
(Nominal) surface contact between steel and concrete $A_b$ (m <sup>2</sup> )	0.794	1.265
Mean compressive cylinder strength of concrete $f_{cm}$ (MPa)	54	91
Mean yield tensile resistance of traversing rebar in the web $f_{sm,w}$ (MPa)	535	561
Mean yield tensile resistance of traversing rebar in the flange $f_{sm,f}$ (MPa)	535	506
Mean ultimate tensile resistance of steel profile $f_{um}$ (MPa)	532	588

### 5.3.1 Design assisted by testing for calibrating the shear resistance of the connectors combined with friction

In this section, we will first apply the procedure from EN1990 (2002) Annex D to evaluate Eq. 5.39 to predict the shear resistance of the CRCDC connectors with the bond at the steel-concrete interface. Based on the predicted resistance function, we will be able to determine the characteristic and design resistance equations and the partial safety factor to be considered.

According to EN1990 (2002) Annex D, the coefficient of variation (CoV) of the basic variables of the resistance function (Eq. 5.39) is required to be defined based on the prior knowledge to perform the statistical evaluation. It is a fact that there is a lack of information for the statistical parameters of the basic variables. In other words, the probabilistic distribution and the related statistical parameters, *i.e.* the mean values and coefficient of variations, of the concrete compressive strength ( $f_{cm}$ ), the mean yield tensile strength of the traversing rebars in the flanges and the web ( $f_{sm,f}$  and  $f_{sm,w}$ ), the mean ultimate tensile resistance of the steel profile ( $f_{um}$ ), the rebar diameters ( $d_{s,f}$  and  $d_{s,w}$ ), the openings in the steel web and flanges ( $d_{c,f}$  and  $d_{c,w}$ ), the thickness of the web and flanges ( $t_{c,f}$  and  $t_{c,w}$ ), the contact surface between the concrete and the steel ( $A_b$ ) are not known.

Therefore, the statistical parameters of the basic variables are estimated based on the available information and according to the relevant literature. Table 5.4 presents the basic variables and their statistical parameters for the evaluation of Eq. 5.39.

TABLE 5.4: Mean values and coefficient of variation of the basic variables  $X_i$ .

Basic variables $X_i$	Mean value $X_m$	Coefficient of variation $V_X$	Reference
$f_c$ (MPa)	54; 91	$8/1.64 f_{cm}$	EN1992-1-1 (2023)
$f_{s,w}$ (MPa)	535; 561	0.045	EN1992-1-1 (2023)
$f_{s,f}$ (MPa)	535; 506	0.045	EN1992-1-1 (2023)
$f_u$ (MPa)	532; 588; 594	0.04; 0.035; 0.035	FprEN1993-1-1 (2022)
$d_{c,w}$ (mm)	40; 60	0.0046; 0.003	ISO9013 (1993)
$d_{c,f}$ (mm)	40; 50	0.0061; 0.0055	ISO9013 (1993)
$d_{s,w}$ (mm)	12; 20	0.018; 0.018	EN10080 (2005)
$d_{s,f}$ (mm)	12; 16	0.018; 0.018	EN10080 (2005)
$t_w$ (mm)	9; 10	0.0474; 0.061	EN10034 (1993)
$t_f$ (mm)	15.5; 18	0.0787; 0.0678	EN10034 (1993)
$A_b$ (m <sup>2</sup> )	0.794; 1.276	0.0177; 0.018	EN10034 (1993)

EN1990 (2002) Annex D, proposes a systematic framework for deriving a design resistance based on the statistical comparison between a theoretical resistance model and an experimental database. The overall procedure may be summarized as follows. The results of the reliability analysis are presented in Fig. 5.14, and the values of the parameters from the analysis are detailed in Annex B.3.

### 1. Formulation of the theoretical resistance

The model prediction for the resistance, denoted by  $r_t$ , is expressed through an analytical function  $g_{rt}(\underline{X})$ , where the vector  $\underline{X}$  includes all governing mechanical and geometric variables:

$$r_t(\underline{X}) = g_{rt}(\underline{X}). \quad (5.41)$$

### 2. Comparison between experimental and predicted values

To evaluate the adequacy of the model, the theoretical values  $g_{rt}(\underline{X})$  (evaluated using mean input parameters) are compared against the corresponding experimental resistances  $r_e$ . Table 5.4 lists the mean values and coefficients of variation adopted for the basic variables.

A first indicator of model suitability is the correlation coefficient  $\rho$  given by

$$\rho = \frac{\sum_{i=1}^n r_{e,i} r_{t,i} - n \bar{r}_e \bar{r}_t}{(n-1) \sigma_{r_e} \sigma_{r_t}}, \quad (5.42)$$

where

$$\begin{aligned} \bar{r}_e &= \frac{1}{n} \sum_{i=1}^n r_{e,i}, & \sigma_{r_e} &= \frac{1}{n-1} \left( \sum_{i=1}^n r_{e,i}^2 - n \bar{r}_e^2 \right), \\ \bar{r}_t &= \frac{1}{n} \sum_{i=1}^n r_{t,i}, & \sigma_{r_t} &= \frac{1}{n-1} \left( \sum_{i=1}^n r_{t,i}^2 - n \bar{r}_t^2 \right). \end{aligned} \quad (5.43)$$

In the present study, a value of  $\rho = 0.99$  is obtained, indicating an almost perfect linear association for the 36 considered results.

### 3. Determination of the mean correction factor $b$

The resistance model is considered to follow

$$r = b r_t \delta, \quad (5.44)$$

where  $\delta$  represents the model error. The factor  $b$  is first estimated through the least-squares slope:

$$b_{LS} = \frac{\sum_{i=1}^n r_{e,i} r_{t,i}}{\sum_{i=1}^n r_{t,i}^2} = 0.96. \quad (5.45)$$

### 4. Estimation of the variability of the model error $V_\delta$

For each test  $i$  the error term is computed as

$$\delta_i = \frac{r_{e,i}}{b r_{t,i}}. \quad (5.46)$$

Since  $\delta_i$  is assumed lognormally distributed, the transformation  $\Delta_i = \ln \delta_i$  is introduced. The sample variance of  $\Delta$  is then obtained as

$$s_\Delta^2 = \frac{1}{n-1} \sum_{i=1}^n (\Delta_i - \bar{\Delta})^2 = 0.0184, \quad (5.47)$$

leading to the coefficient of variation

$$V_\delta^2 = e^{s_\Delta^2} - 1 = 0.0187. \quad (5.48)$$

### 5. Variability of the basic variables $V_{X_i}$

Due to the limited statistical information in the push-out test database, the coefficients of variation  $V_{X_i}$  of the basic variables were taken from prior studies and scientific literature (see Table 5.4). Following EN1990 (2002), all basic variables are assumed to be normally distributed.

### 6. Characteristic resistance $r_k$

If  $V_\delta$  and  $V_{X_i}$  are sufficiently small, the coefficient of variation of the resistance function  $V_r$  can be approximated as

$$V_r^2 = V_\delta^2 + V_{rt}^2 = 0.0187 + 0.001 = 0.0196. \quad (5.49)$$

Here,  $V_{rt}$  denotes the coefficient of variation of the theoretical resistance  $r_t$ , arising from uncertainties in the basic variables  $X$ . Because the resistance function is nonlinear,  $V_{rt}$  was estimated by randomly sampling values of the basic variables according to the probability distributions given in Table 5.4.

This computational method is known as *Monte-Carlo simulations*. For each experimental configuration (12 in total), a Monte-Carlo simulation was realized by randomly varying the 11 parameters. For each configuration, a coefficient of variation was obtained. The largest value,  $V_{rt} = 0.0297$ , is conservatively adopted.

The characteristic resistance is then

$$r_k = b g_{rt}(\underline{X}_m) \exp(-k_\infty \alpha_{rt} Q_{rt} - k_n \alpha_\delta Q_\delta - \frac{1}{2} Q^2) = 0.750 g_{rt}(\underline{X}_m). \quad (5.50)$$

The parameters used are

$$\begin{aligned} Q_\delta &= \sqrt{\ln(V_\delta^2 + 1)} = 0.1358, & \alpha_\delta &= \frac{Q_\delta}{Q} = 0.9738, \\ Q_{rt} &= \sqrt{\ln(V_{rt}^2 + 1)} = 0.0320, & \alpha_{rt} &= \frac{Q_{rt}}{Q} = 0.2294, \\ Q &= \sqrt{\ln(V_r^2 + 1)} = 0.1395. \end{aligned} \quad (5.51)$$

The fractile factors  $k$  were evaluated assuming an unknown coefficient of variation. These factors are based on the  $t$ -distribution, and the fractile factor  $k(p)$  associated with a probability  $p$  is determined following ISO12491 (1997) as:

$$k(p) = t_p(\nu) \sqrt{1 + \frac{1}{n}}, \quad (5.52)$$

where  $t_p(\nu)$  is the  $p$ -fractile of the  $t$ -distribution with  $\nu = n - 1$  degrees of freedom. The characteristic fractile factor  $k_n$  and the design fractile factor  $k_{d,n}$  were computed for  $p = 5\%$  and  $p = 0.1\%$ , respectively. Considering  $n = 36$  in the present study,  $t_{0.05}(35) = 1.69$  and  $t_{0.001}(35) = 3.34$ . Then, we can calculate  $k_n = 1.713$  and  $k_{d,n} = 3.386$  based on Eq. 5.52. The parameter  $k_\infty = 1.64$  can be found in EN1990 (2002) Table D1.

#### 7. Design resistance $r_d$

The design resistance  $r_d$  is obtained as

$$r_d = b g_{rt}(\underline{X}_m) e^{(-k_{d,\infty} \alpha_{rt} Q_{rt} - k_{d,n} \alpha_\delta Q_\delta - 0.5 Q^2)} = 0.595 g_{rt}(\underline{X}_m) \quad (5.53)$$

where the parameter  $k_{d,\infty} = 3.04$  is defined in EN1990 (2002) Table D2.

The corresponding partial safety factor  $\gamma_M$  is

$$\gamma_M = \frac{r_k}{r_d} = 1.261. \quad (5.54)$$

#### 8. Corrected partial safety factor $\gamma_M^*$

In common design practice for steel and steel-concrete composite structures, the design resistance according to a given resistance model is usually evaluated using the nominal values

of the basic variables, rather than characteristic values corresponding to a predefined fractile (often 5%) of the underlying statistical distribution of a material or geometric parameter (EN1994-1-1, 2004).

Therefore, the partial safety factor  $\gamma_M$  defined in Eq. 5.54 is adjusted by a factor  $k_c$  to account for the nominal resistance  $r_n$ . The nominal compressive strength of the concrete is taken as the characteristic value  $f_{ck}$ . The nominal yield strength of the reinforcing steel corresponds to grade B500, in accordance with EN1992-1-1 (2023). The nominal ultimate strength of the structural steel profile is taken as S355 or S460, depending on the configuration, following FprEN1993-1-1 (2022). The nominal geometric values are given in Table 5.3. Finally, the average value of  $k_c$  is used to determine the corrected partial safety factor  $\gamma_M^*$ , defined as follows:

$$\gamma_M^* = k_c \gamma_M = \frac{r_n}{r_d} = 1.282 \times 1.261 = 1.617 \quad (5.55)$$

### 9. Final partial safety factor

Using the corrected partial safety factor  $\gamma_M^*$  obtained from the statistical procedure, the corresponding partial safety factor class  $\gamma_{R_i}$  is selected. The resulting design resistance function is expressed as:

$$r_d = \frac{r_n}{\gamma_M^*} = \frac{r_n}{1.62} \quad (5.56)$$

The theoretical value  $\gamma_M^* = 1.62$  obtained from the test population is not consistent with the use of  $\gamma_V = 1.25$  adopted for headed stud shear connectors in EN1994-1-1 (2004). In view of the statistical evaluation carried out in accordance with EN 1990, a specific partial factor  $\gamma_V$  for CRCD connectors with friction should therefore be calibrated and introduced in EN 1994-1-1, rather than adopting the value defined for headed studs.

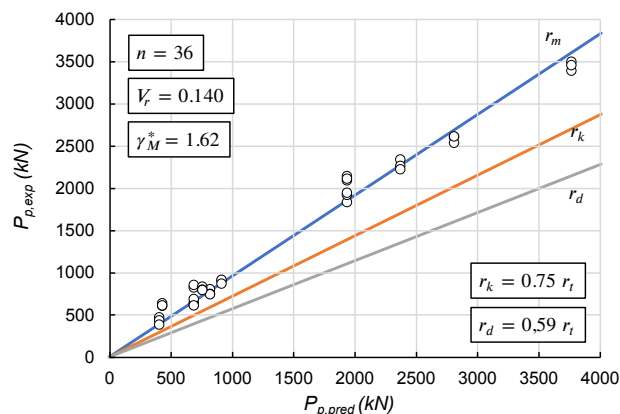


FIGURE 5.14: Comparison between theoretical and experimental resistance and statistical results of the reliability analysis

### 5.3.2 Design assisted by testing for calibrating the stiffness

The same procedure from EN1990 (2002) Annex D as defined in section 5.3.1 was used to evaluate Eq. 5.40, which predicts the stiffness of the adhesion at the steel-concrete interface. Based on the predicted stiffness function, the objective is to determine the characteristic and design stiffness equation and the partial safety factor to use in the design model. The results of the reliability analysis are presented in Fig. 5.15.

Annex B.3 presents the results from the procedure of EN1990 (2002) Annex D. Of the 45 stiffnesses obtained from the push-out tests, only 41 were considered in the study. The 4 other results were considered as outliers with a  $k_s > 15000$  kN/mm, which is two times the average of the results.

The only difference compared to the procedure in Section 5.3.1 concerns Step 6. For the determination of  $V_{rt}$ , Eq. 5.40 is much simpler, and the partial derivatives can be evaluated directly following EN1990 (2002), Annex D:

$$V_{rt}^2 = \frac{\text{VAR}[g_{rt}(\underline{X})]}{g_{rt}^2(\underline{X}_m)} \approx \frac{1}{g_{rt}^2(\underline{X}_m)} \sum_{i=1}^j \left( \frac{\partial g_{rt}}{\partial X_i} \sigma_i \right)^2. \quad (5.57)$$

In the database, two different mean values are available for the two basic variables. Therefore,  $V_{rt}$  is taken as the maximum among the four possible combinations:

$$V_{rt}^2 = \frac{(A_b \sigma_{f_{cm}})^2 + (f_{cm} \sigma_{A_b})^2}{(A_b f_{cm})^2} = \left( \frac{\sigma_{f_{cm}}}{f_{cm}} \right)^2 + \left( \frac{\sigma_{A_b}}{A_b} \right)^2 = V_{f_{cm}}^2 + V_{A_b}^2, \quad (5.58)$$

which results in a maximum value of  $V_{rt} = 0.0085$  for  $f_{cm} = 54.1$  MPa and  $A_b = 1275.9$  mm<sup>2</sup>.

As mentioned in the previous section, the stiffness prediction equation exhibits a large scatter with respect to the experimental results, which leads to a high value of  $\gamma_M^* = 2.66$ . In addition, the equation has been calibrated only for sandblasted steel surfaces, two cross-section types, two concrete compressive strengths, and a single embedded length, resulting in a limited range of applicability.

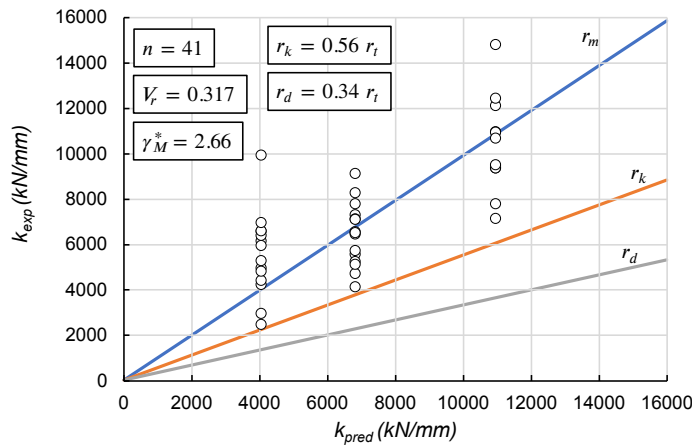


FIGURE 5.15: Comparison between theoretical and experimental stiffness and statistical results of the reliability analysis

## 5.4 Discussion on the limits of the proposed model

In this section, we discuss the limitations of the developed semi-empirical model. Although the model captures the global behaviour of the tested specimens, its applicability is constrained by the simplified assumptions made and the limited experimental data used for calibration. Several key parameters were derived from a narrow range of connector geometries, material strengths, and configuration types, which restricts confident extrapolation to other situations. Further experimental and numerical studies are therefore required to improve the robustness and general applicability of the model.

### 5.4.1 Limits related to the steel surface treatment

The equation developed to predict the friction at the steel–concrete interface has been validated only against the experimental results presented in this thesis. In these tests, the steel beam surfaces were sandblasted, and a frictional shear strength of 0.3 MPa was calibrated. The embedded length was kept constant, and only the cross-section varied, raising questions about whether a uniform shear strength can be assumed for specimens with significantly longer or shorter embedment lengths. Furthermore, Chrzanowski et al. (2019) reported substantial scatter in bond shear strength values across the literature, indicating that this parameter is highly sensitive to factors such as surface condition, concrete strength, and loading history.

Therefore, to enable more reliable predictions of frictional resistance at the steel-concrete interface, further research is needed—particularly studies that systematically classify and quantify the effects of different steel surface conditions.

### 5.4.2 Limits to the introduced parameters in the developed model

In the proposed equation for predicting the resistance of CRCD shear connectors, three empirical parameters are introduced. Each of these parameters is subject to limitations arising from the experimental and numerical data used for their calibration.

First, the coefficient  $\varphi$ , which accounts for the reduction in individual connector resistance when multiple connectors act as a group, requires further experimental investigation. In particular, additional tests are needed for configurations in which shear connectors are placed exclusively on the flanges, as well as for cases involving multiple connectors per row in the web. Moreover, the current study considered only one geometric configuration—openings with a 40 mm diameter, a 12 mm traversing rebar, and a HEB cross-section. A broader experimental program covering different connector geometries and spacing arrangements would enable a more accurate and reliable determination of  $\varphi$ .

Second, the coefficient  $\alpha$ , introduced to capture the influence of the concrete dowel on the shear resistance, was calibrated using only two concrete compressive strengths. The relationship between  $\alpha$  and the concrete strength may not be linear and could follow a different functional form. Additional experiments varying both the concrete strength and the connector geometry are therefore necessary to characterize this relationship more rigorously.

Finally, the coefficient  $\beta$ , which reflects the influence of the steel thickness on the failure mode and, consequently, on the shear resistance, was calibrated primarily through finite element simulations. These simulations largely relied on a single ratio between opening diameter and traversing rebar diameter. To improve the robustness of this coefficient, further experimental studies covering a wider range of opening-to-rebar ratios and thickness of the steel element are required. Such investigations would provide a more reliable basis for defining the dependence of  $\beta$  on connector geometry and the failure mode of the composite connector.

### 5.4.3 Assumption regarding the adhesion contribution to initial stiffness

As discussed in the literature review, assuming a fully rigid shear connector affects the early shear response of composite members. Moreover, Grzeszykowski, Lewandowski-Szewczyk, and Niedóspiał (2023) showed that increasing connector stiffness enables a more effective axial load redistribution across the composite section. Therefore, optimizing shear load transfer in the load introduction zone requires a system that provides substantial shear stiffness.

Considering adhesion as part of the shear transfer mechanism offers the benefit of a very high initial stiffness. However, adhesion is known to be unreliable and highly sensitive to slip. In composite columns, global deformations are relatively limited (Sauerborn and Kretz, 2018) and slip at the steel-concrete interface remains small. During the service life of the column, it is therefore important to exploit the high stiffness provided by adhesion to improve shear transfer in load introduction zones. To do so, it must be ensured that adhesion does not suffer excessive degradation under serviceability limit state (SLS) conditions. Ultimately, long-term and cyclic tests will be required to fully answer this question.

Nevertheless, the available experimental tests allow us to provide a first indication. In each push-out test, a series of 25 load cycles was applied prior to monotonic loading to failure. These cycles were intended to remain between 5% and 40% of the expected ultimate load  $P_u$ . Because of the difficulty in predicting the actual adhesive resistance, the applied cyclic loads  $P_{cyclic}$  ranged between 26% and 50% of the ultimate load (see Table 5.5).

Equation 5.56 gives the design shear resistance  $P_{Rd}$  of the CRCD connectors combined with friction, following the statistical evaluation, corresponding to the maximum allowable shear force at the ultimate limit state (ULS). By considering different ratios of variable  $Q_k$  and permanent loads  $G_k$ , we can compute the SLS/ULS load ratio given by Eq. 5.59 (Hanswille, Illmann, and Dobelmann, 2024). The maximum ratio is 0.74, meaning that SLS loads will not exceed 74% of the ULS resistance during service conditions.

$$\frac{SLS}{ULS} = \frac{G_k + Q_k}{1.35 G_k + 1.5 Q_k} \quad (5.59)$$

Using these values, we estimated for each experiment the maximum SLS characteristic load  $P_{SLS}$  acting on the connection and compared it to the experimentally measured ultimate resistance  $P_u$ . The resulting ratios lie between 12% and 44%, mainly influenced by the number of connectors. Indeed, increasing the number of connectors reduces the ratio between ultimate resistance  $P_u$  and the plateau resistance  $P_p$ , the latter being approximately equal to  $P_{Rd}$ . Roeder (1985) also stated that adhesive layers experience no damage as long as the applied load remains below 40% of their

ultimate resistance  $P_u$ . During the tests, the SLS-level loads  $P_{SLS}$  remained within the elastic range of the adhesion behavior.

TABLE 5.5: Analysis of the SLS characteristic load to the adhesion resistance and cycling load.

Specimen	$P_{Rd}$ (kN)	$P_{SLS}$ (kN)	$P_u$ (kN)	$\frac{P_{SLS}}{P_u}$	$P_{cyclic}$ (kN)	$\frac{P_{SLS}}{P_{cyclic}}$	$\frac{P_{cyclic}}{P_u}$
B1.1	239	177	1095	0.16	400	0.44	0.37
B1.2	239	177	1015	0.17	400	0.44	0.39
B1.3	239	177	827	0.21	400	0.44	0.48
C1.1	408	301	1124	0.27	480	0.63	0.43
C1.2	408	301	1245	0.24	480	0.63	0.39
C1.3	408	301	958	0.31	480	0.63	0.50
C2.1	408	301	1174	0.26	480	0.63	0.41
C2.2	408	301	1249	0.24	480	0.63	0.38
C2.3	408	301	839	0.36	400	0.75	0.48
C4.1	488	360	1136	0.32	480	0.75	0.42
C4.2	488	360	1016	0.35	480	0.75	0.47
C4.3	488	360	994	0.36	400	0.90	0.40
B2.1	254	188	1478	0.13	480	0.39	0.32
B2.2	254	188	1480	0.13	480	0.39	0.32
B2.3	254	188	1536	0.12	480	0.39	0.31
C3.1	450	332	1820	0.18	480	0.69	0.26
C3.2	450	332	1425	0.23	480	0.69	0.34
C3.3	450	332	1473	0.23	480	0.69	0.33
C5.1	543	401	1693	0.24	480	0.84	0.28
C5.2	543	401	1644	0.24	480	0.84	0.29
C5.3	543	401	1667	0.24	480	0.84	0.29
F2.1	1663	1237	3136	0.39	960	1.29	0.31
F2.2	1663	1237	3207	0.39	960	1.29	0.30
F2.3	1663	1237	3213	0.39	960	1.29	0.30
D1.1	1126	852	3353	0.25	1080	0.79	0.32
D1.2	1126	852	3399	0.25	1080	0.79	0.32
D1.3	1126	852	3334	0.26	1080	0.79	0.32
D2.1	1126	852	3371	0.25	1080	0.79	0.32
D2.2	1126	852	3084	0.28	1080	0.79	0.35
D2.3	1126	852	3307	0.26	1080	0.79	0.33
E1.1	1416	1043	4335	0.24	1280	0.82	0.30
E1.2	1416	1043	3183	0.33	1280	0.82	0.40
E1.3	1416	1043	3759	0.28	1280	0.82	0.34
F1.1	2248	1659	3820	0.43	1440	1.15	0.38
F1.2	2248	1659	3732	0.44	1440	1.15	0.39
F1.3	2248	1659	4069	0.41	1440	1.15	0.35

We can further compare SLS loads  $P_{SLS}$  to the cyclic loads  $P_{cyclic}$  applied during testing. These SLS-to-cyclic load ratios are shown in Table 5.5. For most series, the ratio ranges between 39%

and 83%. Only series F1 and F2—those with the highest number of connectors—exceed unity, reaching 1.14 and 1.28, respectively. This indicates that, for the majority of specimens, the SLS load remained within the range of loads already sustained 25 times during cyclic testing without causing any observable damage to the adhesion bond. When the number of connectors is very high, and the load plateau  $P_p$  approaches the ultimate resistance  $P_u$ , SLS loads  $P_{SLS}$  remain elastic but slightly exceed the cyclic loading level  $P_{cyclic}$ .

Overall, the comparison between SLS loads, cyclic loads, and ultimate resistance indicates that for most configurations, the expected service loads remain safely within the elastic behavior range of the adhesion layer. Adhesion, therefore, appears capable of contributing meaningfully to initial shear stiffness in composite columns without suffering degradation under normal service conditions. Only in cases with a very large number of connectors—where the ultimate resistance is close to the plateau resistance—does the SLS load exceed the cyclic load applied during testing. Nevertheless, even in these cases, the SLS load remains well below the ultimate adhesive capacity. These findings suggest that adhesion can be reliably exploited to enhance the stiffness of the shear transfer in load introduction zones, although long-term and cyclic testing remain necessary for full validation of the tested configurations.

## 5.5 Design considerations

This section aims to provide qualitative design recommendations derived from the experimental and numerical investigations conducted in this thesis. In all cases, the provisions of EN1994-1-1 (2004) and the relevant execution standards remain fully applicable and govern the design.

The design considerations from this section have been applied to a real design example in Annex C. This example considers a composite column with a concrete-encased steel section and compares the application of headed studs and CRCD shear connectors.

### 5.5.1 Shear connection

The experimental and numerical results underline that the performance of the load introduction zone strongly depends on an appropriate design of the shear connection between the steel profile and the surrounding concrete.

**Shear resistance.** The characteristic shear resistance  $P_{Rk}$  may be estimated using Eq. 5.60, developed in Section 5.2.3.

$$P_{Rk} = \tau_r A_b + \varphi \beta (n_w (P_{c,1,w} + P_{s,1,w}) + n_f (P_{c,1,f} + P_{s,1,f})) \quad (5.60)$$

with

$$\begin{aligned}
P_{c,1,w} &= \frac{A_{c,w} f_{ck}}{\alpha}, \\
P_{s,1,w} &= \min(1.155 A_{s,w} f_{sk,w}; k_1 \alpha_b f_{uk} d_{s,w} t_w), \\
P_{c,1,f} &= \frac{A_{c,f} f_{ck}}{\alpha}, \\
P_{s,1,f} &= \min(1.155 A_{s,f} f_{sk,f}; k_1 \alpha_b f_{uk} d_{s,f} t_f), \\
\varphi &= 1 - 0.077 \ln(n_w + n_f), \\
\beta &= 1.7556 \sqrt{d_s/t} - 0.8078 (d_s/t), \\
d_s/t &= \min\left(\frac{d_{s,w}}{t_w}, \frac{d_{s,f}}{t_f}\right), \\
\alpha &= 0.0054 f_{ck} + 0.3085
\end{aligned} \tag{5.61}$$

where the parameters are defined in Section 5.2.3 and  $\tau_r = 0.3$  for a sandblasted steel surface.

This expression is valid for HE 200 to HE 360 sections; C50/60–C80/95 concrete;  $d_c = 40$ – $60$  mm;  $d_s = 12$ – $20$  mm; an embedded length of  $690$  mm; sandblasted steel surfaces; and monotonic push-out loading.

The design shear resistance  $P_{Rd}$  is defined by Eq. 5.62 using the partial safety coefficient defined in Section 5.3. When applying the proposed models, the designer shall remain within the parameter ranges covered by the experimental and numerical investigations (in particular for the ratio  $d_s/d_c$ ). Extrapolation beyond these ranges should be undertaken with caution and, where possible, supported by additional verification.

$$P_{Rd} = \frac{P_{Rk}}{1.62} \tag{5.62}$$

If a central position of the traversing rebar within the opening cannot be guaranteed, a more conservative expression to predict the shear resistance of the connector group, combined with interfacial friction, should be adopted. This formulation accounts for an unfavourable rebar position close to the steel element in the loading direction, which may lead to rebar behaviour governed by pure shear, see Eq. 5.63.

$$P_{Rk,conservative} = \tau_r A_b + n_w \min\left\{\frac{1.155 A_{s,w} f_{sk,w}}{k_1 \alpha_b f_{uk} d_{s,w} t_w}\right\} + n_f \min\left\{\frac{1.155 A_{s,f} f_{sk,f}}{k_1 \alpha_b f_{uk} d_{s,f} t_f}\right\} \tag{5.63}$$

where the parameters are defined in Section 5.2.3 and  $\tau_r = 0.3$  for a sandblasted steel surface.

This expression is valid for HE 200 to HE 360 sections; C50/60–C80/95 concrete;  $d_c = 40$ – $60$  mm;  $d_s = 12$ – $20$  mm; an embedded length of  $690$  mm; sandblasted steel surfaces; and monotonic push-out loading.

**Stiffness.** The characteristic stiffness  $k_{s,k}$  can be estimated by equation 5.64.

$$k_{s,k} = 0.094 f_c A_b \tag{5.64}$$

Proposed for: HE 200 to HE 360 sections; C50/60–C80/95 concrete; 690 mm embedded length; sandblasted steel surfaces; monotonic push-out loading.

The design stiffness  $k_{s,d}$  is defined by Eq. 5.65 using the partial safety coefficient defined in Section 5.3. The designer should be aware that the equation to predict the stiffness was assessed based on only one steel surface conditions, two types of steel cross-sections, and two concrete compressive strengths, and presents high scatter.

$$k_{s,d} = \frac{k_{s,k}}{2.66} \quad (5.65)$$

**Slip capacity of the shear connectors.** The slip capacity of the shear connectors is a key parameter for a redistribution of the load between a group of shear connectors. In cases where connectors are positioned both in the web openings and on the flanges of the steel profile, their geometry should be chosen so that the estimated slip capacity of web and flange connectors is of the same order of magnitude. This promotes a more uniform sharing of shear forces between the different connector lines and avoids early overloading of one connector type. The equation 5.66 developed in section 5.2.5 to estimate the slip capacity  $s_{pred}$  can help to optimize the flanges/web connectors geometries. A similar value  $s_{pred}$  for the flanges and the web should be found to ensure an optimal utilization of the CRCD connectors.

$$s_{pred} = 1.96 \frac{(d_c - d_s) d_s}{\sqrt{f_{cm} t}} + 2 \quad (5.66)$$

Proposed for: HE 200 to HE 360 sections; C50/60–C80/95 concrete;  $d_c = 40$ – $65$  mm;  $d_s = 12$ – $20$  mm;  $t_w = 9$ – $20$  mm;  $t_f = 10$ – $20$  mm; 690 mm embedded length; sandblasted steel surfaces; monotonic push-out loading.

**Spacing and overlapping of stresses.** The longitudinal spacing of the shear connectors should be chosen to limit excessive overlap of the concrete stress fields developing around each connector. According to the experimental results, a minimum vertical centre-to-centre distance of 100 mm for CRCD connectors with 40 mm openings should be maintained. A distance of 200 mm was optimal.

**Diametral bearing resistance of the steel profile.** The local diametral bearing resistance of the steel profile must be verified according to EN1993-1-8 (2005) by considering the diameter of the traversing rebar. The local bearing stresses induced by the traversing rebar should remain below acceptable limits to prevent excessive ovalization of the holes.

## 5.5.2 Detailing and constructability

Beyond global resistance checks, the experimental and numerical results highlight the importance of an appropriate detailing of reinforcement, connectors layout, and construction sequence to achieve the intended behaviour of the load introduction zone.

**Transverse reinforcement and confinement.** A sufficiently dense and well-anchored transverse reinforcement (stirrups and longitudinal bars) is essential to confine the concrete around the connectors, particularly for connectors anchored in the flanges, which are less deeply embedded than the connectors placed through web openings. The good confinement from the reinforcements will also provide sufficient friction at the steel-concrete interface. The stirrup spacing and diameter should ensure good confinement without creating excessive congestion of the reinforcement with the shear connectors. In the experiments, stirrups of diameter 10 mm, each 100 mm proved to be sufficient.

**Position and diameter of traversing rebars in openings.** The rebars passing through the openings should be centrally positioned or placed as low as reasonably possible within the opening, to maximize the infill concrete cover between the bar and the opening edge and keep a sufficient ductile behavior. The traversing rebar diameter should be selected taking into account the available concrete cross-section, the required anchorage length, and the geometric constraints of the openings. Indeed, the size of the rebar will determine the bending diameter according to EN1992-1-1 (2023). Oversized bars with insufficient anchorage or minimal clear cover may lead to premature splitting or slip of the rebar and should be avoided. The shape of the traversing reinforcement in the flange regions, where anchorage is more challenging, should be given particular attention; bent or hooked bars must be detailed such that adequate anchorage and cover are achieved without excessive bending radii that could conflict with other reinforcement.

**Reinforcement congestion and connector layering.** To avoid reinforcement congestion in the load introduction zone, web and flange connectors should, where possible, be arranged in different vertical layers, and the reinforcement cage should be designed to leave clear paths for placing and compacting the concrete. The spacing between stirrups should be sufficient to allow the insertion of longitudinal bars through the openings and the correct positioning of all connectors, while still providing the confinement required by the design.

**Influence of concrete aggregate size.** The maximum size of the concrete aggregate should be compatible with the distances between the web openings and the traversing reinforcement. To ensure that aggregates can fit in the openings, the aggregate size should not exceed  $(d_c - d_s)/2$ .

**Perforation of the openings.** The holes in the web and the flanges should be produced by drilling or by another execution process in accordance with EN1090-2 (2018) that provides an equivalent mechanical performance and satisfies the project specifications. The use of punched holes for composite dowels lies outside the scope of the configurations studied in this thesis and is therefore not covered by the provided recommendations.

**Casting and compaction of the concrete.** The casting procedure and the vibration of the concrete must ensure that the vicinity of the web openings and the flanges is carefully filled with concrete.

**Construction sequence.** A practical construction sequence for the investigated configurations consists of:

1. Fabrication of the steel beam with pre-drilled openings in the workshop.
2. Installation and alignment of the steel profile, for the column, on site, including temporary supports.
3. Assembly of the steel reinforcement cage around the encased steel profile.
4. Installation of the traversing rebars (web and flange connectors) in the openings of the steel profile, and fixation to the reinforcement cage.
5. Installation of the formwork and concreting of the composite column.

**Avoidance of unintended load paths.** Where steel plates or L-shaped profiles are used to connect floor beams to the steel profile of composite columns, a compressible layer (*e.g.* Styropor) should be provided between these elements and the concrete surface. This prevents inadvertent transfer of vertical loads through secondary elements that are not designed as load introduction devices, and reduces the risk of local concrete damage or failure of steel plates due to high localised bearing stresses.

Overall, the recommendations outlined in this section should be applied in conjunction with the general requirements of EN1994-1-1 (2004) and the project-specific design checks. Where the design deviates from the parameter range or detailing principles investigated in this thesis, an appropriate level of additional verification is required.

## Chapter 6

# Conclusion

### 6.1 Conclusion

This dissertation investigated a new shear transfer mechanism for the load introduction zones of concrete-encased steel (CES) columns made with normal- and high-strength concrete. The proposed system relies on the natural bond at the steel-concrete interface acting in combination with circular reinforced composite dowel (CRCD) shear connectors placed on the web and/or flanges of H-shaped steel profiles. Compared with conventional headed studs, CRCD connectors offer the potential for increased shear resistance and higher initial stiffness, and, based on their load–slip characteristics reported in the literature, may also provide favourable ductility and fatigue performance.

The research combined (1) a critical synthesis of the state of the art on load introduction in composite columns and on shear transfer via bond and CRCD connectors, (2) an extensive experimental campaign of push-out tests, (3) a nonlinear three-dimensional finite element (FE) model, and (4) the development of semi-empirical design expressions. This section first summarizes the main and exploratory contributions, then discusses the principal limitations of the work, and finally outlines directions for future research.

#### 6.1.1 Main contributions

##### **Conceptual and experimental validation of a new shear transfer mechanism**

A primary contribution of this thesis is the development and validation of a shear transfer mechanism for CES column load introduction zones that intentionally combines interfacial bond and CRCD connectors. Through a series of 45 push-out tests covering 15 different configurations, the work has shown that:

- The shear connection response can be consistently characterized by an initial adhesion-dominated phase, followed by an abrupt adhesion failure, a plateau governed by CRCD resistance and Coulomb friction, and ultimately connector shear failure and residual frictional behaviour.
- Increasing concrete strength substantially enhances adhesion resistance, sliding friction, and overall stiffness, but tends to reduce the ductility and alter the failure mechanism of the CRCD connectors, particularly in high-strength concrete.

- CRCD connectors placed on the web and/or flanges can effectively mobilize composite action over short load introduction lengths, making them suitable for highly concentrated load transfer in CES columns.

### **Comprehensive experimental database on bond and CRCD behaviour**

The experimental program produced a detailed dataset on the interaction of bond and CRCD connectors under longitudinal shear. The tests systematically investigated the influence of concrete strength, steel cross-section geometry, connector number and spacing, connector positioning (web, flange, or both), and connector sizes. Key outcomes include:

- Quantification of the bond contribution in the absence of connectors, including the impact of concrete strength on adhesion and sliding friction, and the influence of steel section geometry on peak and residual bond stresses.
- Identification and characterization of two main CRCD failure modes, supported by strain gauge measurements along the steel web.
- Demonstration that increasing the number and density of CRCD connectors significantly increases shear peak and plateau resistance but systematically reduces slip capacity.
- Evidence that connectors placed on the flanges, even with relatively small concrete cover, can provide efficient shear transfer, and that configurations combining web and flange connectors offer very high shear resistance. In such mixed layouts, the slip capacity is typically governed by the connectors on the flanges, due to the thicker flanges compared to the web providing a more confined concrete dowel.

### **Validated three-dimensional nonlinear finite element model**

A further major contribution is the development of a three-dimensional FE model of the push-out specimens in ABAQUS/EXPLICIT, calibrated and validated against experimental load–slip curves and observed failure mechanisms. The model:

- Reproduced the global response and failure mechanism of the tested specimens with very good accuracy within the calibration domain, confirming its suitability as a robust interpretive and parametric tool for the investigated range of configurations.
- Enabled a decomposition of the shear–slip response into separate contributions from adhesion, friction, and CRCD connector resistance, thereby providing a clear mechanistic interpretation of the composite shear transfer mechanism.
- Supported parametric studies on rebar diameter, opening size, rebar positioning within the opening, concrete strength, web and flanges thickness, concrete cover, connectors layout, and rebar steel grade, thereby extending the experimental findings and clarifying the relative importance of each parameter.

The model is intentionally calibrated against the experimental database and is therefore intended primarily for mechanical interpretation and parametric studies within the tested domain, rather than for blind prediction of arbitrary configurations.

### **Semi-empirical model for CRCD connectors with friction**

Based on the combined experimental and numerical results, the thesis proposes a semi-empirical model for groups of CRCD connectors acting together with interfacial friction. The model provides:

- A shear resistance equation for groups of CRCD connectors on the web and/or flanges in combination with friction, calibrated against the experimental database and numerically generated data, and statistically evaluated in accordance with EN1990 (2002).
- An expression for the initial shear stiffness of the composite connection, which, despite the inherent scatter associated with adhesion, captures the main trends and provides a rational basis for serviceability assessments.
- A slip capacity expression that relates ductility to connector geometry and section properties, and can be used to approximately balance the slip capacities of connectors on the web and on the flanges through suitable choices of CRCD dimensions and steel thickness.

Within the investigated domain, the resistance model shows statistically validated predictive quality when evaluated in accordance with EN1990 (2002). In contrast, the stiffness and slip capacity formulations exhibit higher scatter and more limited experimental support; they are therefore proposed as first design-oriented approximations, suitable for preliminary sizing and sensitivity studies rather than code-level verification.

#### **6.1.2 Exploratory contributions**

In addition to the core contributions above, the thesis includes several exploratory results and concepts that extend beyond the strictly validated range of configurations and loading conditions.

- **Qualitative design recommendations.** The parametric FE studies yield qualitative design guidance regarding optimal connector positioning (web versus flange), the benefits and trade-offs of combining web and flange connectors, the influence of connector spacing, and the sensitivity of performance to fabrication tolerances such as rebar eccentricity within openings. These recommendations support engineering judgement but require further validation for codified use.
- **Preliminary models for stiffness and ductility.** The stiffness and slip-capacity expressions, while calibrated against available data, are affected by significant scatter due to variability in adhesion and lack of experiments. They are therefore presented as exploratory tools for preliminary design.

- **Broader structural applications.** The same design principles could be applied to structural components beyond CES columns, including anchorage systems for suspension bridges, hybrid arch–beam systems, wind turbine foundations, composite bridge decks, hybrid bridge pylons, and connections between battered steel piles and concrete foundations. These proposals are based on the underlying mechanics of CRCD connectors and bond, and are intended as conceptual pathways for future implementation.
- **Implications for design codes.** The observed interaction between friction and CRCD connectors provides evidence that the current prohibition on combining natural bond and mechanical shear connectors in major standards may be overly conservative, at least within the investigated parameter range. However, the present results are not sufficient on their own to justify immediate code changes; they constitute an exploratory step towards possible future revisions of design rules for composite columns.

### 6.1.3 Limitations

This work is subject to several limitations, which must be considered when interpreting the results and applying the proposed models.

- **Range of geometries and materials.** The experimental program examined a limited number of steel profiles, connector geometries, and concrete strength classes, with particular emphasis on two representative cross-sections and normal- and high-strength concretes.
- **Steel surface conditions.** The bond behaviour was investigated for sandblasted steel surface conditions. Effects of alternative surface treatments (*e.g.* coatings, strong corrosion, or intentionally roughened surfaces) were not explored.
- **Specimen type and loading regime.** The experimental work was confined to push-out tests under monotonic quasi-static axial loading. These provide detailed insight into local shear transfer at the steel-concrete interface, but do not capture the full global response of CES columns. Bending, combined axial-bending, and transverse loads in full columns and joints were not directly tested.
- **Numerical model assumptions.** The FE model, while carefully validated, relies on specific material laws, interface formulations, and simplifications in geometry and boundary conditions. Extrapolation to very different configurations, loading scenarios, or material combinations may require additional calibration.
- **Scope of the semi-empirical model.** The proposed resistance, stiffness, and slip-capacity equations are strictly valid within the range of parameters covered by the experimental and numerical databases used for calibration. Their extension to substantially different connector geometries, concrete classes, or steel sections entails additional uncertainty.
- **Time-dependent and cyclic effects.** Creep, temperature variations, environmental degradation, and fatigue were not explicitly considered in either the tests or the models. The

long-term performance and fatigue of the combined bond–CRCD system, therefore, remain outside the scope of the present work.

These limitations motivate the need for further investigations before the proposed models can be fully generalized and integrated into major design standards.

## 6.2 Future research

Based on the findings, limitations, and insights gained throughout this study, several directions for future research have been identified. These directions aim to deepen the understanding of shear transfer mechanisms in composite columns, expand the applicability of CRCD connectors, and support the development of robust design provisions. Potential areas for further investigation include:

### Material variations

- Investigate the performance of CRCD connectors and bond in a broader range of concrete strength classes, including both lower-strength concretes and ultra-high-performance concrete, to fully capture the influence of concrete mechanical properties.
- Examine different steel surface conditions—such as painted surfaces, intentionally rusted steel, or as-rolled rough steel—to characterize the bond resistance better and to improve predictive accuracy for real construction conditions.
- Investigate the distribution of interface friction stresses along the H-shaped steel section (web and flanges), accounting for variations in concrete cover thickness and steel cross-section geometry. Extend the assessment to longer push-out specimens to validate (or refine) the assumption of a uniform stress distribution along the bonded length.

### Geometrical variations and detailing

- Explore a wider spectrum of connector geometries (opening diameters, rebar diameters, and thickness of steel element) to better quantify the effect of the steel element thickness and the ratio of rebar diameter to opening size.
- Investigate different levels and layouts of transverse reinforcement to assess how confinement modifies sliding friction and enhances CRCD connectors performance.
- Conduct tests that vary the position of the traversing rebar within the opening to assess fabrication tolerances more accurately.

### Structural configurations and full-scale behaviour

- Experimentally isolate the contribution of connectors on the web and/or flanges by minimizing surface friction through controlled steel surface treatments, thereby enabling a clearer separation between bond and mechanical shear transfer.

- Assess the influence of CRCD openings on the global axial and flexural stiffness of composite columns, as well as on local buckling phenomena in the steel profile.
- Study the impact of load eccentricity and combined axial–bending loading on both the bond interface and the CRCD connectors, in order to establish robust design rules for realistic load introduction scenarios.
- Carry out full-scale tests on CES columns with CRCD connectors in the load introduction zones, including cases with combined axial load and bending, to validate the proposed mechanisms and design models at the structural element level and under realistic boundary conditions.
- Investigate different load introduction types (via concrete, via the steel core, or combined) to quantify their effects on stress distribution and shear transfer mechanisms in the load introduction zone.

### **Long-term and cyclic performance**

- Evaluate the long-term behaviour of the combined bond–CRCD system under sustained loading, incorporating creep, temperature, and humidity variations, to assess potential degradation of stiffness and resistance over time.
- Perform cyclic and fatigue tests on the shear connection to clarify the evolution of adhesion, friction, and connector performance under repeated loading, particularly in applications such as bridges and wind turbine foundations.

### **Analytical and numerical methods**

- Develop improved analytical models for friction stress evolution at the steel–concrete interface, accounting for steel surface condition, confinement, and time-dependent phenomena.
- Extend and diversify the experimental database with additional configurations, including different steel sections, connector section geometries, connector geometries, and concrete classes, to refine and enhance the reliability of the semi-empirical model proposed in this thesis.

### **Design and practical implementation**

- Formulate comprehensive design guidelines for CRCD connectors combined with friction, integrating experimental, numerical, and analytical findings to support engineering practice.
- Work toward the inclusion of CRCD connectors and combined bond–connector mechanisms in major design standards and building codes, thereby enabling their broader adoption in steel–concrete composite construction.



# Appendix A

## Energy balance of FEA

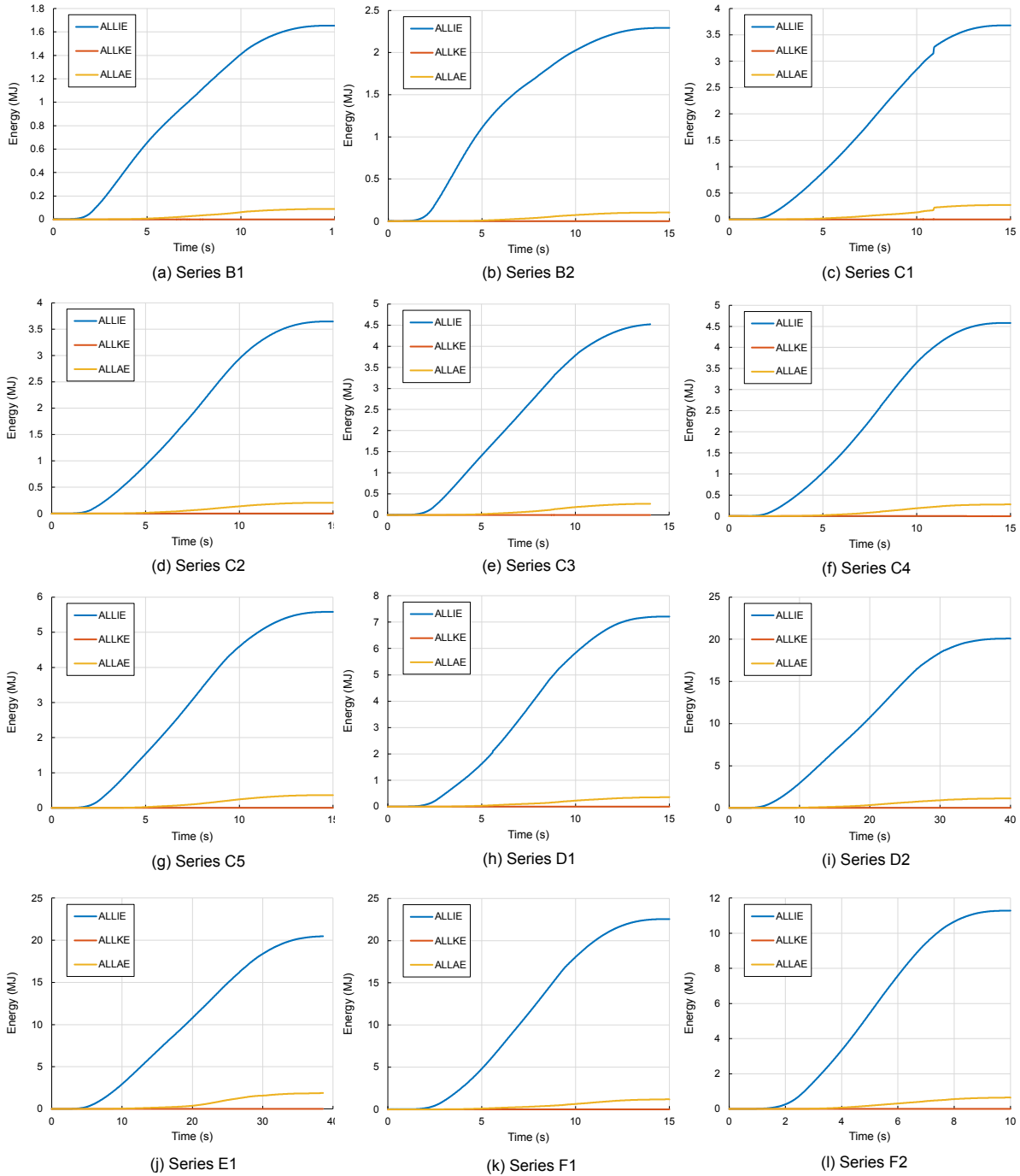


FIGURE A.1: Comparison between the internal (ALLIE), kinetic (ALLKE), and artificial (ALLAE) energies for all series.



## Appendix B

# Results from the design model

### B.1 CRCD resistance: prediction *vs.* FE results

TABLE B.1: Comparison between the predictions of the CRCD connectors resistance by the proposed equations and FE results.

Series	Steel profile	$f_c$ (MPa)	Connector position	$n_w$	$d_s$ (mm)	$d_c$ (mm)	$t$ (mm)	$f_s$ (MPa)	$P_{u,FEA}$ (kN)	$P_{u,pred}$ (kN)	$\frac{P_{u,pred}}{P_{u,FEA}}$
B1	HEB200	52	web	1	12	40	9	530	173	161	0.93
B2	HEB200	90	web	1	12	40	9	530	191	189	0.99
C1	HEB200	56	web	3	12	40	9	530	457	454	0.99
C2	HEB200	56	web	3	12	40	9	530	474	454	0.96
C3	HEB200	90	web	3	12	40	9	530	554	518	0.93
C4	HEB200	56	web	4	12	40	9	530	640	590	0.92
C5	HEA360	90	web	4	12	40	9	530	728	674	0.93
F2	HEA360	92	web & flg	6 & 12	12 & 12	40 & 40	9 & 15	540 & 540	2406	2600	1.08
D1	HEA360	92	web	4	20	60	10	561	1652	1518	0.92
D2	HEA360	92	web	4	20	60	10	561	1662	1518	0.91
E1	HEA360	92	flange	8	16	50	17.5	506	2282	2013	0.88
F1	HEA360	92	web & flg	4 & 8	20 & 16	60 & 50	10 & 17.5	561 & 506	3374	3429	1.02
G1	HEB200	56	web	3	16	40	9	506	564	531	0.94
G2	HEB200	56	web	3	20	40	9	561	642	626	0.98
G3	HEB200	90	web	3	16	40	9	506	649	588	0.91
G4	HEB200	90	web	3	20	40	9	561	733	672	0.92
H1	HEB200	56	web	3	12	50	9	530	598	623	1.04
H2	HEB200	56	web	3	12	65	9	530	853	946	1.11
H4	HEB200	90	web	3	12	50	9	530	763	727	0.95
H5	HEB200	90	web	3	12	65	9	530	974	1127	1.16
I1	HEB200	56	web	3	16	50	9	506	642	692	1.08
I2	HEB200	56	web	3	20	65	9	561	873	1052	1.20
I3	HEB200	90	web	3	16	50	9	506	778	787	1.01
I4	HEB200	90	web	3	20	65	9	561	1085	1198	1.10
J1	HEB200	56	web	3	12	40	15	530	469	441	0.94
J2	HEB200	56	web	3	12	40	20	530	441	418	0.95
J3	HEB200	90	web	3	12	40	15	530	478	504	1.05
J4	HEB200	90	web	3	12	40	20	530	445	477	1.07
K1	HEB200	56	web	3	16	50	20	506	674	708	1.05
K2	HEB200	56	web	3	20	65	20	561	1162	1246	1.07
K3	HEB200	90	web	3	16	50	20	506	751	804	1.07
K4	HEB200	90	web	3	20	65	20	561	1221	1414	1.16
S1	HEB200	90	flange	12	12	40	10	530	1851	1838	0.99
S2	HEB200	56	flange	12	12	40	10	530	1622	1609	0.99
S3	HEB200	90	flange	12	12	40	20	530	1565	1687	1.08
S4	HEB200	56	flange	12	12	40	20	530	1654	1477	0.89
O7	HEB200	56	flange	12	12	40	15	530	1714	1560	0.91
O8	HEB200	90	flange	12	12	40	15	530	1783	1781	1.00

## B.2 CRCD + friction resistance: prediction vs. test results

TABLE B.2: Comparison between the predictions of the CRCD connectors combined with friction resistances by the proposed equations and test results.

Specimen	$n$	$f_c$ (MPa)	Steel profile	Connector position	$d_s/d_c$ (mm)	$P_{p,exp}$ (kN)	$P_{p,pred}$ (kN)	$\frac{P_{p,pred}}{P_{p,exp}}$	$k_{exp}$ (kN/mm)	$k_{pred}$ (kN/mm)	$\frac{k_{pred}}{k_{exp}}$
A1.1	/	52	HEB200	/	/				2470	4037	1.63
A1.2	/	52	HEB200	/	/				9942	4037	0.41
A1.3	/	52	HEB200	/	/				24323		
A2.1	/	90	HEB200	/	/				15841		
A2.2	/	90	HEB200	/	/				5572	6811	1.22
A2.3	/	90	HEB200	/	/				4129	6811	1.65
A3.1	/	90	HEA360	/	/				6563	6811	1.04
A3.2	/	90	HEA360	/	/				22647		
A3.3	/	90	HEA360	/	/				5250	6811	1.30
B1.1	1	52	HEB200	web	12/40	471	401	0.85	6152	4037	0.66
B1.2	1	52	HEB200	web	12/40	435	401	0.92	5962	4037	0.68
B1.3	1	52	HEB200	web	12/40	389	401	1.03	4244	4037	0.95
C1.1	3	56	HEB200	web	12/40	649	685	1.06	6571	4037	0.61
C1.2	3	56	HEB200	web	12/40	825	685	0.83	6395	4037	0.63
C1.3	3	56	HEB200	web	12/40	619	685	1.11	2956	4037	1.37
C2.1	3	56	HEB200	web	12/40	691	685	0.99	4412	4037	0.92
C2.2	3	56	HEB200	web	12/40	859	685	0.80	4958	4037	0.81
C2.3	3	56	HEB200	web	12/40	616	685	1.11	4823	4037	0.84
C4.1	4	56	HEB200	web	12/40	805	820	1.02	6604	4037	0.61
C4.2	4	56	HEB200	web	12/40	752	820	1.09	6962	4037	0.58
C4.3	4	56	HEB200	web	12/40	746	820	1.10	5289	4037	0.76
B2.1	1	90	HEB200	web	12/40	638	427	0.67	7314	6811	0.93
B2.2	1	90	HEB200	web	12/40	607	427	0.70	7116	6811	0.96
B2.3	1	90	HEB200	web	12/40	612	427	0.70	7110	6811	0.96
C3.1	3	90	HEB200	web	12/40	838	756	0.90	6453	6811	1.06
C3.2	3	90	HEB200	web	12/40	802	756	0.94	9136	6811	0.75
C3.3	3	90	HEB200	web	12/40	798	756	0.95	8276	6811	0.82
C5.1	4	90	HEB200	web	12/40	909	912	1.00	6512	6811	1.05
C5.2	4	90	HEB200	web	12/40	916	912	1.00	24178		
C5.3	4	90	HEB200	web	12/40	873	912	1.05	4718	6811	1.44
F2.1	18	90	HEB200	web & flg	12/40 & 12/40	2610	2796	1.07	7801	6811	0.87
F2.2	18	90	HEB200	web & flg	12/40 & 12/40	2542	2796	1.10	5727	6811	1.19
F2.3	18	90	HEB200	web & flg	12/40 & 12/40	2617	2796	1.07	5116	6811	1.33
D1.1	4	90	HEA360	web	20/60	2097	1893	0.90	9366	10941	1.17
D1.2	4	90	HEA360	web	20/60	2147	1893	0.88	9442	10941	1.16
D1.3	4	90	HEA360	web	20/60	2116	1893	0.89	10967	10941	1.00
D2.1	4	90	HEA360	web	20/60	1837	1893	1.03	12126	10941	0.90
D2.2	4	90	HEA360	web	20/60	1925	1893	0.98	10936	10941	1.00
D2.3	4	90	HEA360	web	20/60	1947	1893	0.97	12432	10941	0.88
E1.1	8	90	HEA360	flg	16/50	2345	2377	1.01	7797	10941	1.40
E1.2	8	90	HEA360	flg	16/50	2268	2377	1.05	10681	10941	1.02
E1.3	8	90	HEA360	flg	16/50	2227	2377	1.07	7146	10941	1.53
F1.1	12	90	HEA360	web & flg	20/60 & 16/50	3501	3780	1.08	9363	10941	1.17
F1.2	12	90	HEA360	web & flg	20/60 & 16/50	3396	3780	1.11	14810	10941	0.74
F1.3	12	90	HEA360	web & flg	20/60 & 16/50	3458	3780	1.09	9507	10941	1.15

### B.3 Statistical assessment according to EN1990

TABLE B.3: Statistical analysis of current equations.

Property	Plateau resistance $r_{t,p}$	Stiffness $r_{t,k}$
$n$	36	41
$\rho$	0.993	0.739
$b$	0.96	0.99
$\bar{\Delta}$	0.072	0.051
$s_{\Delta}^2$	0.018	0.096
$V_{\Delta}^2$	0.019	0.100
$V_{rt}^2$	0.001	0.00007
$V_r^2$	0.020	0.100
$Q_{\delta}$	0.136	0.309
$Q_{rt}$	0.032	0.008
$Q$	0.139	0.309
$\alpha_{\delta}$	0.974	0.999
$\alpha_{rt}$	0.229	0.027
$k_n$	1.713	1.704
$k_{infty}$	1.64	1.64
$r_k/g_{rt}(\underline{X}_m)$	0.750	0.557
$k_{d,n}$	3.386	3.347
$k_{d,infty}$	3.04	3.04
$r_d/g_{rt}(\underline{X}_m)$	0.595	0.335
$\gamma_M$	1.261	1.661
$k_c$	1.282	1.601
$\gamma_M^*$	1.617	2.661

## Appendix C

# Design example

To illustrate the application of circular reinforced composite dowels (CRCD) with friction in the load introduction zone, the design model is applied to a real case study. The case study also compares CRCD connectors with headed studs. It is taken from Prof. Schäfer's course *Composite Structures and Fire Design* taught at the University of Luxembourg. The example considers the most heavily loaded steel–concrete composite column at the ground floor, which supports the loads from four upper floors as well as the library floor: the composite beams are connected directly to the steel profile of the composite column (see Fig. C.1).

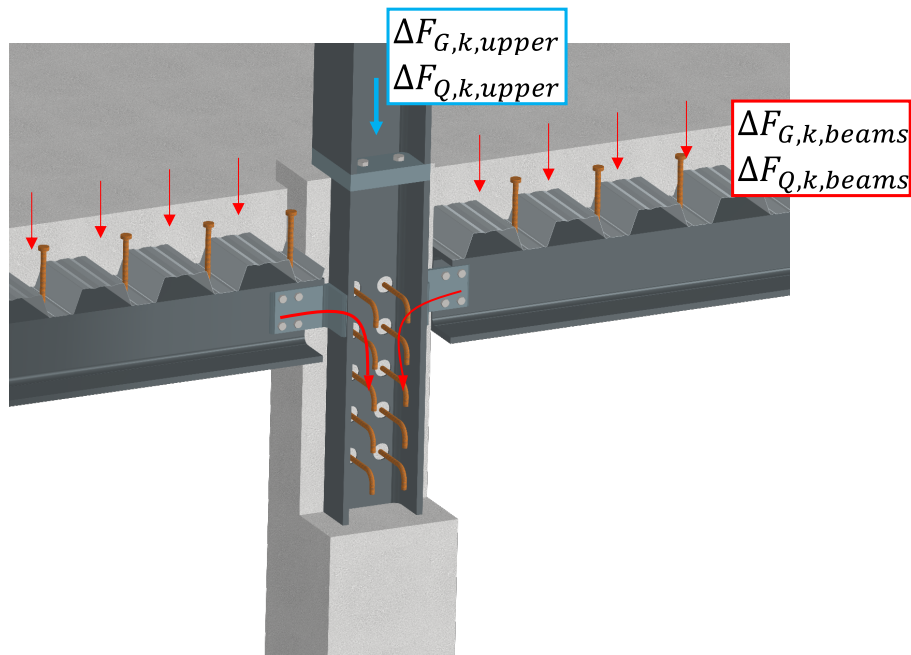


FIGURE C.1: Detail of the load introduction zone.

The composite column consists of a 4 m high, concrete-encased steel section. The member and cross-section design are not discussed here; only the verification of the shear connection is addressed. The final design comprises an HEB280 section in S355 embedded in a  $400 \times 400$  mm reinforced concrete section of C50/60, reinforced with eight B500 longitudinal bars of 20 mm diameter (see Fig. C.2). The column is centrally loaded and is therefore subjected to axial force only.

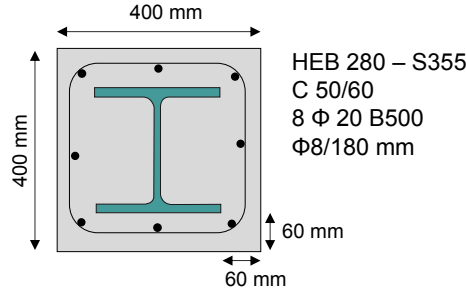


FIGURE C.2: Detail of the concrete-encased steel section.

The plastic resistance of the cross-section to compression is given by:

$$\begin{aligned}
 N_{pl,Rd} &= A_a \times f_{yd} + 0.85 A_c \times f_{cd} + A_{s,tot} \times f_{sd} \\
 &= 0.01314 \times 355/1.1 + 0.85 \times 0.14434 \times 50/1.5 + 0.002513 \times 500/1.15 \\
 &= 9423 \text{ kN}
 \end{aligned} \tag{C.1}$$

This leads to a factor  $\delta$  representing the part of the steel profile resistance to:

$$0.2 < \delta = \frac{A_a \times f_{yd}}{N_{pl,Rd}} = 0.45 < 0.9 \tag{C.2}$$

The loads from the library floor to be supported by the column and introduced via the composite beams are:

$$\begin{aligned}
 \Delta F_{G,k,beams} &= 697 \text{ kN} \\
 \Delta F_{Q,k,beams} &= 644 \text{ kN} \\
 N_{Ed,beams} &= 1.35 \times 697 + 1.5 \times 644 = 1907 \text{ kN}
 \end{aligned} \tag{C.3}$$

The loads from the upper levels to be supported by the column and introduced via the upper composite column are:

$$\begin{aligned}
 \Delta F_{G,k,upper} &= 2427 \text{ kN} \\
 \Delta F_{Q,k,upper} &= 1112 \text{ kN} \\
 N_{Ed,upper} &= 1.35 \times 2427 + 1.5 \times 1112 = 4944 \text{ kN}
 \end{aligned} \tag{C.4}$$

## C.1 Considering headed stud shear connectors

### C.1.1 Design of composite connectors

To design the shear connectors, the part of the actions taken by the reinforced concrete of the column is considered:

$$N_{rc,Ed} = N_{Ed,slab} (1 - \delta) = 1907 \times 0.55 = 1049 \text{ kN} \tag{C.5}$$

Studs with a 16mm diameter are selected for the shear connection:

$$\begin{aligned} f_u &= 450 \text{ MPa}, & h_{sc} &= 0.1 \text{ m} \\ d &= 0.016 \text{ m}, & h_{sc}/d &= 0.1/0.016 = 6.25 > 4 \rightarrow \alpha = 1 \end{aligned} \quad (\text{C.6})$$

The shear resistance of a single stud will be defined by:

$$P_{Rd} = \min \left\{ \begin{array}{l} 0.8 f_u \frac{\pi d^2}{4} \frac{1}{\gamma_V} = 57.9 \text{ kN} \\ 0.29 \alpha d^2 \sqrt{E_{cm} f_{ck}} \frac{1}{\gamma_V} = 127.8 \text{ kN} \end{array} \right. \quad (\text{C.7})$$

In each row, two studs will be placed with a distance of 150mm, considering the frictional forces that develop from the prevention of the lateral expansion of the concrete struts by the steel flanges, an additional resistance can be added as follows:

$$\frac{\mu P_{Rd}}{2} = 0.5 \times 57.9/2 = 14.5 \text{ kN/flange} \quad (\text{C.8})$$

The total resistance of a single stud will be  $P_{Rd} = 72.4 \text{ kN}$ .

The number of studs required to transmit the shear loads from the steel to the reinforced concrete will be:

$$n_{min} = \frac{N_{rc,Ed}}{P_{Rd}} = 1049/72.4 = 14.48 \rightarrow 16 \text{ studs} \quad (\text{C.9})$$

The maximum shear load per stud will be  $P_{Rd,max} = 1049/16 = 65.6 \text{ kN} < 72.4 \text{ kN}$

### C.1.2 Verification of steel strength

The part of the actions from the upper levels taken by the steel profile is considered:

$$N_{a,Ed,upper} = \delta N_{Ed,upper} = 0.45 \times 4944 = 2225 \text{ kN} \quad (\text{C.10})$$

The total stresses applied on the steel profile in the connection, considering the loads from the slab and the upper levels is:

$$\frac{N_{a,Ed,upper} + N_{Ed,slab}}{A_a} = (2225 + 1907)/0.01314 = 314 \text{ MPa} < f_{yd} = 323 \text{ MPa} \quad (\text{C.11})$$

### C.1.3 Verification of shear resistance of concrete surfaces

The shear connectors are placed along the load introduction zone (LIZ) length in two rows on the web in the longitudinal direction.

The length of the LIZ is defined by:

$$L_{LIZ} = \min \left\{ \begin{array}{l} 2b = 0.8 \text{ m} \\ L/3 = 4/3 = 1.33 \text{ m} \end{array} \right. \quad (\text{C.12})$$

Different surfaces need to be verified for the shear forces to be transmitted from the steel profile to the reinforced concrete via the shear connectors, as represented in Fig. C.3.

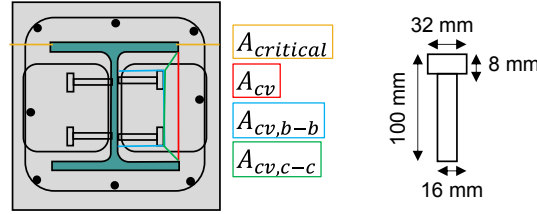


FIGURE C.3: Sections where to verify the shear resistance of the concrete surfaces.

The shear force considered is:

$$V_{L,Eq} = N_{rc,Ed}/2 = 1049/2 = 524.5 \text{ kN} \quad (\text{C.13})$$

The action taken by the concrete and reinforcement around the profile is divided by 2 because only one side along the profile is considered.

The dimensions of the headed studs are described in Fig. C.3. The transversal spacing  $s_t$  between two studs is 150 mm and fulfilled the rule  $s_t = 150 \text{ mm} > 4d = 64 \text{ mm}$ . The longitudinal spacing  $s_l$  needs to follow the rule  $s_l > 5d = 80 \text{ mm}$ . Thus, a spacing  $s_l = 200 \text{ mm}$  has been selected.

The objective is to determine the smallest surface area as presented in Fig. C.3. The different section areas are detailed as follows:

$$A_{cv} = 0.8 (0.28 - 2 \times 0.018) = 0.1952 \text{ m}^2 \quad (\text{C.14})$$

$$A_{cv,b-b} = 0.8 (2 \times 0.1 + 0.15 + 0.032) = 0.3056 \text{ m}^2 \quad (\text{C.15})$$

$$A_{cv,c-c} = 0.8 (2 \times x + 0.15 + 0.032) = 0.2202 \text{ m}^2 \quad (\text{C.16})$$

with  $x = \sqrt{a^2 + b^2} = \sqrt{34.75^2 + 31^2} = 46.6 \text{ mm}$ ,  $a = (280 - 10.5)/2 - 100 = 34.75 \text{ mm}$  and  $b = (244 - 150 - 32)/2 = 31 \text{ mm}$ .

The lower shear resistance of the concrete struts will be found in section  $A_{cv}$  as follows:

$$V_{L,Rd,max} = A_{cv} v f_{cd} \sin \theta_f \cos \theta_f \quad (\text{C.17})$$

with

$$\begin{aligned} \cot \theta_f = 1.2 &\rightarrow \sin \theta_f = 0.64 \text{ and } \cos \theta_f = 0.77 \\ v &= 0.6 (1 - f_{ck}/250) = 0.48 \end{aligned} \quad (\text{C.18})$$

This leads to a longitudinal shear resistance of the concrete struts:

$$V_{L,Rd,max} = 0.1952 \times 0.48 \times 28.33 \cdot 10^3 \times 0.64 \times 0.77 = 1308 \text{ kN} > V_{L,Eq} = 524.5 \text{ kN} \quad (\text{C.19})$$

The shear resistance of the stirrups below the studs (see Fig. C.3) needs to be verified. We will consider 1 stirrup below each row of studs, thus 4 stirrups with a diameter of 14mm. The

resistance of the stirrups is considered as follows:

$$V_{L,Rd,s} = A_{sc} f_{sd} \cot \theta_f = (2 \times 14^2 * \pi/4 \times 4) \times 500/1.15 \times 1.2 = 642.5 \text{ kN} > V_{L,Eq} = 524.5 \text{ kN} \quad (\text{C.20})$$

The verification of section  $A_{critical}$  must be verified as well. The applied longitudinal shear load  $V_{L,Ed,nc}$  to this area  $A_{c1}$ , which is not directly connected to the shear connectors, is:

$$\begin{aligned} V_{L,Ed} &= N_{Ed,beams} \left( 1 - \frac{N_{pl,a}}{N_{pl,Rd}} \right) \frac{A_{c1} 0.85 f_{cd} + A_{s1} f_{sd}}{A_c 0.85 f_{cd} + A_s f_{sd}} \\ &= 1907 \left( 1 - \frac{4241}{9423} \right) \frac{0.06 \times 0.4 \times 0.85 \times 50/1.5 + 3 \times 20^2 \pi/4 \times 500/1.15}{0.85 \times 0.14434 \times 50/1.5 + 0.002513 \times 500/1.15} \\ &= 220.5 \text{ kN} \end{aligned} \quad (\text{C.21})$$

The critical area between these two zones  $A_{critical} = 2 \times 0.06 \times 0.8 = 0.096 \text{ m}^2$ . This leads to a longitudinal shear resistance of the concrete struts:

$$V_{L,Rd,max} = 0.096 \times 0.48 \times 28.33 \times 10^3 \times 0.64 \times 0.77 = 643 \text{ kN} > V_{L,Eq} = 220.5 \text{ kN} \quad (\text{C.22})$$

The longitudinal shear resistance of the stirrups around the longitudinal reinforcement, which have a diameter of 8mm and arranged each 180mm, will follow:

$$\begin{aligned} V_{L,Rd,s} &= 4 \frac{A_s}{s_w} f_{yd} \cot \theta L_{LIZ} \\ &= 4 \frac{50.3}{180} 435 \times 1.2 \times 800 \\ &= 466.8 \text{ kN} > V_{L,Eq} = 220.5 \text{ kN} \rightarrow \text{OK} \end{aligned} \quad (\text{C.23})$$

## C.2 Considering circular reinforced composite dowel shear connectors

### C.2.1 Design of composite connectors

For CRCD connectors, the same actions need to be transferred from the steel profile by the shear connectors to the reinforced concrete:

$$N_{rc,Ed} = 1049 \text{ kN} \quad (\text{C.24})$$

#### Only on the web

To have similar geometries with the studs, traversing rebars with a diameter of 16mm and openings 50mm to respect the ratio  $d_c/d_s \approx 3$  are selected. Fig. C.4 describes the shear connectors, extra reinforcements, and strut and tie model. We assume the steel surface was sandblasted, and the traversing rebars are centrally positioned into the openings.

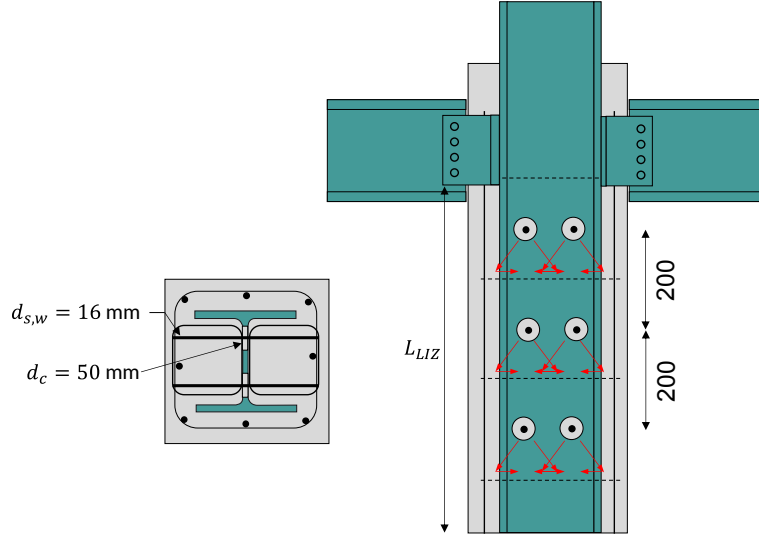


FIGURE C.4: Detail of the load introduction zone for CRCD connectors positioned on the web.

The resistance of a group of connectors only positioned on the web is given by:

$$P_{Rd} = \left( \tau_r A_b + \varphi \beta \left( n_w (P_{c,1,w} + P_{s,1,w}) + n_f (P_{c,1,f} + P_{s,1,f}) \right) \right) \frac{1}{\gamma_V} \quad (\text{C.25})$$

with

$$P_{c,1,w} = \frac{A_{c,w} f_{ck}}{\alpha} = (50^2 - 16^2) \pi / 4 \times 50 / 0.58 = 152.3 \text{ kN}$$

$$P_{s,1,w} = \min \begin{cases} 1.155 A_{s,w} f_{yk,w} = 1.155 \times 16^2 \pi / 4 \times 500 = 116.1 \text{ kN} \\ k_1 \alpha_b f_{uk} d_{s,w} t_w = 2.5 \times 1 \times 490 \times 16 \times 10.5 = 205.8 \text{ kN} \end{cases}$$

$$\varphi = 1 - 0.077 \ln(n_w + n_f) = 1 - 0.077 \ln(6) = 0.86$$

$$\beta = 1.7556 \sqrt{d_s/t} - 0.8078 (d_s/t) = 1.7556 \sqrt{16/10.5} - 0.8078 \times 16/10.5 = 0.94$$

$$\alpha = 0.0054 f_{ck} + 0.3085 = 0.0054 \times 50 + 0.3085 = 0.58$$

$$\tau_r = 0.3 \text{ MPa}$$

$$A_b = L_{LIZ} A_{CS} - 2 n_w d_c^2 \pi / 4 = 0.8 \times 1.62 - 2 \times 6 \times 50^2 \pi / 4 = 1.272 \text{ m}^2$$

Thus, the shear resistance of the group of connectors positioned on the web follows:

$$P_{Rd} = \left( 0.3 \times 1272 + 0.86 \times 0.94 \times 6 \times (152.3 + 116.1) \right) \frac{1}{1.62} = 1039.2 \text{ kN}$$

$$\eta = \frac{N_{rc,Ed}}{P_{Rd}} = \frac{1049}{1039} = 1.01 \rightarrow \text{OK} \quad (\text{C.27})$$

### On the web and the flanges

To arrange shear connectors on the flanges, the concrete cover of the steel section must be considered. In particular, the cover limits the bending radius achievable for the reinforcing bars. With a 60 mm concrete cover, the maximum allowable diameter for a traversing rebar is therefore 12 mm. Moreover, because the flange thickness (18 mm) differs from the web thickness (10.5 mm),

the concrete dowel in the opening of the flanges will be more confined. Consequently, a reduced slip capacity for flange-mounted connectors is expected.

Considering the same geometry for the connectors on the web as the previous design, we can estimate the slip capacity of the connectors on the web by:

$$s_{web} \approx 1.96 \frac{(50 - 16) \times 16}{\sqrt{50 \times 10.5}} + 2 = 16 \text{ mm} \quad (\text{C.28})$$

The most efficient design objective is to identify a flange-connector configuration that provides a slip capacity comparable to that achieved in the web, *i.e.*  $s_{web} \approx 16 \text{ mm}$ . However, to streamline fabrication—in particular, the machining of openings in the steel section—the flange opening diameter is fixed at  $d_{c,f} = 50 \text{ mm}$ . With the concrete cover governing the detailing of transverse reinforcement, the maximum permissible traversing rebar diameter is taken as  $d_{s,f} = 12 \text{ mm}$ . The corresponding slip capacity in the flange configuration is then estimated as

$$s_{flange} \approx 1.96 \frac{(50 - 12) \times 12}{\sqrt{50 \times 18}} + 2 = 9 \text{ mm}, \quad (\text{C.29})$$

where  $t_f = 18 \text{ mm}$  is the flange thickness. Although this value remains below the web target, it is expected to be sufficient to promote stress redistribution among the connectors.

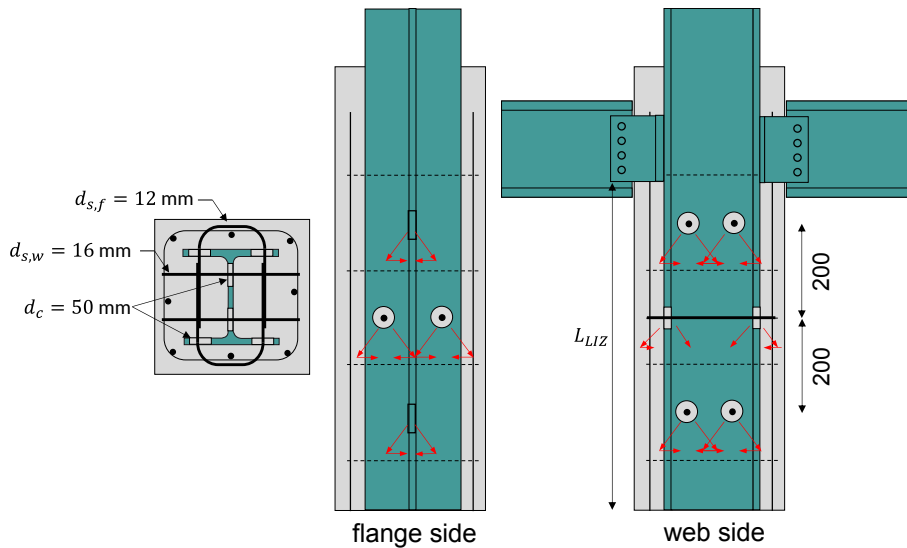


FIGURE C.5: Detail of the load introduction zone for CRCD connectors positioned on the web and the flanges.

Then, it is possible to predict the shear resistance of a group of connectors positioned on the web and the flanges. We will assume 2 rows of 2 connectors on the web and 1 row of 4 connectors on the flanges, see Fig. C.5:

$$P_{Rd} = (\tau_r A_b + \varphi \beta (n_w (P_{c,1,w} + P_{s,1,w}) + n_f (P_{c,1,f} + P_{s,1,f}))) \frac{1}{\gamma_V} \quad (\text{C.30})$$

with

$$\begin{aligned}
P_{c,1,w} &= \frac{A_{c,w} f_{ck}}{\alpha} = (50^2 - 16^2) \pi / 4 \times 50 / 0.58 = 152.3 \text{ kN} \\
P_{s,1,w} &= \min \begin{cases} 1.155 A_{s,w} f_{yk,w} = 1.155 \times 16^2 \pi / 4 \times 500 = 116.1 \text{ kN} \\ k_1 \alpha_b f_{uk} d_{s,w} t_w = 2.5 \times 1 \times 490 \times 16 \times 10.5 = 205.8 \text{ kN} \end{cases} \\
P_{c,1,f} &= \frac{A_{c,f} f_{ck}}{\alpha} = (50^2 - 12^2) \pi / 4 \times 50 / 0.58 = 159.9 \text{ kN} \\
P_{s,1,f} &= \min \begin{cases} 1.155 A_{s,f} f_{yk,f} = 1.155 \times 12^2 \pi / 4 \times 500 = 65.3 \text{ kN} \\ k_1 \alpha_b f_{uk} d_{s,f} t_f = 2.5 \times 1 \times 490 \times 16 \times 10.5 = 264.6 \text{ kN} \end{cases} \\
\varphi &= 1 - 0.077 \ln(n_w + n_f) = 1 - 0.077 \ln(4 + 4) = 0.84 \\
\beta &= 1.7556 \sqrt{d_s/t} - 0.8078 (d_s/t) = 1.7556 \times \sqrt{2.78} - 0.8078 \times 2.78 = 0.89 \\
d_s/t &= \min \left( \frac{d_{s,w}}{t_w}, \frac{d_{s,f}}{t_f} \right) = 50/18 = 2.78 \\
\alpha &= 0.0054 f_{ck} + 0.3085 = 0.0054 \times 50 + 0.3085 = 0.58 \\
\tau_r &= 0.3 \\
A_b &= L_{LIZ} A_{CS} - 2 (n_w + n_f) d_c^2 \pi / 4 = 0.8 \times 1.62 - 2 \times 8 \times 50^2 \pi / 4 = 1.264 \text{ m}^2
\end{aligned} \tag{C.31}$$

Thus, the shear resistance of the group of connectors positioned on the web follows:

$$\begin{aligned}
P_{Rd} &= (0.3 \times 1264 + 0.84 \times 0.89 \times (4 \times (152.3 + 116.1) + 4 \times (159.9 + 65.3))) \frac{1}{1.62} \\
&= 1150 \text{ kN} > N_{rc,Ed} = 1049 \text{ kN} \rightarrow OK
\end{aligned} \tag{C.32}$$

### C.2.2 Verification of steel strength

The verification of the steel strength will be equal to that of the one with headed studs.

### C.2.3 Verification of shear resistance of concrete surfaces

The length of the load introduction zone is kept at 0.8 m. Nevertheless, distinct modifications must be considered in the verification of the shear resistance of the concrete surfaces, depending on whether the connector layout is provided on the web only or on both the web and the flanges.

#### Only on the web

If the connectors are installed on the web only, the load-transfer mechanism is as shown in Fig. C.6. The design shear resistance is decomposed into a friction contribution and a CRCD contribution, equal to 235.6 kN and 802.4 kN, respectively. The frictional resistance is assumed to be uniformly mobilized over the full steel–concrete interface of the section and along the load introduction zone (LIZ) length. Accordingly, the corresponding compression struts are idealized as uniformly distributed and are equilibrated by transverse reinforcement (stirrups) surrounding the longitudinal reinforcement.

The friction component is assumed to be uniformly mobilized along the perimeter of the steel–concrete interface and along the LIZ length. The outer flange-related surface represents 34.6% of

the total perimeter, while the inner surface represents 65.4%. Accordingly, the friction resistance is taken as

$$V_{L,Rd,friction,out} = 81.5 \text{ kN in } A_{s1}, \quad V_{L,Rd,friction,in} = 154.2 \text{ kN in } A_{s0}.$$

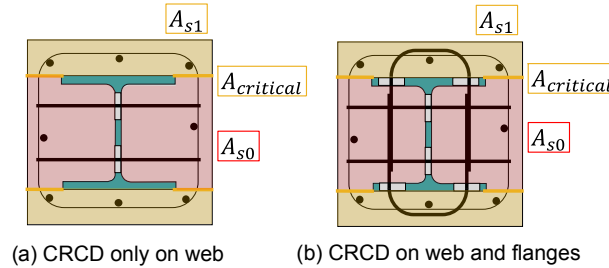


FIGURE C.6: Detail of the different areas in the concrete-encased steel section.

The minimum transverse reinforcement required to balance the CRCD-related strut action is therefore

$$\frac{A_{s,min}}{s_w} = \frac{235.6 \times 10^3}{f_{yd} \cot \theta L_{LIZ}} = \frac{235.6 \times 10^3}{435 \times 1.2 \times 0.8 \times 10^3} = 0.56 \text{ mm}^2/\text{mm}, \quad (\text{C.33})$$

where  $f_{yd} = 435 \text{ MPa}$ ,  $\cot \theta = 1.2$ , and  $L_{LIZ} = 0.8 \text{ m}$ . For a stirrup spacing of  $s_w = 200 \text{ mm}$ , this yields  $A_{s,min} = 112 \text{ mm}^2$ , which corresponds to additional equivalent reinforcement  $\phi 6/200$  to be added to the existing stirrups.

Since the traversing rebar reaches the outer leg of the stirrups, it must also be verified that it can equilibrate the tensile tie force associated with the concrete strut system. The available tie resistance from the traversing reinforcement is estimated as

$$V_{L,Rd,s} = A_{sc} f_{sd} \cot \theta_f = \left(6 \cdot \frac{\pi}{4} 16^2\right) \left(\frac{500}{1.15}\right) \cdot 1.2 = 629.7 \text{ kN} < V_{L,Ed,CRCD} = 802.4 \text{ kN}, \quad (\text{C.34})$$

leaving a residual demand of

$$\Delta V = 802.4 - 629.7 = 172.7 \text{ kN}. \quad (\text{C.35})$$

This deficit can be covered by adding one supplementary closed bar in each chamber of the steel section (square layout), using  $\phi 12$  bars (see Fig. C.4). The resulting total tie resistance becomes

$$\begin{aligned} V_{L,Rd,s,tot} &= 629.7 + \left(2 \cdot \frac{\pi}{4} 12^2 \cdot 2\right) \left(\frac{500}{1.15}\right) \cdot 1.2 \\ &= 629.7 + 236.1 = 865.8 \text{ kN} > V_{L,Ed,CRCD} = 802.4 \text{ kN} \rightarrow \text{OK}. \end{aligned} \quad (\text{C.36})$$

Finally, the verification of the critical section  $A_{critical}$  shall also be performed. This check is analogous to the headed-stud configuration with the outer friction  $V_{L,Rd,friction,out}$  taken out from the shear load to be transferred to zone  $A_{s1}$  and is therefore not repeated here.

### On the web and the flanges

The key difference with respect to the previous configuration is that the connectors placed on the flanges transfer shear directly into the edge concrete zones adjacent to the flanges, denoted  $A_{s1}$ , see Fig. C.6. In order to quantify the share of the design shear force carried by the concrete inside the flanges ( $A_{s0}$ ) and outside the flanges ( $A_{s1}$ ), it is assumed that the shear resistance of the flange connectors is symmetrically distributed, *i.e.* one half is transferred to each side of the flanges. The friction is assumed uniformly distributed along the cross-section perimeter and LIZ length. The outer part of the flanges accounts for 34.6% of the surface and the inner part for 65.4%, thus the friction resistance in the area  $A_{s1}$  is 81.5 kN and in  $A_{s0}$  is 154.2 kN.

With this, we can decompose the contribution of the CRCD connectors to the inner and outer parts of the flanges:

$$\begin{aligned} P_{Rd,inner} &= (0.84 \times 0.89 \times (4 \times (152.3 + 116.1) + \frac{4}{2} \times (159.9 + 65.3))) \frac{1}{1.62} = 707.2 \text{ kN} \\ P_{Rd,outer} &= (0.84 \times 0.89 \times (\frac{4}{2} \times (159.9 + 65.3))) \frac{1}{1.62} = 209 \text{ kN} \end{aligned} \quad (\text{C.37})$$

Under this assumption, the shear demand applied to the outer zones is

$$V_{Ed}(A_{s1}) = 2 V_{L,Ed} - V_{L,Rd,friction,out} = 441 - 81.5 = 359.5 \text{ kN}, \quad (\text{C.38})$$

while the remaining shear demand applied to the inner zone is

$$V_{Ed}(A_{s0}) = N_{rc,Ed} - 2 V_{L,Ed} - V_{L,Rd,friction,in} = 1049 - 441 - 154.2 = 453.8 \text{ kN}. \quad (\text{C.39})$$

The four CRCD connectors located on the flanges provide a design shear resistance of 209 kN within  $A_{s1}$ . Consequently, an additional

$$\Delta V_{A_{s0} \rightarrow A_{s1}} = 359.5 - 209 = 150.5 \text{ kN} \quad (\text{C.40})$$

must be transferred from the connector system acting in  $A_{s0}$  towards  $A_{s1}$ . This transfer demand is lower than in the web-only configuration; hence, the verification of  $A_{critical}$  is not governing and was already covered in the headed-stud case.

The flange-mounted CRCD connectors generate compression struts both towards the interior of the section and towards the exterior. The interior struts are equilibrated through the opposite flange, whereas the exterior struts must be balanced by longitudinal tension ties. Therefore, only half of the flange-connector contribution needs to be equilibrated by reinforcement, taken as 209 kN. The available tie resistance provided by the traversing reinforcement associated with the four flange connectors is

$$V_{L,Rd,s} = A_{sc} f_{sd} \cot \theta_f = \left(4 \cdot \frac{\pi}{4} 12^2\right) \left(\frac{500}{1.15}\right) \cdot 1.2 = 236.1 \text{ kN} > 209 \text{ kN} \rightarrow \text{OK}. \quad (\text{C.41})$$

In addition, the compression struts induced by the CRCD connectors on the web must be equilibrated. The corresponding tie demand is 498 kN. The resistance provided by the existing

traversing reinforcement is

$$V_{L,Rd,s} = \left(4 \cdot \frac{\pi}{4} 16^2\right) \left(\frac{500}{1.15}\right) \cdot 1.2 = 419.8 \text{ kN} < 498 \text{ kN}. \quad (\text{C.42})$$

Hence, supplementary ties are required. Providing one closed square bar of diameter  $\phi 8$  in each chamber yields

$$\begin{aligned} V_{L,Rd,tot} &= 419.8 + \left(4 \cdot \frac{\pi}{4} 8^2\right) \left(\frac{500}{1.15}\right) \cdot 1.2 \\ &= 419.8 + 105.0 = 524.8 \text{ kN} > 498 \text{ kN} \rightarrow \text{OK}. \end{aligned} \quad (\text{C.43})$$

### C.3 Conclusion

The comparative design using headed studs and CRCD connectors highlights the respective strengths and limitations of both shear-transfer solutions. In terms of shear resistance, the CRCD option requires only six connectors placed on the web, whereas the stud solution requires eight headed studs welded on each side of the web. Placing CRCD connectors on both the web and the flanges also promotes a more uniform distribution of shear over the composite cross-section. For a given embedment length, this configuration provides a higher shear-transfer capacity.

These advantages come at the cost of increased design effort. When CRCD connectors are used on the web and flanges, additional verification steps are needed, particularly with respect to slip capacity, and the wider parameter space leads to more potential design iterations. A further practical limitation of CRCD connectors is the detailing requirement for the traversing reinforcement: the rebar should be centred within the opening, or—specifically for the top load introduction zone—at least positioned at the bottom of the opening



# Bibliography

- 1-102, prCEN/TS1994 (2022). *Eurocode 4: Design rules for the use of Composite Dowels*. European Standard prCEN/TS 1994-1-102. Brussels: European Committee for Standardization.
- ACI (2010). *ACI 363R-10: Report on High-Strength Concrete*. Tech. rep. Farmington Hills, MI: American Concrete Institute.
- Ahn, Jin-Hee et al. (2010). "Shear resistance of the perfobond-rib shear connector depending on concrete strength and rib arrangement". In: *Journal of Constructional Steel Research* 66.10, pp. 1295–1307. DOI: 10.1016/j.jcsr.2010.04.008.
- AIJ (1991). *Standard for Structural Calculation of Steel Reinforced Concrete Structures*. Standard. Tokyo: Architectural Institute of Japan.
- Akçaoğlu, Tülin, Mustafa Tokyay, and Tahir Çelik (2004). "Effect of coarse aggregate size and matrix quality on ITZ and failure behavior of concrete under uniaxial compression". In: *Cement and Concrete Composites* 26.6, pp. 633–638. DOI: 10.1016/S0958-9465(03)00092-1.
- Al-Darzi, S. Y. K., A. R. Chen, and Y. Q. Liu (2007). "Finite Element Simulation and Parametric Studies of Perfobond Rib Connector". In: *American Journal of Applied Sciences* 4.3, pp. 122–127.
- Alenezi, K. et al. (2015). "Behavior of shear connectors in composite column of cold-formed steel with lipped C-channel assembled with ferro-cement jacket". In: *Construction and Building Materials* 84, pp. 39–45. DOI: 10.1016/j.conbuildmat.2015.03.015.
- Almusaed, Amjad et al. (2024). "Assessing the Impact of Recycled Building Materials on Environmental Sustainability and Energy Efficiency: A Comprehensive Framework for Reducing Greenhouse Gas Emissions". In: *Buildings* 14.6, p. 1566. DOI: 10.3390/buildings14061566.
- Altoubat, S. A. (2002). "The Pickett effect at early age and experiment separating its mechanisms in tension". In: *Materials and Structures* 35.248, pp. 211–218. DOI: 10.1617/13730.
- Andrä, H.-P. (1990). "Economical shear connectors with high fatigue strength". In: *IABSE Symposium Brussels*. Vol. 60, pp. 167–172. DOI: 10.5169/SEALS-46457.
- ANSI/AISC360 (2016). *Specification for Structural Steel Buildings*. American National Standard ANSI/AISC 360-16. United States of America: American Institute of Steel Construction.
- AS/NZS2327 (2017). *Composite structures—Composite steel-concrete construction in buildings*. Standard AS/NZS 2327:2017. Australia: Australian/New Zealand Standard.
- Berman, Alan D., William A. Ducker, and Jacob N. Israelachvili (1996). "Origin and Characterization of Different StickSlip Friction Mechanisms". In: *Langmuir* 12.19, pp. 4559–4563. DOI: 10.1021/1a950896z.
- Bogdan, T. et al. (2023). "Load introduction for concrete-encased steel composite columns using high-performance materials". In: *ce/papers* 6.3-4, pp. 320–325. DOI: 10.1002/cepa.2709.

- Bonilla, Jorge et al. (2018). "Review of stud shear resistance prediction in steel-concrete composite beams". In: *Steel and Composite Structures* 27.3, pp. 355–370. DOI: 10.12989/scs.2018.27.3.355.
- Braun, Matthias, Renata Obiala, and Christoph Odenbreit (2015). "Analyses of the loadbearing behaviour of deep-embedded concrete dowels, CoSFB: Analyses of the loadbearing behaviour of deep-embedded concrete dowels, CoSFB". In: *Steel Construction* 8.3, pp. 167–173. DOI: 10.1002/stco.201510024.
- Braun, Matthias, Renata Obiala, and Christoph Odenbreit (2017). "Numerical simulation of the load bearing behaviour of concrete dowels in slim-floor construction - CoSFB". In: *ce/papers* 1.2-3, pp. 1831–1840. DOI: 10.1002/cepa.227.
- Braun, Matthias Volker (2018). "Investigation of the Load-Bearing Behaviour of CoSFB-Dowels". PhD thesis. University of Luxembourg, Luxembourg, Luxembourg.
- Cabeza, Luisa F. et al. (2014). "Life cycle assessment (LCA) and life cycle energy analysis (LCEA) of buildings and the building sector: A review". In: *Renewable and Sustainable Energy Reviews* 29, pp. 394–416. DOI: 10.1016/j.rser.2013.08.037.
- Caldarone, Michael A. (2009). *High-strength concrete: a practical guide*. London: Taylor & Francis.
- Chamasemani, Niyousha Fallah et al. (2023). "Environmental Impacts of Reinforced Concrete Buildings: Comparing Common and Sustainable Materials: A Case Study". In: *Construction Materials* 4.1, pp. 1–15. DOI: 10.3390/constrmater4010001.
- Chen, Cheng-Chih and Nan-Jiao Lin (2006). "Analytical model for predicting axial capacity and behavior of concrete encased steel composite stub columns". In: *Journal of Constructional Steel Research* 62.5, pp. 424–433. DOI: 10.1016/j.jcsr.2005.04.021.
- Chen, Hai et al. (2017). "Shear Performance of Nonparallel Type Twin Perfobond Steel Plate Shear Connectors: FEM Analysis and Experimental Verification". In: *8th International Conference on Composite Construction in Steel and Concrete*.
- Chrzanowski, Maciej (2019). "Shear Transfer in Heavy Steel-Concrete Composite Columns with Multiple Encased Steel Profiles". PhD thesis. Luxembourg: Université du Luxembourg.
- Chrzanowski, Maciej et al. (2019). "Transfer of shear stresses at steel-concrete interface: Experimental tests and literature review". In: *Steel Construction* 12.1, pp. 44–54. DOI: 10.1002/stco.201800024.
- Cândido-Martins, J.P.S., L.F. Costa-Neves, and P.C.G. da S. Vellasco (2010). "Experimental evaluation of the structural response of Perfobond shear connectors". In: *Engineering Structures* 32.8, pp. 1976–1985. DOI: 10.1016/j.engstruct.2010.02.031.
- Dassault, System (2014). *ABAQUS Documentation*. Tech. rep. Version 6.14. USA: Dassault System.
- Di, Jin et al. (2018). "Push-out test of large perfobond connectors in steel-concrete joints of hybrid bridges". In: *Journal of Constructional Steel Research* 150, pp. 415–429. DOI: 10.1016/j.jcsr.2018.09.002.
- Du, Yong et al. (2021). "Behaviour of ultra-high strength concrete encased steel columns subject to ISO-834 fire". In: *Steel and Composite Structures* 38.2, pp. 121–139.
- Dunberry, E., D. Leblanc, and R. G. Redwood (1987). "Cross-section strength of concrete-filled HSS columns at simple beam connections". In: *Canadian Journal of Civil Engineering* 14.3. Publisher: NRC Research Press, pp. 408–417. DOI: 10.1139/187-059.

- El-Tawil, Sherif and Gregory Deierlein (1999). "Strength and Ductility of Concrete Encased Composite Columns". In: *Journal of Structural Engineering*. DOI: 10.1061/(ASCE)0733-9445(1999)125:9(1009).
- Ellobody, Ehab and Ben Young (2011). "Numerical simulation of concrete encased steel composite columns". In: *Journal of Constructional Steel Research* 67.2, pp. 211–222. DOI: 10.1016/j.jcsr.2010.08.003.
- EN10034 (1993). *Structural steel I and H sections - Tolerances on shape and dimensions*. European Standard. Brussels.
- EN10080 (2005). *Steel for the reinforcement of concrete - Weldable reinforcing steel - General*. European Standard. Brussels.
- EN1090-2 (2018). *Execution of steel structures and aluminium structures - Part 2: Technical requirements for steel structures*. European Standard. Brussels.
- EN12390-13 (2021). *Testing hardened concrete — Part 13: Determination of secant modulus of elasticity in compression*. European Standard. Brussels.
- EN12390-3 (2019). *Testing hardened concrete — Part 3: Compressive strength of test specimens*. European Standard. Brussels.
- EN12390-5 (2019). *Testing hardened concrete — Part 5: Flexural strength of test specimens*. European Standard. Brussels.
- EN12390-6 (2023). *Testing hardened concrete — Part 6: Tensile splitting strength of test specimens*. European Standard. Brussels.
- EN197-1 (2000). *Cement: Part 1, Composition, specifications and conformity criteria for common cements*. European Standard. Brussels.
- EN197-5 (2021). *Cement - Part 5: Portland-composite cement CEM II/C-M and Composite cement CEM VI*. European Standard. Brussels.
- EN1990 (2002). *Eurocode: Basis of structural design*. European Standard. Brussels.
- EN1992-1-1 (2023). *Eurocode 2: Design of concrete structures - Part 1-1: General rules and rules for buildings, bridges and civil engineering structures*. European Standard. Brussels.
- EN1993-1-8 (2005). *Eurocode 3: Design of steel structures - Part 1-8: Design of joints*. European Standard. Brussels.
- EN1994-1-1 (2004). *Eurocode 4: Design of composite steel and concrete structures - Part 1-1: General rules and rules for buildings*. European Standard. Brussels.
- Fang, Zhuangcheng et al. (2023). "Shear performance of high-strength friction-grip bolted shear connector in prefabricated steel-UHPC composite beams: Finite element modelling and parametric study". In: *Case Studies in Construction Materials* 18, e01860. DOI: 10.1016/j.cscm.2023.e01860.
- fib (2008). *Constitutive modelling of high strength/high performance concrete*. Bulletin 42. Lausanne: International Federation for Structural Concrete (fib).
- FprEN1993-1-1 (2022). *Eurocode 3: Design of steel structures - Part 1-1: General rules and rules for buildings*. European Standard. Brussels.
- Goralski, Claus and Josef Hegger (2006). *Zusammenwirken von Beton und Stahlprofil bei kammerbetonierten Verbundträgern*. 22. Aachen: Technische Hochschule Aachen.

- Grzeszykowski, B., M. J. Lewandowski-Szewczyk, and M. Niedośpiał (2023). "Load introduction to composite columns revisited—Significance of force allocation and shear connection stiffness". In: *Engineering Structures* 295, p. 116800. DOI: 10.1016/j.engstruct.2023.116800.
- Grzeszykowski, Bartosz and Elżbieta Danuta Szmigiera (2017). "Analysis of the load transfer between materials in composite concrete encased steel columns loaded axially". In: *ce/papers* 1.2-3, pp. 2090–2099. DOI: 10.1002/cepa.254.
- Gu, Dawei et al. (2025). "Shear performance of perfobond leiste (PBL) connectors in engineered cementitious composites (ECC)". In: *Engineering Structures* 322, p. 119093. DOI: 10.1016/j.engstruct.2024.119093.
- Gu, Ji-Cheng et al. (1984). "Slip motion and stability of a single degree of freedom elastic system with rate and state dependent friction". In: *Journal of the Mechanics and Physics of Solids* 32.3, pp. 167–196. DOI: 10.1016/0022-5096(84)90007-3.
- Guse, Ulf and Hubert K. Hilsdorf (1998). *Dauerhaftigkeit hochfester Betone*. Deutscher Ausschuss für Stahlbeton 487. Berlin: Beuth.
- Hamdan, M. and Y. Hunaiti (1991). "Factors affecting bond strength in composite columns". In: *Proc., 3rd Int. Conf. on Steel-Concrete Composite Structures*. Fukuoka, Japan: Association for International Cooperation and Research in Steel-Concrete Composites, pp. 213–218.
- Hanswille, Gerhard, Marc Illmann, and Berthold Dobelmann (2024). "Federsteifigkeit von Kopfbolzendübeln und Ermittlung der Längsschubkräfte in langen Schwertkonstruktionen". In: *Stahlbau* 93. DOI: 10.1002/stab.202400022.
- Hanswille, Gerhard, Markus Schäfer, and Marco Bergmann (2020). *Eurocode 4 - DIN EN 1994-1-1 Bemessung und Konstruktion von Verbundtragwerken aus Stahl und Beton*. Ernst und Sohn. Berlin.
- Hawkins, N. M. (1973). "Strength of concrete-encased steel beams". In: *Institution of Engineers (Australia) Civ Eng Trans* 1-2, pp. 39–46.
- He, Shaohua, Zhi Fang, and Ayman S. Mosallam (2017). "Push-out tests for perfobond strip connectors with UHPC grout in the joints of steel-concrete hybrid bridge girders". In: *Engineering Structures* 135, pp. 177–190. DOI: 10.1016/j.engstruct.2017.01.008.
- He, Shaohua et al. (2016). "Experimental study on perfobond strip connector in steel-concrete joints of hybrid bridges". In: *Journal of Constructional Steel Research*.
- He, Shaohua et al. (2021). "Investigation on structural performance of perfobond strip connector group in steel-concrete joints". In: *Engineering Structures* 242, p. 112571. DOI: 10.1016/j.engstruct.2021.112571.
- Hegger, J, J Gallwoszus, and S Rauscher (2009). "Load-Carrying Behaviour of Connectors under Shear, Tension and Compression in Ultra High Performance Concrete". In: *Nordic Steel Construction Conference 2009*. Lulea.
- Hegger, J. and S. Rauscher (2008). "High performance materials – Advances in composite constructions". In: *International FIB Symposium*. Amsterdam: CRC Press. DOI: 10.1201/9781439828410.CH60.
- Hegger, Josef et al. (2001). "Testing of shear connectors in high strength concrete". In: *International Symposium on Connections between Steel and Concrete*. Stuttgart: RILEM Publications.

- Hegger, Josef et al. (2006). "Load-Deformation Behavior of Shear Connectors in High Strength Concrete Subjected to Static and Fatigue Loading". In: *IABSE Symposium Budapest 2006*. Budapest, pp. 17–24.
- Hegger, Josef et al. (2009). "High-Performance Materials in Composite Construction". In: *Structural Engineering International* 19.4, pp. 438–446.
- Heinemeyer, Sabine (2011). "Zum Trag- und Verformungsverhalten von Verbundträgern aus ultrahochfestem Beton mit Verbundleisten". PhD thesis. Aachen: RWTH Aachen University.
- Hosseinpour, Emad (2018). "Push-out test on the web opening shear connector for a slim-floor steel beam - Experimental and analytical study". In: *Engineering Structures*. DOI: 10.1016/j.engstruct.2018.02.047.
- Huang, Zhenyu et al. (2021). "Bond-slip behaviour of H-shaped steel embedded in UHPFRC". In: *Steel and Composite Structures* 38.5. DOI: 10.12989/scs.2021.38.5.563.
- Hunaiti, Y. M. (1991). "Bond strength in battened composite columns". In: *Journal of Structural Engineering* 117.3, pp. 699–714.
- ISO12491 (1997). *Statistical methods for quality control of building materials and components*. International Standard. Geneva.
- ISO15630-1:2019 (2019). *Steel for the reinforcement and prestressing of concrete — Test methods — Part 1: Reinforcing bars, rods and wire*. International Standard. Geneva / Brussels.
- ISO6892-1:2019 (2019). *Metallic materials — Tensile testing — Part 1: Method of test at room temperature*. International Standard. Geneva / Brussels.
- ISO8501-1 (1988). *Preparation of steel substrates before application of paints and related products*. International Standard. Geneva.
- ISO9013 (1993). *Thermal cutting — Classification of thermal cuts — Geometrical product specification and quality tolerances*. International Standard. Geneva.
- Jacobs V, William P. and Jerome F. Hajjar (2010). "Load Transfer in Composite Construction". In: *Structures Congress 2010*. Orlando, Florida, United States: American Society of Civil Engineers, pp. 1229–1240. DOI: 10.1061/41130(369)112.
- JGJ138 (2016). *Code for design of composite structures*. Standard JGJ 138-2016. Beijing: Ministry of Housing and Urban-Rural Construction of the People's Republic of China.
- Johansson, Mathias (2003). "Composite action in connection regions of concrete-filled steel tube columns". In: *Steel and Composite Structures* 3.1, pp. 47–64. DOI: 10.12989/SCS.2003.3.1.047.
- Johnson, R.P. (2004). *Composite Structures of Steel and Concrete*. Blackwell Publishing. Oxford, UK.
- Kang, Jae Yoon et al. (2014). "Evaluation of the Shear Strength of Perfobond Rib Connectors in Ultra High Performance Concrete". In: *Engineering* 06.13, pp. 989–999. DOI: 10.4236/eng.2014.613089.
- Kim, Chang-Soo et al. (2012). "Eccentric Axial Load Testing for Concrete-Encased Steel Columns Using 800 MPa Steel and 100 MPa Concrete". In: *Journal of Structural Engineering* 138.8. Publisher: American Society of Civil Engineers, pp. 1019–1031. DOI: 10.1061/(ASCE)ST.1943-541X.0000533.
- Kim, Sang-Hyo et al. (2011). "Experimental study on joint of spliced steel-PSC hybrid girder, Part I: Proposed parallel-perfobond-rib-type joint". In: *Engineering Structures* 33.8, pp. 2382–2397. DOI: 10.1016/j.engstruct.2011.04.012.

- Kosmatka, Kerkhoff, and Panarese (2002). "Fly Ash, Slag, Silica Fume, and Natural Pozzolans". In: *Design and Control of Concrete Mixtures*. Skokie, IL.
- Kraus, D. and O. Wurzer (1997). "Bearing capacity of concrete dowels". In: *Composite Construction - Conventional and Innovative*. IABSE, pp. 133–138. DOI: 10.5169/SEALS-957.
- Lacki, Piotr, Anna Derlatka, and Przemysław Kasza (2018). "Comparison of steel-concrete composite column and steel column". In: *Composite Structures* 202, pp. 82–88. DOI: 10.1016/j.compstruct.2017.11.055.
- Lai, Binglin and J. Y. Richard Liew (2021). "Investigation on axial load-shortening behaviour of high strength concrete encased steel composite section". In: *Engineering Structures* 227, p. 111401. DOI: 10.1016/j.engstruct.2020.111401.
- Lai, Binglin, J. Y. Richard Liew, and An Le Hoang (2019). "Behavior of high strength concrete encased steel composite stub columns with C130 concrete and S690 steel". In: *Engineering Structures* 200, p. 109743. DOI: 10.1016/j.engstruct.2019.109743.
- Le Minh, Hoang et al. (2021). "A concrete damage plasticity model for predicting the effects of compressive high-strength concrete under static and dynamic loads". In: *Journal of Building Engineering* 44, p. 103239. DOI: 10.1016/j.jobbe.2021.103239.
- Lee, Pil-Goo, Chang-Su Shim, and Sung-Pil Chang (2005). "Static and fatigue behavior of large stud shear connectors for steel–concrete composite bridges". In: *Journal of Constructional Steel Research* 61.9, pp. 1270–1285. DOI: 10.1016/j.jcsr.2005.01.007.
- Leng, Jingchen et al. (2024). "Mechanical behavior of a novel compact steel-UHPC joint for hybrid girder bridges: Experimental and numerical investigation". In: *Journal of Constructional Steel Research* 218, p. 108742. DOI: 10.1016/j.jcsr.2024.108742.
- Leonhardt, F. et al. (1987). "Neues, vorteilhaftes Verbundmittel für Stahlverbund-Tragwerke mit hoher Dauerfestigkeit." In: *Beton- und Stahlbetonbau* 82.12, pp. 325–331. DOI: 10.1002/best.198700500.
- Li, Junquan et al. (2020). "Durability of ultra-high performance concrete – A review". In: *Construction and Building Materials* 255, p. 119296. DOI: 10.1016/j.conbuildmat.2020.119296.
- Li, Zhixiang et al. (2018). "Load Sharing and Slip Distribution in Multiple Holes of a Perfobond Rib Shear Connector". In: *Journal of Structural Engineering* 144.9, p. 04018147. DOI: 10.1061/(ASCE)ST.1943-541X.0002152.
- Liu, Yangqing et al. (2023). "Shear performance and failure process of perfobond connector in steel-UHPC composite structures". In: *Structures* 50, pp. 1461–1475. DOI: 10.1016/j.istruc.2023.02.106.
- MacRae, Gregory et al. (2004). "Brace-Beam-Column Connections for Concentrically Braced Frames with Concrete Filled Tube Columns". In: *Journal of Structural Engineering* 130.2, pp. 233–243. DOI: 10.1061/(ASCE)0733-9445(2004)130:2(233).
- Maso, J. C., ed. (1996). *Interfacial Transition Zone in Concrete*. London: CRC Press. DOI: 10.1201/9781482271560.
- Mehta, P Kumar and Paulo J M Monteiro (2001). *Concrete, Microstructure, Properties and Materials*. 3rd ed. United States: The McGraw-Hill Companies.

- Mishra, Sunny and S.R. Satish Kumar (2022). "Confinement detailing of concrete encased steel concrete composite columns". In: *ASPS Conference Proceedings* 1.1, pp. 111–119. DOI: 10.38208/acp.v1.481.
- Model Code, fib (2013). *Model Code for Concrete Structures*. Tech. rep. fib Model Code 2010. Lausanne Switzerland: Fédération Internationale du Béton.
- Moradian, Mohammadreza and Munzer Hassan (2024). "The Seismic Behavior of Rectangular Concrete-Encased Steel Bridge Piers: A Review". In: *Applied Sciences* 14.15, p. 6627. DOI: 10.3390/app14156627.
- Morikawa, H. et al. (1993). "Experimental study on connecting structure for the Tsurumi Fairy Bridge". In: *Jpn. J. Struct. Eng. A* 39, pp. 1335–1346.
- Mu, Yasojima, and Kanakubo (2019). "Shear Performance of FRCC Beam-Column Joints Using Various Polymer Fibers". In: *Journal of Civil Engineering and Architecture* 13.9. DOI: 10.17265/1934-7359/2019.09.003.
- Neville, Adam (1997). "Aggregate Bond and Modulus of Elasticity of Concrete". In: *Materials Journal* 94.1, pp. 71–74. DOI: 10.14359/287.
- Neville, Adam M. (1996). *Properties of concrete*. 4th ed. New York: Wiley.
- Oguejofor, E. C. and M. U. Hosain (1994). "A parametric study of perfobond rib shear connectors". In: *Canadian Journal of Civil Engineering* 21.4, pp. 614–625. DOI: 10.1139/194-063.
- Ovuoba, Brianna and Gary S. Prinz (2018). "Headed Shear Stud Fatigue Demands in Composite Bridge Girders Having Varied Stud Pitch, Girder Depth, and Span Length". In: *Journal of Bridge Engineering* 23.11, p. 04018085. DOI: 10.1061/(ASCE)BE.1943-5592.0001303.
- Paoletti, Maxence and Markus Schäfer (2023). "Load transfer of circular reinforced composite dowel connector: a comparison of existing analytical equations". In: *10th European Conference on Steel and Composite Structures*. Vol. 6. Amsterdam, Netherlands: Ernst und Sohn, pp. 101–106. DOI: 10.1002/cepa.2613.
- Papastergiou, Dimitrios and Jean-Paul Lebet (2014). "Design and experimental verification of an innovative steel–concrete composite beam". In: *Journal of Constructional Steel Research* 93, pp. 9–19. DOI: 10.1016/j.jcsr.2013.10.017.
- Pavlović, Marko et al. (2013). "Bolted shear connectors vs. headed studs behaviour in push-out tests". In: *Journal of Constructional Steel Research* 88, pp. 134–149. DOI: 10.1016/j.jcsr.2013.05.003.
- Rao, G. Appa and B. K. Raghu Prasad (2002). "Fracture energy and softening behavior of high-strength concrete". In: *Cement and Concrete Research* 32.2, pp. 247–252. DOI: 10.1016/S0008-8846(01)00667-6.
- Raous, Michel and M'hamed Ali Karray (2009). "Model coupling friction and adhesion for steel concrete interfaces". In: *International Journal of Computer Applications in Technology* 34.1, p. 42. DOI: 10.1504/IJCAT.2009.022701.
- Rauscher, Sabine et al. (2006). "Load deformation behavior of shear connectors in high strength concrete". In: *IABSE Symposium Budapest 2006*. Vol. 92. IABSE reports. Budapest: IABSE.
- Reinhardt, Hans W (2000). "Structural behaviour of high performance concrete". In: *Otto Graf Journal* 11, p. 10.

- Rommel, Gerd (1994). *Zum Zug- und Schubtragverhalten von Bauteilen aus hochfestem Beton*. Deutscher Ausschuss für Stahlbeton. Berlin: Beuth.
- Roberts, Wayne and Robert Heywood (1995). "Development and testing of a new shear connector for steel concrete composite bridges". In: *Fourth International Bridge Engineering Conference*. Washington, DC: National Academy Press, pp. 137–145.
- Roeder, Charles W. (1985). "Bond stress of embedded steel shapes in concrete". In: *Effects of Damage and Redundancy on Structural Performance*. ASCE, pp. 227–240.
- Roeder, Charles W., Robert Chmielowski, and Colin B. Brown (1999). "Shear Connector Requirements for Embedded Steel Sections". In: *Journal of Structural Engineering* 125.2, pp. 142–151. DOI: 10.1061/(ASCE)0733-9445(1999)125:2(142).
- Roik, K, M Breit, and K Schwalbenhofer (1984). *Untersuchung der Verbundwirkung zwischen Stahlprofil und Beton bei Stützenkonstruktionen*. Projekt 51. Düsseldorf: Studiengesellschaft für Anwendungstechnik von Eisen und Stahl e.V.
- Sauerborn, Norbert and Joachim Kretz (2018). "Verbundstützen: Grundlagen der Bemessung, Konstruktion und Ausführung". In: *Stahlbau Kalender 2018*. Ed. by Ulrike Kuhlmann. Wiley, pp. 569–630. DOI: 10.1002/9783433607701.ch6.
- Saw, H. S. and J. Y. Richard Liew (2000). "Assessment of current methods for the design of composite columns in buildings". In: *Journal of Constructional Steel Research* 53.2, pp. 121–147. DOI: 10.1016/S0143-974X(99)00062-0.
- Shen, Dejian et al. (2016). "Experimental study of early-age bond behavior between high strength concrete and steel bars using a pull-out test". In: *Construction and Building Materials* 113, pp. 653–663. DOI: 10.1016/j.conbuildmat.2016.03.094.
- Su, Qing-Tian et al. (2014). "Experimental research on bearing mechanism of perfobond rib shear connectors". In: *Journal of Constructional Steel Research* 95, pp. 22–31. DOI: 10.1016/j.jcsr.2013.11.020.
- Su, Qingtian, Guotao Yang, and Mark A. Bradford (2016). "Bearing Capacity of Perfobond Rib Shear Connectors in Composite Girder Bridges". In: *Journal of Bridge Engineering* 21.4, p. 06015009. DOI: 10.1061/(ASCE)BE.1943-5592.0000865.
- Sutter, Larry, Thomas Van Dam, and Renee Munn (2016). *Supplementary Cementitious Materials*. Tech. rep. FHWA-HIF-16-001. Washington, DC: Federal Highway Administration.
- Taerwe, Luc (1992). "Influence of steel fibers on strain-softening of high-strength concrete". In: *ACI Materials Journal* 89.1, pp. 54–60.
- Tan, Xingyu, Zhi Fang, and Xuanwei Xiong (2022). "Experimental study on group effect of perfobond strip connectors encased in UHPC". In: *Engineering Structures* 250, p. 113424. DOI: 10.1016/j.engstruct.2021.113424.
- Ushijima, Yoshitaka et al. (2001). "An experimental study on shear characteristics of perfobond strip and its rational strength equations". In: *International Symposium on Connections between Steel and Concrete*. RILEM Publications, pp. 1066–1075.
- Verissimo, Gustavo et al. (2007). "Avaliação do desempenho de um conector de cisalhamento em chapa dentada para estruturas mistas de aço e concreto". In: *Congresso de Métodos Numéricos em Engenharia*. Porto, Portugal: Universidade do Porto.

- Vianna, J. et al. (2013). "Experimental study of Perfobond shear connectors in composite construction". In: *Journal of Constructional Steel Research* 81, pp. 62–75. DOI: 10.1016/j.jcsr.2012.11.002.
- Vianna, J.da.C. et al. (2008). "Structural behaviour of T-Perfobond shear connectors in composite girders: An experimental approach". In: *Engineering Structures* 30.9, pp. 2381–2391. DOI: 10.1016/j.engstruct.2008.01.015.
- Vianna, J.da.C. et al. (2009). "Experimental assessment of Perfobond and T-Perfobond shear connectors' structural response". In: *Journal of Constructional Steel Research* 65.2, pp. 408–421. DOI: 10.1016/j.jcsr.2008.02.011.
- Wang, Wei et al. (2023). "Interfacial bonding stress transfer and failure mechanism between corrugated steel plate and reinforced concrete". In: *Engineering Failure Analysis* 153, p. 107555. DOI: 10.1016/j.engfailanal.2023.107555.
- Wang, Wei'an et al. (2014). "Study on Load-Slip Characteristic Curves of Perfobond Shear Connectors in Hybrid Structures". In: *Journal of Advanced Concrete Technology* 12.10, pp. 413–424. DOI: 10.3151/jact.12.413.
- Wang, Xianlin, Airong Chen, and Yuqing Liu (2022). "Explainable ensemble learning model for predicting steel section-concrete bond strength". In: *Construction and Building Materials* 356, p. 129239. DOI: 10.1016/j.conbuildmat.2022.129239.
- Wang, Xianlin, Yuqing Liu, and Haohui Xin (2021). "Bond strength prediction of concrete-encased steel structures using hybrid machine learning method". In: *Structures* 32, pp. 2279–2292. DOI: 10.1016/j.istruc.2021.04.018.
- Wang, Xianlin et al. (2019). "Effect of concrete cover on the bond-slip behavior between steel section and concrete in SRC structures". In: *Construction and Building Materials* 229, p. 116855. DOI: 10.1016/j.conbuildmat.2019.116855.
- Wang, Xianlin et al. (2020). "Bond behavior and shear transfer of steel section-concrete interface with studs: Testing and modeling". In: *Construction and Building Materials* 264, p. 120251. DOI: 10.1016/j.conbuildmat.2020.120251.
- Wang, Xianlin et al. (2022). "Shear transfer mechanism of perforated web connection for concrete encased steel structures". In: *Engineering Structures* 252, p. 113418. DOI: 10.1016/j.engstruct.2021.113418.
- Wium, J. A. and J. P. Lebet (1992). "Colonnes mixtes: transfert des forces du profilé métallique au béton d'enrobage". PhD thesis. Lausanne: Ecole Polytechnique Fédérale de Lausanne.
- Ye, M. and R. Luo (1999). "Study of shear force of steel-concrete composite with a large number of closely arranged studs". In: *Steel Constr* 14.3, pp. 39–42.
- Yoo, Doo-Yeol and Hyun-Oh Shin (2018). "Bond performance of steel rebar embedded in 80–180MPa ultra-high-strength concrete". In: *Cement and Concrete Composites* 93, pp. 206–217. DOI: 10.1016/j.cemconcomp.2018.07.017.
- Zapfe, C. (2001). "Trag- und Verformungsverhalten von Verbundträgern mit Betondübeln zur Übertragung der Längsschubkräfte". PhD thesis. München: Universität der Bundeswehr München.
- Zeng, Ming-gen, Qing-tian Su, and Chng Wu (2008). "Shear force distribution of welded studs in anchorage zone of steel and concrete composite pylon of cable-stayed bridge". In: *Bridge Constr* 4, pp. 27–30.

- Zhang, Jianrui et al. (2023). "Push-out tests of interfacial bond slip between H-shaped steel and ultra-high performance concrete". In: *Structures* 57, p. 105268. DOI: 10.1016/j.istruc.2023.105268.
- Zhang, Qinghua et al. (2017a). "Analytical Study on Internal Force Transfer of Perfobond Rib Shear Connector Group Using a Nonlinear Spring Model". In: *Journal of Bridge Engineering* 22.10, p. 04017081. DOI: 10.1061/(ASCE)BE.1943-5592.0001123.
- Zhang, Qinghua et al. (2017b). "Theoretical and Experimental Studies of the Internal Force Transfer Mechanism of Perfobond Rib Shear Connector Group". In: *Journal of Bridge Engineering* 22.2, p. 04016112. DOI: 10.1061/(ASCE)BE.1943-5592.0000997.
- Zhang, S.L. (2006). "Friction, Damage and Stick-Slip in the Scratching of Polymers". In: *Tribology and Interface Engineering Series*. Vol. 51. Elsevier, pp. 56–84. DOI: 10.1016/S0167-8922(06)80039-8.
- Zhang, Youyou et al. (2019). "Numerical parametric study on ultimate load and ductility of concrete encased equal-leg angle steel composite columns". In: *Engineering Structures* 200, p. 109679. DOI: 10.1016/j.engstruct.2019.109679.
- Zhao, Canhui et al. (2018). "Experimental investigation on the bearing mechanism of Perfobond rib shear connectors". In: *Engineering Structures* 159, pp. 172–184. DOI: 10.1016/j.engstruct.2017.12.047.
- Zheng, Shuangjie et al. (2016a). "Parametric study on shear capacity of circular-hole and long-hole perfobond shear connector". In: *Journal of Constructional Steel Research* 117, pp. 64–80. DOI: 10.1016/j.jcsr.2015.09.012.
- Zheng, Shuangjie et al. (2016b). "Shear behavior and analytical model of perfobond connectors". In: *Steel and Composite Structures* 20.1, pp. 71–89. DOI: 10.12989/SCS.2016.20.1.071.
- Zhou, Y. et al. (2015). "Study on mechanical behavior and fatigue performance of steel-concrete composite joints of railway hybrid girder cable-stayed bridges". In: *China Civ. Eng* 48.11, pp. 77–83.
- Zou, Yang et al. (2020). "Shear behavior of perfobond connectors in the steel-concrete joints of hybrid bridges". In: *Journal of Constructional Steel Research* 172, p. 106217. DOI: 10.1016/j.jcsr.2020.106217.
- Zou, Yang et al. (2021). "Mechanical behavior of perfobond connector group in steel-concrete joint of hybrid bridge". In: *Structures* 30, pp. 925–936. DOI: 10.1016/j.istruc.2021.01.046.
- Šavor, Zlatko (2010). "Croatian Bridges designed by Structural Department of Zagreb Civil Engineering Faculty utilizing SOFiSTiK Software". In: *Bridges Eurasia 2010*.